CONSTITUTIVE MODELLING AND FINITE ELEMENT ANALYSIS IN GEOMECHANICS

by

L. RESENDE B.Sc.(Eng.), M.Sc.(Eng)

A thesis submitted in fulfilment of the requirements for the degree of Doctor of Philosphy

Department of Civil Engineering
University of Cape Town

September 1984

ABSTRACT

The major objective of the work presented in this thesis was the development of a constitutive model for hard rock at high pressure. The model should capture the important features of material behaviour and should be soundly based on mechanical principles; furthermore it should be simple enough to permit implementation and use in large general purpose finite element codes.

As a preliminary exercise, a state-of-the-art plasticity cap model was developed in order to provide a basis for comparison with the new model. Existing cap models were shown to exhibit certain inconsistencies associated with the suppression of a regime of potentially unstable behaviour; these inconsistencies were identified and eliminated in the formulation which is presented in this thesis. The new rock model was based on internal damage concepts. The model is isotropic, and internal damage is measured by a scalar damage parameter. The properties of the material degrade as the damage parameter increases, and an evolution law governs the rate at which damage occurs.

The damage model was calibrated against experimental results for Bushveld Norite, which is a very hard, brittle rock. The general form of the model, however, is suitable for application to soil and concrete. Both the plasticity cap model and the damage model were implemented into the finite element code NOSTRUM (developed by the Applied Mechanics Research Unit at the University of Cape Town). Solutions of a series of boundary value problems, including typical mining excavation problems, are presented to illustrate and compare the models.

DECLARATION

I hereby declare that this thesis is essentially my own work and that it has not been submitted for a degree at any other university.

Signed by candidate

Signature Removed

L.RESENDE

September 1984

ACKNOWLEDGEMENTS

I wish to express my gratitude to the following:

My supervisor, Professor J.B. Martin, for his patience and encouragement that made my research a pleasant task.

My postgraduate colleagues, especially Gino Duffet, Dave Hawla and Colin Mercer, for many useful discussions.

The staff of the Rock Mechanics Laboratory of the Chamber of Mines of South Africa Research Organization for their cooperation, in particular Vasso Stavropoulou who provided some experimental data.

The staff of the Computer Centre of the University of Cape Town who kept the UNIVAC going.

The Chamber of Mines of South Africa for their financial support.

The Council for Scientific and Industrial Research for their financial assistance.

Mrs. Val Atkinson and Mrs. Bridget Atkinson for being kind enough to type the manuscript.

Mr. Harold Cable for the printing of this thesis.

Finally, my parents and friends for their continuous support and encouragement.

CONTENTS

TITLE PAGE		(i)
ABSTRACT		(ii)
DECLARATION		(iii)
ACKNOWLEDGEMENTS		(iv)
CONTENTS		(v)
NOMENCLATURE		(ix)
1.	INTRODUCTION	1
2.	LITERATURE REVIEW	5
2.1	Necessary features of a constitutive model for geomaterials	5
2.1.1	Material charachteristics	6
2.1.2	Other desirable characteristics	7
2.2	Existing models	8
2.2.1	Models based on elasticity	8
2.2.2	Open surface plasticity models	10
2.2.3	Closed surface plasticity models	14
2.2.4	Other inelastic models	16
2.3	Performance of existing models with regard to the desired features	17
2.3.1	Models based on elasticity	17
2.3.2	Open surface plasticity models	18
2.3.3	Closed surface plasticity models	19
2.3.4	Other inelastic models	20
2.4	Directions for further development of constitutive models	21
3.	A STATE OF THE ART PLASTICITY CAP MODEL	22
3.1	Introduction	22
3.2	Structure of the plasticity constitutive equations	24

3.3	Treatment of the constitutive equations in multi-surface plasticity	27
3.4	Cap model yield functions	28
3.5	Invariant form of the constitutive equations	31
3.6	Stability and completeness of some existing cap models	51
3.7	Constitutive equations for plane and axisymmetric problems	56
4.	IMPLEMENTATION OF THE PLASTICITY CAP MODEL AND APPLICATIONS	62
4.1	Finite element implementation using an incremental tangent approach	63
4.2	Integration of the constitutive equations	65
4.3	Illustration of cap model behaviour	71
4.3.1	Uniaxial strain test on McCormack Ranch sand	71
4.3.2	Proportional loading triaxial test	72
4.4	Illustration of corner behaviour	73
4.5	Analysis of boundary value problems	84
4.5.1	Rigid and rough strip footing	89
4.5.2	Flexible and smooth strip footing	94
5.	AN INTERNAL DAMAGE CONSTITUTIVE MODEL	100
5.1	Characteristics of rock material of interest and modelling	100
5.2	Framework of the damage constitutive equations	103
5.3	Invariant form of the constitutive equations and its physical interpretation	105
5.4	Model parameters and forms of the damage evolution law	120
5.5	Constitutive equations for the three dimensional case	123

5.6	Illustration of damage model behaviour	129
5.6.1	Hydrostatic compression test	129
5.6.2	Triaxial compression tests	131
5.6.3	Hydrostatic tension test	136
5.6.4	Triaxial tension test	136
6.	CALIBRATION OF THE DAMAGE MODEL FOR BUSHVELD NORITE	140
6.1	Experimental results for Norite	140
6.2	Calibration of material parameters	141
6.3	Importance and sensitivity of damage parameters	155
7.	IMPLEMENTATION OF THE DAMAGE MODEL AND APPLICATIONS	160
7.1	Finite element implementation using an incremental tangent approach	160
7.2	Integration of the constitutive equations	160
7.3	Analysis of excavation problems	163
7.3.1	Square tunnel	164
7.3.2	Seam excavation	179
7.4	Analysis of standard configurations	191
7.4.1	Brazilian test	191
7.4.2	Bridgman anvil	199
8.	CONCLUSIONS AND DIRECTIONS FOR FUTURE WORK	204
8.1	Conclusions	204
8.2	Directions for future work	205
REFERENCES		208

APPENDIX A	Second Order Work	A.1
APPENDIX B	Treatment of the Constitutive Equations in Multisurface Plasticity	B.1
APPENDIX C	Extracts from NOSTRUM User's Manual	C.1
APPENDIX D	Published Work	D.1

NOMENCLATURE

This is a list of symbols used in the main text of this thesis.

Special Symbols

$\dot{}$	the differential with respect to a time scale
$\underset{\sim}{}$	a vector or matrix
[ ]	a matrix
| |	the absolute value of
T (superscript)	the transpose of a vector or matrix
-1(superscript)	the inverse of a matrix
d	the differentiation with respect to
∂	the partial differentiation with respect to

Lower Case Characters

$a_1 - a_6$	material constants
$a_{11}, a_{12}, a_{21}, a_{22}$	constitutive coefficients
$b_1 - b_3$	material constants
c	cohesion
$c_1 - c_3$	material constants
d_1	material constant
e	effective shear strain
$\underset{\sim}{e}$	deviator strain vector
e_{ij}	deviator strain tensor
g	gravity acceleration constant
h	depth
$\underset{\sim}{h}$	defined in equn.(3.89b)
k	material constant
$\underset{\sim}{n}$	defined in equn. (3.81b)

$\underset{\sim}{R}$	total load vector
T	tension cutoff value
V	volume of element
W	material constant

Greek Characters

α	material constant
γ_{ij}	engineering shear strain
δ_{ij}	Kronecker delta
Δ	increment in
$\underset{\sim}{\varepsilon}$	strain vector
ε_{ij}	strain tensor
ε_{kk}, ε_v	volumetric strain
κ	internal variables
λ	plastic multiplier or measure of damage
ν	Poisson's ratio
ρ	mass density
$\underset{\sim}{\sigma}$	stress vector
σ_{ij}	stress tensor
σ_{kk}	volumetric stress
σ_m	hydrostatic stress
$\sigma_1,\sigma_2,\sigma_3$	principal stresses
σ_y	vertical stress
σ_x,σ_z	horizontal stresses
τ_{xy}	shear stress
ϕ	angle of friction

$\underset{\sim}{R}$	total load vector
T	tension cutoff value
V	volume of element
W	material constant

Greek Characters

α	material constant
γ_{ij}	engineering shear strain
δ_{ij}	Kronecker delta
Δ	increment in
$\underset{\sim}{\varepsilon}$	strain vector
ε_{ij}	strain tensor
ε_{kk}, ε_v	volumetric strain
κ	internal variables
λ	plastic multiplier or measure of damage
ν	Poisson's ratio
ρ	mass density
$\underset{\sim}{\sigma}$	stress vector
σ_{ij}	stress tensor
σ_{kk}	volumetric stress
σ_m	hydrostatic stress
$\sigma_1,\sigma_2,\sigma_3$	principal stresses
σ_y	vertical stress
σ_x,σ_z	horizontal stresses
τ_{xy}	shear stress
ϕ	angle of friction

Subscripts

e	e-th element
i,j,k,ℓ	tensorial indeces
t	time
o,(o)	initial value of
max	maximum value of
α	active yield surface number

Right Superscripts

c	current value of
e,p,d,c	elastic,plastic, damage and coupling components
i	i-th iteration
o	initial value of

Left Superscript

e	e-th element

CHAPTER 1

INTRODUCTION

There are a large number of situations in geotechnical engineering which require the detailed analysis of boundary value problems involving nonlinear material behaviour. The development of finite element and associated techniques has reached a state where the solution of many of these problems is possible. However, the range of constitutive models which can be used in conjunction with numerical procedures is still limited, and this aspect is the weakest link in the simulation of geotechnical problems at the present time.

In this thesis, we shall be concerned with the development of realistic and soundly based (in the mechanics sense) constitutive laws for geomaterials as well as their effective implementation in finite element codes for the solution of general boundary value problems. The main aim is to develop laws which capture the important features of the material behaviour and yet are simple enough to permit implementation and use in large scale finite element codes.

Although the subject of research undertaken in this thesis is broader, the immediate motivation was to solve problems associated with deep underground excavations in rock such as those arising in the South African gold mining industry. The nature and mechanism of deformation and fracture of rock are particularly important since they dictate the strategy to be adopted in supporting the mining excavations. The development of constitutive models to predict the patterns and extent of fracturing in the vicinity of excavations then becomes a necessary adjunct to the experimental investigations, both in the laboratory and in situ.

One of the goals of this thesis is to produce a constitutive model which includes the important characteristics exhibited by the rock material in

laboratory tests. This model is implemented in a finite element code to solve the excavation problems of interest and the results are compared with experimental observations. The comparisons then provide feedback for further development of the constitutive model. This process, which has previously been referred to as the identification problem, is a continuing one and it must be emphasised that the research contained in this work constitutes only the first few steps of the identification process.

The availability of a fairly complete set of laboratory data as well as some in situ observation data for Bushveld Norite made it logical to concentrate the first efforts on this material. However, the development of the constitutive model has been carried out considering a variety of materials which exhibit similar behaviour, specifically soils and concrete. Consequently, the models produced can in principle be generalised for materials other than Bushveld Norite. In fact, a considerable amount of input for the development of the rock constitutive model came from observations of behaviour of other materials such as concrete.

It is important to point out from the outset that the models of constitutive behaviour investigated in this thesis are of a continuum nature in contrast to models based on fracture mechanics where the performance of the structure is determined by the severity of a single or a few major cracks. The model which is finally proposed in this work is based on damage mechanics where the performance of the structure is determined by the progressive deterioration of the material as loading takes place. This deterioration, or damage, is described in terms of a continuous defect field. The most realistic assessment of the behaviour of the geotechnical problems we are concerned with would be obtained by combining the two approaches, but this is outside the scope of this thesis.

The implementation and testing of the models proposed is carried out using NOSTRUM, a large scale finite element code developed by the University of Cape Town Applied Mechanics Research Unit (formerly known

as the Nonlinear Structural Mechanics Research Unit) for the analysis of nonlinear boundary value problems including continua and structures.

To best describe the spirit in which the work contained in this thesis concerning the development of constitutive laws was carried out, it is appropriate to use the words of J.W. Dougill[5]:

> "A variety of approaches have been used in describing the behaviour of materials such as rock and concrete. At one extreme, attempts are made to generate rules to reproduce the results of experiments but without dependence on any general principles of mechanics. The resulting equations can be exceedingly useful. However, there can be no guarantee of general utility outside the range of behaviour covered by the data on which the rules are based. At the other extreme, attention is focused on a class of ideal materials defined by elementary postulates that are sufficient to provide a general theory of behaviour. Of course, this generality is concerned with the ideal behaviour so that the question remains as to how closely this can be made to correspond to that of any particular physical material. The two approaches are complementary. Both have attractions in particular circumstances. The experimentalist's view can provide precision over a narrow range. The mechanician's broader brush treatment may be less responsive to the fine detail of behaviour of a given material, but has the potential for greater generality in applications.
>
> In practice, neither extreme is followed to the exclusion of the other. In designing and interpreting experiments, the range of variables may be constrained using mechanics arguments that

as the Nonlinear Structural Mechanics Research Unit) for the analysis of nonlinear boundary value problems including continua and structures.

To best describe the spirit in which the work contained in this thesis concerning the development of constitutive laws was carried out, it is appropriate to use the words of J.W. Dougill[5]:

> "A variety of approaches have been used in describing the behaviour of materials such as rock and concrete. At one extreme, attempts are made to generate rules to reproduce the results of experiments but without dependence on any general principles of mechanics. The resulting equations can be exceedingly useful. However, there can be no guarantee of general utility outside the range of behaviour covered by the data on which the rules are based. At the other extreme, attention is focused on a class of ideal materials defined by elementary postulates that are sufficient to provide a general theory of behaviour. Of course, this generality is concerned with the ideal behaviour so that the question remains as to how closely this can be made to correspond to that of any particular physical material. The two approaches are complementary. Both have attractions in particular circumstances. The experimentalist's view can provide precision over a narrow range. The mechanician's broader brush treatment may be less responsive to the fine detail of behaviour of a given material, but has the potential for greater generality in applications.
>
> In practice, neither extreme is followed to the exclusion of the other. In designing and interpreting experiments, the range of variables may be constrained using mechanics arguments that

> reflect the consequences of assessing isotropy, linearity, elasticity, etc. Similarly, the choice of initial postulates, central to the development of a more general theory, is conditioned by knowledge of the physical phenomena obtained from experiments on real materials."

To conclude the introduction, a brief account of the organisation of this thesis is given. Chapter 2 is a literature review of existing constitutive models for soils, rock and concrete. A mechanics based classification of the models is adopted and an attempt is made to evaluate their merits according to a stated set of required features of a constitutive model for geological materials. In Chapter 3, a state of the art plasticity cap model is developed and particular attention is given to the behaviour of the model at the intersections of the yield surfaces. The finite element implementation and applications of the cap model are given in Chapter 4. A constitutive model for rock materials based on an internal damage theory is proposed in Chapter 5. In Chapter 6, the damage model is calibrated for Bushveld Norite and the importance of its material parameters evaluated. Finally, Chapter 7 deals with the finite element implementation of the damage model and some real excavation problems are solved using the model.

CHAPTER 2

LITERATURE REVIEW

In this chapter, attention will be given only to the behaviour of the solid skeleton under isothermal conditions. Time dependent behaviour will also not be considered. The constitutive behaviour of the other components of geomaterials, water and sometimes air is reasonably well understood. The analysis of the coupled equations governing the mechanical behaviour of the multiphase material is possible but beyond the scope of the present work.

Although this is a review of the mechanics of geomaterials in general (i.e. soils, rocks and concretes), special reference is made to particular types of materials at different times. A brief and more specific review of the mechanical behaviour of rocks is undertaken later as an introduction to chapter 5.

A considerable number of reviews of this nature have appeared in the literature recently, including Chen [1], Chen and Saleeb [2], Christian and Desai [3], Desai [4], Dougill [5], Marti and Cundall [6], Naylor [7] and Nelson [8] among others.

2.1 Necessary Features of a Constitutive Model for Geomaterials

The heterogeneous nature of geomaterials probably accounts for the complex behaviour which they exhibit. This complexity is illustrated by the large number of constitutive models which have been proposed for different conditions and stress paths. In addition, constitutive descriptions are normally attempted on the basis of limited data due to the difficulties arising in the physical testing of geomaterials under complex stress paths. Only a few simple stress histories can be reliably monitored and the observations must be generalised to more

complex stress histories. An untested constitutive bias is introduced in this generalisation and as a result there is no generally accepted constitutive theory at present.

The complexity of the material behaviour together with the experimental difficulties make it impossible to state a set of rules for evaluating the adequacy of a particular consitutive law. However, there are a number of features of geomaterial behaviour which are known with enough certainty and can be used as a starting platform.

2.1.1 Material Characteristics

The material characteristics to be displayed by a constitutive model for geomaterials are listed.

Behaviour under monotonically increasing shear:

- The secant slope of the shear stress/strain curve should never increase
- A shear stress limit should exist
- Nonlinearity appears at very low strains
- Some materials exhibit shear strain softening in the 'post failure' region followed by a residual stress state
- Hydrostatic stresses should affect the shear stress limit (increased compression producing a higher limiting shear stress as well as a higher residual shear stress)
- Volumetric changes should accompany shear strains, normally some compaction followed by dilatation for denser materials or compaction alone for looser materials. The volume changes should be bounded.

Behaviour under cyclic shear:

- Shear stiffness should decrease as deformation increases
- The model should exhibit initial elastic unloading followed by loss of stiffness on further unloading

- Permanent deformations for all stress levels should be present. These deformations should be bounded
- Irrecoverable cumulative volume changes, which are bounded, should be induced by cyclic shear
- The model should produce hysteresis loops which are progressively narrower and stiffer as the number of cycles increases.

Behaviour under monotonically increasing hydrostatic compression:

- The hydrostatic stress/strain curve should exhibit progressively stiffer response
- The compressive volumetric strain should be bounded.

Behaviour under cyclic hydrostatic compression:

- With some exceptions, permanent volumetric strains should be present. These are cumulative but bounded
- Initial unloading is elastic.

History induced behaviour:

- History induced anisotropy should be present both due to stress state and oriented fabric microstructure
- The model should have a certain amount of memory, e.g. maximum stresses and strains.

2.1.2 Other Desirable Characteristics

The items presented in 2.1.1 represent experience gained in geomaterial behaviour but alone are not enough to provide a model capable of solving engineering boundary value problems using finite element or associated techniques. Additional desirable features are:

- The constitutive law should satisfy the theoretical

requirements needed to prove existence, uniqueness and stability of solutions provided the physical evidence supports it. If there is no such physical evidence it is important to show that the model produces numerical solutions which are an approximation of the physical problems and not something that will vary widely with slightly different input, algorithm variation or computer accuracy

- The parameters in the constitutive model should be as few as possible and determinable from simple experimental tests

- The number of state variables required to define the material behaviour at each point should not be so great that it becomes practically unfeasible to run the model with present computer technology

- Models are most useful when written in modular form so as to make them code independent and easily transportable.

2.2 Existing Models

It is not practical to consider all the existing constitutive models in a brief review such as this. Therefore an attempt is made to include models which represent all the main categories according to a mechanics classification. There is also a bias towards the models which are more commonly used in the solution of practical boundary value problems.

2.2.1 Models Based on Elasticity

The simplest model is the isotropic linear elastic which is defined by Young's modulus and Poisson's ratio or by shear modulus and bulk modulus. It is generally accepted that it is not capable of representing geomaterial behaviour except at very low stresses. The reason for considering this model, apart from completeness, is its usefulness for providing simple numerical and even sometimes analytical

solutions which often constitute a qualitative guide for subsequent more sophisticated analyses. Linear elasticity is also the starting point for the development of other more complex models. Anisotropic linear elastic behaviour can be modelled by relaxing the symmetries of the constitutive tensor $D_{ijk\ell}$ in

$$\sigma_{ij} = D_{ijk\ell}\, \varepsilon_{k\ell} \tag{2.1}$$

where σ_{ij} and $\varepsilon_{k\ell}$ are the stress and strain tensor respectively (note that all stresses are to be interpreted as effective stresses).

The elastic models can be extended to nonlinear elasticity by making the material constants depend on stress and strain. This has given rise to stress/strain laws of the hyperbolic, exponential, polynomial, logarithmic and power law type. One of the most frequently used such laws is the hyperbolic model first developed by Kondner [9] for undrained saturated clays under triaxial conditions. It required two constants to define the shear behaviour while the volumetric behaviour was considered to be incompressible. The hyperbolic model was later generalised, by introducing more parameters, and used to solve realistic boundary value problems [10 - 12].

Another class of nonlinear elastic models are the so called variable moduli models and an example is the model proposed by Nelson and Baron [13]. In these models both the shear and bulk moduli are defined as nonlinear functions of the stress and/or strain invariants. One common choice is

$$\begin{aligned} &\text{shear modulus } G = G\,(s,\ \sigma_m) \\ &\text{bulk modulus } K = K\,(\sigma_m,\ \varepsilon_v) \end{aligned} \tag{2.2}$$

where ε_v is the volumetric strain ($= \varepsilon_{kk}$), σ_m is the hydrostatic stress ($= 1/3\ \sigma_{kk}$) and s is the second invariant of the deviator stress tensor ($= \sqrt{1/2\, s_{ij}\, s_{ij}}$, $s_{ij} = \sigma_{ij} - 1/3\ \sigma_{kk}\ \delta_{ij}$).

There is no doubt that the nonlinear elastic models can be refined until

they approach the real behaviour as closely as desired simply by progressively increasing the number of parameters. However, this becomes a curve-fitting exercise which cannot claim generality and will only be successful for the particular case under consideration. In particular, the generalisation to multiaxial behaviour presents special difficulties.

Some investigators have also used elasticity based models in conjunction with failure criteria and unloading rules in order to build some degree of path dependency into these models. Such models cannot be strictly considered in this section since the reversibility characteristic of elasticity has been relaxed.

2.2.2 Open Surface Plasticity Models

The fact that geomaterials yield indefinitely when subjected to sufficient shear stress and also exhibit permanent strains, has led investigators to use plasticity theory to represent their behaviour. Elastic-plastic models provide inviscid equations relating stress rates to strain rates. These rates are denoted by $\dot{\sigma}_{ij}$ and $\dot{\varepsilon}_{ij}$ and it is assumed that the strain rate can be written as the sum of an elastic and a plastic component,

$$\dot{\varepsilon}_{ij} = \dot{\varepsilon}^{e}_{ij} + \dot{\varepsilon}^{p}_{ij} \tag{2.3}$$

The elastic equations are written as

$$\dot{\varepsilon}^{e}_{ij} = (D^{-1})_{ijk\ell}\, \dot{\sigma}_{k\ell} \quad . \tag{2.4}$$

The onset of yielding is given by

$$F(\sigma_{ij},\kappa) = 0 \tag{2.5}$$

where F is a yield function which depends on stress and some internal variables κ which could be plastic strains. The plastic components of strain rate $\dot{\varepsilon}^{p}_{ij}$ are given by a flow rule

$$\dot{\varepsilon}^{p}_{ij} = \lambda \frac{\partial Q}{\partial \sigma_{ij}} \tag{2.6}$$

where $Q = Q(\sigma_{ij}, \kappa)$ is a plastic potential (Hill [14]) and λ is a non-negative multiplier,

$$\begin{aligned} &\text{with} \quad \lambda > 0 \quad \text{if } F = 0 \text{ and } \dot{F} = 0 \\ &\text{and} \quad \lambda = 0 \quad \text{if } F = 0 \text{ and } \dot{F} < 0 \\ &\qquad\qquad\quad \text{or } F < 0 \\ &\qquad\qquad\quad (F > 0 \text{ not allowed}). \end{aligned} \tag{2.7}$$

If $Q \equiv F$ we have associated plasticity while for $Q \neq F$ we have a non-associated flow rule. The constitutive equations for elastic-plastic behaviour are then obtained from equations (2.3, 2.4 and 2.6) as

$$\dot{\sigma}_{ij} = D_{ijk\ell} \left(\dot{\varepsilon}_{k\ell} - \dot{\varepsilon}^{p}_{k\ell} \right) \quad . \tag{2.8}$$

The different plasticity models are based on different choices of yield surface (F), hardening law (κ) and flow rule plastic potential (Q). Many forms of the yield function have been proposed in the past . The classical ones are all isotropic, thus reducing the six dimensional stress space to at the most three invariant stresses (or alternatively three principal stresses). The first category includes the Von-Mises and Tresca yield surfaces [15] shown in Fig. 2.1(a) and (b). The Von-Mises yield law can be written as

$$F = s - k = 0 \tag{2.9}$$

where k is a material parameter while the Tresca yield law is given by

$$F = \left| \sigma_1 - \sigma_3 \right| - k \tag{2.10}$$

where σ_1 , σ_3 are the maximum and minimum principal stresses and k is a material constant. An obvious shortcoming of these two laws is the lack of dependence of yielding on the hydrostatic stress state. This has led to the Drucker-Prager [16] generalisation of the Von-Mises law where the yield function is given as (compressive stress is negative)

$$F = \alpha\sigma_m + s - k = 0 \qquad (2.11)$$

and the Mohr-Coulomb yield criterion which constitutes a generalisation of the Tresca law

$$F = \alpha(\sigma_1+\sigma_3) + |\sigma_1-\sigma_3| - k = 0 \qquad (2.12)$$

where α, k are material constants. These laws are illustrated in Fig. 2.1(c) and (d). The Mohr-Coulomb has been the most popular of these yield surfaces since it is thought to be a good representation of the failure envelope of many geomaterials over a wide range of stress. However, it possesses the shortcoming that it is not continuously differentiable in the Π-plane. To overcome this and also to provide even better approximations to the failure envelope, several attempts have been made to smooth the Π-section of the Mohr-Coulomb model, Fig. 2.1(e). These are due to Gudehus [17], Zienkiewicz and Pande [18] and Lade and Duncan [19] for soil and rock materials; and Bresler and Pister [20], Willam and Warnke [21], Ottosen [22], Reimann [23] and Hsieh et al [24] for concrete. Some of the above models also include a meridionally curved yield surface, a parabola being a common choice.

The classic elastic-plastic models behave linearly if the yield or failure surface is not active, and this is clearly not a very good representation of geomaterial behaviour. To overcome this difficulty, models have been proposed in which a series of loading surfaces where yielding initiates are defined inside the failure surface [25, 26]. Alternatively, a single failure surface is used and nonlinear elastic behaviour is incorporated.

Associated or non-associated flow rules can be used with any of the hydrostatic stress dependent models. Associated flow rules tend to predict excessive dilatancy and many non-associated models have been proposed to control the inelastic volume changes, for example Zienkiewicz et al [27] and Mizuno and Chen [28].

Meridional section

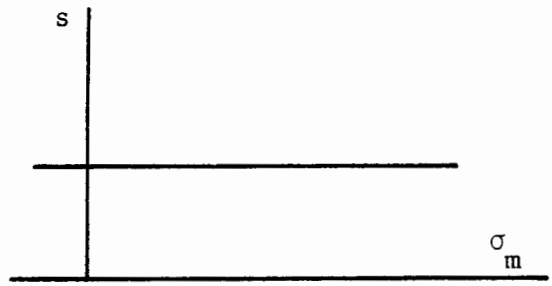

Π - plane section

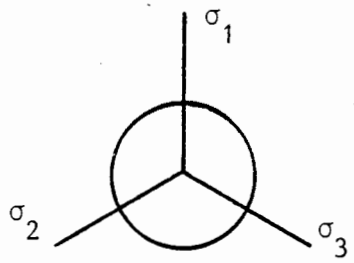

(a) Von-Mises

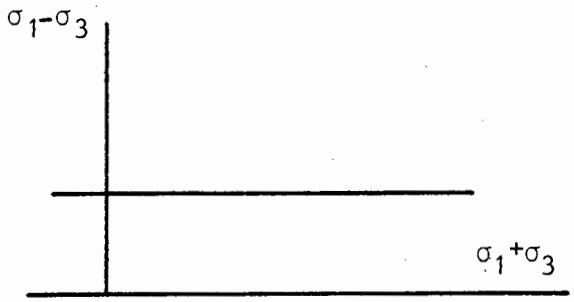

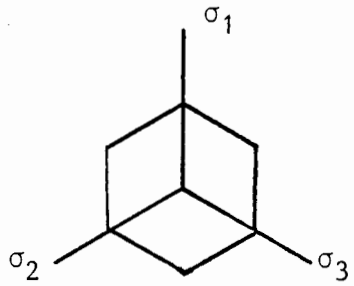

(b) Tresca

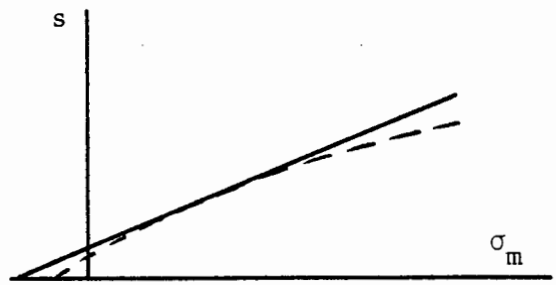

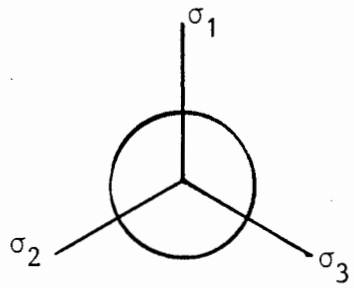

(c) Drucker-Prager (straight and parabolic)

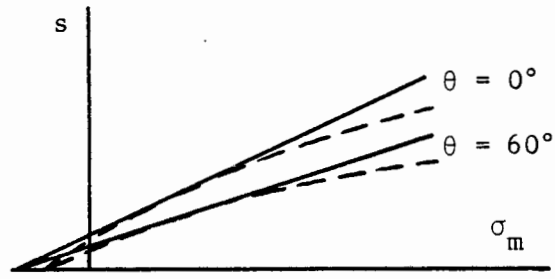

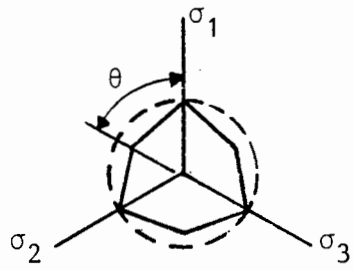

(d) Mohr-Coulomb (straight and parabolic)

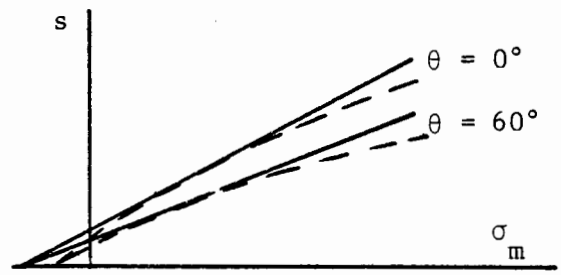

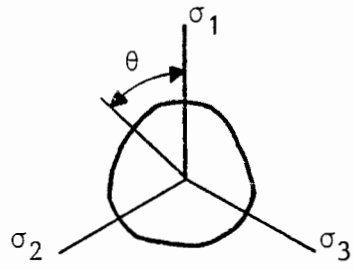

(e) Smoothed Mohr-Coulomb (straight and parabolic)

Figure 2.1: Open yield surface plasticity models (σ_1, σ_2, σ_3 are the principal stresses).

2.2.3 Closed Surface Plasticity Models

The primary shortcomings of the classical hydrostatic stress dependent plasticity models are that they predict dilatancy which greatly exceeds that observed experimentaly (when used with an associated flow rule), and that the behaviour under hydrostatic compression and subsequent unloading is poorly represented. To overcome these difficiencies, Drucker, Gibson and Henkel [29] introduced a second yield function which hardens and, in the case of soil, softens; this is a movable cap. More recent models of this type were developed by Sandler et al [30-32] where an elliptically shaped cap was used together with a meridionally curved failure surface, as shown in Fig. 2.2(a). The shape of the cap is somewhat arbitrarily chosen and other shapes have been proposed by Lade [33-34] who uses a spherical cap, Fig. 2.2(b), Resende and Martin [35-36] who use a parabolic cap, and Bathe et al [37] who suggest a straight cap. Associated flow rules are used on both yield surfaces and the control of the inelastic volume changes is achieved by the interaction of the two yield surfaces. Recent improvements to the cap model are the inclusion of nonlinear elastic behaviour inside the yield surfaces [31] and the introduction of a kinematic hardening yield surface in place of the fixed failure surface [32]. A numerical implementation of the cap model has been described by Sandler and Rubin [38]. A particular cap model developed by the author at the University of Cape Town is described in Chapter 3 of this thesis where emphasis is placed on the behaviour of cap models at the intersection of the cap and failure yield surfaces.

As a development parallel to the cap models, Roscoe and his co-workers at Cambridge introduced the critical state model which has many similarities to the earlier cap models. It used a log spiral cap which was later modified to an elliptical cap by Roscoe and Burland [39] and this became known as the modified Cam Clay model, Fig. 2.2(c). Zienkiewicz et al [27] also suggested a Cam Clay type of model with a single ellipsoidal yield surface but a Mohr-Coulomb Π -plane section as shown in Fig. 2.2(d).

Meridional section

Π - plane section

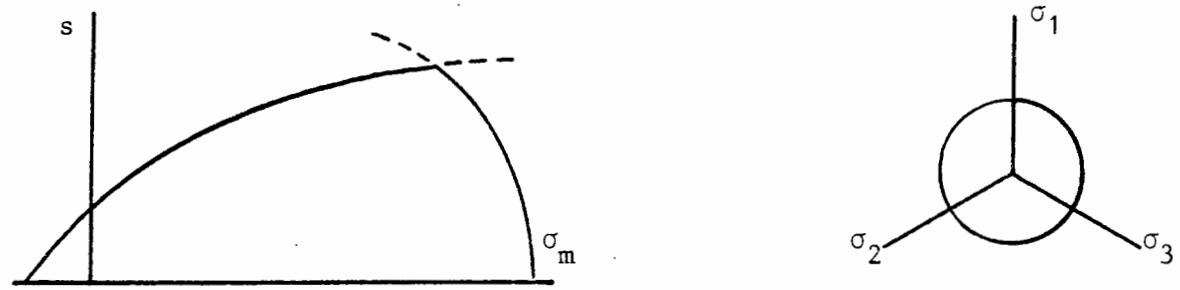

(a) Cap model

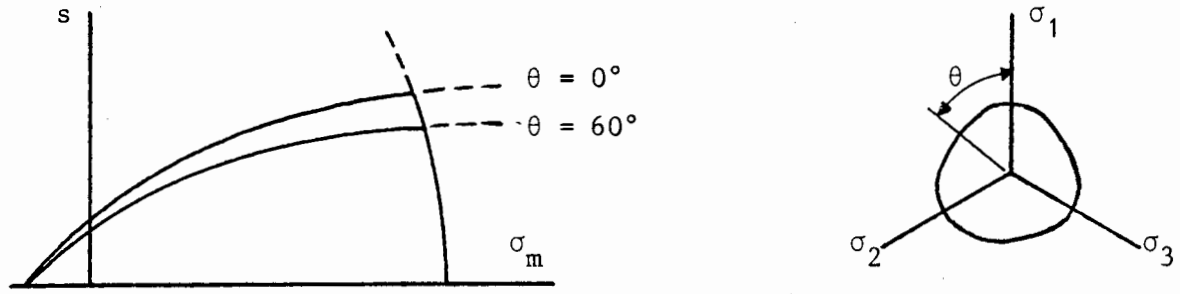

(b) Lade

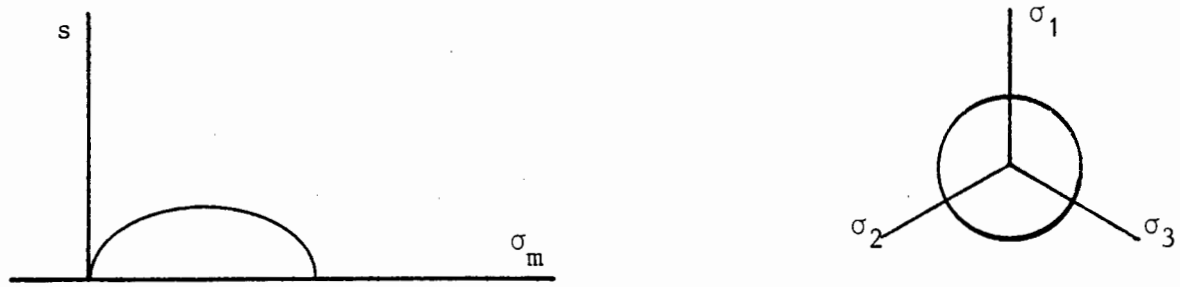

(c) Modified cam-clay

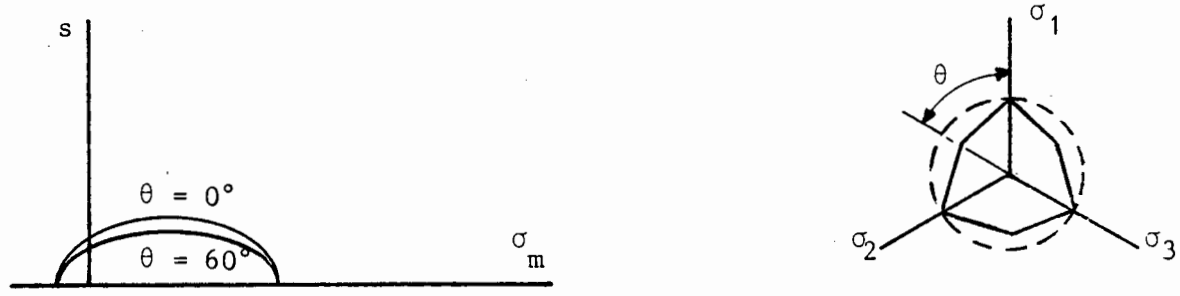

(d) Zienkiewicz et al

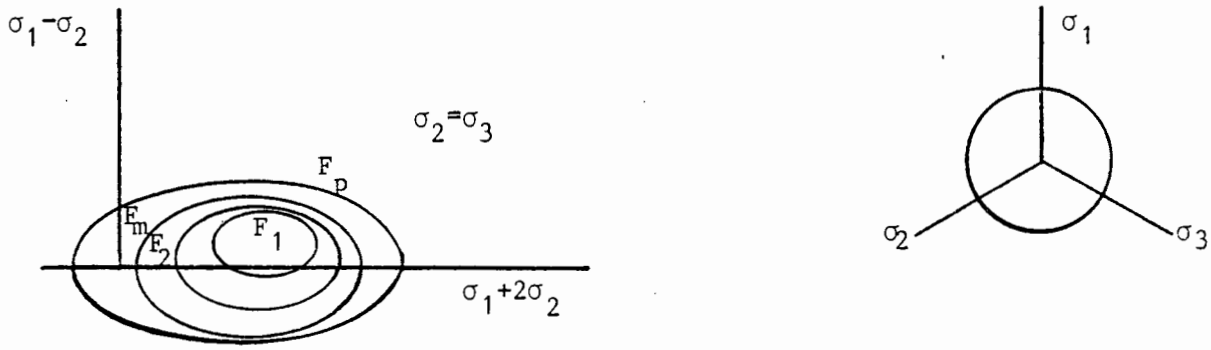

(e) Prevost (anisotropic with rotational symmetry about the 1 axis)

Figure 2.2: Closed surface plasticity models (σ_1, σ_2, σ_3 are the principal stresses).

As a final category of closed surface plasticity models let us consider the model suggested by Prevost. His first version, for the behaviour of clays under undrained conditions was proposed in 1977 [40]. Later, it was extended to include volumetric behaviour [41]. Prevost's model incorporates isotropic and kinematic hardening by using a number of nested yield surfaces, the outermost of which represents a failure envelope (Fig. 2.2(e)). The idea of nested yield surfaces that are carried by a stress point which tries to intersect them was first proposed by Mroz [42,43] in the context of metal plasticity and adopted by Prevost for soils. In the model of Prevost, the yield surfaces are ellipsoids of revolution with the axis initially aligned with the hydrostatic axis. Each surface is characterised by a shear and a bulk stiffness and a dilatancy property. An associated flow rule is used for the failure surface while the inner surfaces employ a non-associated flow rule. The material constants associated with each location along the stress path are those of the yield surface most recently touched providing a natural means of incorporating anisotropy, continuous non-linearity and hysteresis. Some applications of Prevost's model can be found in references [44,45].

More recently, models similar to Prevost's have been proposed by other investigators: the bounding surface plasticity model of Dafalias et al [46,47], the reflecting surface model of Pande and Pietruszczak [48] and the anisotropic hardening model suggested by Mroz et al [49,50]. These models constitute an attempt to represent the smooth nonlinear behaviour exhibited by geological materials which the classical models with a single yield surface cannot capture. They have one possible drawback in that they require a large amount of material memory.

2.2.4 Other Inelastic Models

In this section, we briefly review constitutive laws which cannot be strictly classified under elasticity or plasticity but which nevertheless incorporate some ingredients from those theories.

Endochronic theories were first suggested by Valanis [51,52] to describe

metal plasticity without introducing yield or failure surfaces. Fundamentally, the endochronic models do not make use of a yield or loading condition, but instead use a quantity, called intrinsic time, which is introduced into the constitutive laws of viscoelasticity in place of real time. The intrinsic time is a monotonically increasing measure of the deformation history. Through its use, behaviour very similar to classical plasticity can be achieved without the concept of a yield surface.

An improved endochronic model was applied to soils by Valanis [53] while Bazant et al [54,55] have formulated endochronic models both for concrete and soils. The use of endochronic models in practice is still restricted at present due to the large amount of material memory necessary for its implementation.

Further inelastic constitutive models will be discussed in chapter 5 of this thesis when dealing with brittle rocks, but particularly promising are those based on the progressive fracturing theory of Dougill [56] and damage theory [57]. Progressive damage theory forms the basis of the internal damage constitutive law proposed in this thesis (chapters 5, 6 and 7).

2.3 Performance of the Existing Models with Regard to the Desired Features

In this section, we evaluate the models presented in section 2.2 with respect to the features they should ideally display and which were listed in section 2.1.

2.3.1 Models Based on Elasticity

Nobody would defend the proposition that linear elastic models represent the behaviour of geological materials accurately; in fact, they fail to display almost all the features listed in section 2.1 However, the material constants required to define such models are very few (2 in the

isotropic case and 5 in the orthotropic case) and easily determined from standard tests. Solutions are straight forward in finite element terms and are always stable and unique.

The nonlinear elastic hyperbolic model was primarily developed for uniaxial shear behaviour and the volumetric behaviour is very crudely represented. It does not allow for permanent strains and energy dissipation. Its generalisation to multiaxial behaviour also presents difficulties. The variable moduli models can be made very accurate for the stress paths for which they are developed but essentially suffer from the same problems as the hyperbolic model or any other nonlinear elastic model. The basic problem presented by all nonlinear elastic models is that they allow an infinite number of generalisations to multiaxial behaviour. This is the result of the fact that such models are not formulations of theories of material deformation but simply constitutive curve-fitting of experimental data under specific stress paths. Gross errors can be introduced in the multiaxial generalisations and it must be concluded that these models should only be used for the conditions under which they were developed. The lack of path dependency and material memory are also a severe drawback.

2.3.2 Open Surface Plasticity Models

Open surface plasticity models are useful for many problems. An example is the calculation of bearing capacities which can be effected accurately with simple open surface models; this is because the failure mechanism is often independent of the non-yielding material. However, these models cannot be used to represent geomaterial behaviour accurately under all loading histories.

The reasons are obvious and we examine a few. The Von-Mises and Tresca laws lack hydrostatic stress dependence. No classical open surface model predicts nonlinearity or inelastic volume changes prior to failure. At failure, the hydrostatic pressure dependent models predict continuing dilatation which is normally too large while the Von-Mises and Tresca laws predict zero dilatancy. No permanent deformations or energy

dissipation are present prior to failure. Hydrostatic compression is always elastic.

Experimental evidence indicates that the behaviour on the Π-plane is influenced by the intermediate principal stress suggesting a Mohr-Coulomb or smoothed Mohr-Coulomb octahedral section rather than a circular Von-Mises section. In practice, provided the choice of the circular Π-plane section is made apropriately, the effect of ignoring the intermediate principal stress influence is very small [16,58,59]. Similar comments apply to the use of a straight meridional section of the yield surface rather than a curved one.

Lastly, the existence of corners in the Tresca and Mohr-Coulomb type yield surfaces has presented difficulties to some investigators in the development and implementation of such laws. The author has examined this problem in references [36,60].

The comments about the shapes of the cross-section and the existence of corners in the open surface models also apply to some of the more sophisticated closed surface models.

2.3.3 Closed Surface Plasticity Models

Closed surface models, in general, provide nonlinearity and permanent strains prior to failure as well as a better representation of the hydrostatic behaviour. The extent of inelastic volume change is also effectively controlled by the introduction of a second yield surface (in the multisurface models) or by the shape of the plastic potentials used in the single yield surface closed surface models. Because of their greater flexibility, closed suface models are more affected by the lack of reliable experimental data. One example concerns the transition between hydrostatic and deviatoric behaviour which one would expect to be a reasonably smooth one. However, one has to reconcile the vastly different behaviours observed experimentally for purely hydrostatic and purely deviatoric paths. Sufficient experimental data is not available for this.

One criticism aimed at cap models is that while they represent behaviour

close to hydrostatic paths well, the behaviour along deviatoric paths is rather poorly modelled. This is due to the single failure surface used in the cap models. The inclusion of anisotropic behaviour in the cap models is difficult due to its invariant based formulation. The number of parameters for the simpler cap models is acceptable (less than ten), but more advanced cap models require an excessive amount of material parameters. Finally, the architects of the cap models [30-32] strongly emphasize that, by using associated flow rules, well posed problems are generated by their models where existence, uniqueness and stability are guaranteed. This is a debatable claim, but its discussion is taken up in Chapter 3.

Prevost's model ranks as one of the best for soil behaviour and it fulfills most of the requirements listed in section 2.1. The introduction of a series of yield surfaces with different properties has the effect of discretizing the stress-strain laws and thus increases the accuracy of the representation of real material behaviour. The model has the drawback that it requires a large number of material constants and also it has not yet been widely used in the solution of boundary value problems. The same criticisms can be levelled at the models of Dafalias et al, Mroz et al and Pande and Pietruszczak.

2.3.4 Other Inelastic Models

The endochronic model idea of following a series of events by measuring the amount of deformation that has taken place is a very attractive one. However, the complexity of the formulation, the number of functions that have to be determined and the need to solve convolution integrals with nonlinear terms has precluded the application of endochronic models. Simpler one-dimensional shear behaviour endochronic models have been used but they simply become curve-fitting models.

The idea of discretized or even continuous representation of nonlinear behaviour forms the basis of the models of Dougill and the damage models. These hold promise but so far most of the work has been one-

dimensional.

2.4 Directions for Further Development of Constitutive Models

It is clear that a move towards fairly simple models (simpler than endochronic) which represent geomaterial behaviour in a continuous fashion has a lot to offer. It is attractive to pursue developments based on progressive fracturing and damage theories. This does not mean that plasticity based models should be abandoned, but certain questions related to hydrostatic/deviatoric transition, flow rules and hardening rules need to be answered.

More experimental investigation is necessary; in particular special rigs need to be developed in order to test certain stress paths. This must go hand in hand with the mechanics developments.

From the point of view of computer technology, the better models require an excessive number of material parameters . An attempt to reduce this number, perhaps by studying relationships and dependencies between material parameters, should be made.

CHAPTER 3

A STATE OF THE ART PLASTICITY CAP MODEL

The Drucker-Prager cap and similar models for the constitutive behaviour of geotechnical materials are widely used in finite element stress analysis. They are multisurface plasticity models, used most frequently with an associated flow rule. As an example of a state of the art plasticity cap model, it was decided to study and develop a fully coupled Drucker-Prager model with a parabolic cap and a perfectly plastic tension cutoff. This model could also be used as a basis for comparison with other models.

3.1 Introduction

The Drucker-Prager model [16] is elastic, perfectly plastic with a yield surface which depends on hydrostatic pressure (in fact a cone in the principal stress space) and an associated flow rule. The primary shortcomings of the model are that it predicts plastic dilatancy which greatly exceeds that which is observed experimentally, and that the behaviour in hydrostatic compression is poorly represented. To overcome these deficiencies Drucker, Gibson and Henkel [29] introduced a second yield function which hardens and, in the case of a soil, softens; this is the cap, so called because it closes the cone in the principal stress space. The shape of the cap in the principal stress space can be chosen in various ways; models developed by Sandler et al [30-32, 38] use an elliptically shaped cap, whereas Bathe et al [37] allow only for a plane cap.

The constitutive equations for the cap describe behaviour in hydrostatic compression, with hardening occurring when plastic deformation takes place. If, however, the Drucker-Prager cone and the cap are coupled, through the plastic volume strain, the cap softens when plastic volume

strain occurs on the cone. When the cap-cone vertex overtakes the stress point plastic deformation in pure shear becomes possible. The introduction of the cap thus overcomes to some extent the principal difficulties of the Drucker-Prager model.

One of the main concerns in this chapter is the behaviour when yielding occurs simultaneously on the Drucker-Prager cone and the cap. The yield surfaces are coupled, in the sense that the cap position depends on the total plastic volume strain produced on the Drucker-Prager and cap surfaces, among other parameters. The functional form of the yield surfaces, with full coupling and the assumption of an associated flow rule, is sufficient to permit the complete behaviour during simultaneous yielding to be derived. However, full coupling is not assumed in the models of Sandler et al [30-32,38] and Bathe et al [37]. This is in order to suppress an instability (in the sense that the stability postulate of Drucker [61,62] is not satisfied) which occurs in certain ranges of behaviour. Sandler et al [30-32,38] chose a limited form of coupling, whereas Bathe et al [37] impose additional assumptions on the plastic strain rate vector. Lade [33,63] and Desai et al [65], among others, also make modifications of the same type.

A consistent treatment of coupled yield surfaces has been set out by Maier [64]. In the following sections this process is applied to a fully coupled model. A particular form of the failure surface and the cap are chosen for this illustration, but the general conclusions are not limited to this choice. Stress rates are written in terms of strain rates for all regimes in the shear strain rate, volume strain rate space. Using this framework we consider the models of Sandler and Rubin [38] and Bathe et al [37] (chosen because full details are given in the respective papers) and show that they are not fully consistent, although for different reasons.

Although emphasis is placed on the behaviour of the Drucker-Prager and cap intersection, a complete model is developed in this Chapter.

3.2 Structure of the Plasticity Constitutive Equations

Plasticity models provide inviscid relations between stress rate $\dot{\sigma}_{ij}$ and strain rate $\dot{\varepsilon}_{ij}$. We assume that the total strain rate $\dot{\varepsilon}_{ij}$ can be written as the sum of an elastic and a plastic component,

$$\dot{\varepsilon}_{ij} = \dot{\varepsilon}^{e}_{ij} + \dot{\varepsilon}^{p}_{ij} \quad , \tag{3.1}$$

and that the elastic behaviour is isotropic. The elastic equations are written as

$$\dot{\varepsilon}^{e}_{kk} = \frac{1}{3K}\dot{\sigma}_{kk} \quad , \qquad \dot{e}^{e}_{ij} = \frac{1}{2G}\dot{s}_{ij} \quad , \tag{3.2}$$

where K, G are respectively the bulk and shear moduli, and $\dot{e}_{ij}$, $\dot{s}_{ij}$ are the deviatoric components of $\dot{\varepsilon}_{ij}$, $\dot{\sigma}_{ij}$.

The plastic strain rate $\dot{\varepsilon}^{p}_{ij}$ is given as the sum of contributions from the associated flow rate for n active yield surfaces,

$$\dot{\varepsilon}^{p}_{ij} = \lambda_{\alpha}\frac{\partial F_{\alpha}}{\partial \sigma_{ij}} \quad , \tag{3.3}$$

where $\alpha = 1, 2, \ldots, n$ and the summation rule applies. The F_{α} are yield functions, and λ_{α} are non-negative multipliers, with

$$\begin{aligned} &\lambda_{\alpha} > 0 \quad \text{if } F_{\alpha} = 0 \text{ and } \dot{F}_{\alpha} = 0, \\ &\lambda_{\alpha} = 0 \quad \text{if } F_{\alpha} = 0 \text{ and } \dot{F}_{\alpha} < 0 \\ &\qquad\quad \text{or } F_{\alpha} < 0 \quad . \end{aligned} \tag{3.4}$$

In the Drucker-Prager cap model the yield surfaces are assumed to depend on the first and second invariants of the stress tensor. For our present purposes, we shall choose these invariants as the mean hydrostatic tension σ_m and an effective shear stress s, where

$$\sigma_m = \frac{1}{3}\sigma_{kk} \quad ,$$

$$s = \sqrt{\frac{1}{2} s_{ij} s_{ij}} \quad . \tag{3.5}$$

Equation (3.3) thus becomes

$$\dot{\varepsilon}^p_{ij} = \lambda_\alpha \left(\frac{\partial F_\alpha}{\partial \sigma_m} \frac{\partial \sigma_m}{\partial \sigma_{ij}} + \frac{\partial F_\alpha}{\partial s} \frac{\partial s}{\partial \sigma_{ij}} \right) \quad . \tag{3.6}$$

By standard manipulations ,we see that

$$\frac{\partial \sigma_m}{\partial \sigma_{ij}} = \frac{1}{3}\delta_{ij} \quad , \quad \frac{\partial s}{\partial \sigma_{ij}} = \frac{1}{2s} s_{ij} \quad . \tag{3.7}$$

From these results, it follows that the plastic volume strain rate is

$$\dot{\varepsilon}^p_{kk} = \lambda_\alpha \frac{\partial F_\alpha}{\partial \sigma_m} \tag{3.8a}$$

and the deviatoric plastic strain rate is

$$\dot{e}^p_{ij} = \frac{\lambda_\alpha}{2s} \frac{\partial F_\alpha}{\partial s} s_{ij} \quad . \tag{3.8b}$$

In our initial discussion, when basic ideas will be developed, it is convenient to simplify these equations. In particular, it is convenient to sketch the yield surfaces and the plastic constitutive relations in a two-dimensional space of the invariants σ_m and s. To be able to do this we must define effective strain rate quantities which are conjugate to the stress invariants. The first of these is simple to define, and is the volume strain rate which we will now denote by $\dot{\varepsilon}_v$,

$$\dot{\varepsilon}_v = \dot{\varepsilon}_{kk} \quad . \tag{3.9}$$

The effective shear strain rate we shall define as

$$\dot{e} = \frac{1}{s} s_{ij} \dot{e}_{ij} \quad . \tag{3.10}$$

The definition gives a scalar strain rate which is of degree zero in the stress components, and

$$s\dot{e} = s_{ij} \dot{e}_{ij} \quad . \tag{3.11}$$

We may break $\dot{e}$ into elastic and plastic components $\dot{e}^e$, $\dot{e}^p$ without difficulty. The shear stress rate $\dot{s}$ is obtained by differentiating equn. (3.5) and is

$$\dot{s} = \frac{1}{2s} s_{ij} \dot{s}_{ij} \quad . \tag{3.12}$$

Using these definitions, we may now cast the constitutive equations in a very simple form. We have

$$\dot{e} = \dot{e}^e + \dot{e}^p \quad , \quad \dot{\varepsilon}_v = \dot{\varepsilon}_v^e + \dot{\varepsilon}_v^p \quad , \tag{3.13}$$

with the elastic relations, from equn. (3.2), given by

$$\dot{\varepsilon}_v^e = \frac{\dot{\sigma}_m}{K} \quad , \quad \dot{e}^e = \frac{\dot{s}}{G} \quad , \tag{3.14a}$$

and the plastic relations, from equns. (3.8), given by

$$\dot{\varepsilon}_v^p = \lambda_\alpha \frac{\partial F_\alpha}{\partial \sigma_m} \quad , \quad \dot{e}^p = \lambda_\alpha \frac{\partial F_\alpha}{\partial s} \quad . \tag{3.14b}$$

Stability in the sense of Drucker [61,62] is defined in terms of the second order work. It is shown in Appendix A that

$$\dot{s}\dot{e} \leq \dot{s}_{ij} \dot{e}_{ij} \quad , \quad \dot{\sigma}_m \dot{\varepsilon}_v = \frac{1}{3} \dot{\sigma}_{kk} \dot{\varepsilon}_{kk} \tag{3.15a}$$

and hence it follows that if

$$\dot{s}\dot{e} + \dot{\sigma}_m \dot{\varepsilon}_v > 0 \tag{3.15b}$$

then

$$\dot{\sigma}_{ij} \dot{\varepsilon}_{ij} > 0 \quad . \tag{3.15c}$$

If, however, the sign of $(\dot{s}\dot{e} + \dot{\sigma}_m \dot{\varepsilon}_v)$ is negative, the second order work rate may or may not be negative, and thus the relations may be unstable. Consideration of $\dot{\sigma}_{ij} \dot{\varepsilon}_{ij}$ is necessary to establish whether an instability is present.

3.3 Treatment of the Constitutive Equations in Multisurface Plasticity

Before proceeding with the development of the Drucker-Prager cap model, it is useful to review the consistent treatment of the constitutive equations in multisurface plasticity [64]. It is important to realize

the implications and consequences of different couplings between yield surfaces and different flow rule assumptions.
However, to avoid disturbing the continuity of the chapter this discussion is presented in Appendix B.

3.4 Cap Model Yield Functions

The yield functions which make up the complete model are written in terms of the invariants σ_m and s. The elastic domain in the s, σ_m space (note that $s \geq 0$)) is bounded by three distinct yield surfaces, as shown in Fig. 3.1; these are the Drucker-Prager failure surface, the cap and the tension cutoff. Both the failure surface and the tension cutoff are represented as perfectly plastic yield surfaces; this is clearly only a first approximation to the real behaviour.

The Drucker-Prager yield condition [16] is defined by

$$F_1 = \alpha \sigma_m + s - k = 0 \quad . \tag{3.16}$$

The constants α and k are related to the angle of friction and the cohesion of the material respectively. The function F_1 depends only on the stress invariants, and thus remains fixed in stress space.

In our particular model, we have chosen a parabolic cap defined by

$$F_2 = -(\sigma_m - \sigma_m^c) + R^2 s^2 = 0 \quad . \tag{3.17}$$

The constant R is a shape factor; when R is set equal to zero the plane cap used by Bathe et al [37] is recovered. The hardening parameter σ_m^c depends on the plastic volume strain ε_v^p which has occurred since the initial instant. Let $\bar{\varepsilon}_{vo}^p$ denote the initial degree of compaction; the current degree of compaction is then

$$\bar{\varepsilon}_v^p = \bar{\varepsilon}_{vo}^p + \varepsilon_v^p \quad , \tag{3.18}$$

and

$$\bar{\varepsilon}_v^p = W(1 - e^{D\sigma_m^c}) \quad . \tag{3.19}$$

This relation is shown diagramatically in Fig. 3.2, where the significance of the constants W and D can be appreciated. The cap can translate along the σ_m axis, and can move either to the left or the right in Fig. 3.1.

The tension cutoff is regarded as part of the yield surface, given by

$$F_3 = \sigma_m - T = 0 \quad , \tag{3.20}$$

where T is the maximum value that the mean hydrostatic tension σ_m can attain. This yield surface also remains fixed in the stress space.

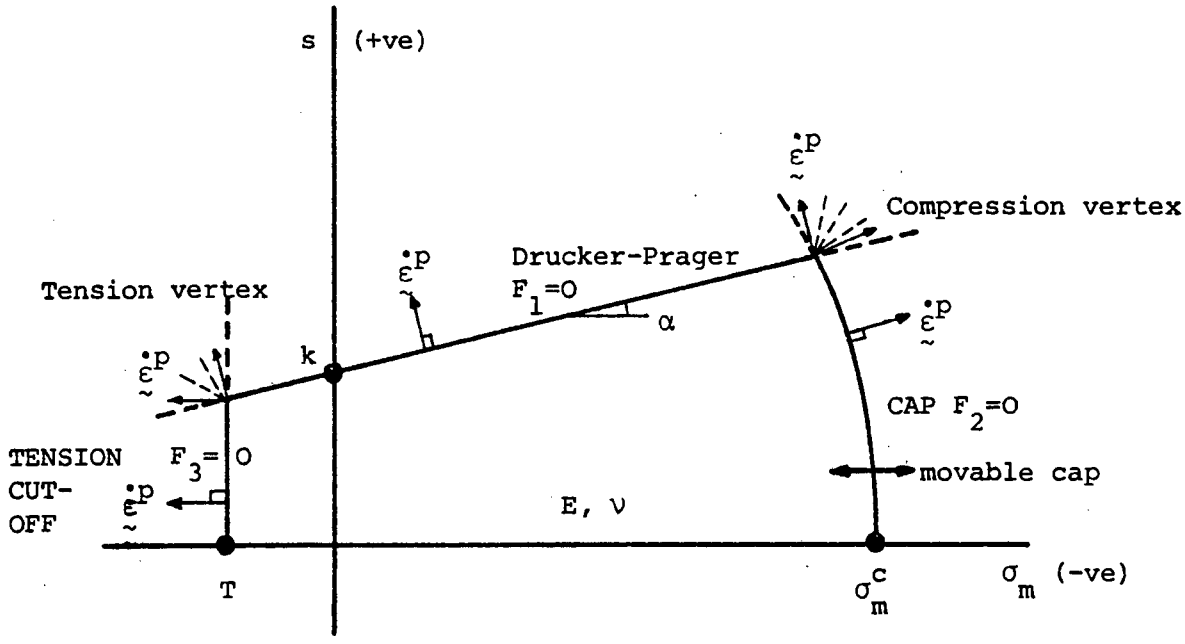

Figure 3.1: Yield surface of plasticity model.

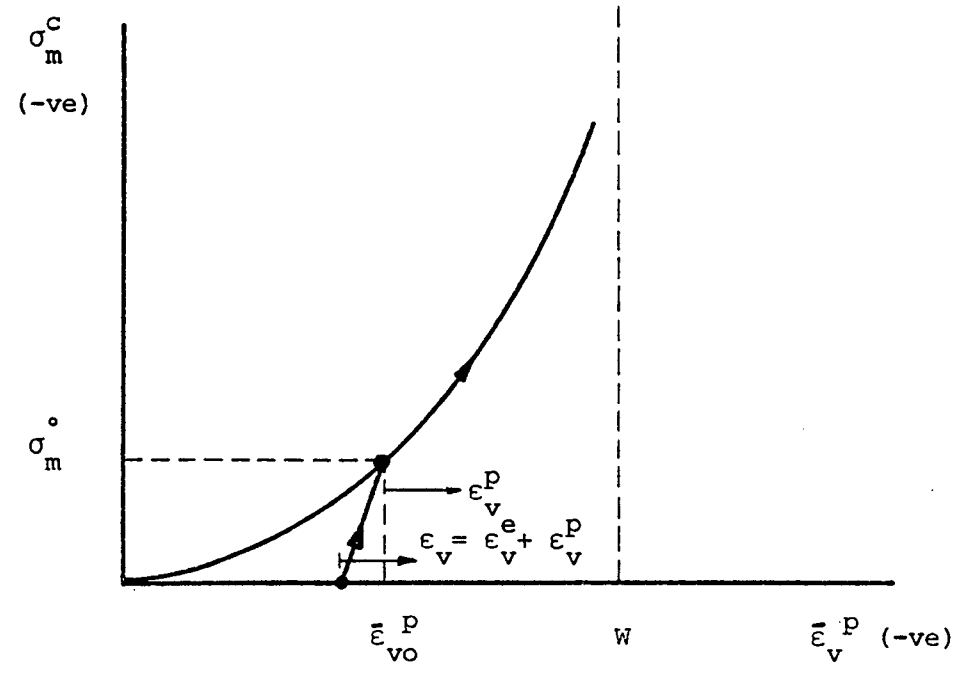

Figure 3.2: Non-linear hardening rule for cap yield surface.

3.5 Invariant Form of the Constitutive Equations

The basic form of the plastic constitutive relations can be most simply appreciated if we work with the stress invariants σ_m, s and the conjugate strain quantities ε_v, e as defined in equns. (3.5-3.15). For a finite element formulation in which displacement rates (or increments) are the fundamental variables, we seek to write stress rates in terms of total strain rates for all possible states.

When the stress point is in the elastic domain in Fig. 3.1 the plastic strain rates are zero, and the behaviour is elastic. Hence, from equn. (3.14a), we have (with $F_1 < 0$, $F_2 < 0$, $F_3 < 0$) ,

$$\begin{bmatrix} \dot{s} \\ \dot{\sigma}_m \end{bmatrix} = \begin{bmatrix} G & 0 \\ 0 & K \end{bmatrix} \begin{bmatrix} \dot{e} \\ \dot{\varepsilon}_v \end{bmatrix} \quad . \tag{3.21}$$

We now consider yielding on each of the three yield surfaces in turn, and then study the two corner points where two yield surfaces are active simultaneously.

First, we treat the case where yielding takes place on the Drucker-Prager yield surface, $F_1 = 0$. Non-zero plastic strain rates are possible, with

$$\begin{aligned} \dot{e}^p &= \lambda_1 \frac{\partial F_1}{\partial s} = \lambda_1 \quad , \\ \dot{\varepsilon}_v^p &= \lambda_1 \frac{\partial F_1}{\partial \sigma_m} = \alpha\lambda_1 \quad . \end{aligned} \tag{3.22}$$

The condition for loading (i.e. $\lambda_1 > 0$) is

$$\dot{F}_1 = \alpha\dot{\sigma}_m + \dot{s} = 0 \quad . \tag{3.23}$$

The total strain rates are

$$\dot{e} = \frac{\dot{s}}{G} + \lambda_1 \quad , \quad \dot{\varepsilon}_v = \frac{\dot{\sigma}_m}{K} + \alpha\lambda_1 \tag{3.24}$$

which give the stress rates as

$$\dot{s} = G\left(\dot{e} - \lambda_1\right) \quad , \quad \dot{\sigma}_m = K\left(\dot{\varepsilon}_v - \alpha\lambda_1\right) \quad . \tag{3.25}$$

These equations are now substituted into equn. (3.23) to give λ_1 ;

$$\lambda_1 = \frac{G}{G+\alpha^2K}\,\dot{e} + \frac{\alpha K}{G+\alpha^2K}\,\dot{\varepsilon}_v \quad . \tag{3.26}$$

Since it is required that $\lambda_1 > 0$, equn. (3.26) also gives the condition for loading and unloading. Thus on substituting equn (3.26) into equn. (3.25) for $\lambda_1 > 0$, we get (with $F_1 = 0$, $F_2 < 0$, $F_3 < 0$)

$$\begin{bmatrix} \dot{s} \\ \dot{\sigma}_m \end{bmatrix} = \begin{bmatrix} G - \dfrac{G^2}{G+\alpha^2K} & -\dfrac{\alpha GK}{G+\alpha^2K} \\ -\dfrac{\alpha GK}{G+\alpha^2K} & K - \dfrac{K^2\alpha^2}{G+\alpha^2K} \end{bmatrix} \begin{bmatrix} \dot{e} \\ \dot{\varepsilon}_v \end{bmatrix} \tag{3.27a}$$

for $G\dot{e} + \alpha K\dot{\varepsilon}_v > 0$, and

$$\begin{bmatrix} \dot{s} \\ \dot{\sigma}_m \end{bmatrix} = \begin{bmatrix} G & 0 \\ 0 & K \end{bmatrix} \begin{bmatrix} \dot{e} \\ \dot{\varepsilon}_v \end{bmatrix} \tag{3.27b}$$

for $G\dot{e} + \alpha K\dot{\varepsilon}_v < 0$.

Second, consider yielding associated with the cap, $F_2 = 0$. From equns. (3.17) and (3.19), we write F_2 as

$$F_2 = -\sigma_m + R^2 s^2 + \frac{1}{D} \ln \left(a - \frac{\varepsilon_v^p}{W} \right) \tag{3.28a}$$

where

$$a = 1 - \frac{\bar{\varepsilon}_{vo}^p}{W} \quad . \tag{3.28b}$$

From equn. (3.14b), the plastic strain rates are

$$\begin{aligned} \dot{e}^p &= \lambda_2 \frac{\partial F_2}{\partial s} = 2R^2 s \lambda_2 \quad , \\ \dot{\varepsilon}_v^p &= \lambda_2 \frac{\partial F_2}{\partial \sigma_m} = -\lambda_2 \quad , \end{aligned} \tag{3.29}$$

with $\lambda_2 > 0$. The total strain rates are then

$$\dot{e} = \frac{\dot{s}}{G} + 2R^2 s \lambda_2 \quad , \qquad \dot{\varepsilon}_v = \frac{\dot{\sigma}_m}{K} - \lambda_2 \quad , \tag{3.30}$$

and hence, on inverting,

$$\dot{s} = G \left(\dot{e} - 2R^2 s \lambda_2 \right) \quad , \qquad \dot{\sigma}_m = K \left(\dot{\varepsilon}_v + \lambda_2 \right) \quad . \tag{3.31}$$

The condition for loading is

$$\dot{F}_2 = -\dot{\sigma}_m + 2R^2 s \dot{s} - \frac{1}{WD \left(a - \frac{\varepsilon_v^p}{W} \right)} \dot{\varepsilon}_v^p = 0 \quad . \tag{3.32}$$

We now substitute equns. (3.29) and (3.31) into equn. (3.32) in order to determine λ_2 ;

$$\lambda_2 = \frac{1}{K+4R^4s^2G - \dfrac{1}{WD\left(a - \dfrac{\varepsilon_v^p}{W}\right)}} \left[2R^2sG\dot{e} - K\dot{\varepsilon}_v\right] \quad . \tag{3.33}$$

The denominator in this expression is always positive, and hence the numerator gives the sign of λ_2 . On substituting back into equns. (3.31), we thus find the cap constitutive equations:
(with $F_1 < 0$, $F_2 = 0$, $F_3 < 0$)

$$\begin{bmatrix} \dot{s} \\ \dot{\sigma}_m \end{bmatrix} = \begin{bmatrix} G - \dfrac{4R^4s^2G^2}{K+4R^4s^2G-H} & \dfrac{2R^2sGK}{K+4R^4s^2G-H} \\ \dfrac{2R^2sGK}{K+4R^4s^2G-H} & K - \dfrac{K^2}{K+4R^4s^2G-H} \end{bmatrix} \begin{bmatrix} \dot{e} \\ \dot{\varepsilon}_v \end{bmatrix} \tag{3.34a}$$

for $2R^2sG\dot{e} - K\dot{\varepsilon}_v > 0$, and

$$\begin{bmatrix} \dot{s} \\ \dot{\sigma}_m \end{bmatrix} = \begin{bmatrix} G & 0 \\ 0 & K \end{bmatrix} \begin{bmatrix} \dot{e} \\ \dot{\varepsilon}_v \end{bmatrix} \tag{3.34b}$$

for $2R^2sG\dot{e} - K\dot{\varepsilon}_v < 0$.

In these equations we have put

$$H = \frac{1}{WD\left(a - \dfrac{\varepsilon_v^p}{W}\right)} \quad . \tag{3.34c}$$

For yielding at the tension cutoff, we have $F_3 = 0$, and

$$\dot{e}^p = \lambda_3 \frac{\partial F_3}{\partial s} = 0 \quad , \qquad \dot{\varepsilon}_v^p = \lambda_3 \frac{\partial F_3}{\partial \sigma_m} = \lambda_3 \quad , \tag{3.35}$$

with $\lambda_3 > 0$.

The condition for loading is

$$\dot{F}_3 = \dot{\sigma}_m = 0 \quad . \tag{3.36}$$

The total strain rates are

$$\dot{e} = \frac{\dot{s}}{G} \quad , \qquad \dot{\varepsilon}_v = \frac{\dot{\sigma}_m}{K} + \lambda_3 \quad , \tag{3.37}$$

leading to

$$\dot{s} = G\dot{e} \quad , \qquad \dot{\sigma}_m = K\left(\dot{\varepsilon}_v - \lambda_3\right) \quad . \tag{3.38}$$

Substituting these equns. into the loading condition (3.36), we then find

$$\lambda_3 = \dot{\varepsilon}_v \quad . \tag{3.39}$$

The constitutive equations for yielding at the tension cutoff then become (with $F_1 < 0$, $F_2 < 0$, $F_3 = 0$)

$$\begin{bmatrix} \dot{s} \\ \dot{\sigma}_m \end{bmatrix} = \begin{bmatrix} G & 0 \\ 0 & 0 \end{bmatrix} \begin{bmatrix} \dot{e} \\ \dot{\varepsilon}_v \end{bmatrix} \tag{3.40a}$$

for $\dot{\varepsilon}_v > 0$, and

$$\begin{bmatrix} \dot{s} \\ \dot{\sigma}_m \end{bmatrix} = \begin{bmatrix} G & 0 \\ 0 & K \end{bmatrix} \begin{bmatrix} \dot{e} \\ \dot{\varepsilon}_v \end{bmatrix} \tag{3.40b}$$

for $\dot{\varepsilon}_v < 0$.

Each of the sets of equations we have so far derived (equns. 3.21, 3.27, 3.34 and 3.40) involve symmetric positive definite matrices, and it can be shown that in all cases so far covered Drucker's stability postulate [61,62] is satisfied in that

$$\dot{s}\,\dot{e} + \dot{\sigma}_m\,\dot{\varepsilon}_v > 0 \quad . \tag{3.41}$$

We must now consider behaviour at the two vertices, when two yield functions are active. The corner where the tension cutoff and the Drucker-Prager yield surface meet behaves in a classical manner, and we shall treat this first. For the case $F_1 = 0$ and $F_3 = 0$, we put

$$\begin{aligned} \dot{e}^p &= \lambda_1 \frac{\partial F_1}{\partial s} + \lambda_3 \frac{\partial F_3}{\partial s} = \lambda_i \quad , \\ \dot{\varepsilon}_v^p &= \lambda_1 \frac{\partial F_1}{\partial \sigma_m} + \lambda_3 \frac{\partial F_3}{\partial \sigma_m} = \alpha\lambda_1 + \lambda_3 \quad . \end{aligned} \tag{3.42}$$

Four distinct loading or unloading paths must now be taken into account. These are shown diagrammatically in Fig. 3.3, and are

1. $\dot{F}_1 < 0$, $\dot{F}_3 < 0$, elastic unloading.
2. $\dot{F}_1 < 0$, $\dot{F}_3 = 0$, yielding on the tension cutoff.
3. $\dot{F}_1 = 0$, $\dot{F}_3 < 0$, yielding on the Drucker-Prager line.
4. $\dot{F}_1 = 0$, $\dot{F}_3 = 0$, yielding on both surfaces.

It is only the fourth case which presents a new set of relations. From equns. (3.23) and (3.36), $\dot{F}_1 = \dot{F}_3 = 0$ requires $\dot{s} = 0$, $\dot{\sigma}_m = 0$, so that the stress point is stationary. The elastic strain rates are zero, and total strain rates can be substituted into equns. (3.42). Hence

$$\lambda_1 = \dot{e} \quad , \qquad \lambda_3 = -\alpha\,\dot{e} + \dot{\varepsilon}_v \quad . \tag{3.43}$$

We require that both $\lambda_1 > 0$ and $\lambda_3 > 0$, and thus the constitutive equation for case 4 is (with $F_1 = 0$, $F_2 < 0$, $F_3 = 0$)

$$\begin{aligned} \dot{s} &= 0 \ , \\ \dot{\sigma}_m &= 0 \ . \end{aligned} \tag{3.44a}$$

for $\dot{e} > 0$, $-\alpha \dot{e} + \dot{\varepsilon}_v > 0$.

In the remaining cases we do not need to rederive the constitutive equations, but only to identify the conditions in terms of total strain rates. It is evident that the elastic unloading case is described by (with $F_1 = 0$, $F_2 < 0$, $F_3 = 0$)

$$\begin{bmatrix} \dot{s} \\ \dot{\sigma}_m \end{bmatrix} = \begin{bmatrix} G & 0 \\ 0 & K \end{bmatrix} \begin{bmatrix} \dot{e} \\ \dot{\varepsilon}_v \end{bmatrix} \tag{3.44b}$$

for $\dot{\varepsilon}_v < 0$, $G\dot{e} + \alpha K \dot{\varepsilon}_v < 0$.

Case 2, $\dot{F}_1 < 0$, $\dot{F}_3 = 0$ is the case $\lambda_1 = 0$, $\lambda_3 > 0$, so that the conditions are

$$\dot{e} < 0 \ , \quad \dot{\varepsilon}_v > 0 \tag{3.44c}$$

with the constitutive equations given by equn. (3.40a).

Case 3, $\dot{F}_1 = 0$, $\dot{F}_3 < 0$ is the case $\lambda_1 > 0$, $\lambda_3 = 0$, and the conditions are

$$G\dot{e} + \alpha K \dot{\varepsilon}_v > 0 \ , \quad -\alpha \dot{e} + \dot{\varepsilon}_v < 0 \ . \tag{3.44d}$$

In this case the constitutive equations are equns. (3.27a). In each of these cases the plastic strain rate vector lies within the fan defined by adjacent normals at the vertex in Fig. 3.1, and the stability postulate (3.41) is satisfied. The conditions which separate the various loading and unloading cases can be conveniently represented in a diagram

in the $\dot{e}$, $\dot{\varepsilon}_v$ space, as shown in Fig. 3.4. This diagram implies completeness and uniqueness of the constitutive model at the tension vertex.

The behaviour we are primarily interested in corresponds to the case when the stress point is yielding at the intersection of the Drucker-Prager and cap yield surfaces. We shall now deal with this state which is defined by the conditions

$$F_1 = 0 \ , \quad F_2 = 0 \ , \quad F_3 < 0 \ .$$

Four cases of loading and unloading can be identified as shown in fig. 3.3 :

1. $\dot{F}_1 < 0$, $\dot{F}_2 < 0$, elastic unloading.

2. $\dot{F}_1 < 0$, $\dot{F}_2 = 0$, yielding on the cap, unloading from the D-P line.

3. $\dot{F}_1 = 0$, $\dot{F}_2 < 0$, yielding on the D-P line, unloading from the cap. The stress point moves along the D-P line from right to left.

4. $\dot{F}_1 = 0$, $\dot{F}_2 = 0$, loading on both yield surfaces: we shall see that the stress point may move along the D-P line in either direction.

It is case 4 which we wish to consider in detail, and this will be done in a manner which is essentially identical to that described by Maier [64]. The yield function F_1 is given by equn. (3.16), and, using equns. (3.18 and 3.19), it is convenient to rewrite F_2 as

$$F_2 = -\sigma_m + R^2 s^2 + \frac{1}{D} \ln \left(a - \frac{\varepsilon_v^p}{W} \right) \qquad (3.45a)$$

where

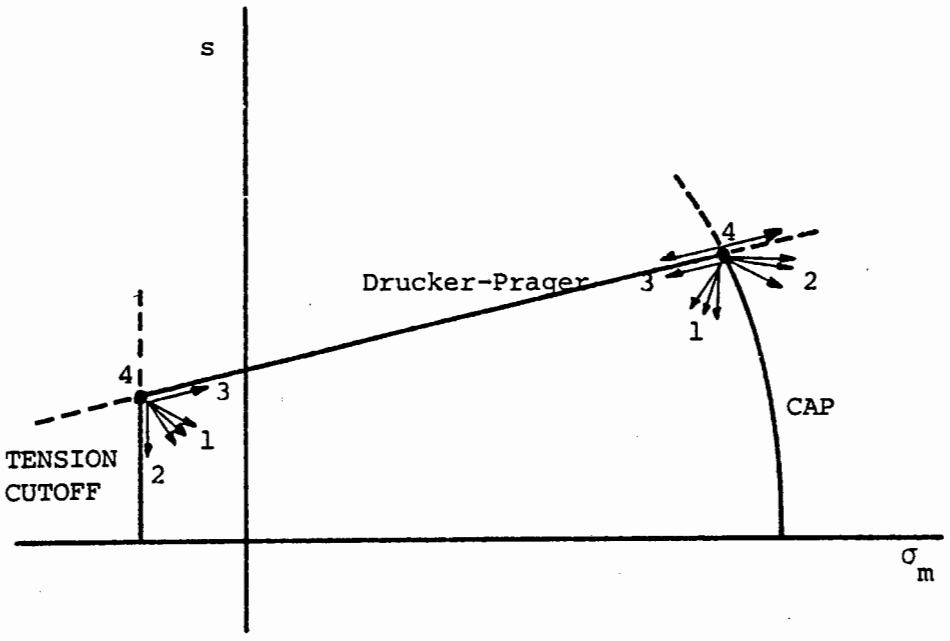

Figure 3.3: Stress space behaviour of compression and tension vertices.

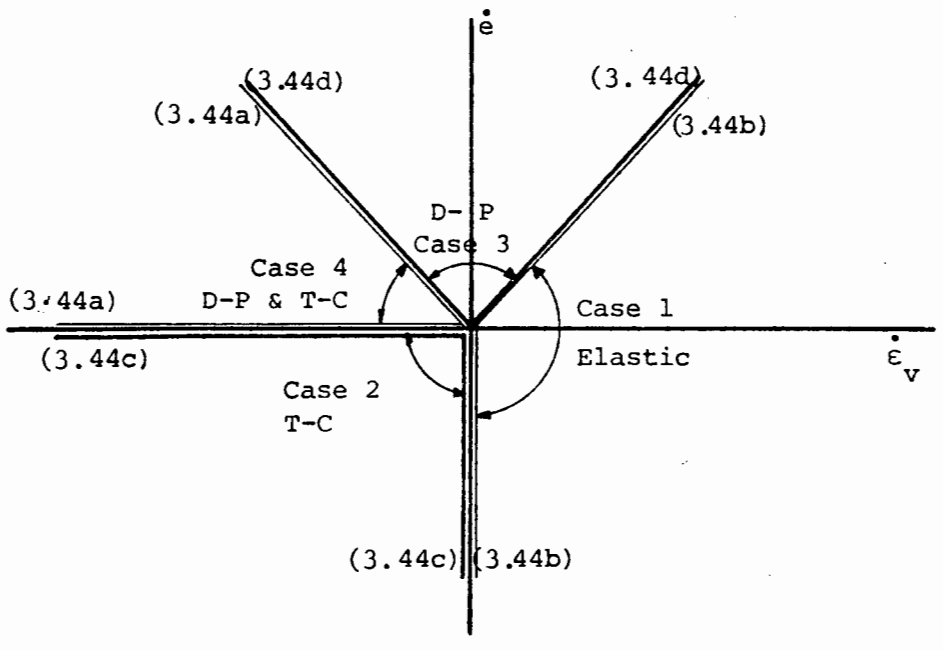

Figure 3.4: Total strain rate space behaviour of tension vertex.

$$a = 1 - \frac{\bar{\varepsilon}^p_{vo}}{W} \quad . \tag{3.45b}$$

For loading on both surfaces, the plastic strain rates are given as (cf. equn. (3.14b))

$$\dot{e}^p = \lambda_1 \frac{\partial F_1}{\partial s} + \lambda_2 \frac{\partial F_2}{\partial s} = \lambda_1 + 2R^2 s\lambda_2 \quad , \tag{3.46a}$$

$$\dot{\varepsilon}^p_v = \lambda_1 \frac{\partial F_1}{\partial \sigma_m} + \lambda_2 \frac{\partial F_2}{\partial \sigma_m} = \alpha\lambda_1 - \lambda_2 \quad , \tag{3.46b}$$

with $\lambda_1 \geq 0, \quad \lambda_2 \geq 0$.

The total strain rates are

$$\dot{e} = \frac{\dot{s}}{G} + \lambda_1 + 2R^2 s\lambda_2 \quad , \quad \dot{\varepsilon}_v = \frac{\dot{\sigma}_m}{K} + \alpha\lambda_1 - \lambda_2 \quad , \tag{3.47}$$

and hence, inverting,

$$\dot{s} = G\left(\dot{e} - \lambda_1 - 2R^2 s\lambda_2\right) \quad , \quad \dot{\sigma}_m = K\left(\dot{\varepsilon}_v - \alpha\lambda_1 + \lambda_2\right) \quad . \tag{3.48}$$

The condition for simultaneous loading on F_1 and F_2 is

$$\dot{F}_1 = \alpha\dot{\sigma}_m + \dot{s} = 0 \quad , \tag{3.49a}$$

$$\dot{F}_2 = -\dot{\sigma}_m + 2R^2 s\dot{s} - \frac{1}{WD\left(a - \frac{\varepsilon^p_v}{W}\right)} \dot{\varepsilon}^p_v = 0 \quad . \tag{3.49b}$$

We now use equn. (3.49a) to express $\dot{s}$ in terms of $\dot{\sigma}_m$, and, with equn. (3.46b) solve equn. (3.49b) for $\left(\alpha\lambda_1 - \lambda_2\right)$ in terms of $\dot{\sigma}_m$;

$$\alpha\lambda_1 - \lambda_2 = -WD\left(a - \frac{\varepsilon_v^p}{W}\right)\left(1 + 2R^2 s\alpha\right)\dot{\sigma}_m \quad . \tag{3.50}$$

The second of equns. (3.48) then gives

$$\dot{\sigma}_m = \frac{KH}{H-K(1+2R^2 s\alpha)}\,\dot{\varepsilon}_v \tag{3.51a}$$

where

$$H = \frac{1}{WD\left(a - \frac{\varepsilon_v^p}{W}\right)} \tag{3.51b}$$

Equn. (3.49a) now gives

$$\dot{s} = -\alpha\dot{\sigma}_m = \frac{-\alpha KH}{H-K(1+2R^2 s\alpha)}\,\dot{\varepsilon}_v \quad . \tag{3.51c}$$

The requirement that $\lambda_1 > 0$, $\lambda_2 > 0$ provides the conditions for loading. We now solve for λ_1, λ_2 from equns. (3.48), using equns. (3.51); after some arithmetic, we find

$$\lambda_1 = \frac{1}{1+2R^2 s\alpha}\,\dot{e} + \frac{2R^2 sGK - \frac{\alpha KH}{1+2R^2 s\alpha}}{GK - HG + 2GK\alpha sR^2}\,\dot{\varepsilon}_v \quad ,$$

$$\lambda_2 = \frac{\alpha}{1+2R^2 s\alpha}\,\dot{e} - \frac{GK + \frac{\alpha^2 HK}{1+2R^2 s\alpha}}{GK-HG+2GK\alpha sR^2}\,\dot{\varepsilon}_v \quad . \tag{3.52}$$

The conditions for loading on both yield surfaces at the vertex are $\lambda_1 > 0$, $\lambda_2 > 0$ in equn (3.52). The expressions can be simplified, with extensive algebraic manipulation which we shall not give in detail.

Thus the constitutive equations for $F_1 = 0$, $F_2 = 0$, $F_3 < 0$ and $\dot{F}_1 = 0$, $\dot{F}_2 = 0$ are given by

$$\begin{bmatrix} \dot{s} \\ \dot{\sigma}_m \end{bmatrix} = \begin{bmatrix} 0 & \dfrac{-\alpha KH}{H-K(1+2R^2 s\alpha)} \\ 0 & \dfrac{KH}{H-K(1+2R^2 s\alpha)} \end{bmatrix} \begin{bmatrix} \dot{e} \\ \dot{\varepsilon}_v \end{bmatrix} \tag{3.53a}$$

for

$$\dot{e} + \frac{(4R^4 s^2 GK\alpha + 2R^2 sGK - \alpha KH)}{(GK - GH + 2R^2 s\alpha GK)} \dot{\varepsilon}_v > 0 \quad , \tag{3.53b}$$

and

$$\dot{e} - \frac{(GK + 2R^2 s\alpha GK + HK\alpha^2)}{\alpha(GK - GH + 2R^2 s\alpha GK)} \dot{\varepsilon}_v > 0 \quad . \tag{3.53c}$$

It should be noted that the stress invariant rates depend only on the volume strain rate, and not on the shear strain rate. The shear strain rate is not of course zero; it is given in equn. (3.47) and it can be seen that the plastic shear strain rate wil be non-negative for the condition $\lambda_1 > 0$, $\lambda_2 > 0$. If the volume strain rate is zero the stress rates are both zero, and plastic shear deformation may take place at constant stress. If the total volume strain rate is negative, the stress point moves along the Drucker-Prager line in Fig. 3.3 to the right, pushing the cap ahead of it. If, on the other hand, the total volume strain rate is positive, the stress point moves along the Drucker-Prager line to the left, pulling the cap behind it. In this latter case the relations are not necessarily stable, since

$$\dot{s}\,\dot{e} + \dot{\sigma}_m\,\dot{\varepsilon}_v = \frac{KH\left(\dot{\varepsilon}_v^2 - \alpha\dot{\varepsilon}_v\dot{e}\right)}{H-K\left(1+2R^2s\alpha\right)} \tag{3.54}$$

is not necessarily nonnegative when $\dot{\varepsilon}_v > 0$, $\dot{e} > 0$.

Before commenting further on these relations in Section 3.6, we shall complete the set of equations for the response at the vertex. First, we treat case 3 where yielding takes place on the Drucker-Prager yield surface only, i.e. $F_1 = 0$, $F_2 = 0$, $F_3 < 0$ and $\dot{F}_1 = 0$, $\dot{F}_2 < 0$. Non-zero plastic strain rates are possible, with

$$\begin{aligned} \dot{e}^p &= \lambda_1 \frac{\partial F_1}{\partial s} = \lambda_1 \quad , \\ \dot{\varepsilon}_v^p &= \lambda_1 \frac{\partial F_1}{\partial \sigma_m} = \alpha\lambda_1 \quad . \end{aligned} \tag{3.55}$$

The condition for loading (i.e. $\lambda_1 > 0$) is

$$\dot{F}_1 = \alpha\dot{\sigma}_m + \dot{s} = 0 \quad . \tag{3.56}$$

The total strain rates are

$$\dot{e} = \frac{\dot{s}}{G} + \lambda_1 \quad , \qquad \dot{\varepsilon}_v = \frac{\dot{\sigma}_m}{K} + \alpha\lambda_1 \quad , \tag{3.57}$$

which give the stress rates as

$$\dot{s} = G\left(\dot{e} - \lambda_1\right) \quad , \qquad \dot{\sigma}_m = K\left(\dot{\varepsilon}_v - \alpha\lambda_1\right) \quad . \tag{3.58}$$

These equations are now substituted into equn. (3.56) to give λ_1;

$$\lambda_1 = \frac{G}{G+\alpha^2 K}\dot{e} + \frac{\alpha K}{G+\alpha^2 K}\dot{\varepsilon}_v \quad . \tag{3.59}$$

Since it is required that $\lambda_1 > 0$, equn. (3.59) also gives the condition for loading. Thus on substituting equn (3.59) into equn.(3.58) for $\lambda_1 > 0$, we get for $F_1 = 0$, $F_2 = 0$, $F_3 < 0$ and $\dot{F}_1 = 0$, $\dot{F}_2 < 0$,

$$\begin{bmatrix} \dot{s} \\ \dot{\sigma}_m \end{bmatrix} = \begin{bmatrix} G - \frac{G^2}{G+\alpha^2 K} & -\frac{\alpha GK}{G+\alpha^2 K} \\ -\frac{\alpha GK}{G+\alpha^2 K} & K - \frac{K^2\alpha^2}{G+\alpha^2 K} \end{bmatrix} \begin{bmatrix} \dot{e} \\ \dot{\varepsilon}_v \end{bmatrix} \tag{3.60a}$$

$$\text{for} \quad G\dot{e} + \alpha K\dot{\varepsilon}_v > 0 \quad , \tag{3.60b}$$

and

$$\dot{e} - \frac{(GK + 2R^2 s\alpha GK + HK\alpha^2)}{\alpha(GK-GH + 2R^2 s\alpha GK)}\dot{\varepsilon}_v < 0 \quad , \quad (\dot{F}_2 < 0) \quad . \tag{3.60c}$$

Second, consider case 2 where yielding is associated with the cap i.e. $F_1 = 0$, $F_2 = 0$, $F_3 < 0$ and $\dot{F}_1 < 0$, $\dot{F}_2 = 0$.

From equn. (3.14b), the plastic strain rates are

$$\dot{e}^p = \lambda_2 \frac{\partial F_2}{\partial s} = 2R^2 s\lambda_2 \quad ,$$

$$\dot{\varepsilon}_v^p = \lambda_2 \frac{\partial F_2}{\partial \sigma_m} = -\lambda_2 \quad , \tag{3.61}$$

with $\lambda_2 > 0$. The total strain rates are then

$$\dot{e} = \frac{\dot{s}}{G} + 2R^2 s\lambda_2 \quad , \quad \dot{\varepsilon}_v = \frac{\dot{\sigma}_m}{K} - \lambda_2 \quad , \tag{3.62}$$

and hence, on inverting,

$$\dot{s} = G(\dot{e} - 2R^2 s\lambda_2) \quad , \quad \dot{\sigma}_m = K(\dot{\varepsilon}_v + \lambda_2) \quad . \tag{3.63}$$

The condition for loading is

$$\dot{F}_2 = -\dot{\sigma}_m + 2R^2 s\dot{s} - H\dot{\varepsilon}_v^p = 0 \quad . \tag{3.64}$$

We now substitute equns. (3.61) and (3.63) into equn. (3.64) in order to determine λ_2 ;

$$\lambda_2 = \frac{1}{K+4R^4 s^2 G-H}\left[\, 2R^2 sG\dot{e} - K\dot{\varepsilon}_v \,\right] \quad . \tag{3.65}$$

The denominator in this expression is always positive, and hence the numerator gives the sign of λ_2 . On substituting back into equns. (3.63) we thus find the cap constitutive equations for $F_1 = 0$, $F_2 = 0$, $F_3 < 0$ and $\dot{F}_1 < 0$, $\dot{F}_2 = 0$.

$$\begin{bmatrix} \dot{s} \\ \dot{\sigma}_m \end{bmatrix} = \begin{bmatrix} G - \dfrac{4R^4 s^2 G^2}{K+4R^4 s^2 G-H} & \dfrac{2R^2 sGK}{K+4R^4 s^2 G-H} \\ \dfrac{2R^2 sGK}{K+4R^4 s^2 G-H} & K - \dfrac{K^2}{K+4R^4 s^2 G-H} \end{bmatrix} \begin{bmatrix} \dot{e} \\ \dot{\varepsilon}_v \end{bmatrix} \tag{3.66a}$$

$$\text{for} \quad 2R^2 sG\dot{e} - K\dot{\varepsilon}_v > 0 \quad , \tag{3.66b}$$

and

$$\dot{e} + \frac{\left(4R^4 s^2 GK\alpha + 2R^2 sGK - \alpha KH\right)}{\left(GK - GH + 2R^2 s\alpha GK\right)}\dot{\varepsilon}_v < 0 \quad , \qquad (\dot{F}_1 < 0) \quad . \tag{3.66c}$$

Finally, for case 1 representing elastic unloading we have the elastic constitutive relation defined by equns. (3.14a). Thus for $F_1 = 0$, $F_2 = 0$, $F_3 < 0$ and $\dot{F}_1 < 0$, $\dot{F}_2 < 0$,

$$\begin{bmatrix} \dot{s} \\ \dot{\sigma}_m \end{bmatrix} = \begin{bmatrix} G & 0 \\ 0 & K \end{bmatrix} \begin{bmatrix} \dot{e} \\ \dot{\varepsilon}_v \end{bmatrix} \quad , \tag{3.67a}$$

for $G\dot{e} + \alpha K\dot{\varepsilon}_v < 0$ (3.67b)

and $2R^2 sG\dot{e} - K\dot{\varepsilon}_v < 0$. (3.67c)

The conditions which separate the various loading and unloading cases are shown diagrammatically in Fig. 3.5 in terms of total strain rate. This diagram shows that for $F_1 = 0$, $F_2 = 0$ we have a complete set of relations. In cases 1, 2 and 3 the constitutive relations involve positive definite symmetric matrices, and in such cases Drucker's stability postulate [61, 62] is satisfied in that $s\dot{e}\dot{e} + \dot{\sigma}_m \dot{\varepsilon}_v > 0$ for all $\dot{e}$, $\dot{\varepsilon}_v$ in these regimes. In all cases (including case 4) the plastic strain rate vector lies in the fan defined by adjacent normals at the singular point defining the intersection of $F_1 = 0$ and $F_2 = 0$ in stress space.

Finally, in our particular model we have also included a provision that the cap cannot move into the domain $\sigma_m > 0$. This is achieved by imposing an upper limit on the magnitude of $\bar{\varepsilon}_v^p$, given from equns. (3.16), (3.17) and (3.18) by the condition that the Drucker-Prager and cap surfaces intersect on the $\sigma_m = 0$ axis. This occurs when

$$\bar{\varepsilon}_v^p = W(1 - e^{-DR^2k^2}) \quad , \tag{3.68}$$

and changes in the hardening parameter σ_m^c are no longer recorded. Under these conditions, the cap becomes perfectly plastic for increases in plastic volume strain. The constitutive equations for the vertex must be modified somewhat, but the exercise is quite straightforward and details will not be given. If, in addition, the known tension cutoff T is set equal to zero, it becomes possible that plastic deformation may take place with $F_1 = 0$, $F_2 = 0$ and $F_3 = 0$, as shown in Fig. 3.6. The constitutive equations can be obtained from our previous cases with minor modifications, and details will again not be given.

A summary of the constitutive equations for the complete fully coupled model is given in Table 3.1. In this summary, the constitutive equations for the cap model are written in invariant form as

$$\begin{bmatrix} \dot{s} \\ \dot{\sigma}_m \end{bmatrix} = \begin{bmatrix} G - a_{11} & -a_{12} \\ -a_{21} & K - a_{22} \end{bmatrix} \begin{bmatrix} \dot{e} \\ \dot{\varepsilon}_v \end{bmatrix} , \tag{3.69}$$

where the coefficients a_{11}, a_{12}, a_{21}, a_{22} depend on the current state. The values of the coefficients are given in Table 3.1. In all cases except one the coefficient matrix is symmetric, with $a_{21} = a_{21}$, and semi-positive definite, in the sense that $\ddot{s}\ddot{e} + \dot{\sigma}_m \dot{\varepsilon}_v > 0$. The exceptional case has been discussed in some detail above.

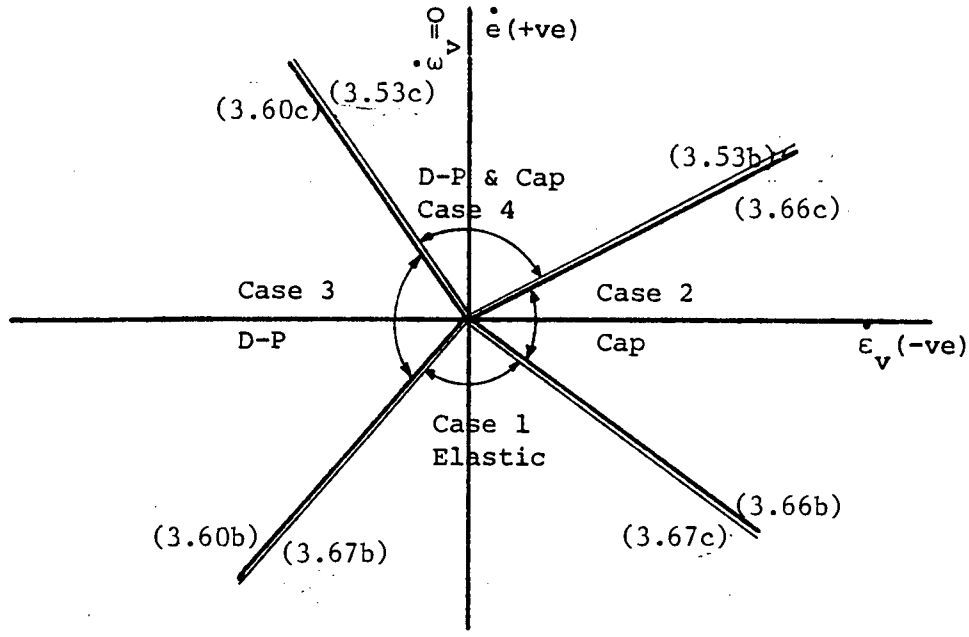

Figure 3.5: Total strain rate space behaviour of compression vertex.

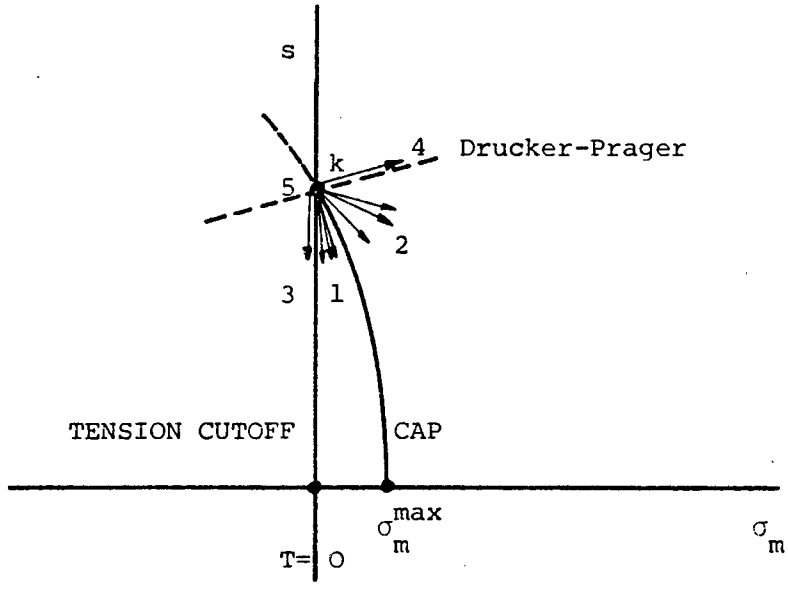

Figure 3.6: Stress space behaviour of compression/tension vertex.

TABLE 3.1 : Constitutive matrix coefficients for equations (3.69) and (3.92).

State	a_{11}	a_{12}	a_{21}	a_{22}	Conditions
Elastic	0	0	0	0	$F_1 < 0,\ F_2 < 0,\ F_3 < 0$ $F_1 = 0,\ F_2 < 0,\ F_3 < 0,\ G\dot{e} + \alpha K\dot{\varepsilon}_v < 0$ $F_1 < 0,\ F_2 = 0,\ F_3 < 0,\ 2R^2 sG\dot{e} - K\dot{\varepsilon}_v < 0$ $F_1 < 0,\ F_2 < 0,\ F_3 = 0,\ \dot{\varepsilon}_v < 0$ $F_1 = 0,\ F_2 < 0,\ F_3 = 0,\ G\dot{e} + \alpha K\dot{\varepsilon}_v < 0,\ \dot{\varepsilon}_v < 0$ $F_1 = 0,\ F_2 = 0,\ F_3 < 0,\ G\dot{e} + \alpha K\dot{\varepsilon}_v < 0,\ 2R^2 sG\dot{e} - K\dot{\varepsilon}_v < 0$ $F_1 = 0,\ F_2 = 0,\ F_3 = 0,\ 2R^2 sG\dot{e} - K\dot{\varepsilon}_v < 0,\ \dot{\varepsilon}_v < 0$
Yielding on Drucker-Prager	$\frac{G}{G+\alpha^2 K}$	$\frac{\alpha GK}{G+\alpha^2 K}$	$\frac{\alpha GK}{G+\alpha^2 K}$	$\frac{K^2\alpha^2}{G+\alpha^2 K}$	$F_1 = 0,\ F_2 < 0,\ F_3 < 0,\ G\dot{e} + \alpha K\dot{\varepsilon}_v \geq 0$ $F_1 = 0,\ F_2 < 0,\ F_3 = 0,\ G\dot{e} + \alpha K\dot{\varepsilon}_v \geq 0,\ -\alpha\dot{e} + \dot{\varepsilon}_v < 0$ $F_1 = 0,\ F_2 = 0,\ F_3 < 0,\ G\dot{e} + \alpha K\dot{\varepsilon}_v \geq 0,\ \dot{e} - \frac{(GK+2R^2 s\alpha GK+HK\alpha^2)}{\alpha(GK-GH+2R^2 s\alpha GK)}\dot{\varepsilon}_v < 0$
Yielding on cap	$\frac{4R^4 s^2 G^2}{K+4R^4 s^2 G-H}$	$\frac{-2R^2 sGK}{K+4R^4 s^2 G-H}$	$\frac{-2R^2 sGK}{K+4R^4 s^2 G-H}$	$\frac{K^2}{K+4R^4 s^2 G-H}$	$F_1 < 0,\ F_2 = 0,\ F_3 < 0,\ 2R^2 sG\dot{e} - K\dot{\varepsilon}_v \geq 0$ $F_1 = 0,\ F_2 = 0,\ F_3 < 0,\ 2R^2 sG\dot{e} - K\dot{\varepsilon}_v \geq 0,\ \dot{e} + \frac{(4R^4 s^2 GK\alpha+2R^2 sGK-\alpha KH)}{(GK-GH+2R^2 s\alpha GK)}\dot{\varepsilon}_v < 0$ $F_1 = 0,\ F_2 = 0,\ F_3 = 0,\ 2R^2 sG\dot{e} - K\dot{\varepsilon}_v \geq 0,\ \dot{e} + \frac{(4R^4 s^2 GK\alpha+2R^2 sGK-\alpha KH)}{(GK-GH+2R^2 s\alpha GK)}\dot{\varepsilon}_v < 0$

TABLE 3.1: (continued)

State	a_{11}	a_{12}	a_{21}	a_{22}	Conditions
Yielding on Tension Cut-off	O	O	O	K	$F_1 < O,\ F_2 < O,\ F_3 = O,\ \dot{\varepsilon}_v \geq O$ $F_1 = O,\ F_2 < O,\ F_3 = O,\ \dot{e} < O,\ \dot{\varepsilon}_v \geq O$ $F_1 = O,\ F_2 = O,\ F_3 = O,\ \dot{e} > O,\ \dot{\varepsilon}_v \geq O$
Yielding on Drucker-Prager and Tension Cut-off	G	O	O	K	$F_1 = O,\ F_2 < O,\ F_3 = O,\ \dot{e} \geq O,\ -\alpha\dot{e} + \dot{\varepsilon}_v \geq O$ $F_1 = O,\ F_2 = O,\ F_3 = O,\ \dot{e} \geq O,\ \dot{\varepsilon}_v < O$
Yielding on Drucker-Prager and cap.	G	$\frac{\alpha KH}{H-K(1+2R^2s\alpha)}$	O	$K - \frac{KH}{H-K(1+2R^2s\alpha)}$	$F_1 = O,\ F_2 = O,\ F_3 < O,$ $\dot{e} + \frac{(4R^4s^2GK\alpha+2R^2sGK-\alpha KH)}{(GK-GH+2R^2s\alpha GK)}\ \dot{\varepsilon}_v \geq O,$ $\dot{e} - \frac{(GK+2R^2s\alpha GK+HK\alpha^2)}{\alpha(GK-GH+2R^2s\alpha GK)}\ \dot{\varepsilon}_v \geq O$ $F_1 = O,\ F_2 = O,\ F_3 = O,\ \dot{\varepsilon}_v < O$ $\dot{e} + \frac{(4R^4s^2GK\alpha+2R^2sGK-\alpha KH)}{(GK-GH+2R^2s\alpha GK)}\ \dot{\varepsilon}_v \geq O$

3.6 Stability and Completeness of Some Existing Cap Models

The regime of behaviour described in case 4 of the Drucker-Prager cap corner, equns. (3.53), is of most interest. This provides the essential element that unlimited plastic shear deformation is possible. From a computational point of view, however, the equations have the disadvantage that they may permit an instability $(\dot{s}\dot{e} + \dot{\sigma}_m \dot{\varepsilon}_v < 0)$ when $\dot{\varepsilon}_v > 0$. This leads to possible difficulties and instabilities in the numerical solution, and forms of the constitutive equations in which the instability does not occur are of interest. We shall discuss two such cases.

In the model of Bathe et al [37] the values of λ_1, λ_2 for the case when both yield surfaces are active are taken as the sum of solutions for F_1 active alone and F_2 active alone; summing equations (3.59) and (3.65) this gives

$$\lambda_1 = \frac{G}{G+\alpha^2 K}\dot{e} + \frac{\alpha K}{G+\alpha^2 K}\dot{\varepsilon}_v \quad ,$$

$$\lambda_2 = \frac{2R^2 sG}{(K+4R^4 s^2 G-H)}\dot{e} - \frac{K}{(K+4R^4 s^2 G-H)}\dot{\varepsilon}_v \quad . \tag{3.70a}$$

The stress rate, strain rate equations effectively then come out to be made up of the terms in equns. (3.60) and (3.66);

$$\begin{bmatrix} \dot{s} \\ \dot{\sigma}_m \end{bmatrix} = \begin{bmatrix} G - \frac{G^2}{G+\alpha^2 K} - \frac{4R^4 s^2 G^2}{K+4R^4 s^2 G-H} & \frac{-\alpha GK}{G+\alpha^2 K} + \frac{2R^2 sGK}{K+4R^4 s^2 G-H} \\ \frac{-\alpha GK}{G+\alpha^2 K} + \frac{2R^2 sGK}{K+4R^4 s^2 G-H} & K - \frac{K^2\alpha^2}{G+\alpha^2 K} - \frac{K^2}{K+4R^4 s^2 G-H} \end{bmatrix} \begin{bmatrix} \dot{e} \\ \dot{\varepsilon}_v \end{bmatrix} . \tag{3.70b}$$

It can be seen immediately from these equations that for $\dot{e} > 0$, $\dot{\varepsilon}_v = 0$ the stress rates are not zero. A modified flow rule is then introduced, of the von Mises form, permitting $\dot{e}^p > 0$, $\dot{\varepsilon}_v^p = 0$ and therefore $\dot{s} = \dot{\sigma}_m = 0$ for $\dot{e} > 0$, $\dot{\varepsilon}_v = 0$.

The additional assumption of a von Mises flow rule is not consistent with the form of the yield function, since it has been seen that no further assumptions are necessary. Equns. (3.53a) and (3.70b) are substantially different in many respects, and could potentially lead to very different responses. One of the most important aspects is the suppression in equn. (3.70b) of any possible instability, since the matrix is positive definite.

The conditions which separate the various loading and unloading cases for the vertex behaviour can be derived for the model of Bathe et al [37] in the same manner as that used for the present model.

This has been done for the case of R = 0 (plane cap of Bathe et al) and the result is shown diagrammatically in Fig. 3.7. It can be seen immediately that the loading/unloading conditions for cases 1 to 3 are identical to the ones derived for the present model. However, the loading conditions for case 4 (yielding on both Drucker-Prager and cap yield surfaces) are given by $\lambda_1 > 0$, $\lambda_2 > 0$ where λ_1, λ_2 are those given in equn. (3.70a), i.e.

$$G\dot{e} + \alpha K \dot{\varepsilon}_v > 0 \qquad (3.71a)$$

$$-K \dot{\varepsilon}_v > 0 \quad (R = 0) \quad . \qquad (3.71b)$$

Comparing equn. (3.60c) to equn. (3.71b) and equn. (3.66c) to equn. (3.71a) it is clear that they do not match and there are in fact two gaps in the total strain rate space. This shows that the model of Bathe et al does not provide solutions for certain strain rate paths, this inconsistency arising from the additional assumptions about the behaviour of the plastic strain vector at the vertex and from the inconsistent calculation of the plastic multipliers λ_1, λ_2 in the case when both yield surfaces are active.

Let us know apply the vertex behaviour suggested by Sandler and Rubin [38] to the framework under discussion in the present work. While Sandler and Rubin use an elliptical cap and a curved failure surface, the essential difference at the vertex is that equn. (3.18) is modified by putting

$$\dot{\bar{\varepsilon}}_v^p = 0 \quad \text{if} \quad \dot{F}_1 = 0 \,, \quad \dot{F}_2 = 0 \,, \quad \dot{\varepsilon}_v^p > 0 \quad , \tag{3.72}$$

$$\dot{\bar{\varepsilon}}_v^p = \dot{\varepsilon}_v^p \quad \text{otherwise.}$$

This condition is introduced to prevent the cap from acting as a softening yield surface: it essentially prevents the cap-Drucker-Prager vertex from moving to the left in Fig. 3.3 with the stress point, and this is intended to suppress the possible instability which is apparent in equn. (3.54) when $\dot{\varepsilon}_v > 0$.

Since we are now dealing with a discontinuous evolution equation (equn. 3.72) it is necessary to satisfy the constraints on $\dot{\bar{\varepsilon}}_v^p$ in addition to the normal loading/unloading constraints. The conditions which separate the various loading and unloading cases can be derived for this modified model, and are shown in Fig. 3.8. The conditions for cases 1 to 3 are identical to those obtained earlier, as would be expected. For case 4, equn. (3.53b) $(\lambda_1 > 0)$ and the condition $\dot{\varepsilon}_v^p < 0$ bound the range of total strain rates for which the evolution equations (3.18) and (3.72) give the same results. The volume plastic strain rate constraint can be expressed in terms of total volume strain using equns. (3.46b) and (3.52).

$$\dot{\varepsilon}_v^p = \alpha \lambda_1 - \lambda_2 = \frac{(1+2R^2 s\alpha)GK}{GK-HG+2GK\alpha s R^2} \dot{\varepsilon}_v < 0 \tag{3.73a}$$

which implies that

$$\dot{\varepsilon}_v < 0 \quad . \tag{3.73b}$$

This means that for λ_1, $\lambda_2 \geq 0$ and zero or negative total volume strain rates there is no difference between the Sandler - Rubin modification and equns. (3.53); however, for λ_1, $\lambda_2 \geq 0$ and positive total volume strain rates $(\dot{\varepsilon}_v^p > 0 \ , \ \bar{\dot{\varepsilon}}_v^p = 0)$ the equations will be different. In this case, using the conditions $\dot{F}_1 = \dot{F}_2 = 0$ and following the same procedures that were used previously, the constitutive equations are found to be

$$\dot{s} = \dot{\sigma}_m = 0 \quad . \tag{3.74}$$

and the associated values of λ_1, λ_2 are

$$\lambda_1 = \frac{1}{(1+2R^2 s\alpha)} \{ \dot{e} + 2R^2 s\dot{\varepsilon}_v \} \quad , \tag{3.75a}$$

$$\lambda_2 = \frac{1}{(1+2R^2 s\alpha)} \{ \alpha\dot{e} - \dot{\varepsilon}_v \} \quad . \tag{3.75b}$$

Also, as an obvious consequence of (3.74) we have

$$\dot{\varepsilon}_v^p = \dot{\varepsilon}_v \quad . \tag{3.76}$$

The total strain rate space bounds for this mode of behaviour are given by $\lambda_1 \geq 0$, $\lambda_2 \geq 0$ of equns. (3.75) and $\dot{\varepsilon}_v > 0$ $(\text{or } \dot{\varepsilon}_v^p > 0)$, which shows a gap in the total strain rate space (Fig. 3.8). We see then that the modification suggested by Sandler and Rubin leads to an inconsistent model, the inconsistency arising from the choice of the evolution law for the history parameters.

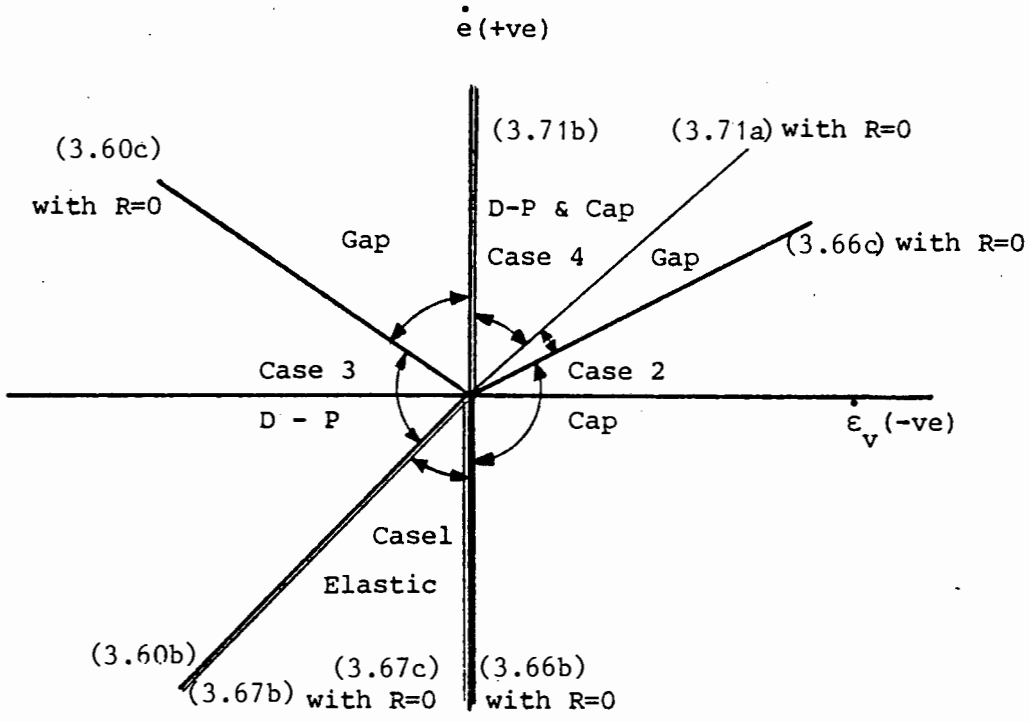

Figure 3.7: Bathe et al [37] model : total strain rate space behaviour of compression vertex.

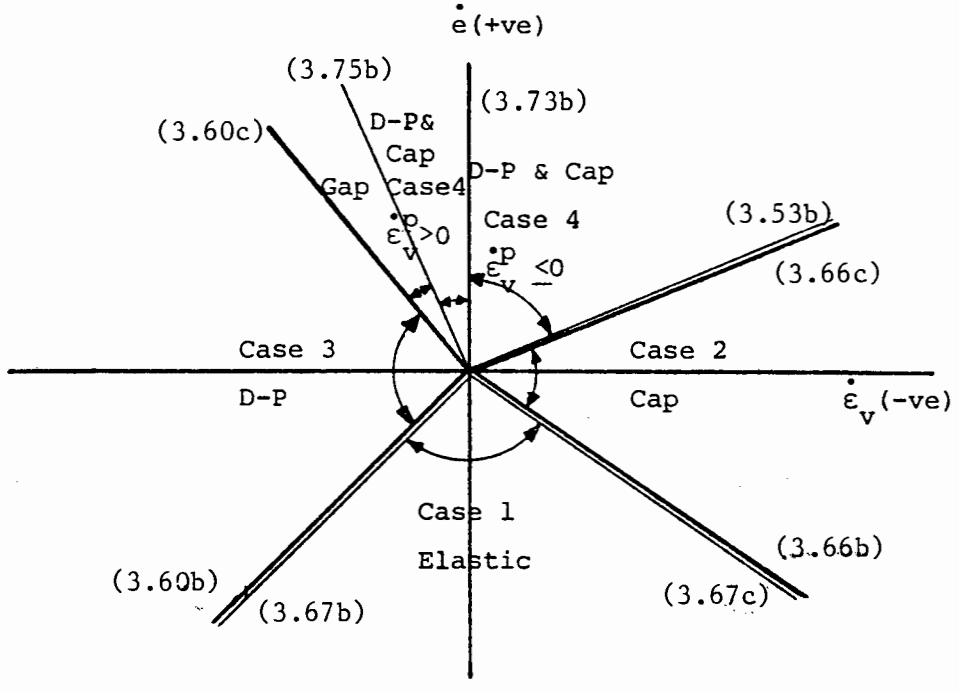

Figure 3.8: Sandler and Rubin [38] model : total strain rate space behaviour of compression vertex.

3.7 Constitutive Equations for Plane and Axisymmetric Problems

The constitutive equations for the cap model have been given in invariant form, which permits a simple two-dimensional representation. For finite element implementation, however, a more general matrix form is required. For completeness, we present a generalisation for the case of axisymmetric problems which can be reduced to plane stress and plane strain without difficulty.

The nonzero components of the total stress and strain are written in vector form as

$$\underset{\sim}{\sigma} = (\sigma_{11} \quad \sigma_{22} \quad \sigma_{12} \quad \sigma_{33})^T , \tag{3.77a}$$

$$\underset{\sim}{\varepsilon} = (\varepsilon_{11} \quad \varepsilon_{12} \quad \gamma_{12} \quad \varepsilon_{33})^T , \tag{3.77b}$$

where

$$\gamma_{12} = 2\varepsilon_{12} \quad . \tag{3.77c}$$

It is also convenient to identify the deviatoric components of stress and strain, in vector form, as

$$\underset{\sim}{s} = (s_{11} \quad s_{22} \quad s_{12})^T , \tag{3.78a}$$

$$\underset{\sim}{e} = (e_{11} \quad e_{22} \quad e_{12})^T \quad . \tag{3.78b}$$

We make use of the fact that $s_{11} + s_{22} + s_{33} = 0$, $e_{11} + e_{22} + e_{33} = 0$. Simple transformations provide us with the total stress and strain components in terms of the deviatoric stress and strain vectors, the mean hydrostatic stress σ_m and the volume strain ε_v;

$$\underset{\sim}{\sigma} = \begin{bmatrix} \sigma_{11} \\ \sigma_{22} \\ \sigma_{12} \\ \sigma_{33} \end{bmatrix} = \begin{bmatrix} 1 & 0 & 0 & 1 \\ 0 & 1 & 0 & 1 \\ 0 & 0 & 1 & 0 \\ -1 & -1 & 0 & 1 \end{bmatrix} \begin{bmatrix} s_{11} \\ s_{22} \\ s_{12} \\ \sigma_m \end{bmatrix} = \underset{\sim}{C} \begin{bmatrix} \underset{\sim}{s} \\ \sigma_m \end{bmatrix} , \tag{3.80a}$$

and

$$\begin{bmatrix} \dot{\underset{\sim}{e}} \\ \dot{\varepsilon}_v \end{bmatrix} = \begin{bmatrix} \dot{e}_{11} \\ \dot{e}_{22} \\ \dot{e}_{12} \\ \dot{\varepsilon}_v \end{bmatrix} = \begin{bmatrix} 2/3 & -1/3 & 0 & -1/3 \\ -1/3 & 2/3 & 0 & -1/3 \\ 0 & 0 & 1/2 & 0 \\ 1 & 1 & 0 & 1 \end{bmatrix} \begin{bmatrix} \dot{\varepsilon}_{11} \\ \dot{\varepsilon}_{22} \\ \dot{\gamma}_{12} \\ \dot{\varepsilon}_{33} \end{bmatrix} = \hat{\underset{\sim}{C}} \dot{\underset{\sim}{\varepsilon}} \quad . \tag{3.80b}$$

The deviatoric invariants can be written in terms of $\underset{\sim}{s}$ and $\underset{\sim}{e}$. The invariant shear strain rate is

$$\dot{e} = \frac{1}{s} s_{ij} \dot{e}_{ij} = \frac{1}{s} \underset{\sim}{s}^T \underset{\sim}{n} \dot{\underset{\sim}{e}} \quad , \tag{3.81a}$$

where

$$\underset{\sim}{n} = \begin{bmatrix} 2 & 1 & 0 \\ 1 & 2 & 0 \\ 0 & 0 & 2 \end{bmatrix} \quad . \tag{3.81b}$$

Similarly it can be shown that

$$s = \left\{ \frac{1}{2} s_{ij} s_{ij} \right\}^{1/2} = \left\{ \frac{1}{2} \underset{\sim}{s}^T \underset{\sim}{n} \underset{\sim}{s} \right\}^{1/2} \quad , \tag{3.82a}$$

$$\dot{s} = \frac{1}{2s} s_{ij} \dot{s}_{ij} = \frac{1}{2s} \underset{\sim}{s}^T \underset{\sim}{n} \dot{\underset{\sim}{s}} \quad . \tag{3.82b}$$

The plastic shear strain rate components comprise contributions from yielding on F_1, F_2 and F_3 (not simultaneously, of course). We can thus put

$$\begin{aligned} \dot{\underset{\sim}{e}}^p &= \lambda_1 \frac{\partial F_1}{\partial \underset{\sim}{s}} + \lambda_2 \frac{\partial F_2}{\partial \underset{\sim}{s}} + \lambda_3 \frac{\partial F_3}{\partial \underset{\sim}{s}} \\ &= \frac{\lambda_1}{2s} \frac{\partial F_1}{\partial s} \underset{\sim}{s} + \frac{\lambda_2}{2s} \frac{\partial F_2}{\partial s} \underset{\sim}{s} + \frac{\lambda_3}{2s} \frac{\partial F_3}{\partial s} \underset{\sim}{s} \quad . \end{aligned} \tag{3.83}$$

Substituting for F_1, F_2 and F_3 (equns. 3.16, 3.17 and 3.20), this becomes

$$\dot{\underset{\sim}{e}}^p = \left(\frac{\lambda_1}{2s} + R^2\lambda_2 \right) \underset{\sim}{s} \quad , \tag{3.84a}$$

whereas

$$\dot{\varepsilon}_v^p = \left(\alpha\lambda_1 - \lambda_2 + \lambda_3\right) \quad . \tag{3.84b}$$

The stress rates are then

$$\dot{\underset{\sim}{s}} = 2G\left(\dot{\underset{\sim}{e}} - \dot{\underset{\sim}{e}}^p\right) = 2G\dot{\underset{\sim}{e}} - 2G\left(\frac{\lambda_1}{2s} + R^2\lambda_2\right)\underset{\sim}{s} \quad ,$$

$$\dot{\sigma}_m = K\left(\dot{\varepsilon}_v - \dot{\varepsilon}_v^p\right) = K\dot{\varepsilon}_v - K\left(\alpha\lambda_1 - \lambda_2 + \lambda_3\right) . \tag{3.85}$$

For any particular state we substitute the appropriate expression for λ_1, λ_2 λ_3 and write equns. (3.85) as

$$\dot{\underset{\sim}{s}} = 2G\dot{\underset{\sim}{e}} - \frac{a_{11}}{s}\underset{\sim}{s}\,\dot{e} - \frac{a_{12}}{s}\underset{\sim}{s}\,\dot{\varepsilon}_v \quad , \tag{3.86a}$$

$$\dot{\sigma}_m = K\dot{\varepsilon}_v - a_{21}\,\dot{e} - a_{22}\,\dot{\varepsilon}_v \quad . \tag{3.86b}$$

Premultiplying equn. (3.86a) by $\left(\underset{\sim}{s}^T\underset{\sim}{n}/2s\right)$, equns. (3.86) become

$$\dot{s} = \left(G - a_{11}\right)\dot{e} - a_{12}\,\dot{\varepsilon}_v \quad ,$$

$$\dot{\sigma}_m = -a_{21}\,\dot{e} + \left(K - a_{22}\right)\dot{\varepsilon}_v \quad , \tag{3.87}$$

which is identical to equn. (3.69). Thus the coefficients a_{11}, a_{12}, a_{21}, a_{22} can be taken directly from our discussion of the invariant equations. This leaves us with the task of transforming equns. (3.86) into stress and strain rates $\dot{\underset{\sim}{\sigma}}$ and $\dot{\underset{\sim}{\varepsilon}}$.

Substituting from equn. (3.81a), equns (3.86) can be written in matrix form as

$$\begin{bmatrix} \dot{\underset{\sim}{s}} \\ \dot{\sigma}_m \end{bmatrix} = \begin{bmatrix} 2G\,\underset{\sim}{I} - \frac{a_{11}}{s^2}\,\underset{\sim}{s}\,\underset{\sim}{s}^T\underset{\sim}{n} & \frac{-a_{12}}{s}\,\underset{\sim}{s} \\ \frac{-a_{21}}{s}\,\underset{\sim}{s}^T\underset{\sim}{n} & K - a_{22} \end{bmatrix} \begin{bmatrix} \dot{\underset{\sim}{e}} \\ \dot{\varepsilon}_v \end{bmatrix} \qquad (3.88)$$

$$= \underset{\sim}{D} \begin{bmatrix} \dot{\underset{\sim}{e}} \\ \dot{\varepsilon}_v \end{bmatrix} ,$$

where $\underset{\sim}{I}$ is a 3 x 3 unit matrix.

We note that we may partition the matrices $\underset{\sim}{C}$ and $\hat{\underset{\sim}{C}}$ (equns. 3.80) and write

$$\underset{\sim}{C} = \begin{bmatrix} \underset{\sim}{I} & \underset{\sim}{h} \\ -\underset{\sim}{h}^T & 1 \end{bmatrix} , \quad \hat{\underset{\sim}{C}} = \begin{bmatrix} \underset{\sim}{n}^{-1} & -\frac{1}{3}\,\underset{\sim}{h} \\ \underset{\sim}{h}^T & 1 \end{bmatrix} , \qquad (3.89a)$$

where

$$\underset{\sim}{h}^T = \begin{pmatrix} 1 & 1 & 0 \end{pmatrix} . \qquad (3.89b)$$

It is also convenient to define

$$\hat{\underset{\sim}{s}} = \frac{1}{s}\,\underset{\sim}{s} , \quad \hat{\underset{\sim}{t}} = \frac{1}{s}\,\underset{\sim}{n}\,\underset{\sim}{s} = \underset{\sim}{n}\,\hat{\underset{\sim}{s}} . \qquad (3.89c)$$

Using these relationships, we then form

$$\dot{\underset{\sim}{\sigma}} = \underset{\sim}{C} \begin{bmatrix} \dot{\underset{\sim}{s}} \\ \dot{\sigma}_m \end{bmatrix} = \underset{\sim}{C}\,\underset{\sim}{D}\,\hat{\underset{\sim}{C}}\,\dot{\underset{\sim}{\varepsilon}} = \underset{\sim}{D}^*\,\dot{\underset{\sim}{\varepsilon}} \qquad (3.90a)$$

where

$$\underset{\sim}{D}^{*} = \begin{bmatrix} \underset{\sim}{I} & \underset{\sim}{h} \\ -\underset{\sim}{h}^{T} & 1 \end{bmatrix} \begin{bmatrix} 2G\underset{\sim}{I} - a_{11}\,\hat{\underset{\sim}{s}}\,\hat{\underset{\sim}{t}}^{T} & -a_{12}\,\hat{\underset{\sim}{s}} \\ -a_{21}\,\hat{\underset{\sim}{t}}^{T} & K - a_{22} \end{bmatrix} \begin{bmatrix} \underset{\sim}{n}^{-1} & -\frac{1}{3}\,\underset{\sim}{h} \\ \underset{\sim}{h}^{T} & 1 \end{bmatrix} . \qquad (3.90b)$$

In multiplying out equn. (3.90b), we note several simple relationships;

$$\underset{\sim}{n}^{-1}\,\hat{\underset{\sim}{t}} = \hat{\underset{\sim}{s}} \quad ; \quad \frac{1}{3}\,\hat{\underset{\sim}{t}}^{T}\,\underset{\sim}{h} = \hat{\underset{\sim}{s}}^{T}\,\underset{\sim}{h} \quad ; \quad \underset{\sim}{h}^{T}\,\underset{\sim}{n}^{-1} = \frac{1}{3}\,\underset{\sim}{h}^{T} . \qquad (3.91)$$

Carrying through the multiplications, and simplifying through the use of equns. (3.91), we find that

$$\underset{\sim}{D}^{*} = \left[\begin{array}{l|l} 2G\,\underset{\sim}{n}^{-1} - a_{11}\,\hat{\underset{\sim}{s}}\,\hat{\underset{\sim}{s}}^{T} & -\frac{2}{3}\,G\,\underset{\sim}{h} + a_{11}\,\hat{\underset{\sim}{s}}\,\hat{\underset{\sim}{s}}^{T}\,\underset{\sim}{h} \\ -(a_{12}\,\hat{\underset{\sim}{s}}\,\underset{\sim}{h}^{T} + a_{21}\,\underset{\sim}{h}\,\hat{\underset{\sim}{s}}^{T}) & -a_{12}\,\hat{\underset{\sim}{s}} + a_{21}\,\underset{\sim}{h}\,\hat{\underset{\sim}{s}}^{T}\,\underset{\sim}{h} \\ +(K - a_{22})\,\underset{\sim}{h}\,\underset{\sim}{h}^{T} & +(K - a_{22})\,\underset{\sim}{h} \\ \hline -\frac{2}{3}\,G\,\underset{\sim}{h}^{T} + a_{11}\,\underset{\sim}{h}^{T}\,\hat{\underset{\sim}{s}}\,\hat{\underset{\sim}{s}}^{T} & (\frac{4}{3}\,G + K) - a_{11}\,(\underset{\sim}{h}^{T}\hat{\underset{\sim}{s}})^{2} \\ +a_{12}\,\underset{\sim}{h}^{T}\,\hat{\underset{\sim}{s}}\,\underset{\sim}{h}^{T} - a_{21}\,\hat{\underset{\sim}{s}}^{T} & +(a_{12} + a_{21})\,\underset{\sim}{h}^{T}\,\hat{\underset{\sim}{s}} - a_{22} \\ +(K - a_{22})\,\underset{\sim}{h}^{T} & \end{array}\right] . \qquad (3.92)$$

The matrix $\underset{\sim}{D}^{*}$ is thus given explicity. It reduces to the elasticity matrix when there is no plastic deformation i.e. when $a_{11} = a_{12} = a_{21} = a_{22} = 0$. Careful inspection will show that $\underset{\sim}{D}^{*}$ is symmetric and semi-positive definite when $a_{12} = a_{21}$, but $\underset{\sim}{D}^{*}$ is not symmetric and not necessarily positive definite when $a_{12} \neq a_{21}$. The exceptional behaviour for loading on the Drucker-Prager surface and the cap simultaneously is thus preserved in the full set of equations.

The expressions for the plastic multipliers λ_1, λ_2 and λ_3 developed for the invariant case are preserved in the generalised equations. These are necessary for the calculation of the plastic strain rates.

Summarising, equns. (3.90a) and (3.92), together with Table 3.1, provide the complete constitutive equations for the cap model in the case of axisymmetric problems. The generalisation of the invariant case is essentially straight forward, and the behaviour noted in the invariant case is qualitatively preserved.

CHAPTER 4

IMPLEMENTATION OF THE PLASTICITY CAP MODEL AND APPLICATIONS

The plasticity cap model developed in Chapter 3 has been implemented in NOSTRUM [78-82], a large scale finite element program for the static and dynamic nonlinear analysis of plane (including axisymmetric) continua and structures. The fundamental framework upon which NOSTRUM is built is an incremental strategy employing a tangent stiffness approach [83,84]. Coupled to the incremental solution is an equilibrium iteration procedure of sufficient generality to allow a number of nonlinear solution techniques, such as initial stiffness, Newton-Raphson and some modified Newton-Raphson schemes to be employed.

The elements of interest to this work, which are contained in the NOSTRUM element library, include the standard two-dimensional 4, 8 and 9 noded isoparametric quadrilaterals [85] and their compatible infinite elements [86] used to model unbounded domains.

Included in the NOSTRUM constitutive model library (and of interest to this work) are: the Von-Mises, Tresca, Drucker-Prager and Mohr-Coulomb single surface models; the Drucker-Prager cap model described in Chapter 3; and the internal damage model discussed in chapters 5 - 7. Appendix C contains brief extracts of the NOSTRUM User's Manual describing the input parameters for the constitutive models developed and used in this work.

The NOSTRUM implementation of the Drucker-Prager cap model is described in this chapter. This is followed by applications of the model to uniform stress problems as well as realistic non-uniform boundary value problems.

4.1 Finite Element Implementation Using an Incremental Tangent Approach

We make use of an equilibrium iteration scheme based on the Newton-Raphson method. In this scheme the load is applied incrementally. Two successive values of the total load are identified at $\underset{\sim}{R}_t$ and $\underset{\sim}{R}_{t+\Delta t}$, so that the load increment is

$$\Delta\underset{\sim}{R} = \underset{\sim}{R}_{t+\Delta t} - \underset{\sim}{R}_t \; . \tag{4.1}$$

The subscripts t and $t+\Delta t$ indicate the instants at which the external loads $\underset{\sim}{R}$ are evaluated.

It is assumed that an acceptably accurate set of displacements is known for the loading $\underset{\sim}{R}_t$. By this we mean the displacements $\underset{\sim}{u}_t$, together with the previous history, lead to internal forces $\underset{\sim}{F}_t$ such that a residual $(\underset{\sim}{R}_t - \underset{\sim}{F}_t)$ is within a specified tolerance.

Assume now that the i-th estimate of the displacements for load $\underset{\sim}{R}_{t+\Delta t}$ is $\underset{\sim}{u}^i_{t+\Delta t}$. This leads to internal forces $\underset{\sim}{F}^i_{t+\Delta t}$ which are not equal to the loads $\underset{\sim}{R}_{t+\Delta t}$. In order to improve the displacement increments we compute a tangent stiffness matrix $\underset{\sim}{K}^i_{t+\Delta t}$ and put

$$\underset{\sim}{u}^{i+1}_{t+\Delta t} = \underset{\sim}{u}^i_{t+\Delta t} + \Delta\underset{\sim}{u}^i \tag{4.2}$$

where $\Delta\underset{\sim}{u}^i$ is calculated from the equilibrium equations as

$$\Delta\underset{\sim}{u}^i = (\underset{\sim}{K}^i_{t+\Delta t})^{-1} \, (\underset{\sim}{R}_{t+\Delta t} - \underset{\sim}{F}^i_{t+\Delta t}) \; . \tag{4.3}$$

This iterative procedure is continued until the residual

$$\underset{\sim}{\psi}^i = (\underset{\sim}{R}_{t+\Delta t} - \underset{\sim}{F}^i_{t+\Delta t}) \tag{4.4}$$

is reduced to an acceptable tolerance. At this point, the solution moves to the next load step.

There are a number of options in the program regarding the choice of the stiffness matrix $\underset{\sim}{K}^{i}_{t+\Delta t}$. In the full Newton-Raphson option, $\underset{\sim}{K}^{i}_{t+\Delta t}$ is updated at each iteration, in order to include the improved estimate of displacement $\underset{\sim}{u}^{i}_{t+\Delta t}$. The full Newton-Raphson option is essential for problems which are highly nonlinear, but it is expensive in computer time in that the stiffness must be re-evaluated and re-inverted at each iteration. In the first modified Newton-Raphson option we update only at the beginning of each load step, so that $\underset{\sim}{K}^{i}_{t+\Delta t} = \underset{\sim}{K}^{o}_{t+\Delta t}$. In the second modified Newton-Raphson option the stiffness is updated only once after the first iteration of the load step, i.e. $\underset{\sim}{K}^{i}_{t+\Delta t} = \underset{\sim}{K}^{1}_{t+\Delta t}$. Convergence is slower for both modified Newton-Raphson schemes, but there are circumstances in which the cost of additional iterations is significantly less than the cost of reformulating the stiffness matrix. The final option is the initial stiffness method, in which the stiffness matrix is never updated, but retains the value used on the first iteration of the first load step. There are cases in which the initial stiffness option can be very effective, although convergence is generally very slow for highly nonlinear problems. Combinations of these four options are also possible within one analysis.

The solution of the equilibrium equations (4.3) is carried out using a blocked frontal solution algorithm. For the cases when the stiffness matrix is not symmetric (e.g. for constitutive matrices corresponding to yielding with both Drucker-Prager and cap yield surfaces active - equn. (3.53a)) a non-symmetric front solver has been implemented and is used.

4.2 Integration of the Constitutive Equations

To complete the procedure established in the previous section, the calculation of $\underset{\sim}{F}^{i}_{t+\Delta t}$ has to be dealt with. $\underset{\sim}{F}^{i}_{t+\Delta t}$ is calculated from the stresses $\underset{\sim}{\sigma}^{i}_{t+\Delta t}$ at each integration point (2x2 and 3x3 standard Gauss-Legendre rules are used in this work) as

$$ {}^{e}\underset{\sim}{F}^{i}_{t+\Delta t} = \int_{V_e} \underset{\sim}{B}^{T} \underset{\sim}{\sigma}^{i}_{t+\Delta t} \, dV_e \tag{4.5} $$

and

$$ \underset{\sim}{F}^{i}_{t+\Delta t} = \sum_{e} {}^{e}\underset{\sim}{F}^{i}_{t+\Delta t} \tag{4.6} $$

where the superscript e denotes element e with volume V_e and $\underset{\sim}{B}$ is a strain displacement matrix.

The calculation of the internal forces $\underset{\sim}{F}^{i}_{t+\Delta t}$ requires that we be able to integrate the constitutive equations through the incremental iterative process of analysis. For this, at each Gauss integration point, one has to satisfy the rate relations

$$ \dot{\underset{\sim}{\sigma}} = \underset{\sim}{D} \, \dot{\underset{\sim}{\varepsilon}} \tag{4.7} $$

at every instant. In a displacement based formulation the strain changes are known for every increment and the corresponding changes in stress have to be evaluated according to equn. (4.7) together with the changes in internal variables. The stresses at instant $t+\Delta t$ for the i-th equilibriun iteration can be calculated as follows:

$$ \underset{\sim}{\sigma}^{i}_{t+\Delta t} = \underset{\sim}{\sigma}_{t} + \int_{\underset{\sim}{\varepsilon}_t}^{\underset{\sim}{\varepsilon}^{i}_{t+\Delta t}} \underset{\sim}{D} \, d\underset{\sim}{\varepsilon} \tag{4.8} $$

where $\underset{\sim}{\sigma}_{t}$ represents the equilibrated stresses at instant t. Bathe et al [37] emphasize that the integration should be done from an equilibrated

state which has previously been obtained, for instance the previous step as indicated in equn. (4.8). However, in quasi-static problems where relatively small changes in stress are likely to occur in each increment, equn. (4.8) can be relaxed for ease of computation. Owen and Hinton [84] suggest

$$\underset{\sim}{\sigma}^{t}_{t+\Delta t} = \underset{\sim}{\sigma}^{i-1}_{t+\Delta t} + \int_{\underset{\sim}{\varepsilon}^{i-1}_{t+\Delta t}}^{\underset{\sim}{\varepsilon}^{i}_{t+\Delta t}} \underset{\sim}{D}\, d\underset{\sim}{\varepsilon} = \underset{\sim}{\sigma}^{i-1}_{t+\Delta t} + \Delta\underset{\sim}{\sigma}^{i-1} \quad . \qquad (4.9)$$

The method suggested by Owen and Hinton is used in the calculation of stresses for the present Drucker-Prager cap model.

The integration necessary to implement equn. (4.9) is performed by dividing the inelastic part of the strain increment into a number of subincrements in a manner similar to that described by Owen and Hinton [84]. They suggest a formula for the number of subincrements which depends on the size of the inelastic strain increment. The cap model developed by Bathe et al [37] and implemented in ADINA [87] makes use of a fixed number of subincrements, but a rather large one in the author's opinion: ADINA uses 25 subincrements. A fixed number of 5 subincrements is used in the present cap model.

The method to calculate elastic-plastic stresses adopted in this work is discussed in detail by Owen and Hinton [84] and will not be repeated here, except for Fig. 4.1 which summarizes the sequence of operations necessary to apply it to a multisurface model. Note that although the integration of stresses is in general not performed from an equilibrated state (since we have adopted equn. (4.9)), the decision of which yield surfaces are active is based on an equilibrated state.

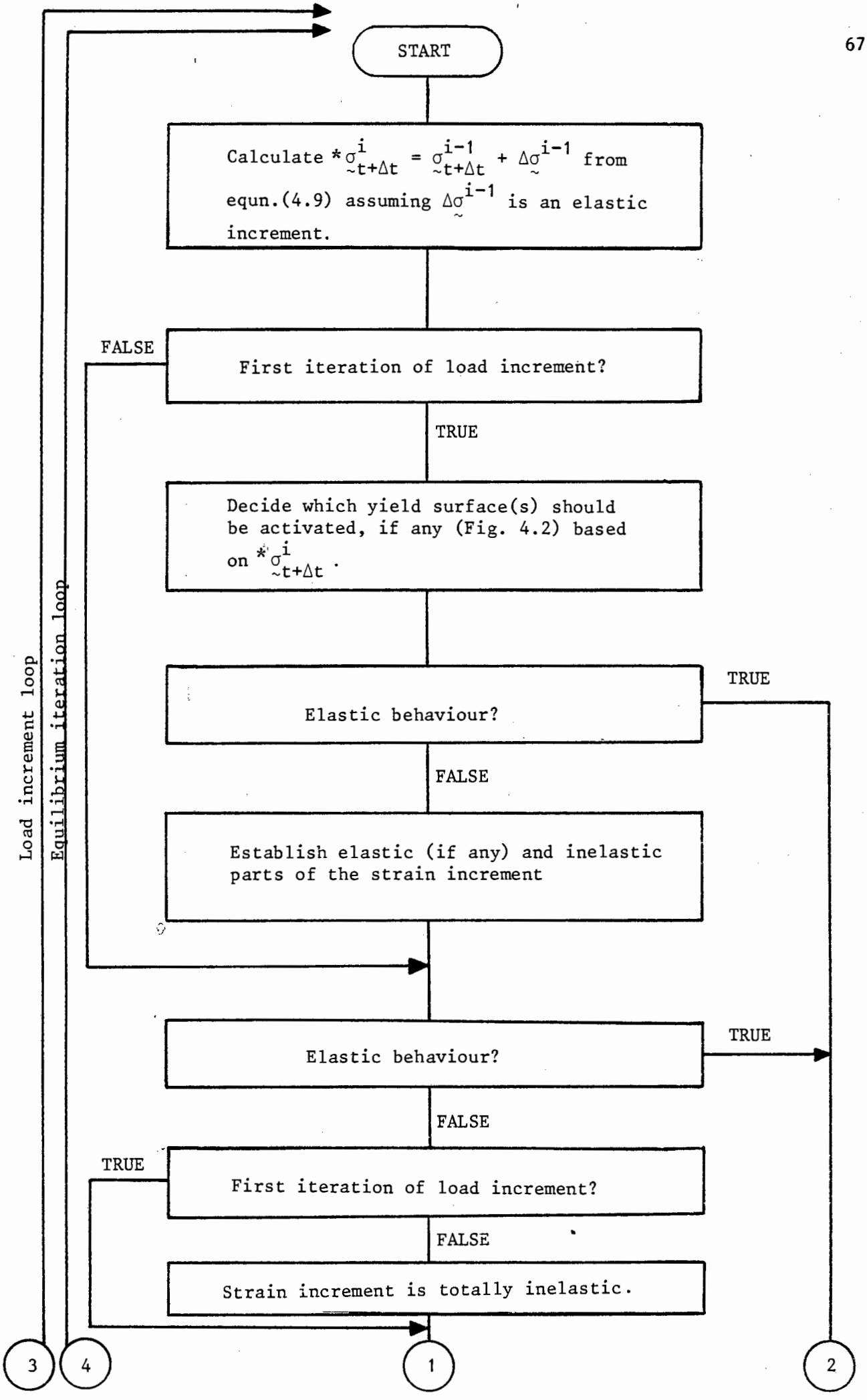
START
Calculate ${}^{*}\sigma^{i}_{t+\Delta t} = \sigma^{i-1}_{t+\Delta t} + \Delta\sigma^{i-1}$ from equn.(4.9) assuming $\Delta\sigma^{i-1}$ is an elastic increment.
First iteration of load increment?
FALSE
TRUE
Decide which yield surface(s) should be activated, if any (Fig. 4.2) based on ${}^{*}\sigma^{i}_{t+\Delta t}$.
Elastic behaviour?
TRUE
FALSE
Establish elastic (if any) and inelastic parts of the strain increment
Elastic behaviour?
TRUE
FALSE
First iteration of load increment?
TRUE
FALSE
Strain increment is totally inelastic.
Load increment loop
Equilibrium iteration loop
3
4
1
2

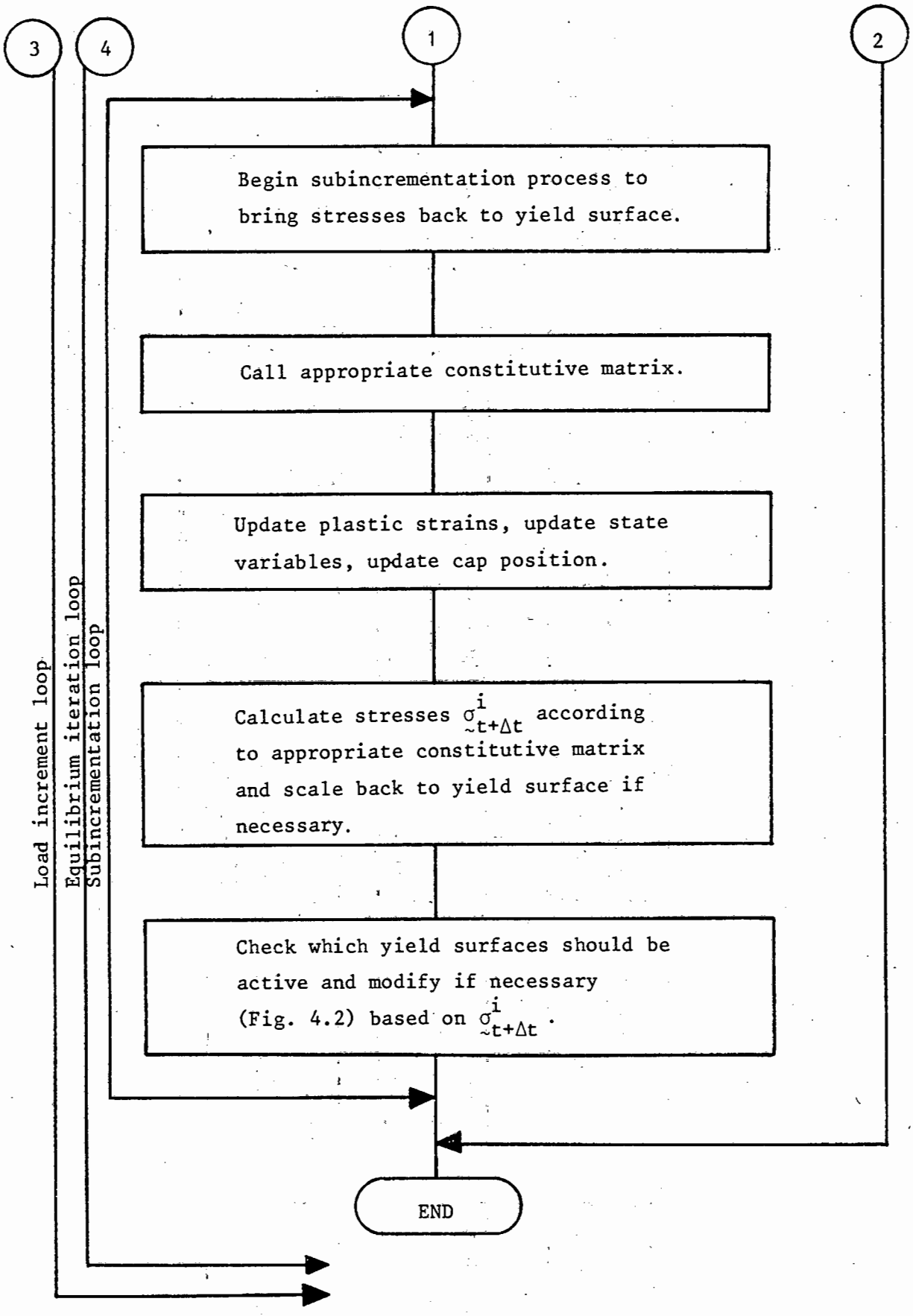

Figure 4.1: Elastic-plastic stress calculation in Drucker-Prager cap model (performed at every integration point).

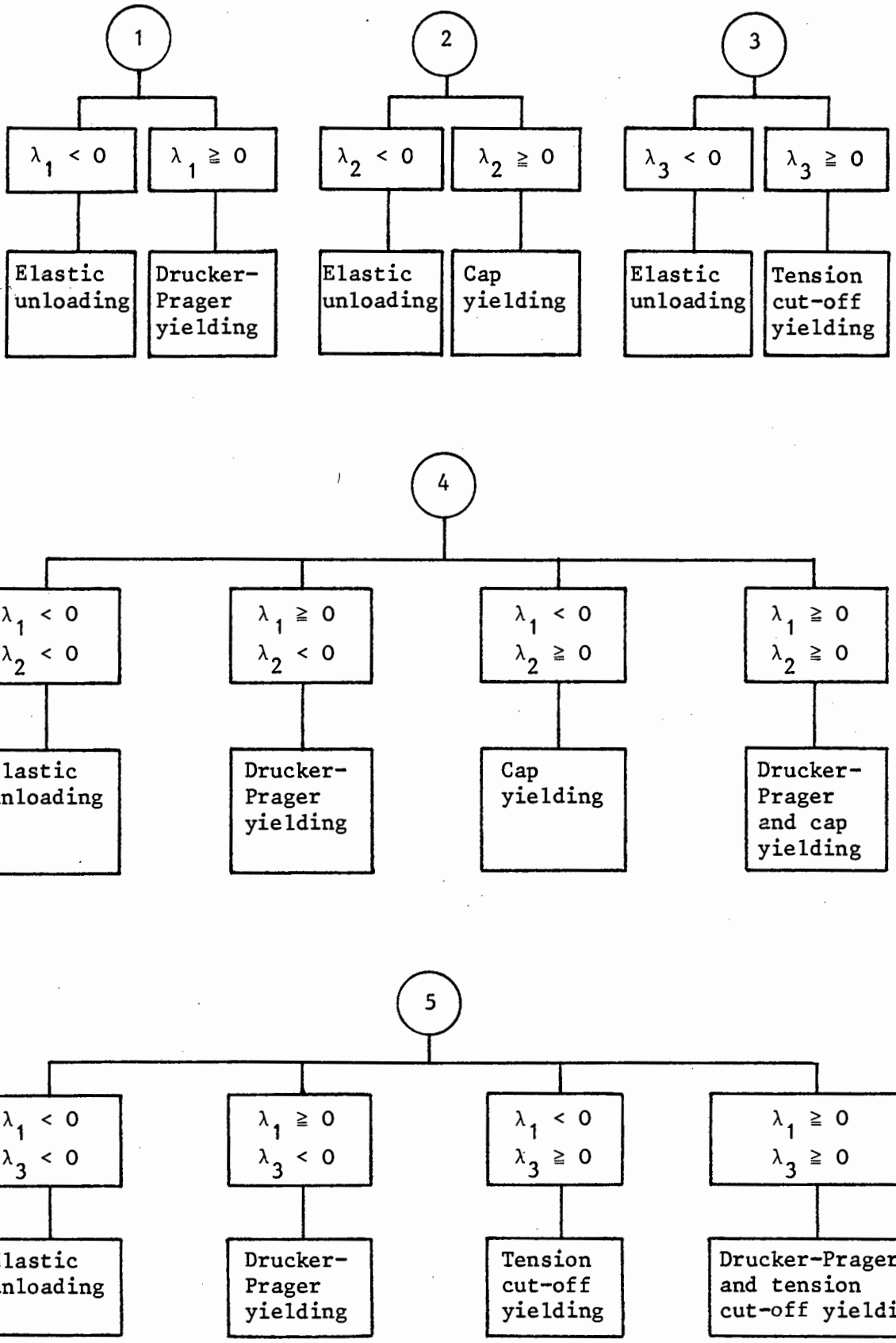

Figure 4.2: (continued)

To complete the process described in fig. 4.1, we need to discuss how the decision of which yield surfaces are active is made. This is illustrated in Fig. 4.2; note that we make use of the various loading and unloading inequalities developed in Chapter 3. Particularly important are the ones illustrated in figs. 3.4 and 3.5 concerning behaviour at the corners of the yield surface.

Finally, it is worth noting that implementations of different plasticity cap models have been reported in the literature recently [88-90]. They are all based on an incremental procedure differing from the present one in detail but not in principle.

4.3 Illustration of Cap Model Behaviour

Two simple laboratory tests are simulated to illustrate the behaviour of the present cap model. The cap model with a straight cap implemented in ADINA [87] is used for comparison purposes. An experimental result is also available for the uniaxial strain test and again it is used for comparison purposes.

4.3.1 Uniaxial Strain Test on McCormack Ranch Sand

Experimental results given by Dimaggio and Sandler [30] for uniaxial loading on a laterally confined cylinder of McCormack Ranch sand have been used as a standard test by a number of writers.

The cylinder is 0.5" in length and 1" in diameter, and is modeled by the four element axisymmetric mesh shown in Fig. 4.3. The loading programme is strain controlled, and consists of monotonic compression until an extreme value of axial strain of -0.066 is reached, followed by monotonic unloading. The resulting stress field is homogeneous, and the stress path in the stress invariant space is also shown in Fig. 4.3. The stress point first follows a radial path, engaging the cap. The Drucker-Prager surface is then reached, and the stress point moves along the Drucker-Prager surface, with the cap also active, until the maximum compressive strain

is achieved. On unloading, elastic behaviour (during which the value of s decreases to zero and then increases) first takes place, followed by further yielding on the Drucker-Prager surface. The experimental results of Dimaggio and Sandler are shown in Fig. 4.3.

In the calculations carried out the elastic constants (E,ν) and the Drucker-Prager parameters (α,k) were kept fixed with E = 100 ksi, ν = 0.25, α = 0.05 and k = 0.1 ksi; the cap parameter W, which is related to the maximum compressive strain applied was also fixed at -0.066. The remaining cap parameters, R and D, were considered as variables in fitting the constitutive equation model to the experimental data: the value of R was first chosen, and then D was selected so that the uniaxial stress reached a value of -1.0 ksi when the axial strain was -0.066 at the end of the loading phase, matching the experimental point.

The results obtained with the present model as implemented in NOSTRUM [79] for a straight cap (R=0) and a parabolically curved cap (R=0.5) are plotted in Fig. 4.3; the stress path is the same in each case. The results are reasonably good; the major difference between simulation and experiment is the stiffer initial response of the mathematical model. Our inability to model the experimental data more closely is a consequence of the way in which the restriction that the cap cannot move into the $\sigma_m>0$ domain (see equn. (3.68)) was implemented. A more sophisticated model in which a curved cap can shrink isotropically once it engages the tension cutoff, Drucker-Prager vertex will permit less stiff initial behaviour corresponding more closely with the experimental data.

The model implemented in ADINA [87], which only incorporates a straight cap R=0, was then run with the same value of D as the NOSTRUM example; the result is also plotted in Fig. 4.3. Although the NOSTRUM and ADINA models are using different plastic multipliers, it is apparent that for the path in this problem there is very little difference between the predictions of the two codes.

4.3.2 Proportional Loading Triaxial Test

The simple four element mesh referred to in the previous subsection was

analysed under conventional triaxial conditions to illustrate the shear behaviour of the model proposed in this paper. The numerical test is load controlled, and the stress path is shown in Fig. 4.4 together with the physical details. The NOSTRUM and ADINA results are in excellent agreement. The only Drucker-Prager, cap vertex action which occurs takes place with the stress point fixed in stress space, and this shows that the NOSTRUM model provides the required unlimited shear deformation at fixed plastic volume strain under these conditions.

4.4 Illustration of Corner Behaviour

The simplest way to illustrate the differences between the present model and previously formulated cap models is to compare the output of numerical analysis in which the models are incorporated. We have chosen to compare the results given by the present model (implemented in NOSTRUM) to those given by the model described by Bathe et al [37] for which we have the software available (ADINA). The major interest in the comparison is the behaviour when both the Drucker-Prager yield surface and the cap are active, and the various possibilities which can occur when the stress point moves along the Drucker-Prager yield surface in the direction of increasing hydrostatic tension. There are other differences between the present and the Bathe et al models, but these are simply the result of different formulations and are of no consequence in our present context.

In order to provide insight into the major differences between the two models, the simple four element plane strain model shown in Fig. 4.5(b) was subjected to a variety of loading paths. The stress and strain fields are uniform, and the block was first loaded so that the stress point is forced onto the Drucker-Prager, cap vertex. The way in which this was done is not important; significant are the subsequent loading paths, which are shown in Fig. 4.5(a). The strain increments are imposed, and fall within the boundaries defined by the various constraints shown in

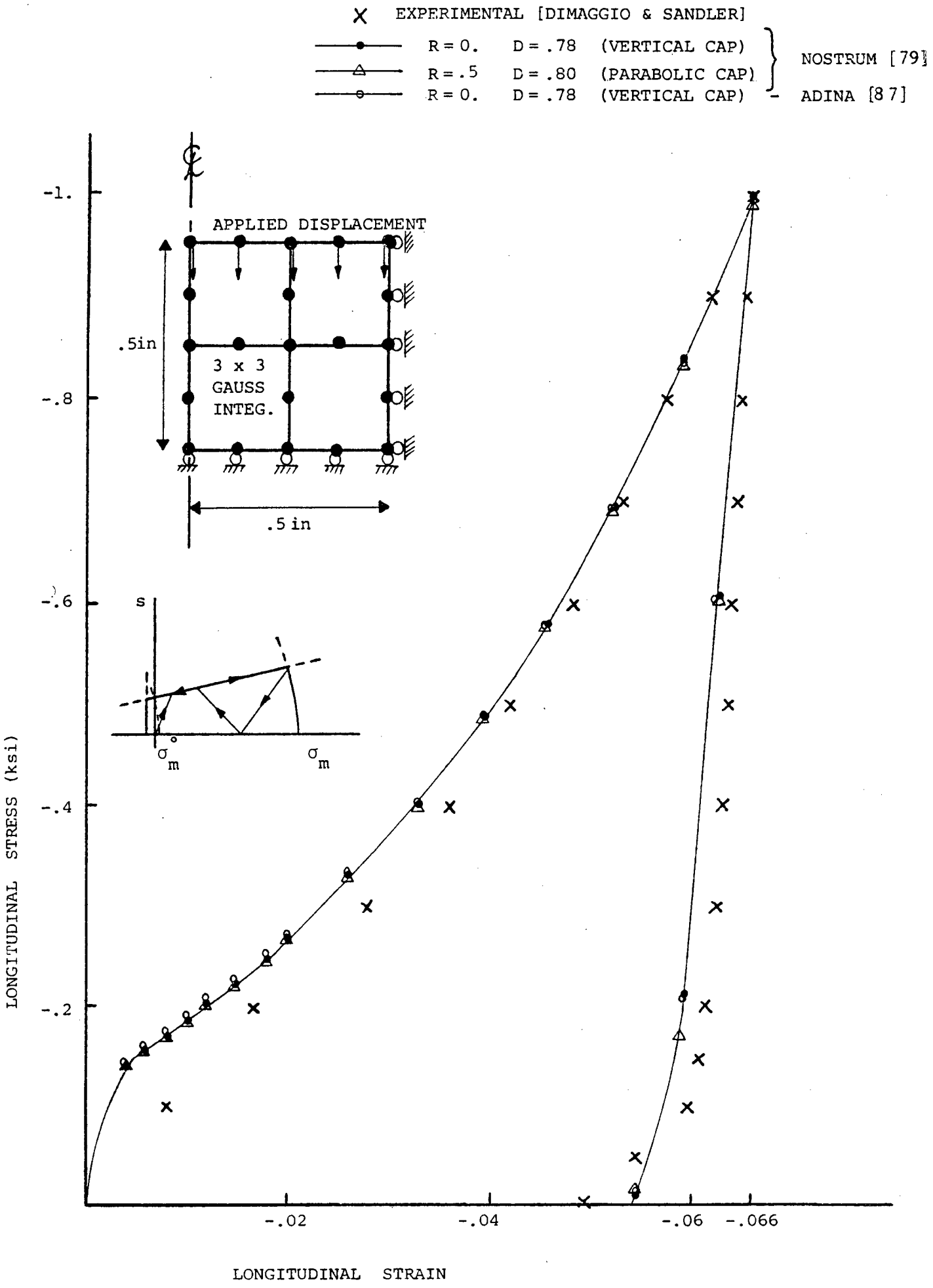

Figure 4.3: Uniaxial strain test for McCormack Ranch Sand.

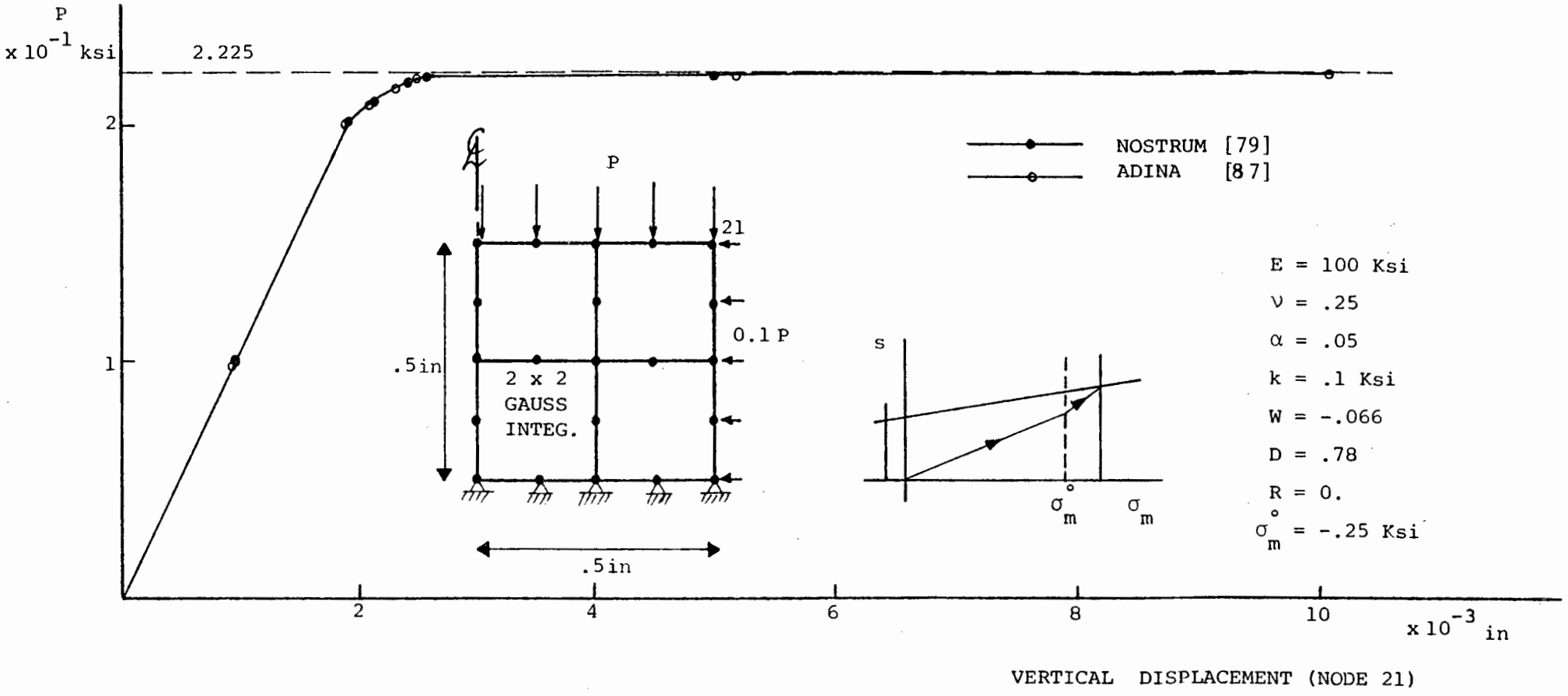

Figure 4.4: Proportional loading triaxial test.

Fig 3.5. The paths imposed are thus categorised as:

Path A : loading on both yield surfaces with the cap moving out

Path B : loading on both yield surfaces with the cap stationary

Path C : loding on both yield surfaces with the cap moving in. This path involves potentially unstable behaviour

Path D : loading on the Drucker-Prager yield surface, but unloading from the cap with $\dot{e}=o$. The cap does not keep up with the stress point.

The results of the various analyses, run with both the present and Bathe et al models are shown in Fig. 4.6 (plot of s against e), Fig. 4.7 (plot of σ_m against ε_v) and Fig. 4.8 (plot σ_m against ε_v^p). For convenience, in discussing these results we shall refer to the absolute magnitude of σ_m and ε_v when using the terms "increasing" and "decreasing".

For path A, the results obtained by the present and Bathe et al models are essentially the same, showing that for this path the differences in the models are slight. Both s and σ_m increase with e and ε_v.

For path B, the results are identical, as expected. The stresses remain constant during plastic shear flow with no plastic volume change.

For path C, the Bathe et al model assumes that only the Drucker-Prager yield surface is active, with $\alpha=0$; however, the cap continues to move with the stress point, in contradiction to the imposed von Mises condition and illustrating the inconsistency introduced by the additional assumptions. As a result of this the predictions of the two models are quite different. The slopes in the s-e plot and the σ_m - ε_v are not the same, and there is a substantial disagreement in the plot of σ_m and ε_v^p .

Path D is treated by the Bathe et al model in the same way as path C, whereas the present model predicts separation of the stress point and the cap together with plastic volume strain associated with plastic defor-

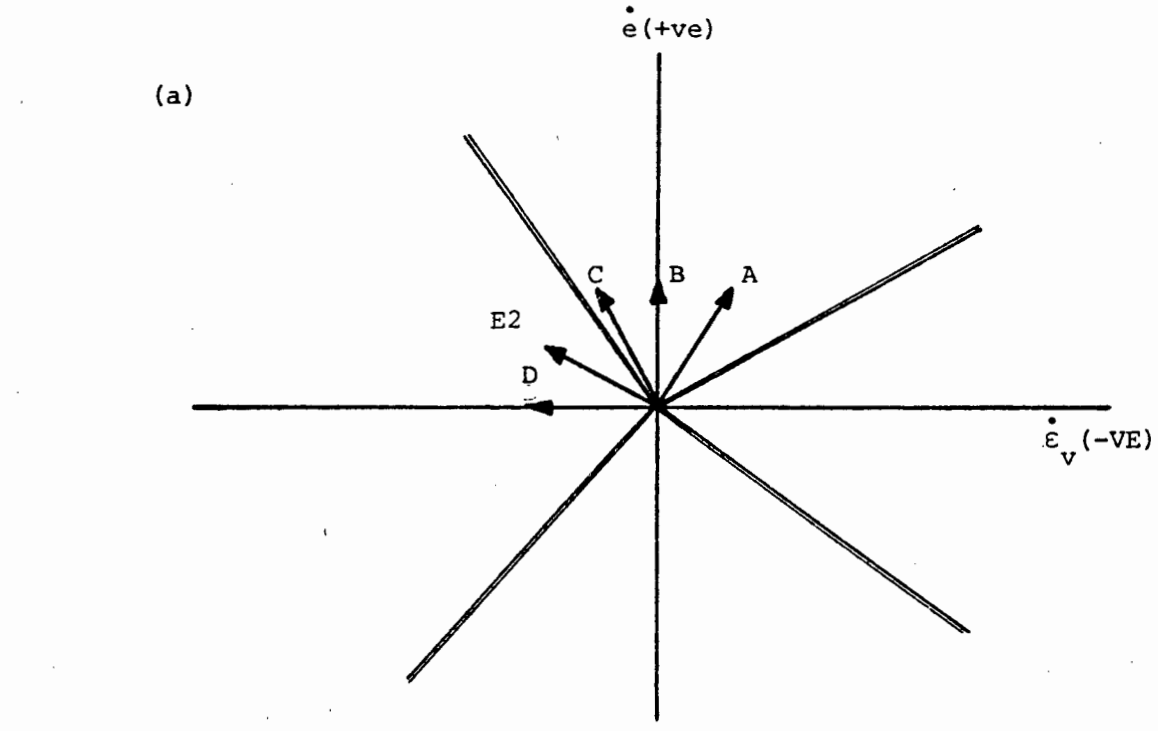

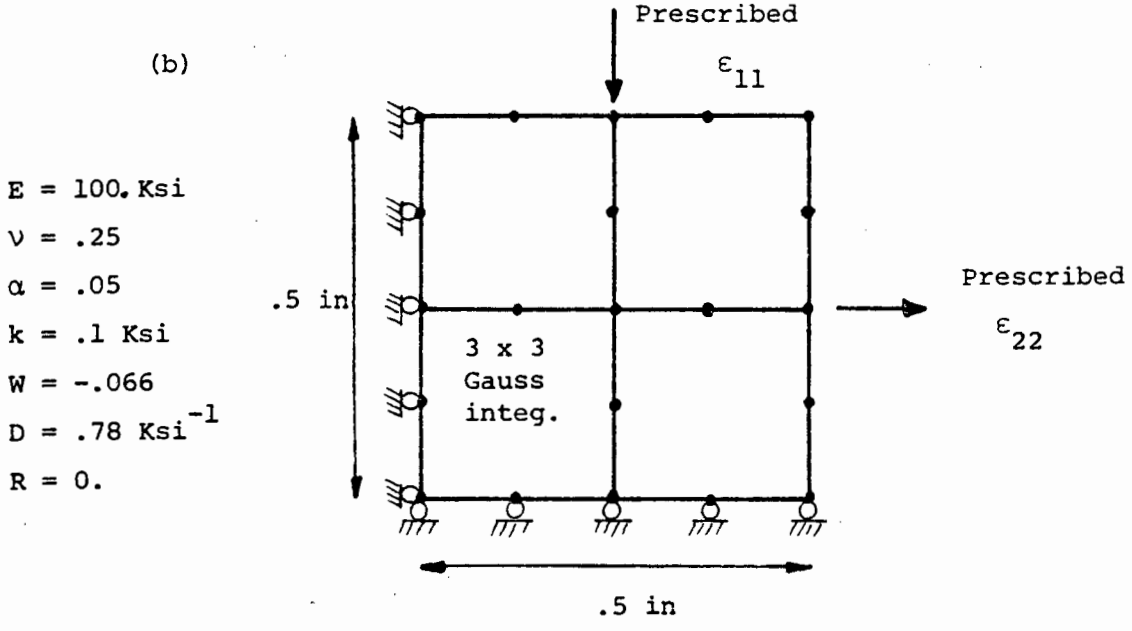

Figure 4.5: Strain paths imposed on model when stress point is at cap/Drucker-Prager intersection.

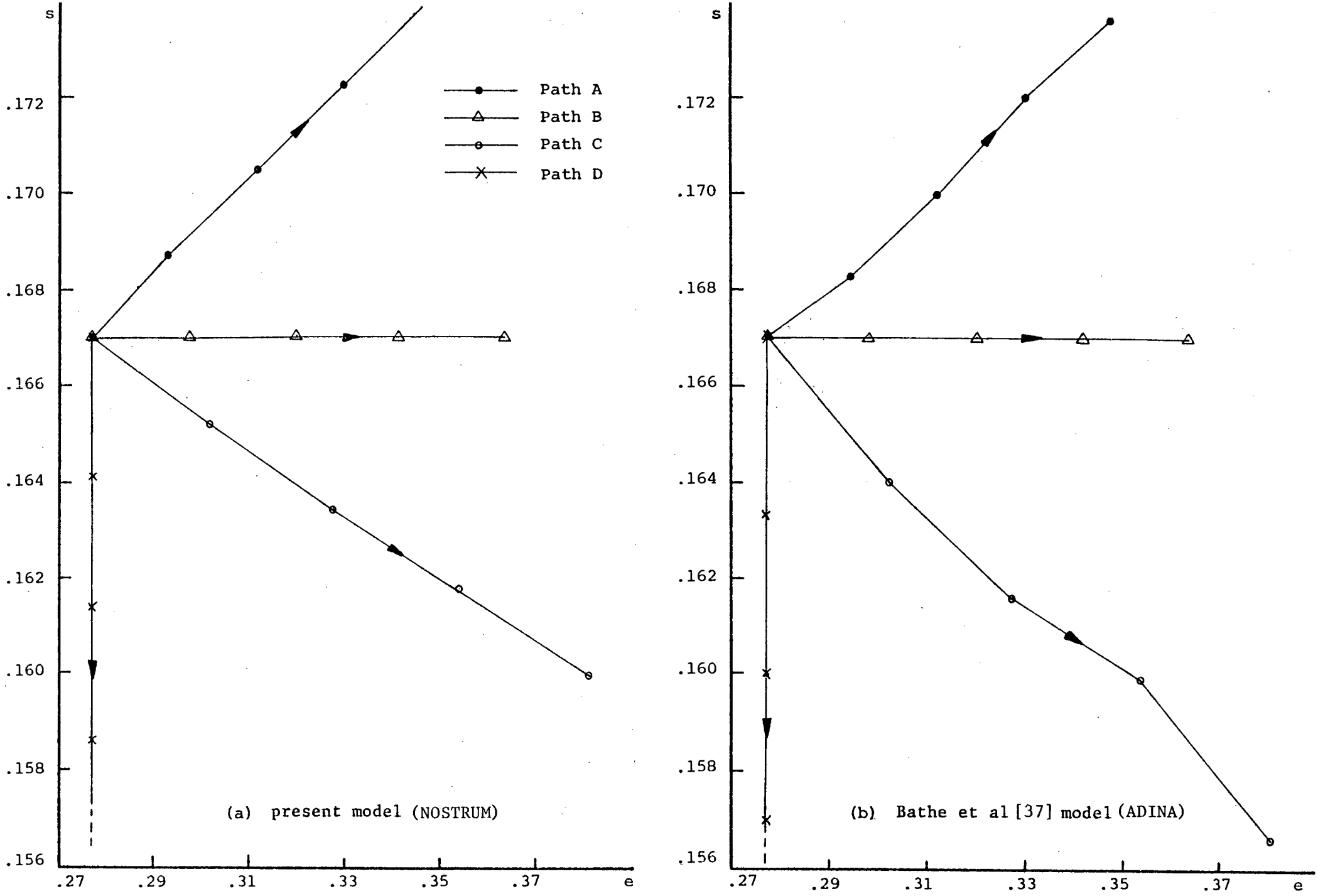

Figure 4.6: Deviator stress vs. deviator strain.

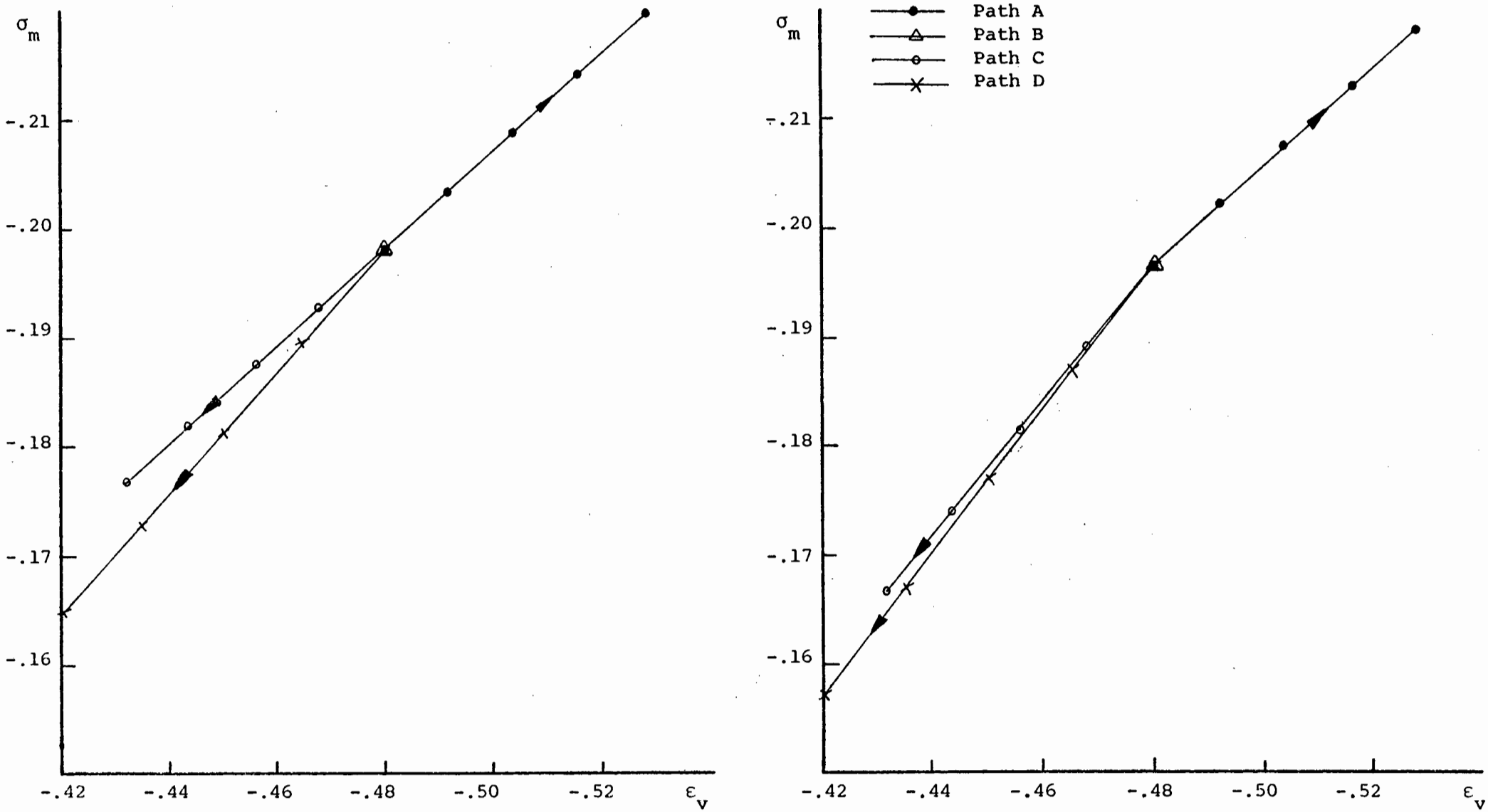

(a) present model (NOSTRUM)

(b) Bathe et al [37] model (ADINA)

Figure 4.7: Hydrostatic stress vs. volume strain.

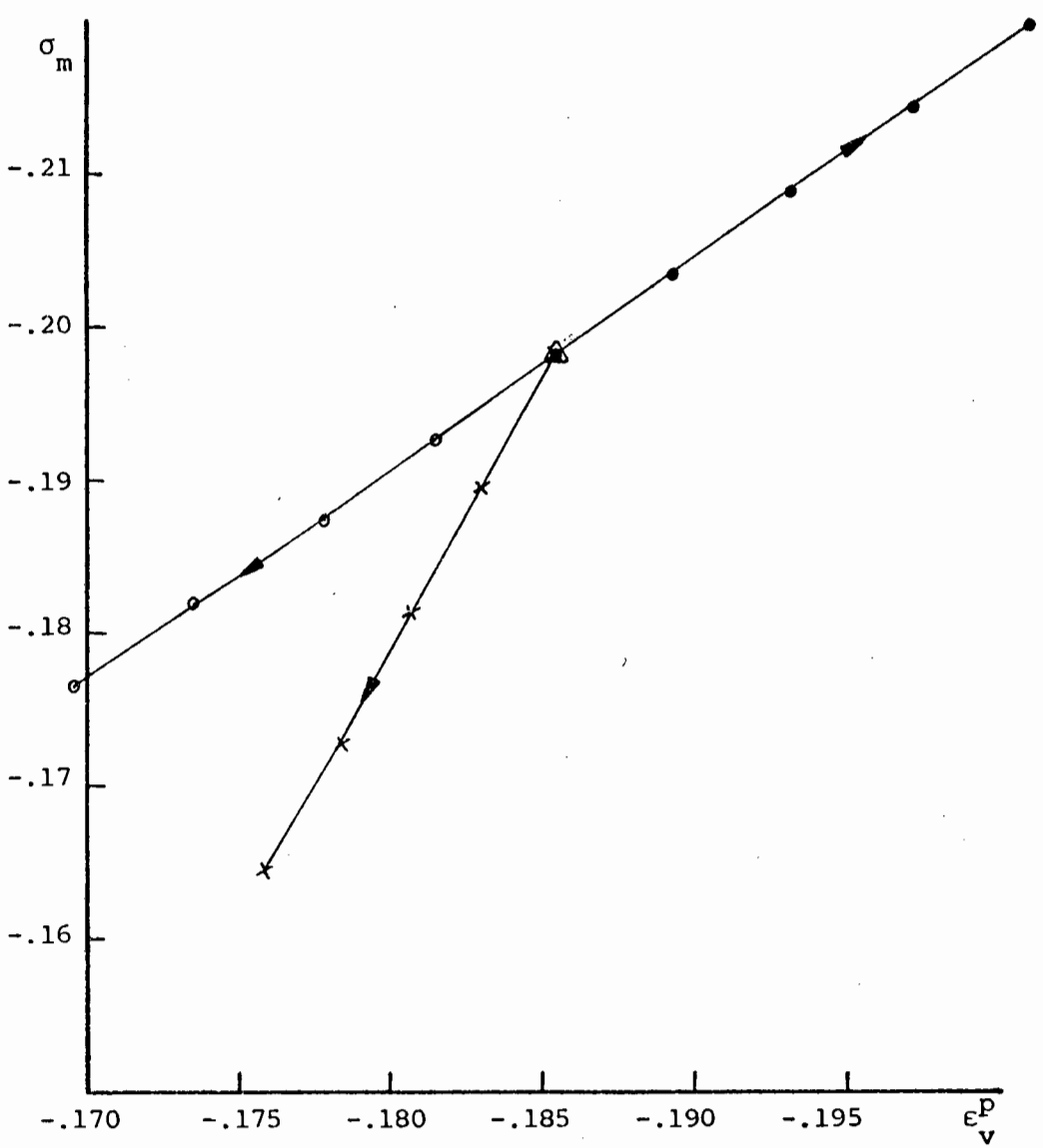

(a) present model (NOSTRUM)

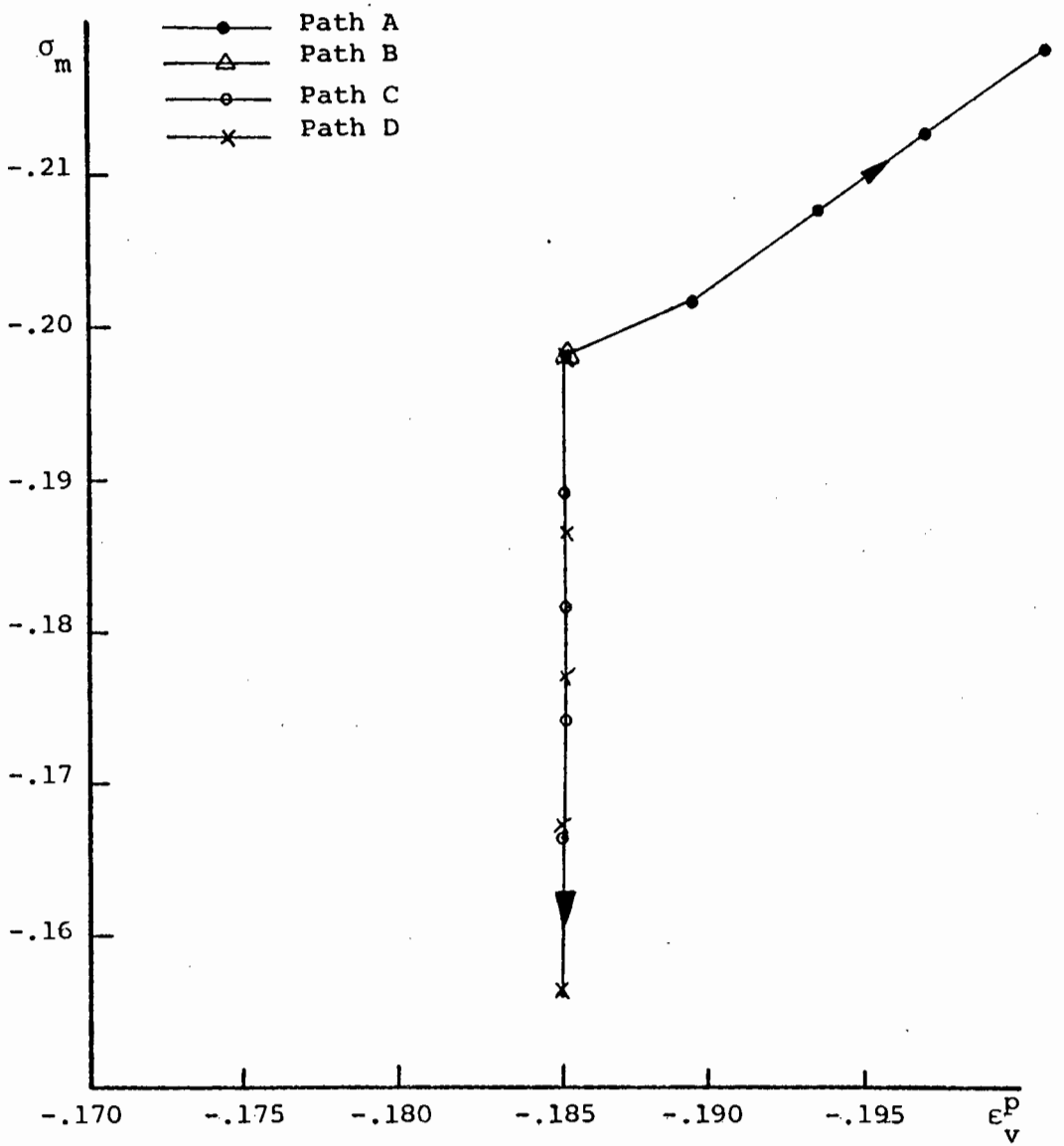

(b) Bathe et al [37] model (ADINA)

Figure 4.8: Hydrostatic stress vs. plastic volume strain.

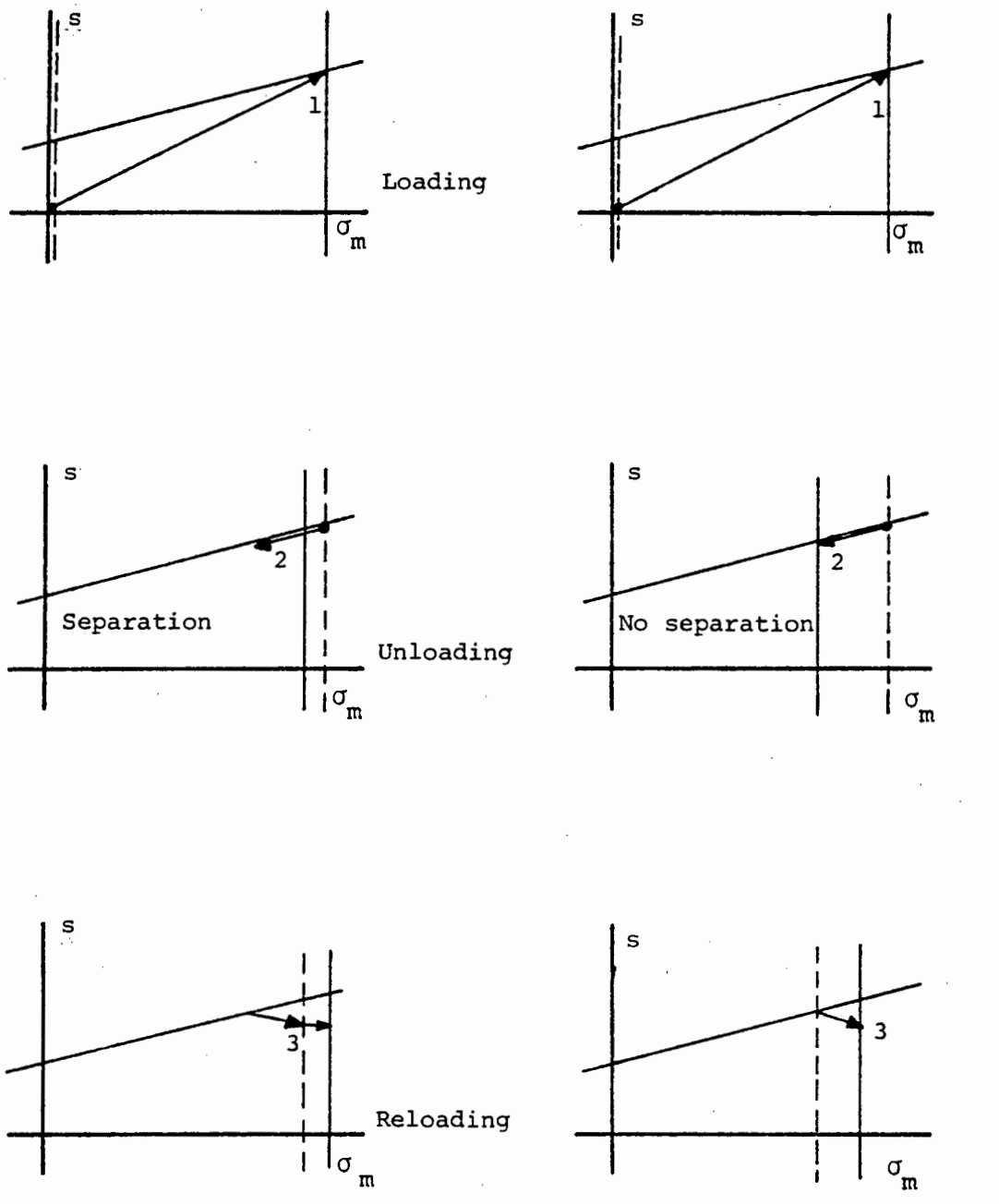

(a) Present Model (NOSTRUM)

(b) Bathe et al Model (ADINA)

Figure 4.9: Cap movement and its consequences on a loading-unloading -reloading cycle (Path E).

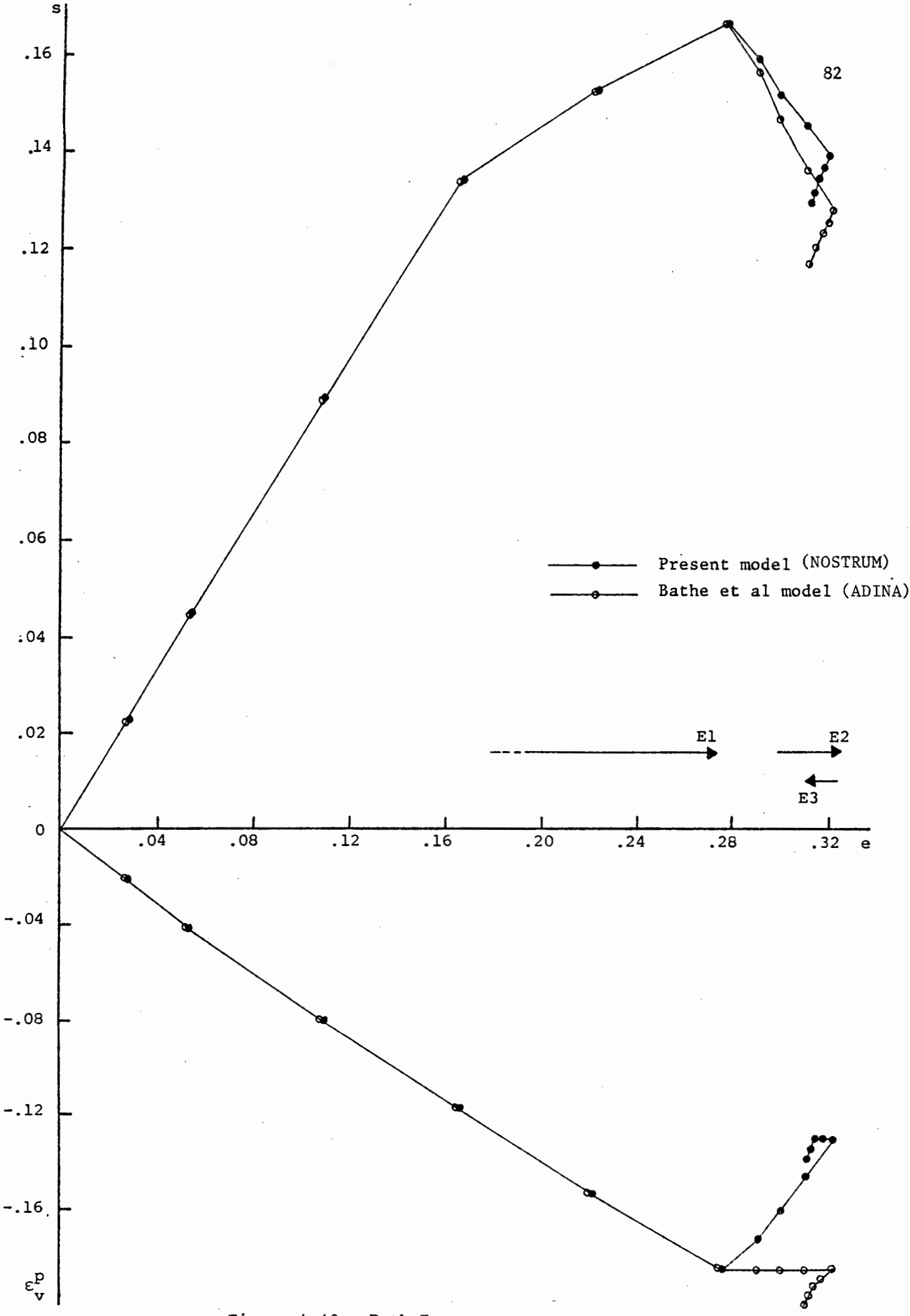

Figure 4.10: Path E responses.

mation on the Drucker-Prager yield surface. The differences are again most distinct in Fig. 4.8.

We see thus that differences occur in the two models when the stress path follows the Drucker-Prager yield surface with s decreasing. This difference has further consequences, which can be seen in the loading, unloading, reloading path shown in Fig. 4.9. In the second part of the path (shown as E2 in Fig. 4.5a), the present model predicts separation from the cap, and thus subsequent reloading is made up of linear elastic behaviour followed by yielding on the cap and elastic plastic hardening behaviour. The Bathe et al model, on the other hand, gives inconsistent behaviour on unloading (i.e. no plastic volume strain accompanied by cap movement), and yielding on the cap occurs immediately on reloading. These differences are illustrated in Fig. 4.10, where s and ε_v^p are plotted against e.

It may also be noted that while path C falls into a potentially unstable regime, the particular path chosen is such that $(\dot{s}\,\dot{e} + \dot{\sigma}_m\,\dot{\varepsilon}_v)$ is positive. Whether or not the path is unstable will depend on the previous loading history; for this particular case unstable behaviour occurs only for $0 \leq \dot{\varepsilon}_v/\dot{e} \leq .33$, whereas the domain of potentially unstable behaviour is $0 \leq \dot{\varepsilon}_v/\dot{e} \leq .88$. This is shown diagrammaticaly in Fig. 4.11.

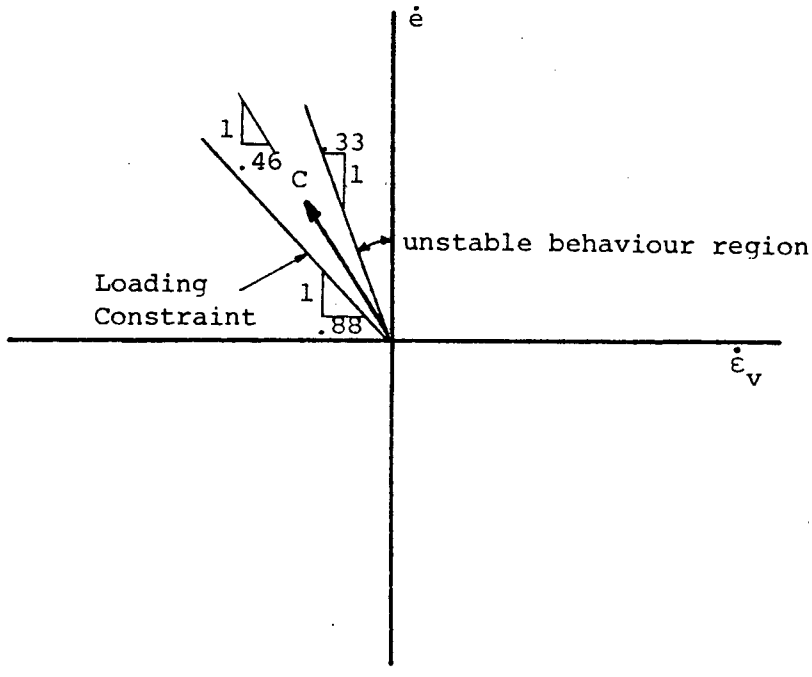

Figure 4.11: Unstable behaviour region.

4.5 Analysis of Boundary Value Problems

The behaviour of strip footings on an infinitely extending layer of overconsolidated clay is investigated. The shallow layer of clay is 12ft. deep and extends infinitely in the horizontal direction, while the strip footings are 10 ft. wide as shown in Fig. 4.12. The problems are modelled in plane strain and we make use of a line of symmetry running along the centre of the footing.

Two types of footings are considered. Firstly, a flexible and smooth footing meaning that vertical loads are applied at the footing and the soil is allowed to move freely horizontally under it. The stresses beneath the footing load are distributed vertically and uniformly. This case has been analysed by Zienkiewicz et al [27] using a Mohr-Coulomb model with both an associated and a non-associated (zero dilatancy) flow rule as well as with a critical state model. Secondly, a rigid and rough footing is considered meaning that uniform vertical displacement boundary conditions are applied at the footing and no horizontal displacements under it are permitted. In this case, the footing pressure is taken as the average pressure under the footing. Mizuno and Chen [91] have analysed both the rigid rough footing and the flexible smooth footing using the Drucker-Prager model (associated and non-associated with zero dilatancy) as well as a cap model (straight and elliptical cap). Note that the rigid and rough assumption is perhaps the more realistic one for this problem.

Three basic finite element discretizations were investigated. The first, due to Mizuno and Chen [91], is a regular mesh of 98 linear Lagrangian (4 noded) isoparametric elements with 2x2 Gauss integration giving a total of 120 nodes as shown in Fig. 4.12(a). The second, due to Zienkiewicz et al [27], is a graded mesh of 32 parabolic elements as shown in Fig. 4.12(b). For this configuration, 8 noded Serendipity elements (121 nodes) as well as 9 noded Lagrangian elements (153 nodes) have been investigated. In the above two discretizations, the mesh is truncated 24 ft. away (in the horizontal direction) from the centre of the footing and only vertical displacements are allowed at the truncated boundaries.

Completely fixed boundary conditions are assumed at the bottom of the clay layer.

A third discretization involving the use of finite and infinite elements has been suggested by Marques and Owen [92]. Here we replace the outer column of finite elements by a column of elements extending to infinity as shown in Fig. 4.12(c) and no boundary conditions are thus necessary. It should be noted that the infinite elements are assumed to behave strictly elastically. From experience gained by the author [86], the 8 noded finite elements are coupled to 5 noded infinite elements (giving a mesh of 112 nodes) while the 9 noded finite elements are coupled to 6 noded infinite elements (giving a mesh of 144 nodes). A 3x3 Gauss integration procedure is used for the higher order elements of Figs. 4.12 (b), (c).

All five meshes shown in Fig. 4.12 (98F4, 32F8, 32F9, 28F8/4I5 and 28F9/4I6) have been shown to give very similar results [93] and thus the NOSTRUM results presented in the following sections are taken to be representative of all five meshes.

In the statement of the strip footing problem Zienkiewicz et al [27] assume that the soil behaves as a Mohr-Coulomb material with cohesion c=10 psi and angle of friction $\phi=20^0$,and that the material is perfectly plastic. The elastic constants are Young's modulus E = 30000 psi and Poisson's ratio $\nu = 0.3$ while the soil is assumed to be weightless. Given a Mohr-Coulomb failure envelope defined by its cohension c and angle of friction ϕ, different Drucker-Prager circular fits are possible. This amounts to choosing the Drucker-Prager constants α, k for the yield surface $F = \alpha\, \sigma_m + s - k = 0$ where σ_m is the hydrostatic stress and s is the second invariant of the deviator stress. However, this choice is not arbitrary but rather depends on the type of problem and state of stress under consideration [58]. In the applications presented in this section, a Drucker-Prager fit under plane strain conditions is used by setting [16]

$$\alpha = \frac{\tan\phi}{\sqrt{(9+12\ \tan^2\phi)}} \quad , \quad k = \frac{3c}{\sqrt{(9+12\ \tan^2\phi)}} \quad . \qquad (4.10)$$

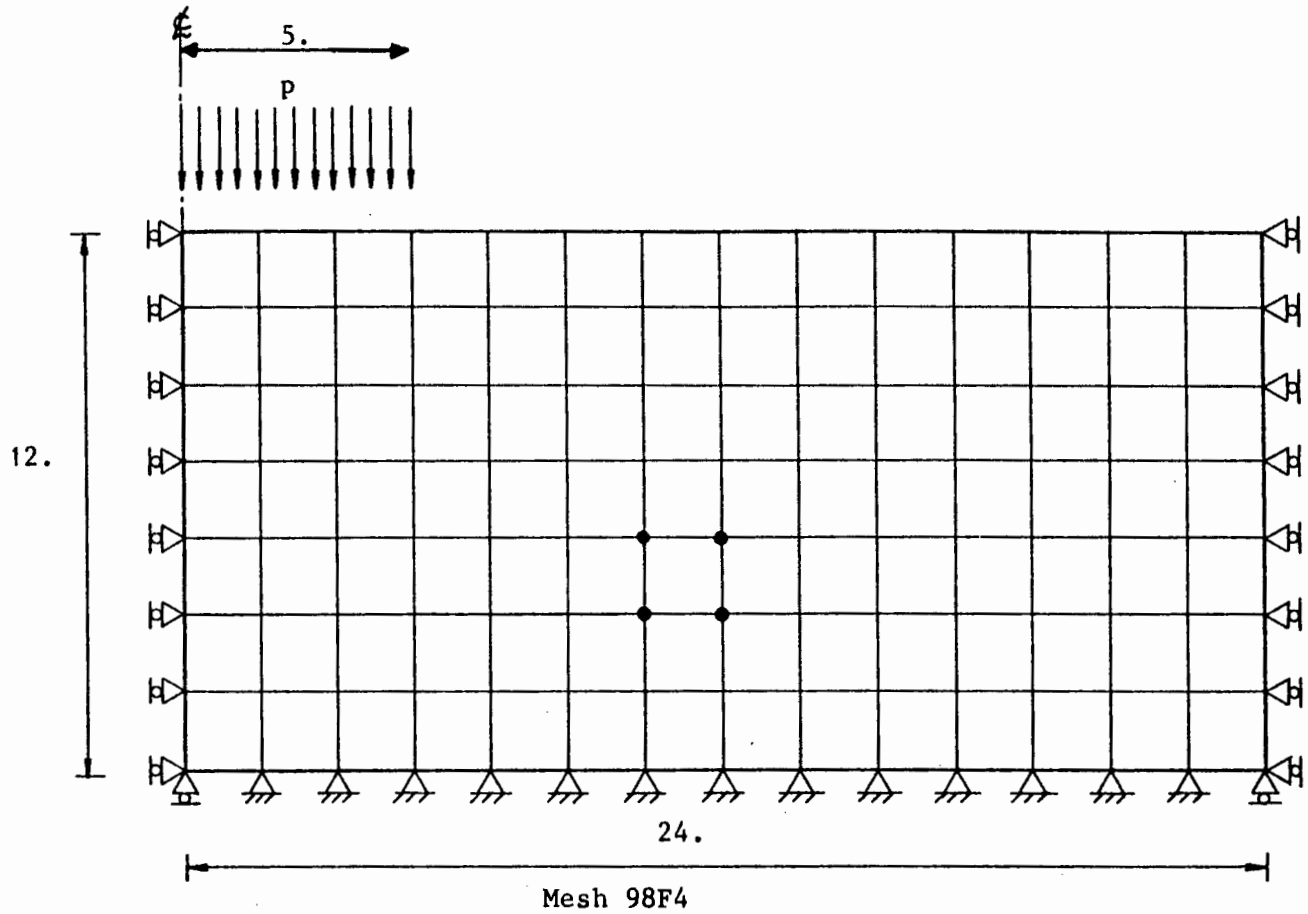

(a) Linear Lagrangian finite element discretization (98 elements)

Figure 4.12: Finite element models of layer of clay under footing loads.

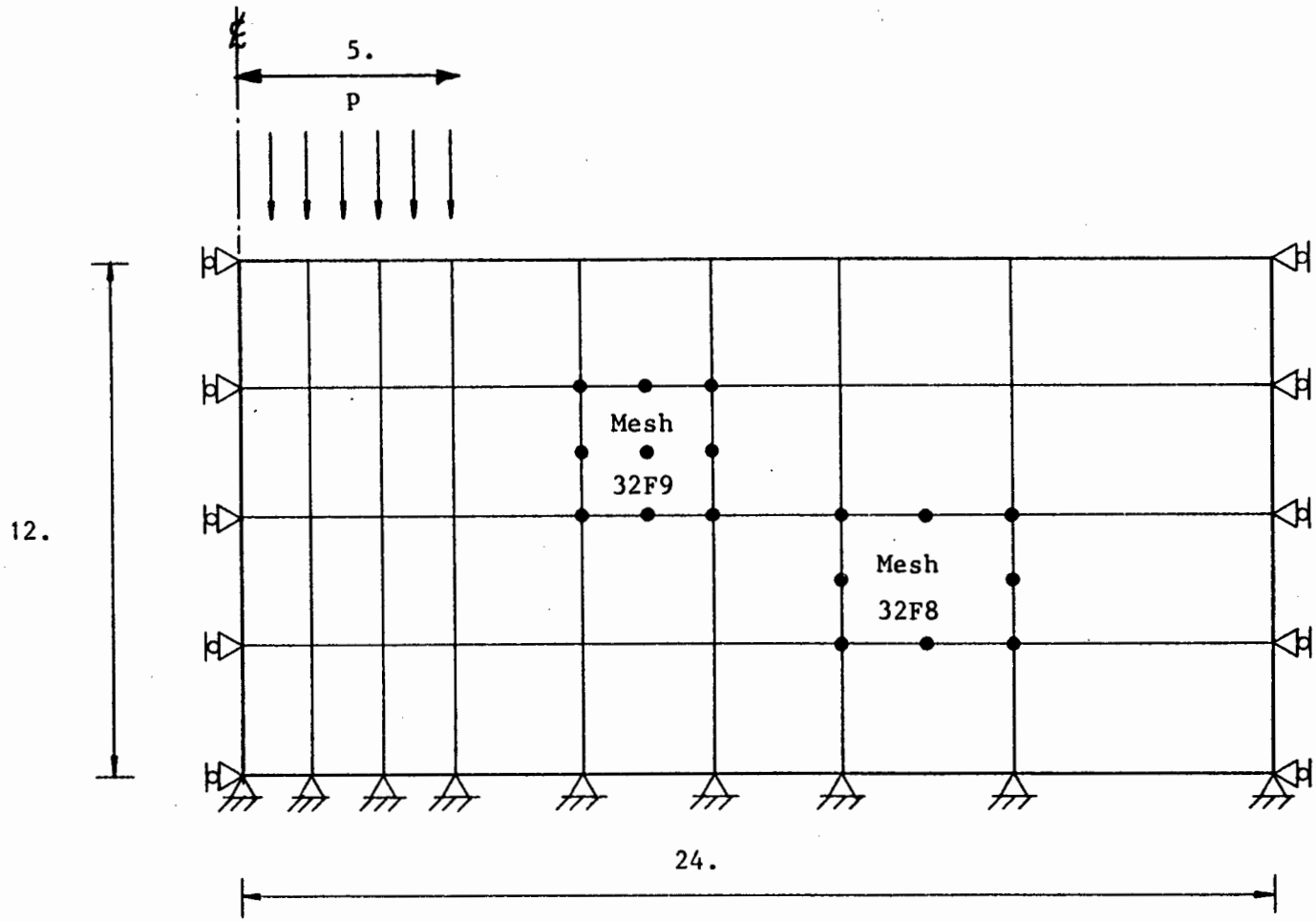

(b) Parabolic Serendipity and Lagragian finite element discretizations (32 elements)

Figure 4.12: (Continued)

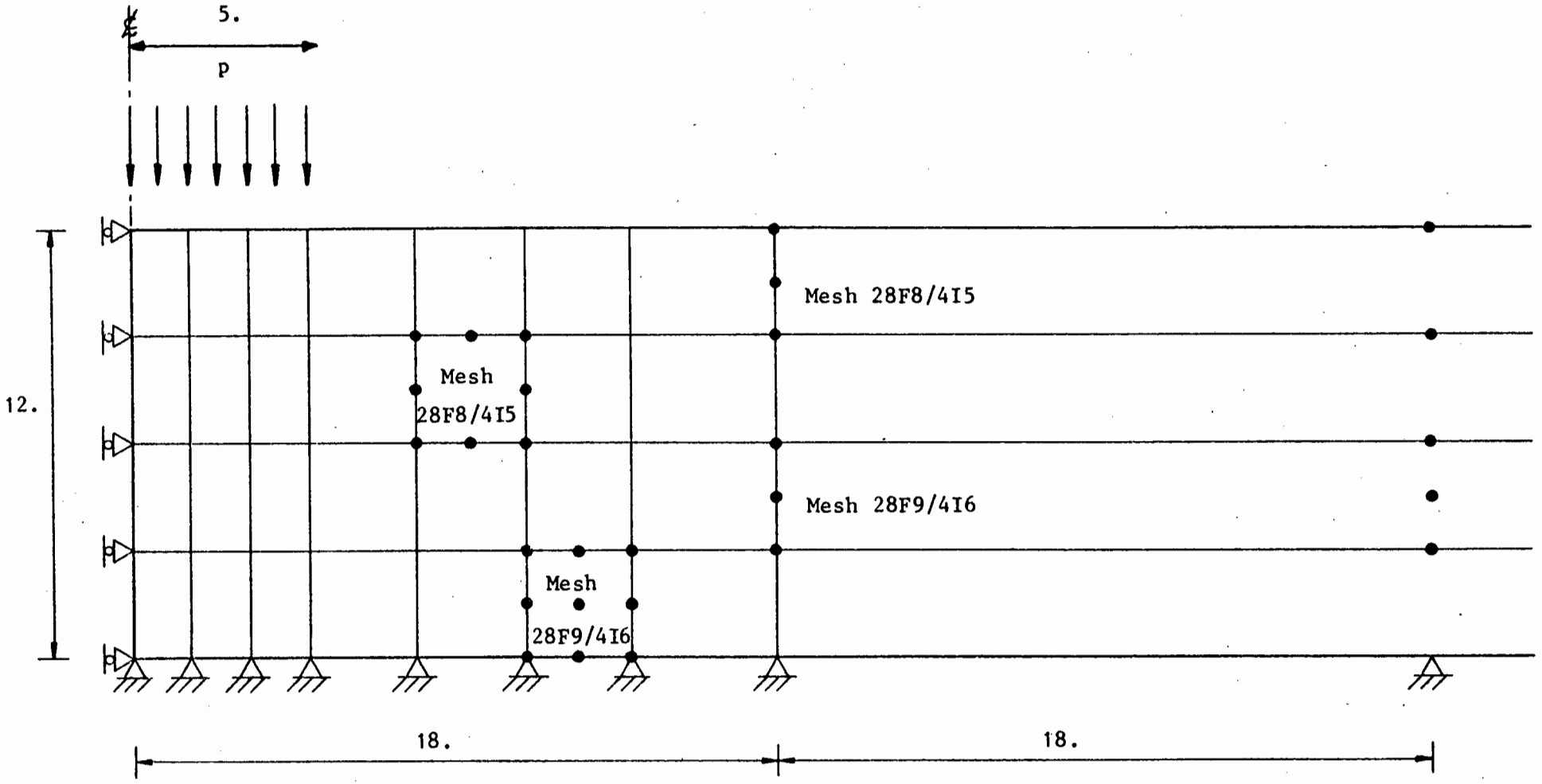

(c) Parabolic Serendipity and Lagrangian finite/infinite element discretizations (28 finite and 4 infinite elements)

Figure 4.12: (Continued)

Equns. (4.10) give α = .112 and k = 9.22 psi. Other Drucker-Prager fits of the Mohr-Coulomb envelope have been investigated for the strip footing problem [91,93] but will not be discussed here.

Although a large number of results for the strip footing problems has been obtained using NOSTRUM [93-96], only some of those concerning the choice of constitutive model are presented in this chapter. Numerical solutions given by Zienkiewicz et al [27] and Mizuno and Chen [91] are used for comparison purposes. The limit analysis (slip line) Prandtl and Terzaghi solutions [25] are taken as limit load benchmarks for the footing problems. The Prandtl solution predicts a limit load of 143 psi while the Terzaghi solution estimates it at 175 psi.

All the NOSTRUM solutions were obtained with a full Newton-Raphson scheme while the Zienkiewicz et al [27] solutions employed an initial stiffness approach and Mizuno and Chen [91] used a mid-point integration rule [90].

4.5.1 Rigid and Rough Strip Footing

The progressive failure analysis of the rigid and rough strip footing is carried out using the Drucker-Prager model with an associated flow rule and the cap model with a plane vertical cap. The additional material constants necessary to define the cap model are [91]: W = -.003, D = .0087 psi^{-1}, R = 0, and σ_m^0 = -15.5 psi , the initial cap position.

The load-deflection curves obtained with NOSTRUM for the two models are given in Fig. 4.13 together with the equivalent solutions obtained by Mizuno and Chen. The agreement between the two sets of numerical solutions is good and all solutions compare favourably with the Prandtl and Terzaghi predictions of the limit load.

Zones indicating various stress states for the NOSTRUM plane cap solution are shown in Fig. 4.14 at a stage when the vertical displacement of the rigid footing is d = .75 in. and at a point close to failure (d = 1.35 in.). These agree well with the results given by Mizuno and Chen.

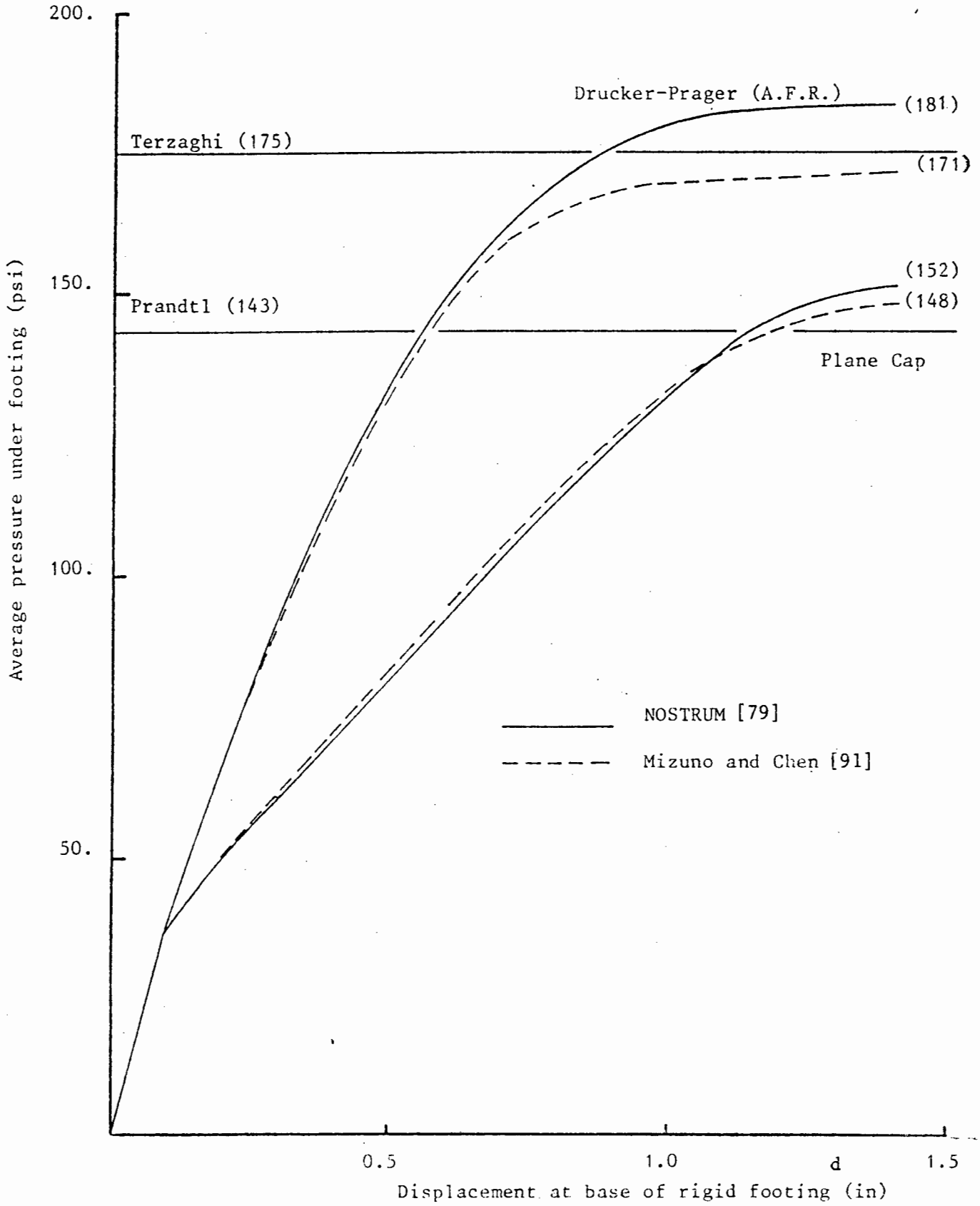

Figure 4.13 : Load-deflection curves for clay layer under footing loads (rigid and rough).

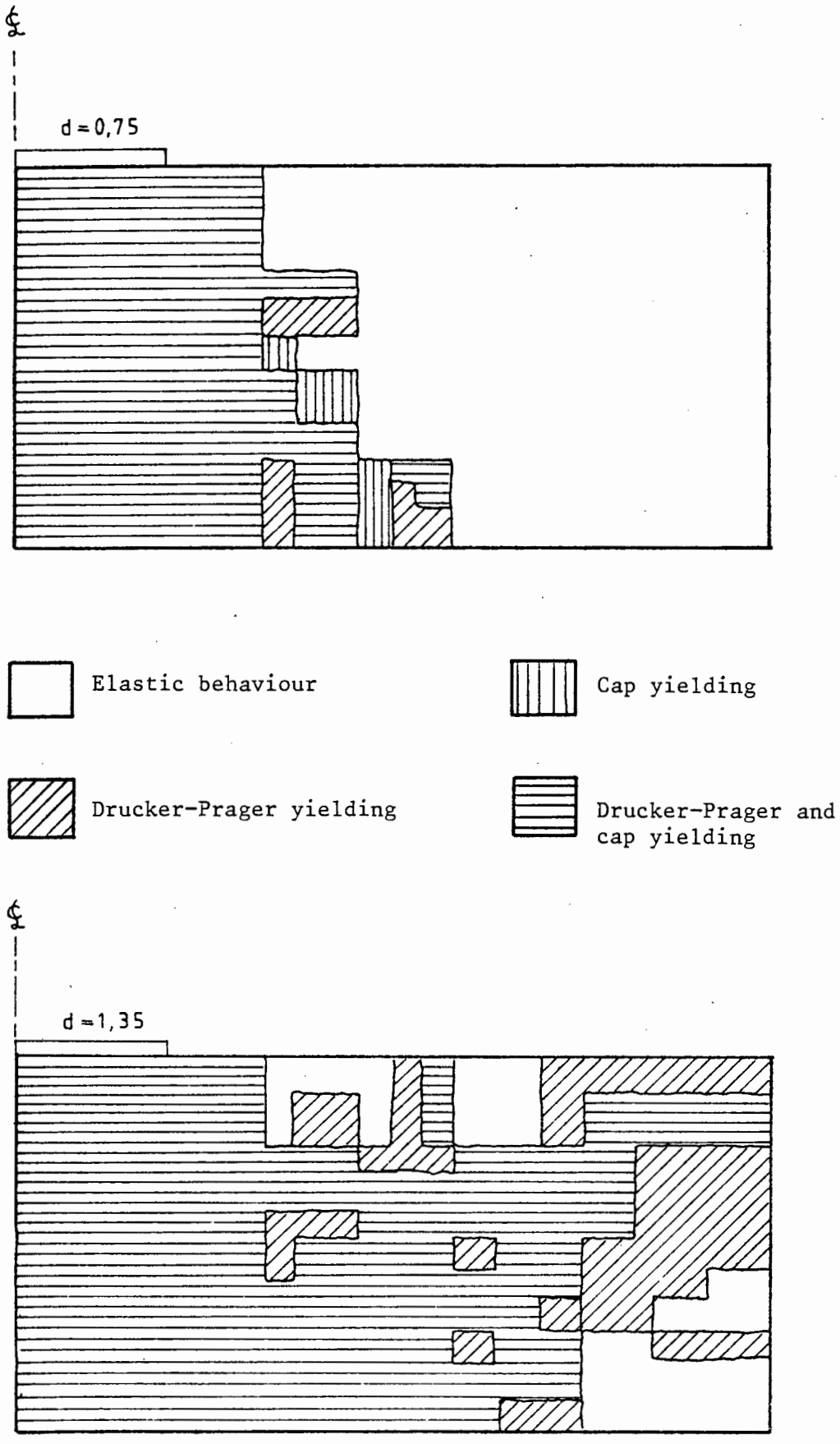

Figure 4.14: Zones of stress state for rigid and rough footing analysed with plane cap model in NOSTRUM.

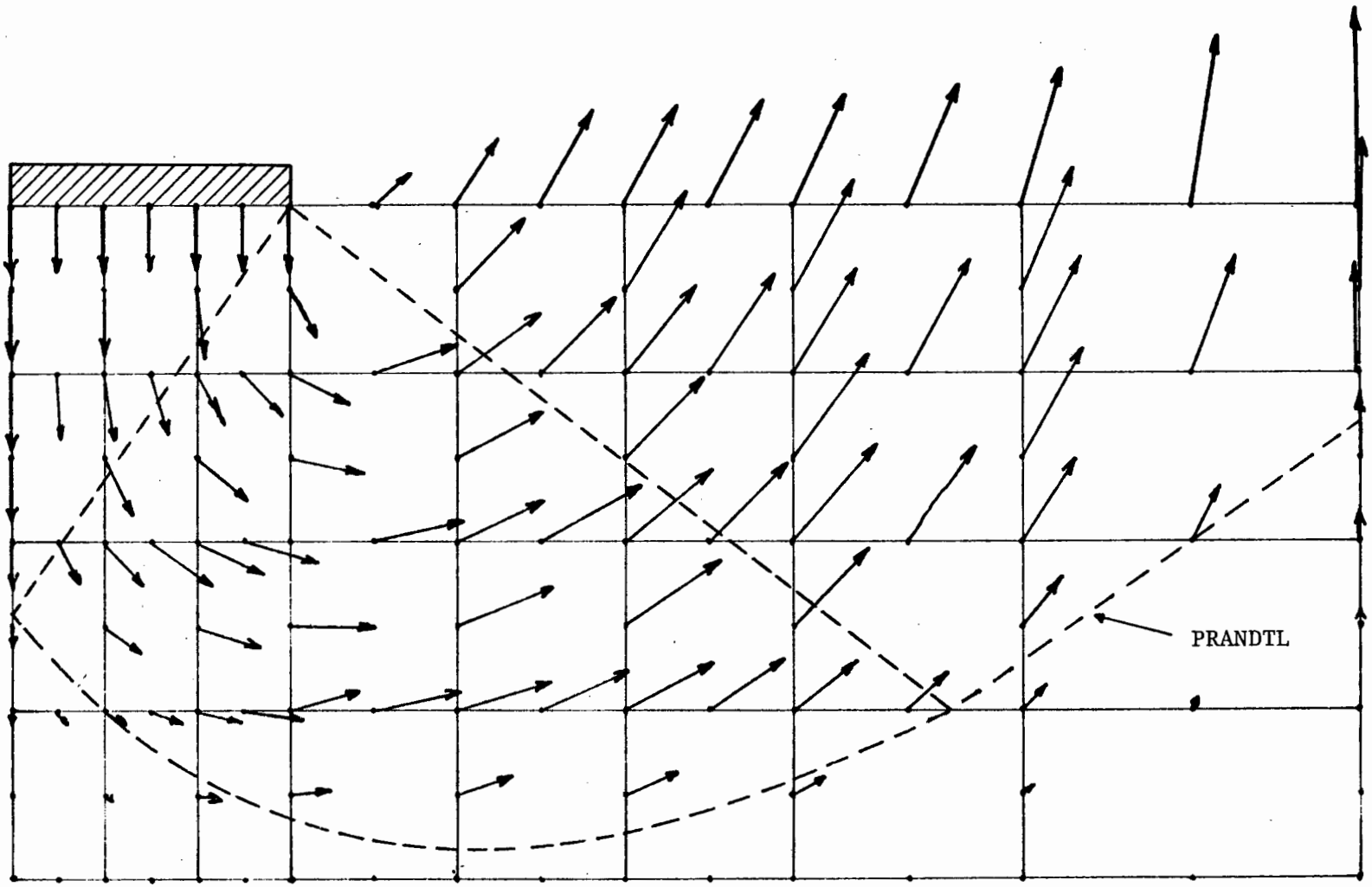

(a) Drucker-Prager model with associated flow rule

Figure 4.15: Velocity fields at collapse for rigid and rough footing.

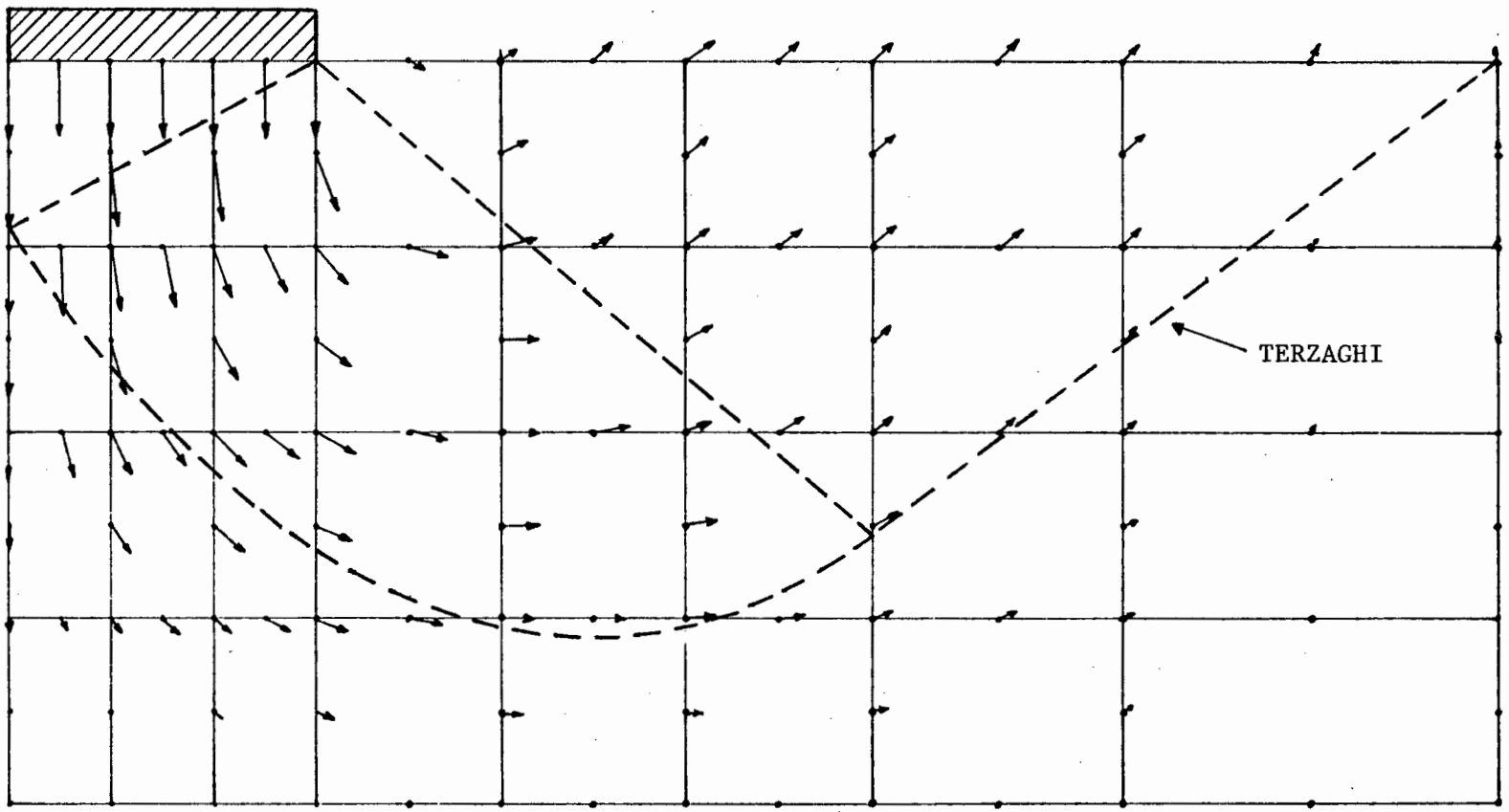

(b) Cap model with plane cap

Figure 4.15: (continued)

The velocity fields at failure for the Drucker-Prager and the cap models are compared in Fig. 4.15 where it is apparent that the Drucker-Prager model predicts dilatancy which far exceeds that predicted by the cap model. The Drucker-Prager velocity field at collapse matches closely the Prandtl collapse field while the plane cap velocity field agrees well with Terzaghi failure field.

4.5.2 Flexible and Smooth Strip Footing

The progressive failure analysis of the flexible and smooth footing is performed using the Mohr-Coulomb model with an associated flow rule and the cap model with a plane vertical cap. These solutions are compared to the associated Mohr-Coulomb and critical state model solutions given by Zienkiewicz et al [27]. The load-deflection curves are shown in Fig.4.16. The two Mohr-Coulomb numerical solutions agree very closely and while the plane cap solution is somewhat softer than the critical state model solution the limit loads predicted are very similar. Again there is close agreement with the slip line solutions of Prandtl and Terzaghi.

Zones indicating various stress states for the NOSTRUM plane cap solution are shown in Fig. 4.17 for applied pressures of 70 psi and 130 psi. These are in agreement with Mizuno and Chen.

Finally, the velocity fields at failure for the associated Mohr-Coulomb model and the plane cap model are compared in Fig. 4.18 where once again the cap model has the effect of reducing the dilatancy prediction.

The Mohr-Coulomb velocity field at failure compares well with the one given by Zienkiewicz et al and it matches the Prandtl field closely as shown in Fig. 4.18(a). The plane cap velocity field is very similar to the one given by Mizuno and Chen and it matches closely the Terzaghi collapse field, Fig. 4.18(b).

Some general conclusions can be drawn from the strip footing analyses performed here and in references [27, 91, 93-96], namely:

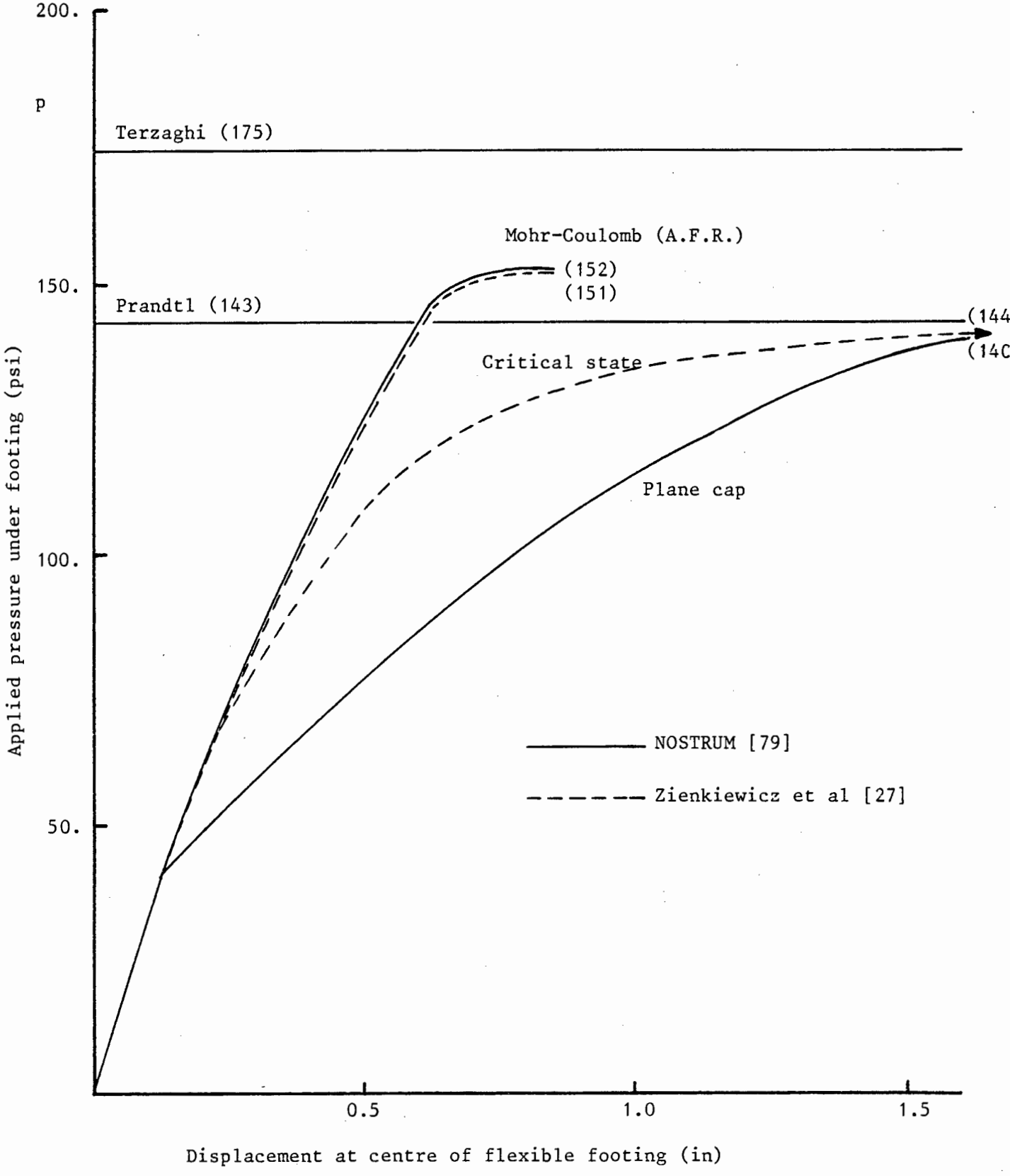

Figure 4.16: Load-deflection curves for clay layer under footing loads (flexible and smooth).

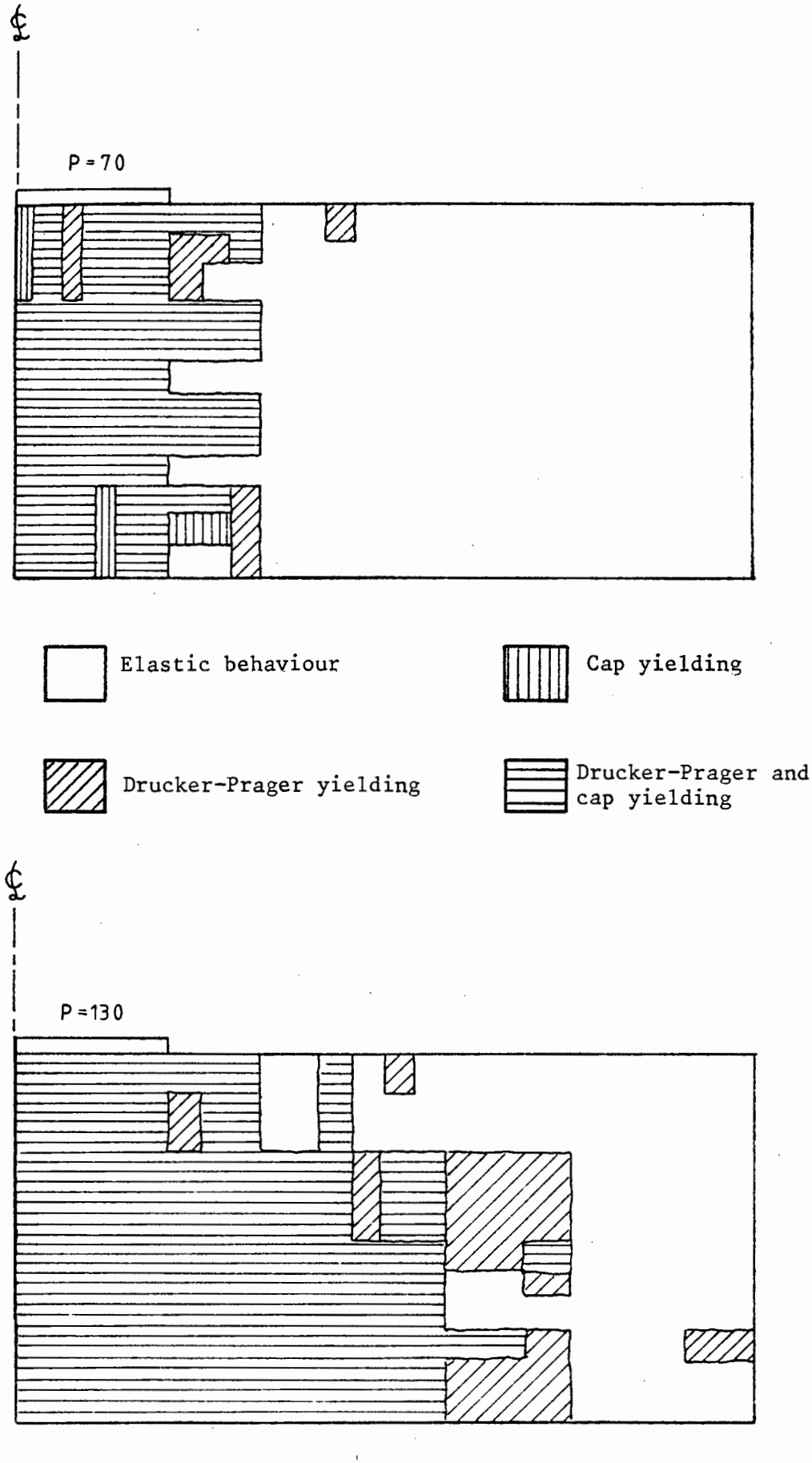

Figure 4.17: Zones of stress state for flexible and smooth footing analysed with plane cap model in NOSTRUM.

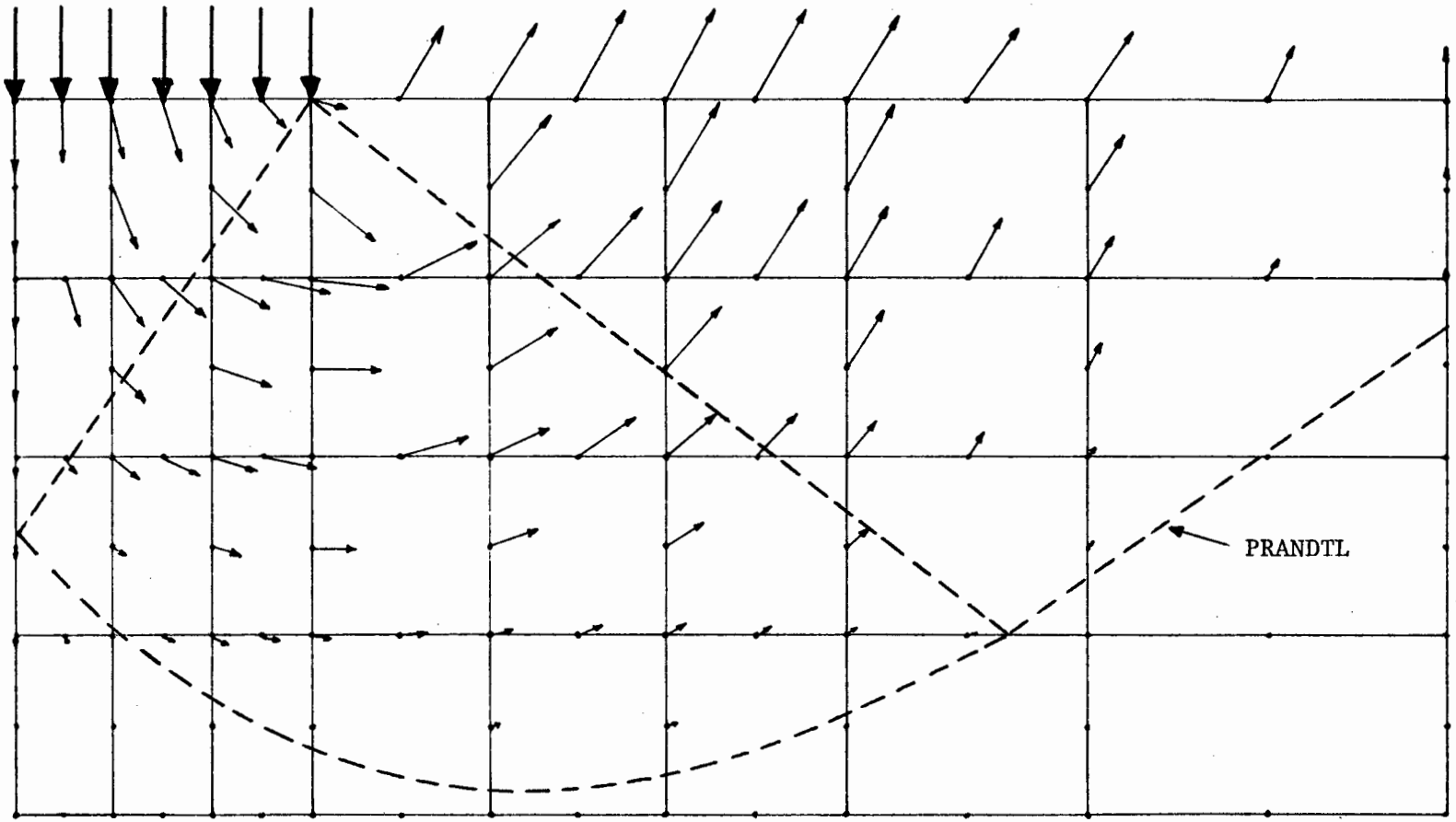

(a) Mohr-Coulomb model with associated flow rule

Figure 4.18: Velocity fields at collapse for flexible and smooth footing.

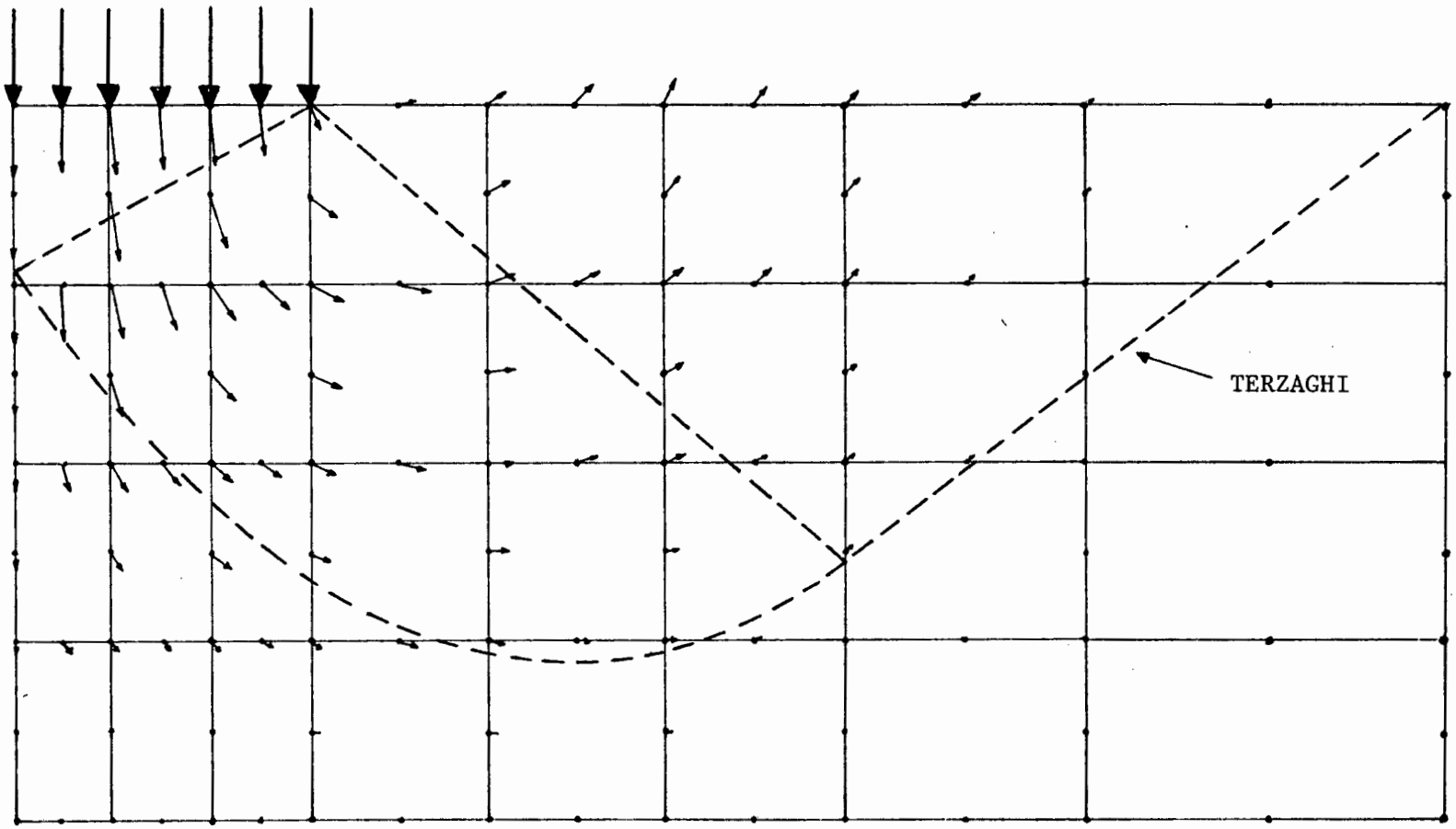

(b) Cap model with plane cap

Figure 4.18: (continued)

(a) All numerical predictions of limit load compare favourably with the Prandtl and Terzaghi solutions.

(b) The predicted limit loads for the rigid and rough footing are generally higher than the corresponding ones for the flexible and smooth footing.

(c) The models in which dilatancy is controlled (cap models, critical state model and non-associated single surface models) predict a softer response and a lower failure load.

(d) The spreading of yielded zones starts from the vicinity of the footing and expands outward.

(e) The velocity fields at collapse agree with the Prandtl solution for the single surface associated models while for the models in which dilatancy is controlled the velocity fields at collapse match the Terzaghi field better.

The boundary value problems solved in this chapter were primarily used to test the cap model in well known standard configurations. In chapter 7, more problems are solved with the cap model and the solutions obtained are used for comparisons with the internal damage model predictions.

CHAPTER 5

AN INTERNAL DAMAGE CONSTITUTIVE MODEL

As stated at the outset, the immediate motivation for the present work on the mechanics of geomaterials was to study the behaviour of deep underground excavations in hard brittle rock. In the next three chapters we propose, implement and apply what is thought to be a realistic yet relatively simple constitutive model for the mechanical behaviour of materials such as rock and concrete. The model proposed is based on a continuum representation of progressive fracturing. This progressive fracturing leads to degradation of the elastic properties and is expressed in terms of an internal variable which is defined as a damage parameter. An evolution law relates the rate of damage to the stress and strain history.

5.1 Characteristics of Rock Material of Interest and Modelling

The behaviour of brittle materials under compressive states of stress has interested researchers in the fields of rock and concrete mechanics for some years. The results reported by experimentalists using stiff testing machines reveal the following essential features of brittle rock time-independent behaviour under general triaxial compression:

(i) under monotonic loading, brittle rocks exhibit strain softening shear behaviour in the post 'failure' region as shown in Fig. 5.1(a) (Bieniawski [97], Bieniawski et al [98], Cook [99], Crouch [100]),

(ii) under cyclic laoding, Fig. 5.1(a), the shear stiffness of the rock decreases as the deformation increases and permanent strains are present on unloading (Bieniawski [101], Wawersik and Fairhurst [102]),

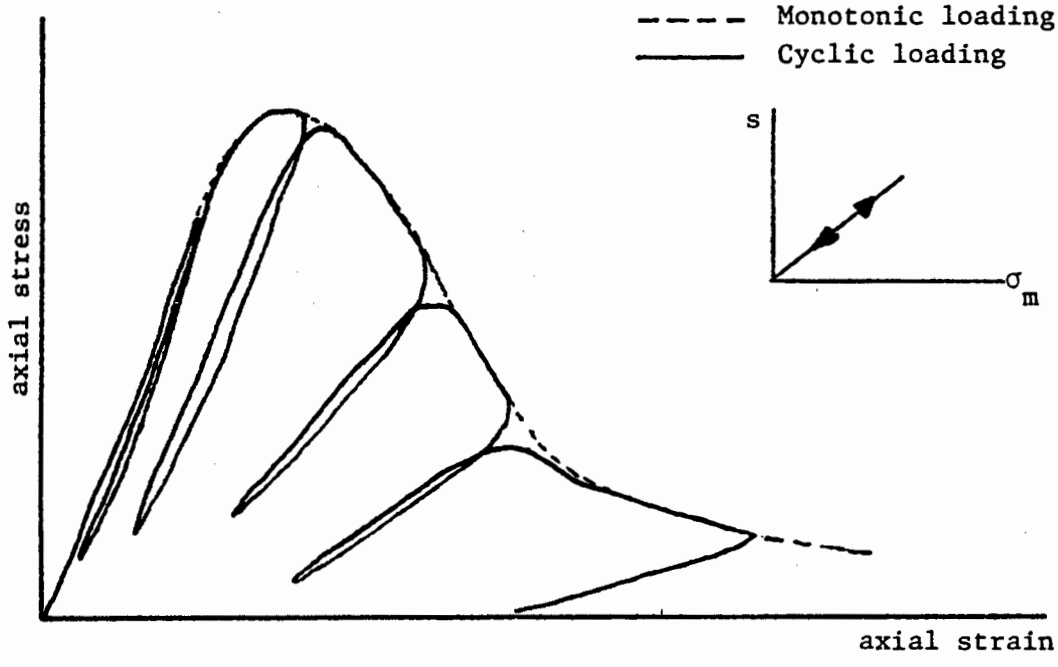

(a) Deviator stress/strain behaviour

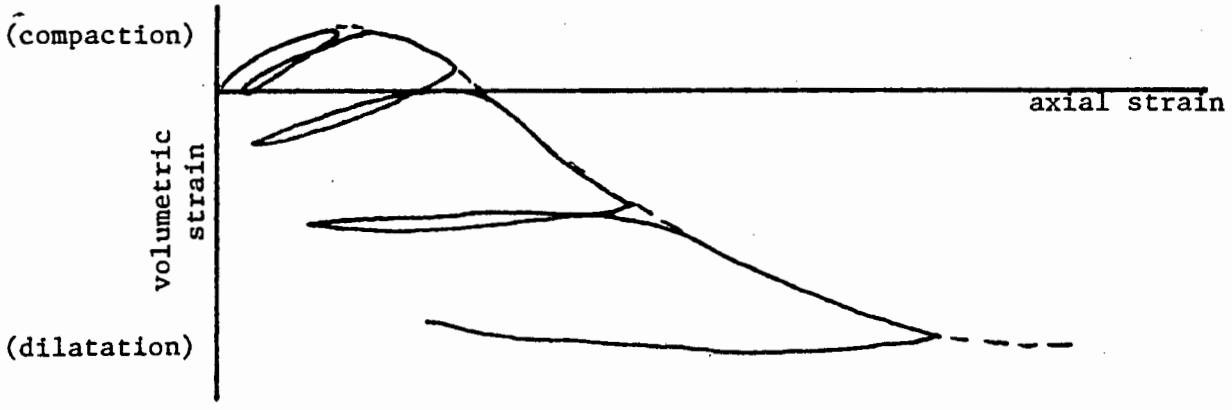

(b) Volumetric strain/deviator strain behaviour

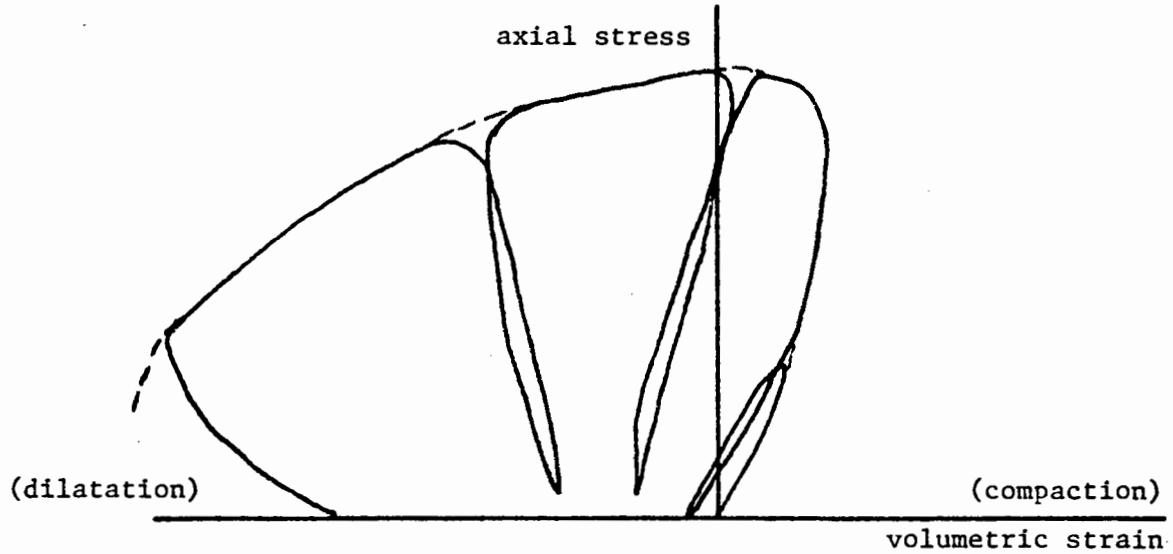

(c) Volumetric stress/strain behaviour

Figure 5.1: Typical experimental curves for uniaxial compression test (radial path in s - σ_m space) for brittle rock.

(iii) the volumetric behaviour under monotonic loading, Figs. 5.1 (b, c) is strongly dilatant (Brace et al [103], Crouch [100]),

(iv) under cyclic loading, the amount of permanent inelastic volume strain varies with the extent of deformation of the material, Figs. 5.1 (b, c), (Hueckel [104]).

More recently, the author has taken special note of the experimental work of Stavropoulou [105] on brittle rocks which confirms the above observations.

Essentially the same features have been noted for concrete by Dougill et al [106] and Spooner and Dougill [107].

However, experimentalists have reported very little on the tensile behaviour of granular brittle materials making it difficult to construct constitutive models which are soundly based on physical evidence. Since mathematical models intended for use in numerical computations must be able to describe behaviour for any arbitrary loading path, they must be complete in the sense that they must be defined for any state of stress and strain. For this reason it is sometimes necessary to build into the mathematical models features which although reasonable and consistent with the rest of the model are not necessarily based on physical evidence. This has in fact been done in the proposed model where the tensile behaviour has been developed from very limited experimental evidence [97]. Nevertheless the tensile behaviour is consistent with the framework of the model and appears to have the important physical as well as computational ingredients. The latter point is critical when seeking solutions for boundary value problems in which the tensile behaviour is dominant. A good illustration of this is given by Hawla [108] when dealing with concrete modelling.

Few theoretical models have been proposed for the dilatant softening constitutive behaviour of brittle materials compared with the many

available models based on classical plasticity. The latter give dilatant hardening inelastic behaviour which is clearly not applicable to brittle materials at low confining pressures. In the category of dilatant softening models the work of Maier and Hueckel [109], Dragon and Mroz [110], Gerogiannopoulos and Brown [111] and Chang and Yang [112] on rock and the work of Dougill [113,114], Dougill and Rida [115] and Bazant and Kim [116] on concrete are noteworthy. However, all these models make use of a yield or fracture surface and some kind of flow rule which defines the nature of the inelastic deformation. In the present work, a constitutive model based on the progressive fracturing (or stiffness degradation) ideas of Dougill is developed for the quasi-static behaviour of brittle materials exhibiting dilatant softening characteristics at low confining pressures. The present model is also capable of representing the non-dilatant hardening behaviour of rock and concrete at high confining pressures. The model does not require a yield/fracture surface or a flow rule, but instead makes use of an internal variable representing the extent of internal damage together with an evolution law defining the rate of damage.

In this work, we assume that the material deforms as a continuum with fracturing damage being distributed homogeneously through the material. In reality, this assumption is certainly not valid after a certain stage of the post 'failure' region, since there is evidence of the formation of shear bands which are zones of localized deformation. However, the description of localization instabilities (Rudnicki and Rice [117], Rice [118]), in the sense that the constitutive equations may allow the homogeneous deformation to lead to a bifurcation point at which non-uniform deformation is incipient in a localized band while homogeneous deformation continues elsewhere, is not attempted in this work.

5.2 Framework of the Damage Constitutive Equations

The constitutive model provides inviscid equations relating the stress rate and the strain rate. We make use of the stress tensor σ_{ij} and the strain tensor ε_{ij}, and denote their rates by $\dot{\sigma}_{ij}$ and $\dot{\varepsilon}_{ij}$. The deviatoric components of $\dot{\sigma}_{ij}$, $\dot{\varepsilon}_{ij}$ are given by

$$\dot{s}_{ij} = \dot{\sigma}_{ij} - \frac{1}{3}\dot{\sigma}_{kk}\,\delta_{ij} \quad , \quad \dot{e}_{ij} = \dot{\varepsilon}_{ij} - \frac{1}{3}\dot{\varepsilon}_{kk}\,\delta_{ij} \quad . \tag{5.1}$$

The model is developed on the basis of the invariant quantities implying that the resulting equations are isotropic.

Following Resende and Martin [36], we choose the stress invariants to be the mean hydrostatic tension σ_m given by

$$\sigma_m = \frac{1}{3}\sigma_{kk} \tag{5.2}$$

and an effective shear stress s defined as

$$s = \left(\frac{1}{2}s_{ij}\,s_{ij}\right)^{1/2} \quad . \tag{5.3}$$

The stress invariant rates are obtained by differentiating equns. (5.2) and (5.3)

$$\dot{\sigma}_m = \frac{1}{3}\dot{\sigma}_{kk} \quad , \quad \dot{s} = \frac{1}{2s}s_{ij}\,\dot{s}_{ij} \quad . \tag{5.4}$$

Conjugate strain invariant rates are then defined as (see Resende and Martin [36])

$$\dot{\varepsilon}_v = \dot{\varepsilon}_{kk} \quad , \quad \dot{e} = \frac{1}{s}s_{ij}\,\dot{e}_{ij} \tag{5.5}$$

and

$$\varepsilon_v = \int \dot{\varepsilon}_v\,dt \quad , \quad e = \int \dot{e}\,dt \quad . \tag{5.6}$$

The measure of damage

$$\lambda = \int \dot{\lambda}\, dt \tag{5.7}$$

is defined as a scalar and therefore has no directional properties (note however that the response of the material is in general non-isotropic).

The constitutive equations can now be developed in the invariant quantities and their generalization to component form is possible with the above definitions.

5.3 Invariant Form of the Constitutive Equations and its Physical Interpretation

The basic form of the damage constitutive equations can be best developed and understood if we work with the stress invariants σ_m, s and the conjugate strain invariants ε_v, e as defined in section 5.2. For a displacement based finite element formulation, we seek to express stress rates (or increments) in terms of total strain rates for all possible states.

We deal first with the shear part of the constitutive equations. We write the elastic constitutive law, in total terms, as

$$s = G_o(1-\lambda)e^e \tag{5.8}$$

where G_o is the initial shear modulus, e^e is the elastic shear strain invariant and λ is a scalar measure of damage (loss of stiffness). The values that λ can assume are restricted to the interval between zero and one. At $\lambda=0$ the material is in its virgin state and possesses its original stiffness; at $\lambda=1$ the material has totally failed and has zero stiffness. The rate form of equn. (5.8) is given by

$$\dot{s} = G_o(1-\lambda)\dot{e}^e - G_o e^e \dot{\lambda} \quad \text{for loading } (\dot{\lambda}>0) \tag{5.9a}$$

and

$$\dot{s} = G_o(1-\lambda)\dot{e}^e \quad \text{for unloading } (\dot{\lambda}=0) \quad , \tag{5.9b}$$

where unloading is interpreted as a path during which no additonal damage takes place. Equns. (5.9) are of the same form as the rate equations for the progressively fracturing solid of Dougill [114]. The characteristics of the progressively fracturing solid as postulated by Dougill are (Figure 5.2):

(i) loss of stiffness due to progressive deformation

(ii) unloading of a linear elastic manner with the stiffness depending on the extent of progressive fracture prior to unloading, and

(iii) having the property that the material may always return to a state of zero stress and strain by linear elastic unloading.

Equns. (5.9), having the above characteristics, have to be modified in order to account for the permanent strains observed after unloading in shear (Fig. 5.1(a)). To do this we assume that the invariant shear strain rate is given as the sum of an elastic part and an inelastic damage component,

$$\dot{e} = \dot{e}^e + \dot{e}^d \tag{5.10}$$

and we define the damage shear strain rate as

$$\dot{e}^d = \dot{e}^d(\lambda,\dot{\lambda}) = d_1 \lambda \dot{\lambda} \tag{5.11}$$

where d_1 is a material parameter. The form of equn. (5.11) suggests that the amount of permanent shear strain on unloading is dependent on the degree of damage of the material prior to unloading (increased damage meaning increased permanent strains).

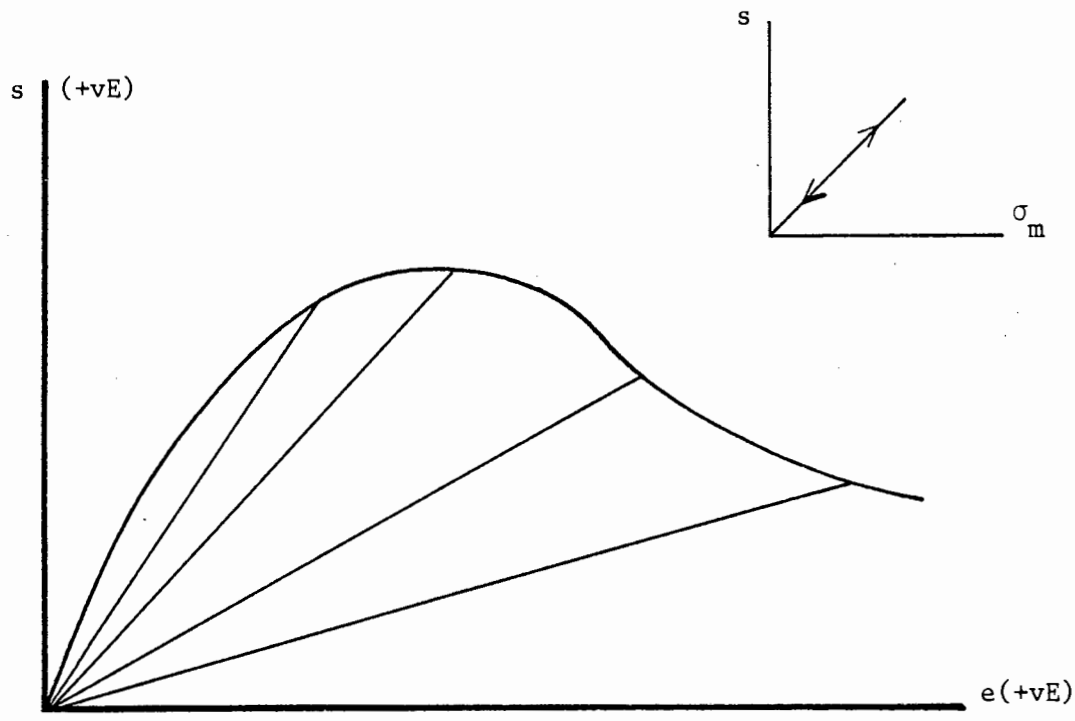

Figure 5.2: Uniaxial stress/strain curve for the progressively fracturing solid of Dougill.

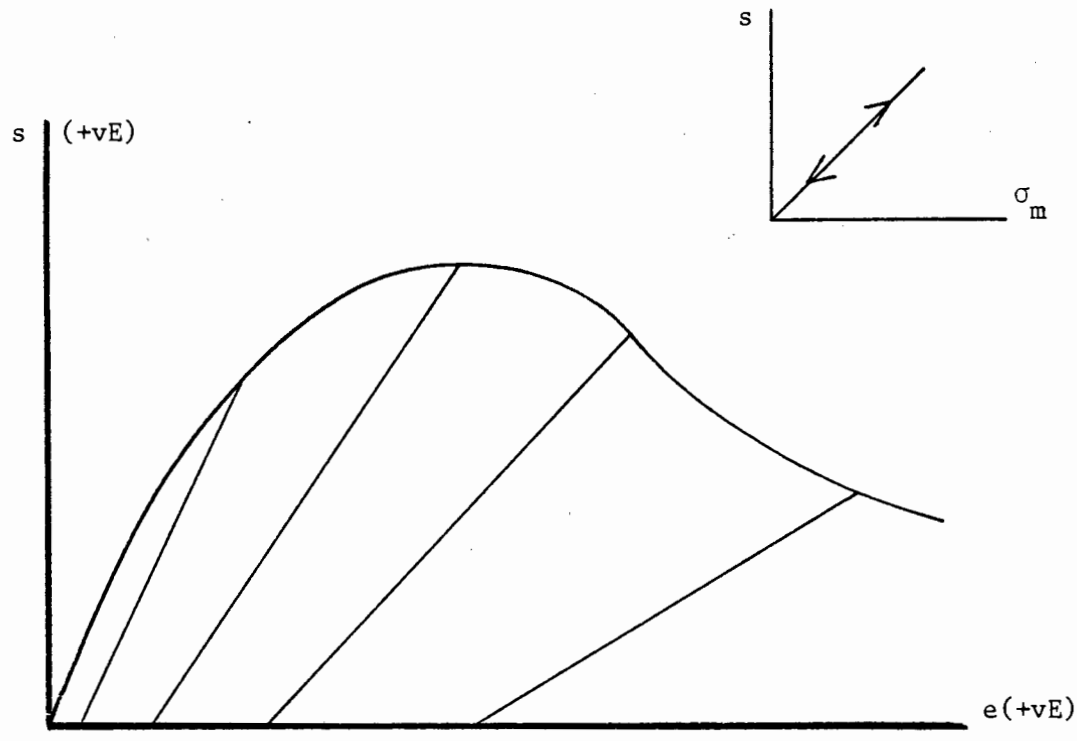

Figure 5.3: Invariant shear stress/strain curve for progressive damage material including damage coupled permanent strains.

Substituting equns. (5.10) and (5.11) into (5.9) we obtain

$$\dot{s} = G_o(1-\lambda)\dot{e} - G_o(1-\lambda)d_1 \lambda \dot{\lambda} - G_o e^{e}\dot{\lambda} \quad \text{for } \dot{\lambda} > 0 \qquad (5.12a)$$

and

$$\dot{s} = G_o(1-\lambda)\dot{e} \quad \text{for } \dot{\lambda} = 0 \quad . \qquad (5.12b)$$

The invariant shear stress/strain relationship of equns. (5.12) including damage coupled permanent strains is illustrated in Fig. 5.3.

The physical basis for this choice of shear constitutive relation is founded on the generally accepted phenomena of microfracturing in rock and microcracking in concrete.

The remaining piece of information required to complete the description of the shear behaviour is the definition of the rate of damage. We postulate an evolution equation of the form

$$\dot{\lambda} = \dot{\lambda}\,(\dot{e},\ e,\ \sigma_m,\ \dot{\varepsilon}_v,\ \varepsilon_v)$$

$$= A(e,\ \sigma_m)\,\dot{e} + B(\varepsilon_v)\,\dot{\varepsilon}_v \qquad (5.13)$$

where $A(e,\sigma_m)$ and $B(\varepsilon_v)$ contain material parameters. The constraints associated with equn. (5.13) are

$$\dot{\lambda} = A\dot{e} + B\,\dot{\varepsilon}_v \quad \text{for } \lambda = \lambda_{max},\ \dot{\lambda} > 0,\ \sigma_m > 0,\ \dot{\varepsilon}_v > 0 \qquad (5.14a)$$

$$= A\dot{e} \quad \text{for } \lambda = \lambda_{max},\ \dot{\lambda} > 0,\ \sigma_m > 0,\ \dot{\varepsilon}_v \leq 0 \qquad (5.14b)$$

$$= 0 \quad \text{otherwise when } \sigma_m > 0 \qquad (5.14c)$$

$$= A\dot{e} \quad \text{for } \lambda = \lambda_{max},\ \dot{\lambda} > 0,\ \sigma_m \leq 0 \qquad (5.14d)$$

$$= 0 \quad \text{otherwise when } \sigma_m \leq 0 \quad . \qquad (5.14e)$$

Clearly equns. (5.14a-5.14c) apply to tensile states of stress ($\sigma_m > 0$) while equns. (5.10d - 5.14e) refer to compressive states of stress ($\sigma_m \leq 0$). It can be seen that the damage evolution law is made up of a shear damage part $A(e,\sigma_m)\dot{e}$ and a hydrostatic tension damage part $B(\varepsilon_v)\dot{\varepsilon}_v$. The term $A(e,\sigma_m)\dot{e}$ implies that the rate of shear damage depends on the deviator strain, on its rate and on the hydrostatic stress which makes shear damage pressure sensitive. The question of which terms should appear in $A(e,\sigma_m)\dot{e}$ is open and this is discussed later. Figure 5.4 shows typical plots of shear damage evolution and corresponding shear stress/strain response for shear tests carried out at different (tensile and compressive) but constant hydrostatic pressures. These are a special case of the triaxial test which exhibits qualitatively the same characteristics. It is interesting to note that the λ curves of Fig. 5.4(a) can be thought of as representing the integration of a normal distribution of micro-fracturing events in a microscopically inhomogenous solid. Dougill based his progressive fracturing theory on similar assumptions.

In the present model, the formulation of the volumetric part of the constitutive laws is done in a way which is significantly different from the previous work on dilatant material models. We assume that the invariant volumetric strain rate can be written as the sum of an elastic and an inelastic (damage) component,

$$\dot{\varepsilon}_v = \dot{\varepsilon}_v^e + \dot{\varepsilon}_v^d \quad . \tag{5.15}$$

Inspired by the hydrostatic compression behaviour of the plasticity cap models [30, 31, 36], we express the elastic volume strain in compression ($\sigma_m \leq 0$) as

$$\varepsilon_v^e = (1 - e^{D\sigma_m})(W - \varepsilon_{vmax}) \quad , \tag{5.16a}$$

which upon inverting yields the elastic total stress/strain relation

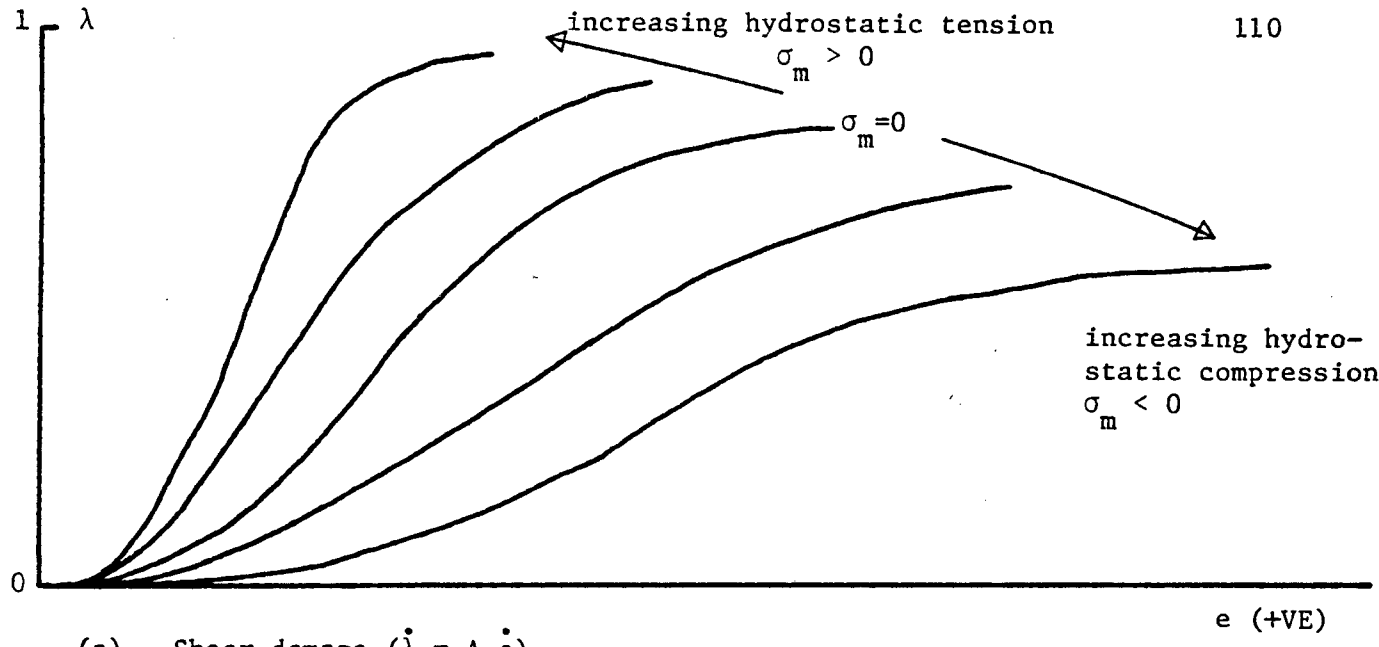

(a) Shear damage ($\dot{\lambda} = A\,\dot{e}$)

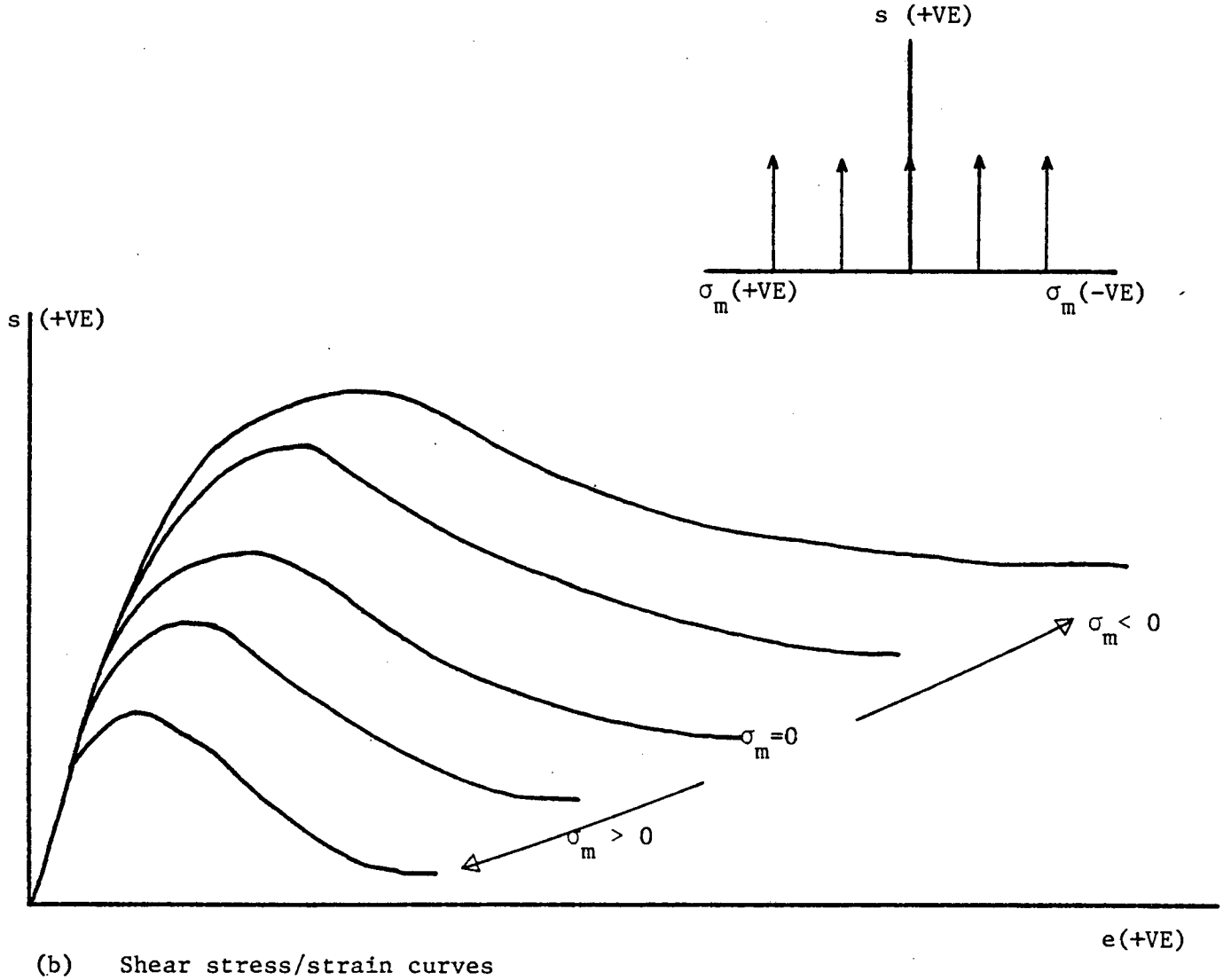

(b) Shear stress/strain curves

Figure 5.4: Typical shear behaviour of damage model for different but constant hydrostatic conditions (note $\dot{\varepsilon}_v = 0$).

$$\sigma_m = \frac{1}{D} \ln \left(1 - \frac{\varepsilon_v^e}{W - \varepsilon_{vmax}}\right) \quad . \tag{5.16b}$$

This assumption would seem appropriate for rock; based on pure hydrostatic tests carried out on hard brittle rocks, Stavropoulou [105] suggests that there are no significant permanent strains after an hydrostatic loading/unloading cycle. This is not the case for concrete and in order to apply the present model to concrete some modifications would be necessary. The relation of equn. (5.16) is shown diagrammatically in Fig. 5.5, where the significance of the parameters W and D can be appreciated. It can also be seen that this nonlinear elastic relation is dependent on the degree of packing of the material represented by ε_{vmax} which includes the contribution of ε_v^e and ε_v^d. The manner in which ε_{vmax} is updated is given by

$$\begin{aligned} &\dot{\varepsilon}_{vmax} = \dot{\varepsilon}_v \quad \text{for} \quad \varepsilon_v = \varepsilon_{vmax} \quad \text{and} \quad \dot{\varepsilon}_v > 0 \\ &\dot{\varepsilon}_{vmax} = 0 \quad \text{for} \quad \varepsilon_v = \varepsilon_{vmax} \quad \text{and} \quad \dot{\varepsilon}_v < 0 \\ &\qquad\qquad \text{or} \quad \varepsilon_v < \varepsilon_{vmax} \\ &\qquad\qquad \text{and} \quad \varepsilon_v > \varepsilon_{vmax} \text{ cannot occur.} \end{aligned} \tag{5.17}$$

The rate form of the hydrostatic compression elastic stress/strain relation of equn. (5.16b) is written as

$$\dot{\sigma}_m = \frac{1}{-D\left(W - \varepsilon_{vmax} - \varepsilon_v^e\right)} \dot{\varepsilon}_v^e \quad . \tag{5.18}$$

We define the damage volume strain rate as

$$\begin{aligned} \dot{\varepsilon}_v^d = \dot{\varepsilon}_v^d \left(\dot{\lambda}, \lambda, \dot{e}, e\right) &= \left(c_1 + c_2 e\right) \dot{\lambda} + c_3 \lambda \dot{e} \\ &= \dot{\varepsilon}_v^p + \dot{\varepsilon}_v^c \end{aligned} \tag{5.19}$$

where c_1 - c_3 are material parameters. The term $(c_1+c_2e)\dot{\lambda}$ represents a permanent strain $\dot{\varepsilon}_v^p$ and is motivated by the fact that as the material is sheared $(\dot{\lambda} > 0)$ dilatant behaviour prevails owing to uplift in sliding at microfracture asperities; this is similar to the shear stress behviour in its dependence on the shear strain (Fig. 5.6). The volume strain/shear strain response of Fig. 5.6(b) can be obtained by scaling (parameter c_1) and rotating (parameter c_2) the shear stress/strain response of Fig. 5.6(a). The term $c_3\lambda\dot{e}$ represents an elastic/damage coupling strain $\dot{\varepsilon}_v^c$ similar to the elastoplastic coupling strain of Maier and Hueckel [109]. It gives, on unloading, a recoverable damage strain which depends on the degree of damage prior to unloading. This is illustrated in Fig. 5.7 where volume stress/strain curves arising from the present formulation are shown. The change in sign of the unloading slope in the volume stress/strain curve for the elastic/damage coupling case, Fig. 5.7(b), can be explained if we think in terms of a combination of a volumetric effect and a shear damage effect. Mathematically, the volumetric effect would always give a positive slope on unloading as shown in Fig. 5.7(a). The shear effect provides a negative slope (via $\dot{\varepsilon}_v^c = c_3\lambda\dot{e}$, $\dot{e}$ negative on unloading) of increasing magnitude as the degree of damage λ prior to unloading is increased. At some stage of the deformation the magnitude of the negative slope becomes larger than the positive slope and the change in sign of the volumetric unloading slope takes place. Physically, it makes sense to argue that if we kept the shear stress constant and reduced the volumetric stress the material would expand in the volume sense (giving the positive unloading slope); while reducing the shear stress and keeping the volumetric stress constant would cause the material to decrease in volume (giving the negative slope). The latter behaviour is the opposite effect to uplift due to sliding at microfracture asperities.Furthermore, the two different signs of the slope would suggest that the mechanisms of unloading deformation are quite different during the late, very damaged states as compared to the early, little damaged states of the material. This observation is also made by Hueckel [104]. The effect of the degree of confinement, under triaxial conditions, on the volumetric behaviour is similar to the one observed in the shear behaviour and is shown diagrammatically in Fig. 5.8.

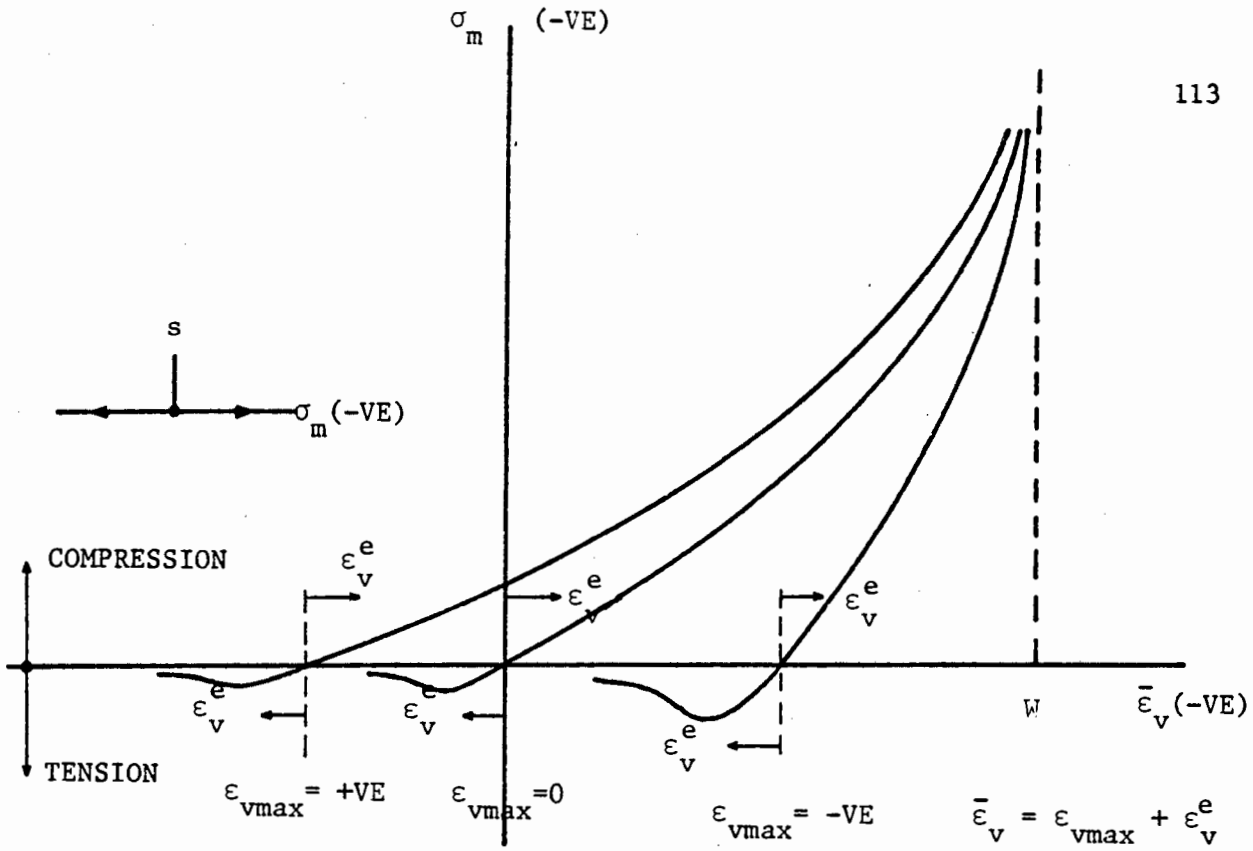

Figure 5.5: Hydrostatic stress/strain behaviour in compression and tension.

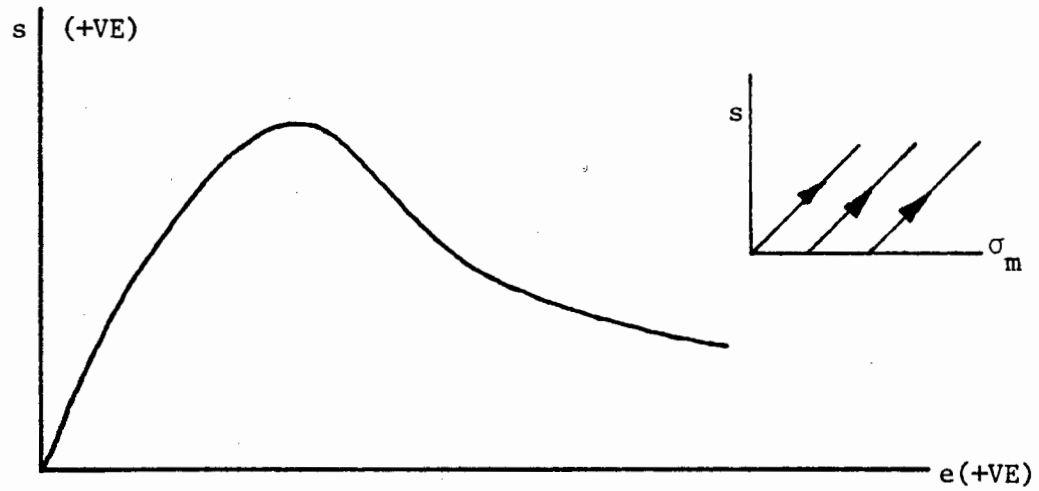

(a) Shear stress/strain curve

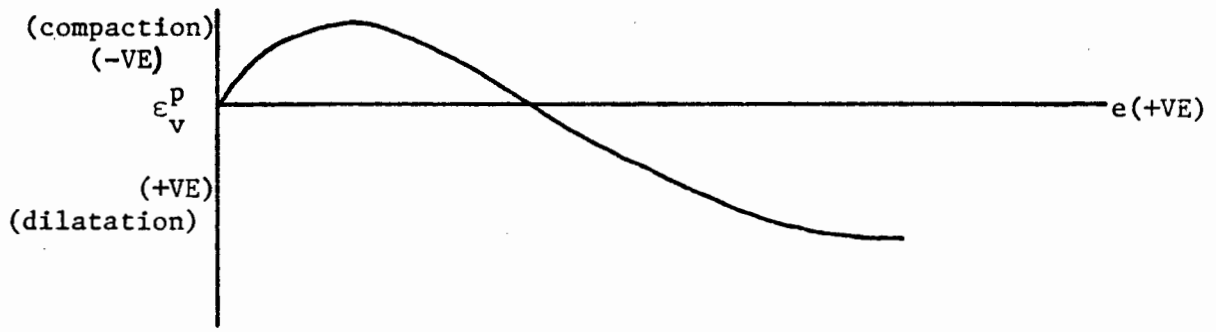

(b) Permanent volume strain/shear strain curve

Figure 5.6: Relation between shear damage and inelastic dilatancy under triaxial loading paths.

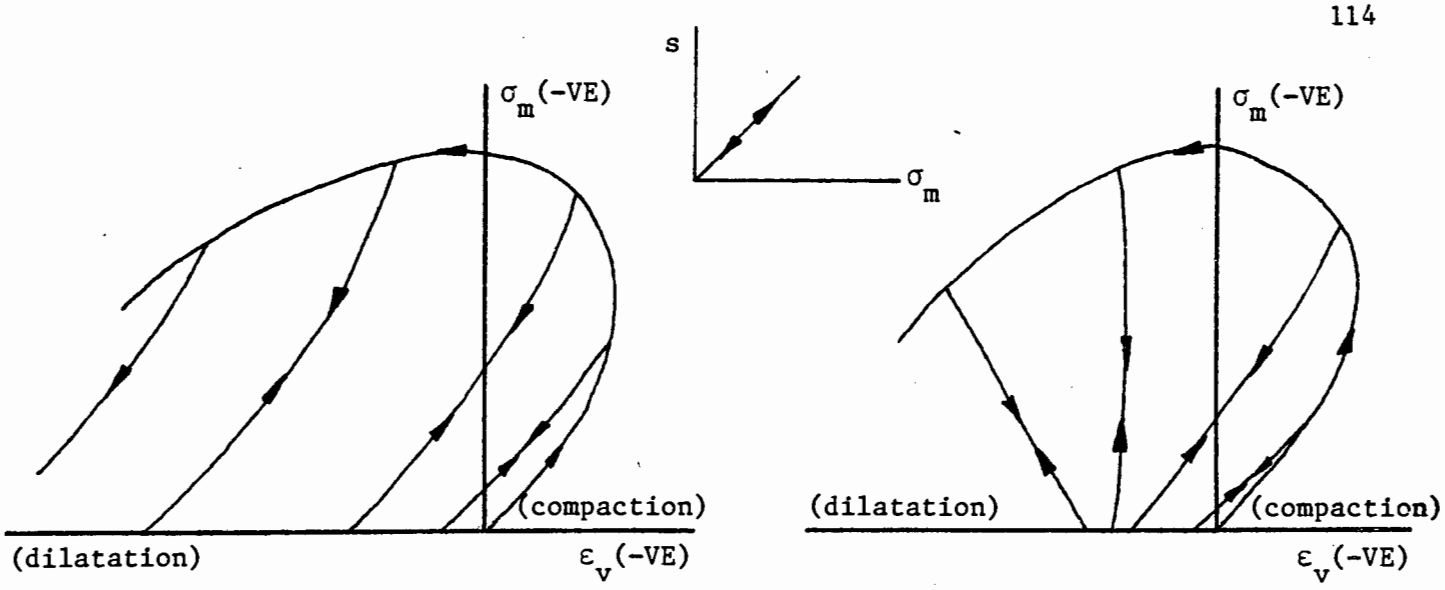

Figure 5.7: Effect of elastic/damage coupling on volumetric unloading behaviour.

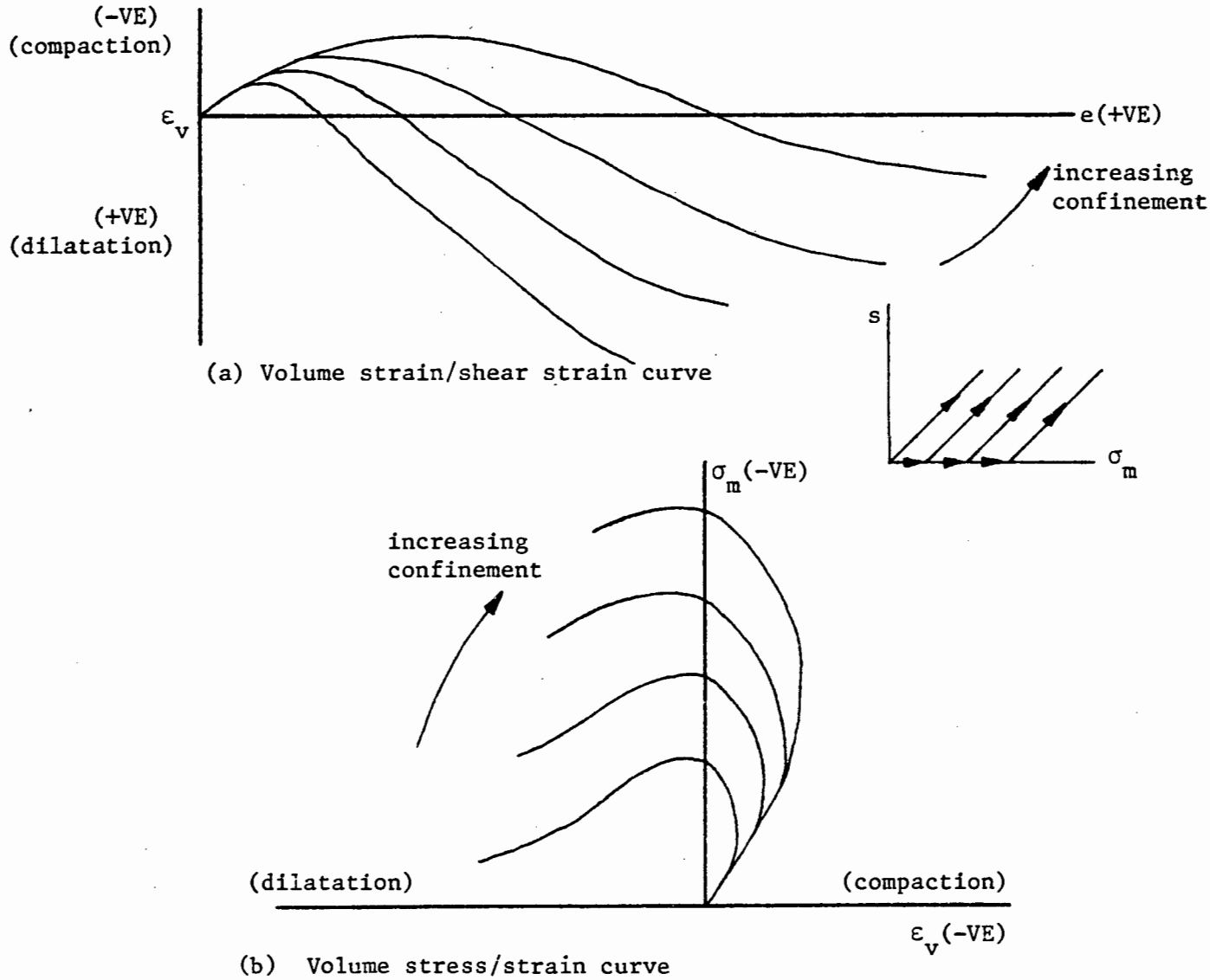

Figure 5.8: Effect of confining pressure on volumetric behaviour under triaxial conditions.

The elastic total stress/strain relation for hydrostatic tension is essentially different from its compression equivalent and is assumed to be of a form similar to equn. (5.8):

$$\sigma_m = K_o(1-\lambda)\ \varepsilon_v^e \qquad (5.20)$$

where K_o is an initial bulk modulus in tension which depends on the compression bulk modulus at zero hydrostatic stress, i.e.

$$K_o = \frac{1}{-D(W - \varepsilon_{vmax} - \varepsilon_v^e)} \quad , \qquad (5.21)$$

calculated for values of ε_{vmax} and ε_v^e corresponding to $\sigma_m = 0$. K_o is then calculated each time the material crosses over to the tensile range and is not updated as long as the material stays in tension. However, ε_{vmax} and ε_v^e are updated at every instant with the rules of equn. (5.17) also applying in tension. Equns. (5.16b) for hydrostatic compression and (5.20) for hydrostatic tension thus provide a continuously differentiable total stress/strain law as illustrated in Fig. 5.5.

The rate form of the hydrostatic tension elastic stress/strain relation of equn. (5.20) can be written as

$$\dot{\sigma}_m = K_o(1 - \lambda)\ \dot{\varepsilon}_v^e - K_o\ \varepsilon_v^e\ \dot{\lambda} \quad \text{for loading } (\dot{\lambda} > 0) \qquad (5.22a)$$

and

$$\dot{\sigma}_m = K_o(1 - \lambda)\ \dot{\varepsilon}_v^e \quad \text{for unloading } (\dot{\lambda} = 0) \quad . \qquad (5.22b)$$

The form of the volumetric strain rate given by equns. (5.15) and (5.19) is also assumed to apply to the tensile behaviour and therefore unloading

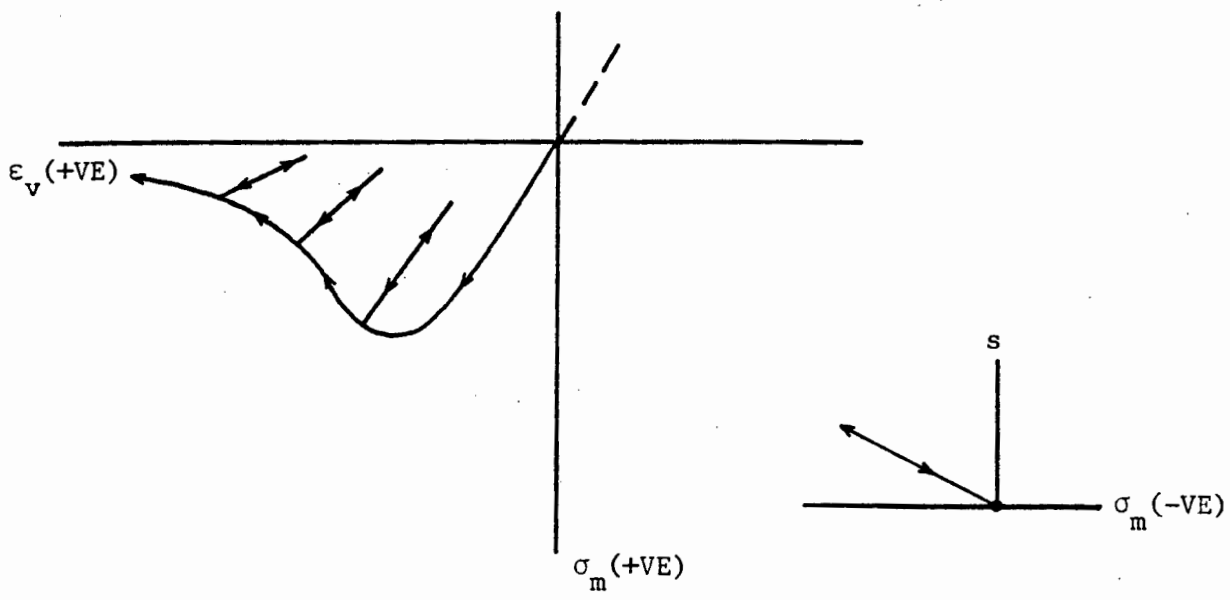

Figure 5.9: Volumetric coupled unloading behaviour under triaxial tension conditions.

in tension exhibits the permanent strain and coupled characteristics shown in Fig. 5.9.

Having developed the shear and volumetric parts of the constitutive relations, we proceed to put them together. We can identify five different cases of loading and unloading as shown in Fig. 5.10:

1. Unloading in compression: $\sigma_m < 0$, $\dot{\lambda} = 0$
2. Loading in compression: $\sigma_m < 0$, $\dot{\lambda} = A\dot{e}$ (shear damage mechanism active)
3. Unloading in tension: $\sigma_m > 0$, $\dot{\lambda} = 0$
4. Loading in tension: $\sigma_m > 0$, $\dot{\varepsilon}_v > 0$, $\dot{\lambda} = A\dot{e} + B\dot{\varepsilon}_v$ (both shear damage and hydrostatic tension damage mechanisms active)
5. Loading in tension: $\sigma_m > 0$, $\dot{\varepsilon}_v < 0$, $\dot{\lambda} = A\dot{e}$ (shear damage mechanism active).

For case 1 we have from equn. (5.12b)

$$\dot{s} = G_o(1 - \lambda)\,\dot{e} \quad , \tag{5.23a}$$

and from equns. (5.15), (5.18) and (5.19)

$$\dot{\sigma}_m = \frac{1}{-D(W - \varepsilon_{vmax} - \varepsilon_v^e)}\,(\dot{\varepsilon}_v - c_3\,\lambda\dot{e}) \quad . \tag{5.23b}$$

For loading in compression, case 2, we have from equns. (5.12a) and (5.14d)

$$\dot{s} = G_o(1 - \lambda)\,\dot{e} - G_o(1 - \lambda)d_1\lambda\,A\dot{e} - G_o\,e^e\,A\dot{e} \quad , \tag{5.24a}$$

and from equns. (5.14d), (5.15), (5.18) and (5.19)

$$\dot{\sigma}_m = \frac{1}{-D(W - \varepsilon_{vmax} - \varepsilon_v^e)} [\dot{\varepsilon}_v - (c_1 + c_2 e) A\dot{e} - c_3 \lambda \dot{e}] \quad . \tag{5.24b}$$

In case 3, unloading in tension, we have from equn. (5.12b)

$$\dot{s} = G_o(1 - \lambda) \dot{e} \quad , \tag{5.25a}$$

and from equns. (5.15), (5.19) and (5.22b)

$$\dot{\sigma}_m = K_o(1 - \lambda)(\dot{\varepsilon}_v - c_3 \lambda \dot{e}) \quad . \tag{5.25b}$$

The constitutive equations for case 4 are obtained from equns. (5.12a) and (5.14a)

$$\dot{s} = G_o(1 - \lambda) \dot{e} - G_o(1 - \lambda) d_1 \lambda (A\dot{e} + B\dot{\varepsilon}_v) - G_o e^e (A\dot{e} + B\dot{\varepsilon}_v) \, , \tag{5.26a}$$

and from equns. (5.14a), (5.15), (5.19) and (5.22a)

$$\dot{\sigma}_m = K_o(1 - \lambda)[\dot{\varepsilon}_v - (c_1 + c_2 e)(A\dot{e} + B\dot{\varepsilon}_v) - c_3 \lambda \dot{e}] \tag{5.26b}$$

$$- K_o \varepsilon_v^e (A\dot{e} + B\dot{\varepsilon}_v) \quad .$$

Finaly, for case 5, we have from equns. (5.12a) and (5.14b)

$$\dot{s} = G_o(1 - \lambda) \dot{e} - G_o(1 - \lambda) d_1 \lambda A\dot{e} - G_o e^e A\dot{e} \quad , \tag{5.27a}$$

and from equns. (5.14b), (5.15), (5.19) and (5.22a)

$$\dot{\sigma}_m = K_o(1 - \lambda)[\dot{\varepsilon}_v - (c_1 + c_2 e)A\dot{e} - c_3 \lambda\dot{e}]$$

$$- K_o \varepsilon_v^e A\dot{e} \quad . \tag{5.27b}$$

Following Resende and Martin [36], we summarize the invariant constitutive equations as

$$\begin{bmatrix} \dot{s} \\ \dot{\sigma}_m \end{bmatrix} = \begin{bmatrix} (G - a_{11}) & - a_{12} \\ - a_{21} & (K - a_{22}) \end{bmatrix} \begin{bmatrix} \dot{e} \\ \dot{\varepsilon}_v \end{bmatrix} \tag{5.28a}$$

where

$$G = G_o(1 - \lambda) \quad \text{for compression or tension,} \tag{5.28b}$$

and

$$K = \begin{cases} \dfrac{1}{- D(W - \varepsilon_{vmax} - \varepsilon_v^e)} & \text{for compression } (\sigma_m < 0) \\ K_o (1 - \lambda) & \text{for tension } (\sigma_m \geq 0) \end{cases} \tag{5.28c}$$

represent current elastic moduli which are updated during the loading history and depend on λ, ε_{vmax} and ε_v^e. The coefficients a_{11}, a_{12}, a_{21}, a_{22}, are related to the damage of the material and depend on its current state and mode of behaviour. The values of the coefficients are

$$a_{11} = 0, \quad a_{12} = 0, \quad a_{21} = \frac{c_3 \lambda}{- D(W - \varepsilon_{vmax} - \varepsilon_v^e)}, \quad a_{22} = 0 \tag{5.28d}$$

for case 1,

$$a_{11} = G_o(1-\lambda)d_1 \lambda A + G_o e^e A, \quad a_{12} = 0, \quad a_{21} = \frac{(c_1 + c_2 e)\, A + c_3 \lambda}{- D(W - \varepsilon_{vmax} - \varepsilon_v^e)}, \quad a_{22} = 0 \tag{5.28e}$$

for case 2,

$$a_{11} = 0, \quad a_{12} = 0, \quad a_{21} = K_o(1-\lambda)c_3\lambda, \quad a_{22} = 0 \tag{5.28f}$$

for case 3,

$$\begin{aligned} a_{11} &= G_o(1-\lambda)d_1\lambda A + G_o e^e A, \quad a_{12} = G_o(1-\lambda)d_1\lambda B + G_o e^e B, \\ a_{21} &= K_o(1-\lambda)[(c_1 + c_2 e)A + c_3\lambda] + K_o \varepsilon_v^e A, \\ a_{22} &= K_o(1-\lambda)(c_1 + c_2 e)B + K_o \varepsilon_v^e B \end{aligned} \tag{5.28g}$$

for case 4, and

$$\begin{aligned} a_{11} &= G_o(1-\lambda)d_1\lambda A + G_o e^e A, \quad a_{12} = 0, \\ a_{21} &= K_o(1-\lambda)[(c_1 + c_2 e)A + c_3\lambda] + K_o \varepsilon_v^e A, \quad a_{22} = 0 \end{aligned} \tag{5.28h}$$

for case 5.

Note that the constitutive matrix is, in general, nonsymmetric. Furthermore, the constitutive relations are not in general unconditionally stable since $\ddot{s}\dot{e} + \dot{\sigma}_m \dot{\varepsilon}_v$ is not necessarily nonnegative for all $\dot{e}$, $\dot{\varepsilon}_v$ under all states of deformation.

5.4 Model Parameters and Forms of the Damage Evolution Law

Before we generalize the constitutive equations to the three dimensional state of stress and strain, it is useful to identify the parameters required to define the constitutive model since they are all contained in the invariant formulation. These can be grouped into seven categories:

(i) G_o, equn. (5.8), the initial shear modulus

(ii) The parameters yet to be introduced, appearing in the term $A(e, \sigma_m)$ of equn. (5.13) which are used to define the evolution of shear damage

(iii) The parameters yet to be introduced, appearing in the term $B(\varepsilon_v)$ of equn. (5.13) which are used to define the evolution of hydrostatic tension damage

(iv) d_1, equn. (5.11), the parameter that defines the amount of permanent shear strain on unloading

(v) W, D and initial ε_{vmax}, equn. (5.16), the parameters defining the elastic volumetric compression behaviour

(vi) c_1 and c_2, equn. (5.19), the parameters which define the amount of permanent volume strain

(vii) c_3, equn. (5.19), the parameter defining the elastic/damage coupling volume strain which is recoverable on unloading.

Assuming that only simple laboratory tests are to be carried out in order to quantify the model parameters, the calibration of the model can be done as follows. G_o and $A(e,\sigma_m)$ are obtained from a series of monotonic loading triaxial tests at different confining pressures. The evolution term $B(\varepsilon_v)$ can be obtained from a single hydrostatic tension test. The parameters c_1 and c_2 are obtained from the volumetric behaviour of the monotonic triaxial tests, and finaly, c_3 and d_1 can be obtained from cyclic triaxial tests including a number of unloading/reloading cycles.

It is clear that this simple calibration procedure has shortcomings in the sense that the model is path dependent and the triaxial and hydrostatic tests only provide information about a limited number of paths. Other, non-standard, tests could be carried out to provide more information about path dependence.

The fewer the parameters required to define a model, the easier it will be to use it. For this reason it would be advantageous if some of the parameters could be made to depend on others so as to reduce the number of independent constants. This will be attempted in the future as part of the identification process cycle. It should also be noted that, depending on the kind of behaviour anticipated, not all material parameters might be necessary. For instance, if no unloading is expected then constants c_3 and d_1 need not be defined. Similarly, simple forms of the damage evolution equation will require only the definition of a few constants in $A(e,\sigma_m)$ and $B(\varepsilon_v)$.

Figure 5.11: Realistic shear behaviour for rock and concrete.

The nature of the damage evolution law in the present model is important since it contains some of the most essential features of the material behaviour. The form of the shear damage term $A(e,\sigma_m)$ in the evolution law of equn. (5.13) presents an open question. How complex need it be? We will attempt to answer this question when calibrating the model for Norite but for the moment it is encouraging to see that even using its simplest possible form ($A = a_1$, linear shear damage evolution), one obtains a material response which is qualitatively correct as shown in the numerical results of Section 5.6. It is also interesting to note that one can remove the hydrostatic pressure dependence from the shear damage term (by not including σ_m terms) and obtain shear behaviour analogous to the Von Mises plasticity theory. The term $A(e,\sigma_m)$ must also reflect the fact that the degradation of the shear stiffness is more rapid under tension conditions than under compression conditions. This is ilustrated in the plots of Fig. 5.4. For materials such as rock and concrete, it appears that the shear damage evolution law should be of the form illustrated in Fig. 5.11: an s-shaped λ vs. e plot with the high strain end of the s-shaped curve being very prominent and assymptotic to a straight line of very low positive slope. This will give a shear stress/strain response exhibiting a peak stress followed by a strain softening branch which tends to some residual stress value. The shape of the λ - e plot in Fig. 5.11 is in fact confirmed by existing experimental data on concrete [119-121] and rock [105].

Experimental evidence [97] suggests that the hydrostatic tension damage term $B(\varepsilon_v)\dot{\varepsilon}_v$ of equn. (5.13) should be chosen to have a form similar to the shear damage term as shown in Fig. 5.11; but again the question of which terms should be included in $B(\varepsilon_v)$ is an open one.

5.5 Constitutive Equations for the Three Dimensional Case

For finite element implementation a more general form of the constitutive equations is required. We present a generalisation of the invariant relations to three dimensional problems. Again, we follow the procedure outlined by Resende and Martin [36].

The components of total stress and total strain are written in vector form as

$$\underset{\sim}{\sigma} = (\sigma_{11}\ \sigma_{22}\ \sigma_{12}\ \sigma_{13}\ \sigma_{23}\ \sigma_{33})^T \quad , \tag{5.29a}$$

$$\underset{\sim}{\varepsilon} = (\varepsilon_{11}\ \varepsilon_{22}\ \gamma_{12}\ \gamma_{13}\ \gamma_{23}\ \varepsilon_{33})^T \quad , \tag{5.29b}$$

where

$$\begin{aligned} \gamma_{12} &= 2\,\varepsilon_{12} \\ \gamma_{13} &= 2\,\varepsilon_{13} \\ \gamma_{23} &= 2\,\varepsilon_{23} \quad . \end{aligned} \tag{5.29c}$$

It is also convenient to identify the deviatoric components of stress and strain, in vector form, as

$$\underset{\sim}{s} = (s_{11}\ s_{22}\ s_{12}\ s_{13}\ s_{23})^T \quad , \tag{5.30a}$$

$$\underset{\sim}{e} = (e_{11}\ e_{22}\ e_{12}\ e_{13}\ e_{23})^T \quad . \tag{5.30b}$$

We make use of the fact that

$$s_{11} + s_{22} + s_{33} = 0 \quad , \quad e_{11} + e_{22} + e_{33} = 0 \quad . \tag{5.31}$$

Simple transformations provide us with the total stress and strain components in terms of the deviatoric stress and strain vectors, the mean hydrostatic stress σ_m and the volume strain ε_v;

$$\underset{\sim}{\sigma} = \begin{bmatrix} \sigma_{11} \\ \sigma_{22} \\ \sigma_{12} \\ \sigma_{13} \\ \sigma_{23} \\ \sigma_{33} \end{bmatrix} = \begin{bmatrix} 1 & 0 & 0 & 0 & 0 & 1 \\ 0 & 1 & 0 & 0 & 0 & 1 \\ 0 & 0 & 1 & 0 & 0 & 0 \\ 0 & 0 & 0 & 1 & 0 & 0 \\ 0 & 0 & 0 & 0 & 1 & 0 \\ -1 & -1 & 0 & 0 & 0 & 1 \end{bmatrix} \begin{bmatrix} s_{11} \\ s_{22} \\ s_{12} \\ s_{13} \\ s_{23} \\ \sigma_m \end{bmatrix} = \mathcal{C} \begin{bmatrix} \underset{\sim}{s} \\ \sigma_m \end{bmatrix} \tag{5.32a}$$

and

$$\begin{bmatrix} \dot{\underset{\sim}{e}} \\ \dot{\varepsilon}_v \end{bmatrix} = \begin{bmatrix} \dot{e}_{11} \\ \dot{e}_{22} \\ \dot{e}_{12} \\ \dot{e}_{13} \\ \dot{e}_{23} \\ \dot{\varepsilon}_v \end{bmatrix} = \begin{bmatrix} 2/3 & -1/3 & 0 & 0 & 0 & -1/3 \\ -1/3 & 2/3 & 0 & 0 & 0 & -1/3 \\ 0 & 0 & 1/2 & 0 & 0 & 0 \\ 0 & 0 & 0 & 1/2 & 0 & 0 \\ 0 & 0 & 0 & 0 & 1/2 & 0 \\ 1 & 1 & 0 & 0 & 0 & 1 \end{bmatrix} \begin{bmatrix} \dot{\varepsilon}_{11} \\ \dot{\varepsilon}_{22} \\ \dot{\gamma}_{12} \\ \dot{\gamma}_{13} \\ \dot{\gamma}_{23} \\ \dot{\varepsilon}_{33} \end{bmatrix} = \hat{\underset{\sim}{C}} \dot{\underset{\sim}{\varepsilon}} \quad . \tag{5.32b}$$

The deviatoric invariants can be written in terms of $\underset{\sim}{s}$ and $\underset{\sim}{e}$.

The invariant shear strain rate is

$$\begin{aligned} \dot{e} &= \frac{1}{s} s_{ij} \dot{e}_{ij} = \frac{1}{s} \{s_{11} \dot{e}_{11} + s_{22} \dot{e}_{22} + s_{33} \dot{e}_{33} + 2s_{12} \dot{e}_{12} + 2 s_{13} \dot{e}_{13} \\ &\quad +2 s_{23} \dot{e}_{23}\} \\ &= \frac{1}{s} \{(2s_{11} + s_{22}) \dot{e}_{11} + (s_{11} + 2s_{22}) \dot{e}_{22} + 2s_{12} \dot{e}_{12} + 2s_{13} \dot{e}_{13} \\ &\quad + 2s_{23} \dot{e}_{23}\} \\ &= \frac{1}{s} \underset{\sim}{s}^T \underset{\sim}{n} \dot{\underset{\sim}{e}} \quad , \end{aligned} \tag{5.33a}$$

where

$$\underset{\sim}{n} = \begin{bmatrix} 2 & 1 & 0 & 0 & 0 \\ 1 & 2 & 0 & 0 & 0 \\ 0 & 0 & 2 & 0 & 0 \\ 0 & 0 & 0 & 2 & 0 \\ 0 & 0 & 0 & 0 & 2 \end{bmatrix} \quad . \tag{5.33b}$$

Similarly it can be shown that

$$s = \{\frac{1}{2} s_{ij} s_{ij}\}^{\frac{1}{2}} = \{\frac{1}{2} \underset{\sim}{s}^T \underset{\sim}{n} \underset{\sim}{s}\}^{\frac{1}{2}} \quad , \tag{5.34a}$$

$$\dot{s} = \frac{1}{2s} s_{ij} \dot{s}_{ij} = \frac{1}{2s} \underset{\sim}{s}^T \underset{\sim}{n} \dot{\underset{\sim}{s}} \quad . \tag{5.34b}$$

The definition of the conjugate deviator invariant rates allows us to write the deviator constitutive relation, in vector form, as

$$\dot{\underset{\sim}{s}} = 2G_o(1-\lambda)\,\dot{\underset{\sim}{e}} - 2G_o\,\underset{\sim}{e}\,\dot{\lambda}$$

$$= 2G_o\,(1-\lambda)\,\dot{\underset{\sim}{e}} - \frac{\dot{\lambda}}{1-\lambda}\,\underset{\sim}{s} \quad , \tag{5.35a}$$

while the hydrostatic stress rate is

$$\dot{\sigma}_m = \frac{\dot{\varepsilon}_v - (c_1 + c_2\,e)\,\dot{\lambda} - c_3\,\lambda\,\dot{e}}{-D\,(W - \varepsilon_{vmax} - \varepsilon_v^e)} \quad . \tag{5.35b}$$

Depending on whether the material is loading or unloading, we substitute the appropriate expression for $\dot{\lambda}$ and write equns. (5.35) as

$$\dot{\underset{\sim}{s}} = 2\,G\,\dot{\underset{\sim}{e}} - \frac{a_{11}}{s}\,\underset{\sim}{s}\,\dot{e} - \frac{a_{12}}{s}\,\underset{\sim}{s}\,\dot{\varepsilon}_v \quad , \tag{5.36a}$$

$$\dot{\sigma}_m = K\,\dot{\varepsilon}_v - a_{21}\,\dot{e} - a_{22}\,\dot{\varepsilon}_v \quad . \tag{5.36b}$$

Premultiplying equn. (5.36a) by $\left(\underset{\sim}{s}^T\,\underset{\sim}{n}/2s\right)$, equns. (5.36) become

$$\dot{s} = \left(G - a_{11}\right)\dot{e} - a_{12}\,\dot{\varepsilon}_v \quad , \tag{5.37a}$$

$$\dot{\sigma}_m = -a_{21}\,\dot{e} + \left(K - a_{22}\right)\dot{\varepsilon}_v \quad , \tag{5.37b}$$

which is identical to equn. (5.28a). Thus the coefficients a_{11}, a_{12} a_{21}, a_{22} can be taken directly from the discussion of the invariant equations. This leaves us with the task of transforming equns. (5.36) into stress and strain rates $\dot{\underset{\sim}{\sigma}}$ and $\dot{\underset{\sim}{\varepsilon}}$.

Substituting from equn. (5.33a), equns. (5.36) become

$$\begin{bmatrix} \dot{\underset{\sim}{s}} \\ \dot{\sigma}_m \end{bmatrix} = \begin{bmatrix} 2G\,\underset{\sim}{I} - \frac{a_{11}}{s^2}\,\underset{\sim}{s}\,\underset{\sim}{s}^T\,\underset{\sim}{n} & \frac{-a_{12}}{s}\,\underset{\sim}{s} \\ \frac{-a_{21}}{s}\,\underset{\sim}{s}^T\,\underset{\sim}{n} & K - a_{22} \end{bmatrix} \begin{bmatrix} \dot{\underset{\sim}{e}} \\ \dot{\varepsilon}_v \end{bmatrix}, \tag{5.38}$$

$$= \underset{\sim}{D} \begin{bmatrix} \dot{\underset{\sim}{e}} \\ \dot{\varepsilon}_v \end{bmatrix},$$

where $\underset{\sim}{I}$ is a 5 x 5 unit matrix.

The transformation is written as

$$\dot{\underset{\sim}{\sigma}} = \underset{\sim}{C} \begin{bmatrix} \dot{\underset{\sim}{s}} \\ \dot{\sigma}_m \end{bmatrix} = \underset{\sim}{C}\,\underset{\sim}{D} \begin{bmatrix} \dot{\underset{\sim}{e}} \\ \dot{\varepsilon}_v \end{bmatrix} = \underset{\sim}{C}\,\underset{\sim}{D}\,\hat{\underset{\sim}{C}}\,\dot{\underset{\sim}{\varepsilon}} = \underset{\sim}{D}^*\,\dot{\underset{\sim}{\varepsilon}} \quad . \tag{5.39}$$

Before calculating $\underset{\sim}{D}^*$, we note that we may partition the matrices $\underset{\sim}{C}$ and $\hat{\underset{\sim}{C}}$ (equns. (5.32)) and write

$$\underset{\sim}{C} = \begin{bmatrix} \underset{\sim}{I} & \underset{\sim}{h} \\ -\underset{\sim}{h}^T & 1 \end{bmatrix}, \qquad \hat{\underset{\sim}{C}} = \begin{bmatrix} \underset{\sim}{n}^{-1} & -\frac{1}{3}\,\underset{\sim}{h} \\ \underset{\sim}{h}^T & 1 \end{bmatrix} \tag{5.40a}$$

where $\underset{\sim}{h} = (1 \quad 1 \quad 0 \quad 0 \quad 0)^T$. (5.40b)

It is also convenient to define

$$\hat{\underset{\sim}{s}} = \frac{1}{s}\,\underset{\sim}{s}, \qquad \hat{\underset{\sim}{t}} = \frac{1}{s}\,\underset{\sim}{n}\,\underset{\sim}{s} = \underset{\sim}{n}\,\hat{\underset{\sim}{s}} \quad . \tag{5.40c}$$

Using these relationships, we then form

$$\dot{\underset{\sim}{\sigma}} = \underset{\sim}{D}^*\,\dot{\underset{\sim}{\varepsilon}}, \tag{5.41a}$$

where

$$\underset{\sim}{D}^{*} = \begin{bmatrix} \underset{\sim}{I} & \underset{\sim}{h} \\ -\underset{\sim}{h}^{T} & 1 \end{bmatrix} \begin{bmatrix} 2G\underset{\sim}{I} - a_{11}\,\hat{\underset{\sim}{s}}\,\hat{\underset{\sim}{t}}^{T} & -a_{12}\,\hat{\underset{\sim}{s}} \\ -a_{21}\,\hat{\underset{\sim}{t}}^{T} & K - a_{22} \end{bmatrix} \begin{bmatrix} \underset{\sim}{n}^{-1} & -\frac{1}{3}\underset{\sim}{h} \\ \underset{\sim}{h}^{T} & 1 \end{bmatrix} . \tag{5.41b}$$

In multiplying out equn. (5.41b), we note three simple relationships;

$$\underset{\sim}{n}^{-1}\,\hat{\underset{\sim}{t}} = \hat{\underset{\sim}{s}} \quad , \quad \frac{1}{3}\,\hat{\underset{\sim}{t}}^{T}\,\underset{\sim}{h} = \hat{\underset{\sim}{s}}^{T}\,\underset{\sim}{h} \quad , \quad \underset{\sim}{h}^{T}\,\underset{\sim}{n}^{-1} = \frac{1}{3}\,\underset{\sim}{h}^{T} \; . \tag{5.42}$$

Carrying out the multiplications, and simplifying through the use of equns. (5.42), we obtain

$$\underset{\sim}{D}^{*} = \left[\begin{array}{l|l} 2G\,\underset{\sim}{n}^{-1} - a_{11}\,\hat{\underset{\sim}{s}}\,\hat{\underset{\sim}{s}}^{T} & -\frac{2}{3}G\,\underset{\sim}{h} + a_{11}\,\hat{\underset{\sim}{s}}\,\hat{\underset{\sim}{s}}^{T}\,\underset{\sim}{h} \\ -(a_{12}\,\hat{\underset{\sim}{s}}\,\underset{\sim}{h}^{T} + a_{21}\,\underset{\sim}{h}\,\hat{\underset{\sim}{s}}^{T}) & -a_{12}\,\hat{\underset{\sim}{s}} + a_{21}\,\underset{\sim}{h}\,\hat{\underset{\sim}{s}}^{T}\,\underset{\sim}{h} \\ +(K - a_{22})\,\underset{\sim}{h}\,\underset{\sim}{h}^{T} & +(K - a_{22})\,\underset{\sim}{h} \\ \hline -\frac{2}{3}G\,\underset{\sim}{h}^{T} + a_{11}\,\underset{\sim}{h}^{T}\,\hat{\underset{\sim}{s}}\,\hat{\underset{\sim}{s}}^{T} & (\frac{4}{3}G + K) - a_{11}\,(\underset{\sim}{h}^{T}\hat{\underset{\sim}{s}})^{2} \\ +a_{12}\,\underset{\sim}{h}^{T}\,\hat{\underset{\sim}{s}}\,\underset{\sim}{h}^{T} - a_{21}\,\hat{\underset{\sim}{s}}^{T} & +(a_{12} + a_{21})\,\underset{\sim}{h}^{T}\,\hat{\underset{\sim}{s}} - a_{22} \\ +(K - a_{22})\,\underset{\sim}{h}^{T} & \end{array}\right] . \tag{5.43}$$

The matrix $\underset{\sim}{D}^{*}$ is thus given explicitly and is essentially identical to the one previously obtained by Resende and Martin [36] for the axisymmetric case (note that in the three dimensional case the matrix $\underset{\sim}{n}$ and the vectors $\hat{\underset{\sim}{s}}$ and $\underset{\sim}{h}$ are augmented to include the extra components of shear stress/strain). This generalisation has been shown [36] to preserve the behaviour noted in the invariant formulation. Summarising, equns. (5.41a) and (5.43), together with equns. (5.28b-5.28e), provide the complete constitutive equations for the damage model in three dimensions.

5.6 Illustration of Damage Model Behaviour

The simplest way to illustrate the properties of the progressive damage model is to perform numerical experiments along simple but representative loading paths. The model described in this chapter was first implemented in a simple computer program designed to calculate the stress/strain response of a single material point for any three dimensional loading history. The program allows one to perform stress controlled, strain controlled or mixed stress/strain controlled numerical experiments for paths of any degree of complexity. In the scope of this section we will however, concentrate on simple tests since we are more interested in illustrating the fundamental features of the model. The details of the implementation of this stress/strain integrator are dealt with in Chapter 7.

It should be stressed that, in the following tests, we are not concerned with quantitative results (in fact we have not tried to fit any available experimental data), but we are rather looking at the qualitative behaviour of the model.

5.6.1 Hydrostatic Compression Test

We start with a simple hydrostatic compression test including loading and unloading. Since the present model predicts elastic behaviour under hydrostatic stress paths, only the elastic properties need to be defined. Assuming $G_o = 1.$, $W = -3.3$, $D = .8$, $\varepsilon_{vmax(o)} = 0.$ as the material properties (units are not important here), the response is plotted in Fig. 5.12 both in component form $(\sigma_1 - \varepsilon_1 \ , \ \sigma_2 - \varepsilon_2 \ , \ \sigma_3 - \varepsilon_3)$ and in invariant form $(\sigma_m - \varepsilon_v)$. The elastic behaviour is confirmed since the loading and unloading paths are coincident. Note that on loading the volumetric strain ε_v is asymptotic to $W = -3.3$ as expected from the form of equn. (5.16).

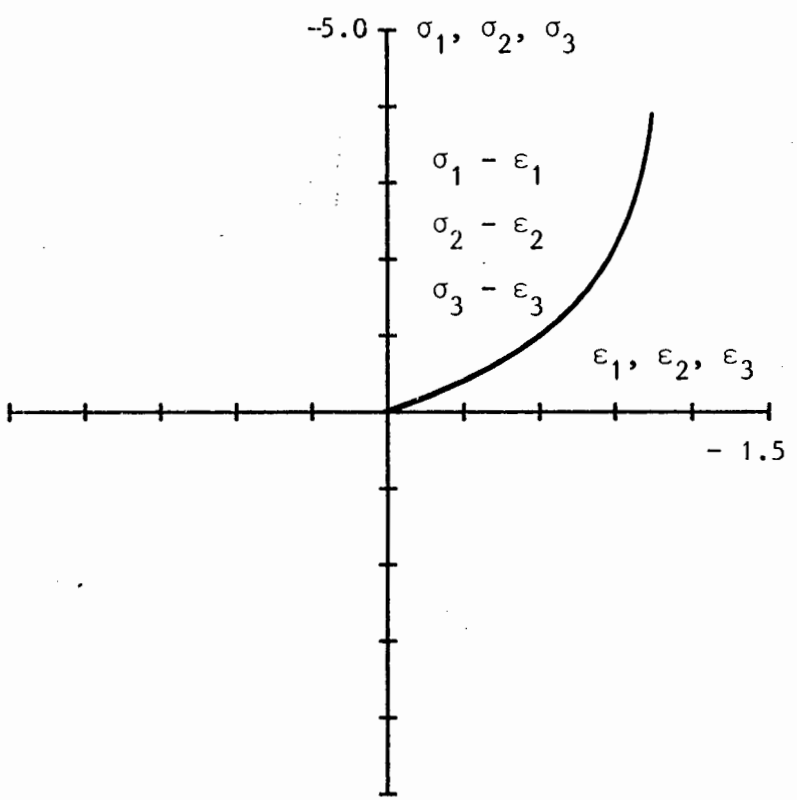

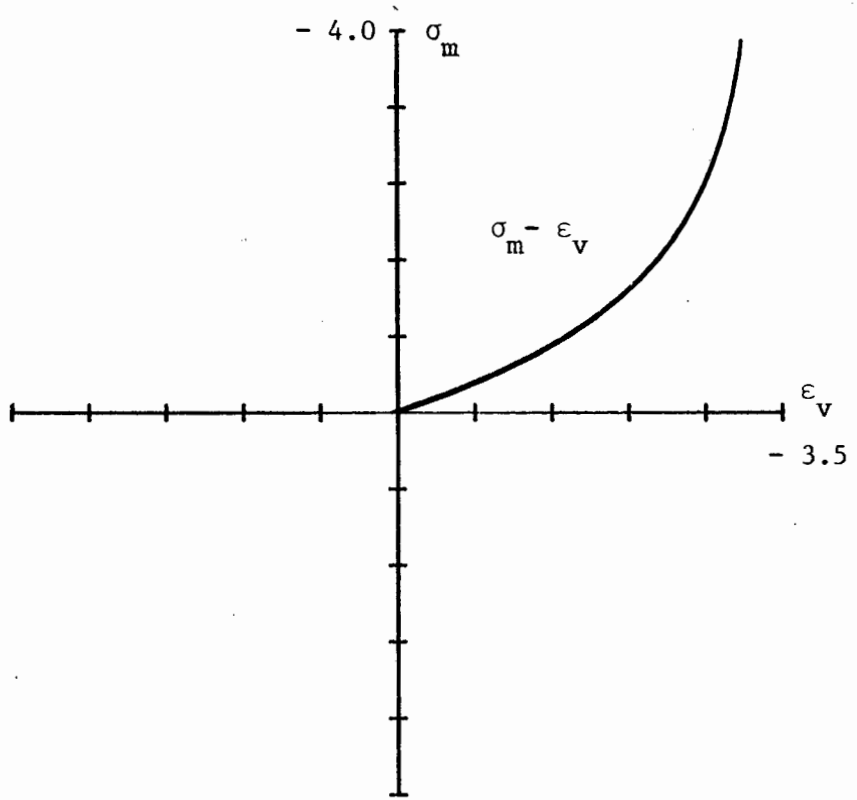

Figure 5.12: Hydrostatic compression test.

5.6.2 Triaxial Compression Tests

Since most of the available experimental results for concrete and rock materials are in some form of triaxial compression, it makes sense to perform some triaxial numerical tests. We subject a single material point to a strain controlled triaxial compression path with zero confining pressure. This corresponds to a radial path in the $s - \sigma_m$ space and is normally referred to as a uniaxial compression test. The elastic properties used are: $G_o = 1.$, $W = -.06$, $D = .8$ and $\varepsilon_{vmax(o)} = 0.$. Let us first consider a monotonic loading test on a material with the simplest possible shear damage evolution law, i.e. $A(e,\sigma_m) = 1.0$, giving $\dot{\lambda} = \dot{e}$; this corresponds to a linear damage evolution law. The other parameters used are $c_1 = .008$, $c_2 = .008$. The response predicted by the model is given in Fig. 5.13 where plots of λ-e , s-e , σ_m-ε_v, ε_v-e , σ_1-ε_1 , σ_1-ε_2 and σ_1-ε_3 are shown. It is interesting to note that although the evolution law chosen is very unrealistic from a physical point of view, a qualitatively correct material response is obtained: the strain softening shear behaviour and the dilatant volumetric behaviour are apparent.

The test is repeated for a material with a more realistic shear damage evolution law, we make $A(e,\sigma_m) = -46.e\sigma_m - 6.e^2$ giving $\dot{\lambda} = (-46.e\sigma_m - 6.e^2)\,\dot{e}$. This represents cumulative damage as a cubic polynomial of the Hermitian kind. The plot of accumulated damage vs. deviator invariant strain (λ-e) is shown in Fig. 5.14 together with plots of s-e , σ_m-ε_v , ε_v-e , σ_1-ε_1 , σ_1-ε_2 and σ_1-ε_3 which represent the stress/strain response of the material both in invariant and component form. Again, the important features of behaviour are captured but now more accurately.

The two previous tests are repeated with three unloading/reloading cycles included in each test. To model the unloading behaviour we define additional material parameters as: $c_3 = .02$ and $d_1 = 0.0$ (no permanent shear strains are included). The invariant and component material responses predicted by the two different evolution equations are shown in Figs. 5.15 and 5.16. The most important point to note in these cyclic

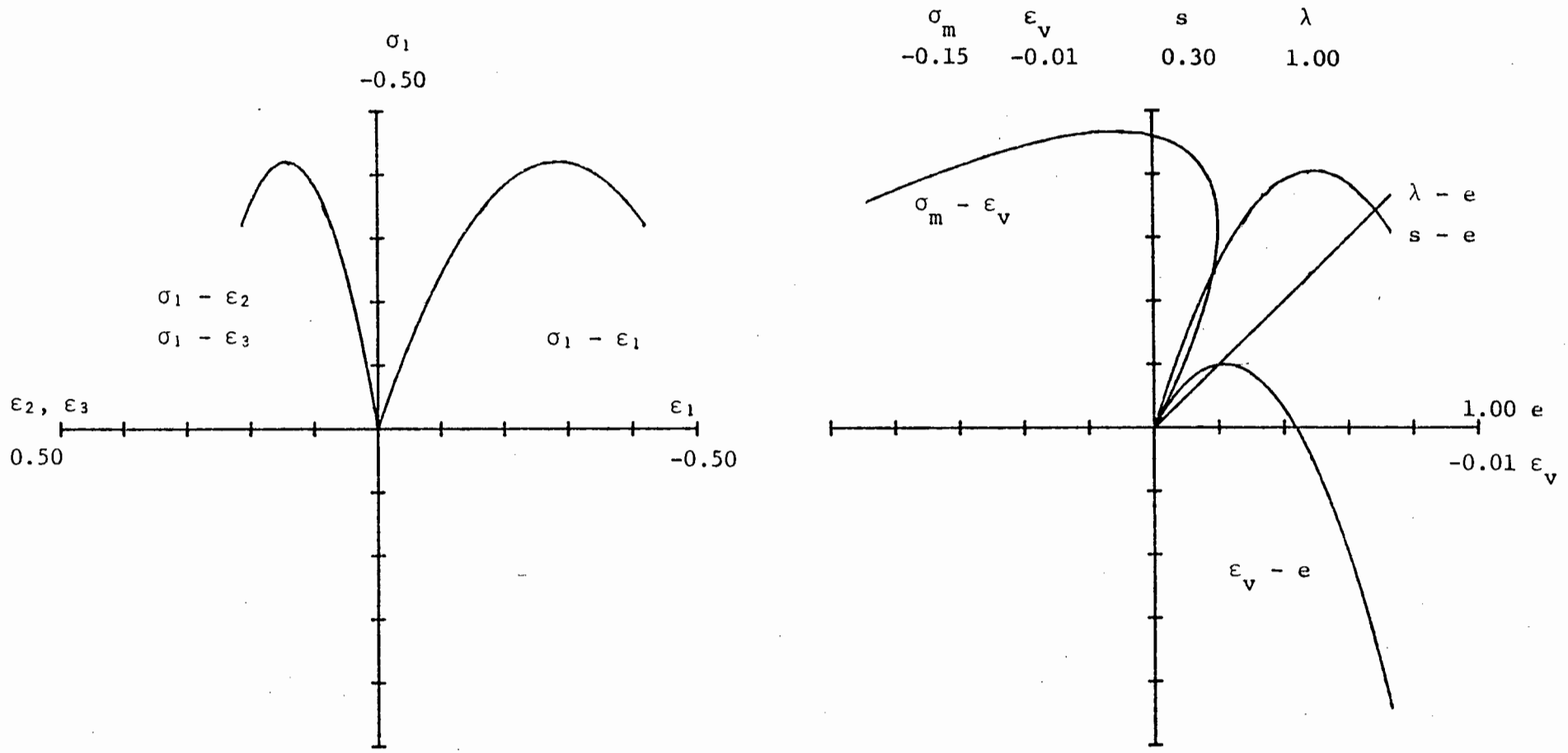

Figure 5.13: Monotonic triaxial compression test with linear evolution law.

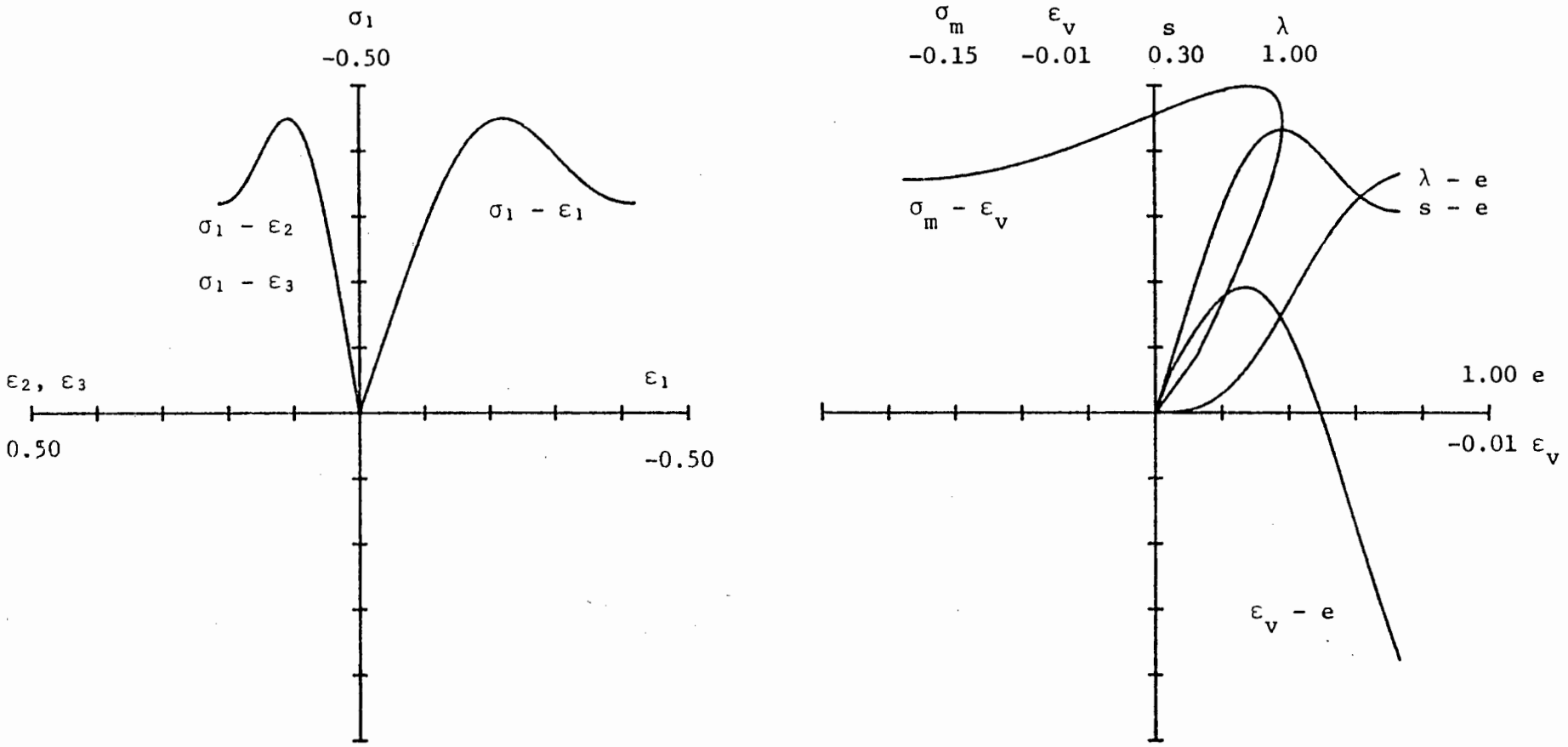

Figure 5.14: Monotonic triaxial compression test with cubic evolution law.

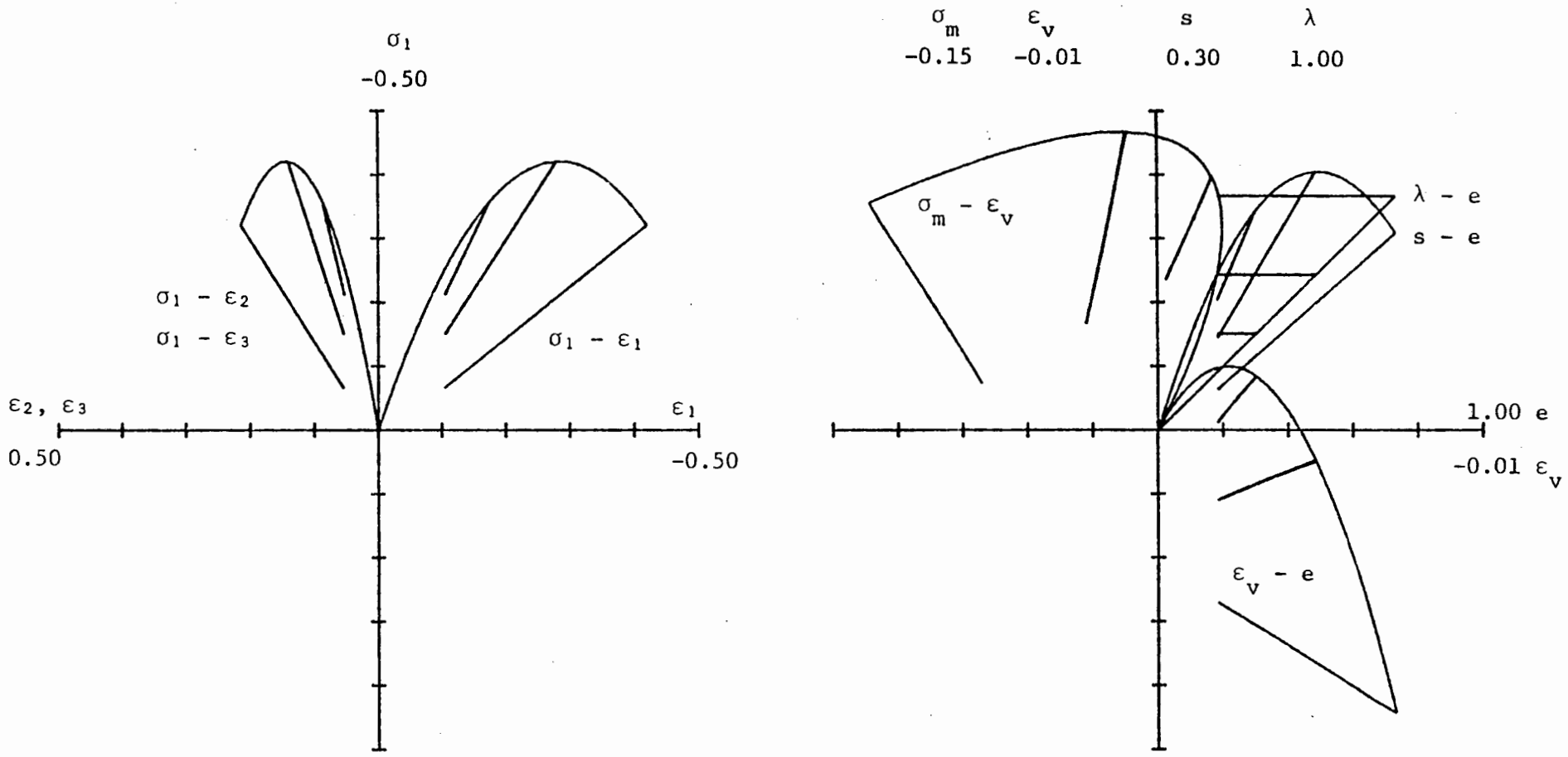

Figure 5.15: Cyclic triaxial compression test with linear evolution law.

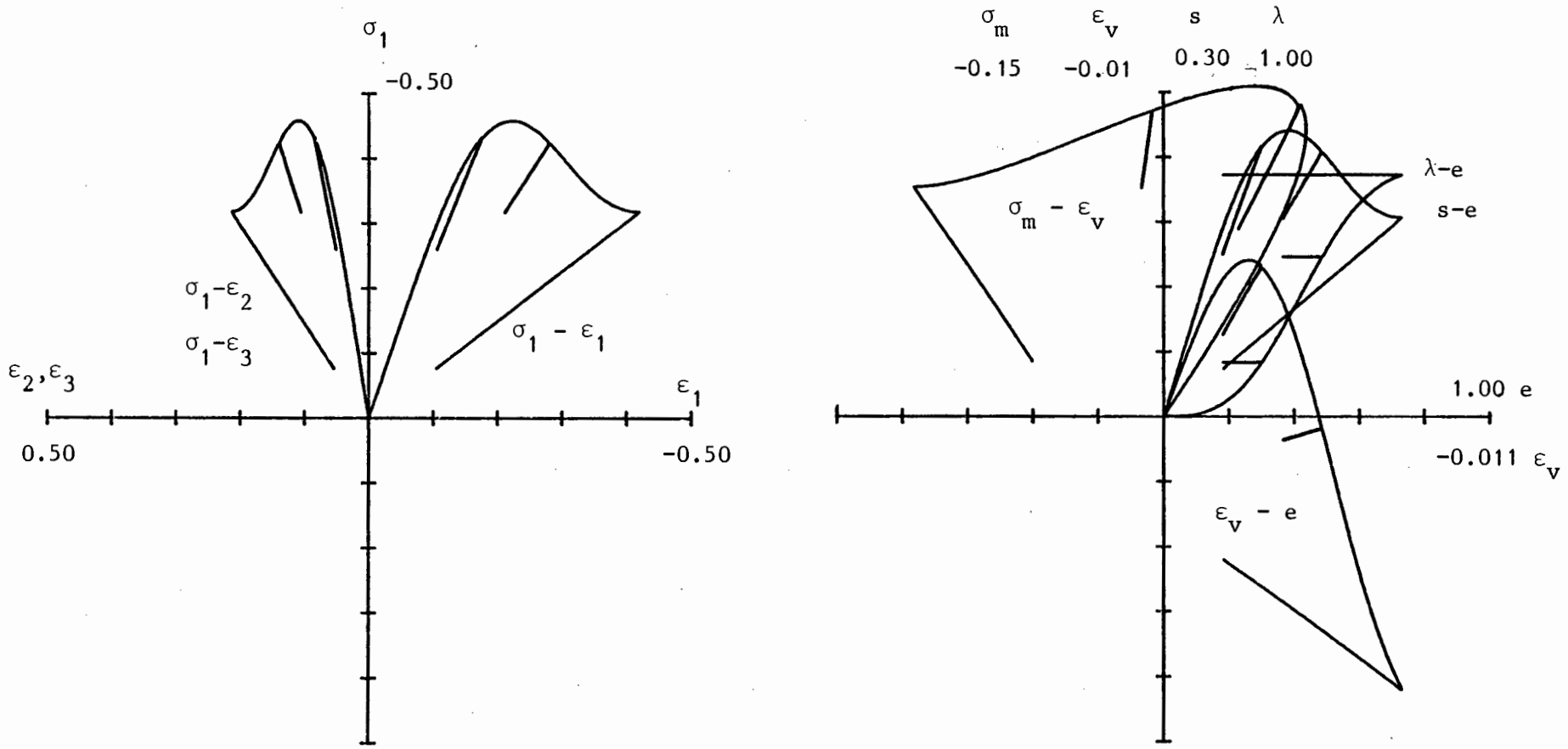

Figure 5.16: Cyclic triaxial compression test with cubic evolution law.

tests is the unloading behaviour in the volumetric sense; the change in sign of the volumetric unloading slope is quite clear from the σ_m-ε_v plots.

Finally, the predictions obtained with the cubic Hermitian evolution law are in particularly good qualitative agreement with the experimental tests shown in Fig. 5.1; 9 material parameters were necessary for this model.

5.6.3 Hydrostatic Tension Test

A hydrostatic tension test, including three unloading/reloading cycles, is performed on a material point which has the following properties: G_o = 1. ,W = .06 , D = .8 , $\varepsilon_{vmax(o)}$ = 0. , c_1 = .008 , c_2 = .008 and c_3 = .02 . A hydrostatic tension damage evolution law of the form $\dot{\lambda} = (2.\ \varepsilon_v)\ \dot{\varepsilon}_v$ is assumed giving a quadratic cumulative damage property to the material. This is shown in the $\lambda - \varepsilon_v$ plot of Fig. 5.17 where $\sigma_m - \varepsilon_v$, σ_1-ε_1 , σ_2-ε_2 and σ_3-ε_3 are also shown. The volumetric strain softening in tension implied by equn. (5.20) is evident and the coupled unloading behaviour is also qualitatively correct.

5.6.4 Triaxial Tension Test

This test is similar to the previous cyclic triaxial compression tests except that now the material is loaded along a radial path in the tension quadrant of the $s - \sigma_m$ space. The material parameters used are identical to the ones of section 5.6.3 apart from the evolution law which is assumed to be $\dot{\lambda} = \dot{e} + 12.\ \varepsilon_v\ \dot{\varepsilon}_v$ for this test. Fig. 5.18 shows the plots of $\lambda - \varepsilon_v$, $s - e$, $\sigma_m - \varepsilon_v$, $\varepsilon_v - e$, $\sigma_1 - \varepsilon_1$, $\sigma_1 - \varepsilon_2$ and $\sigma_1 - \varepsilon_3$ and it can be seen that even with the simple evolution law chosen all the important features of material response are captured. These include shear strain softening, hydrostatic tension softening and coupled unloading volumetric behaviour in tension.

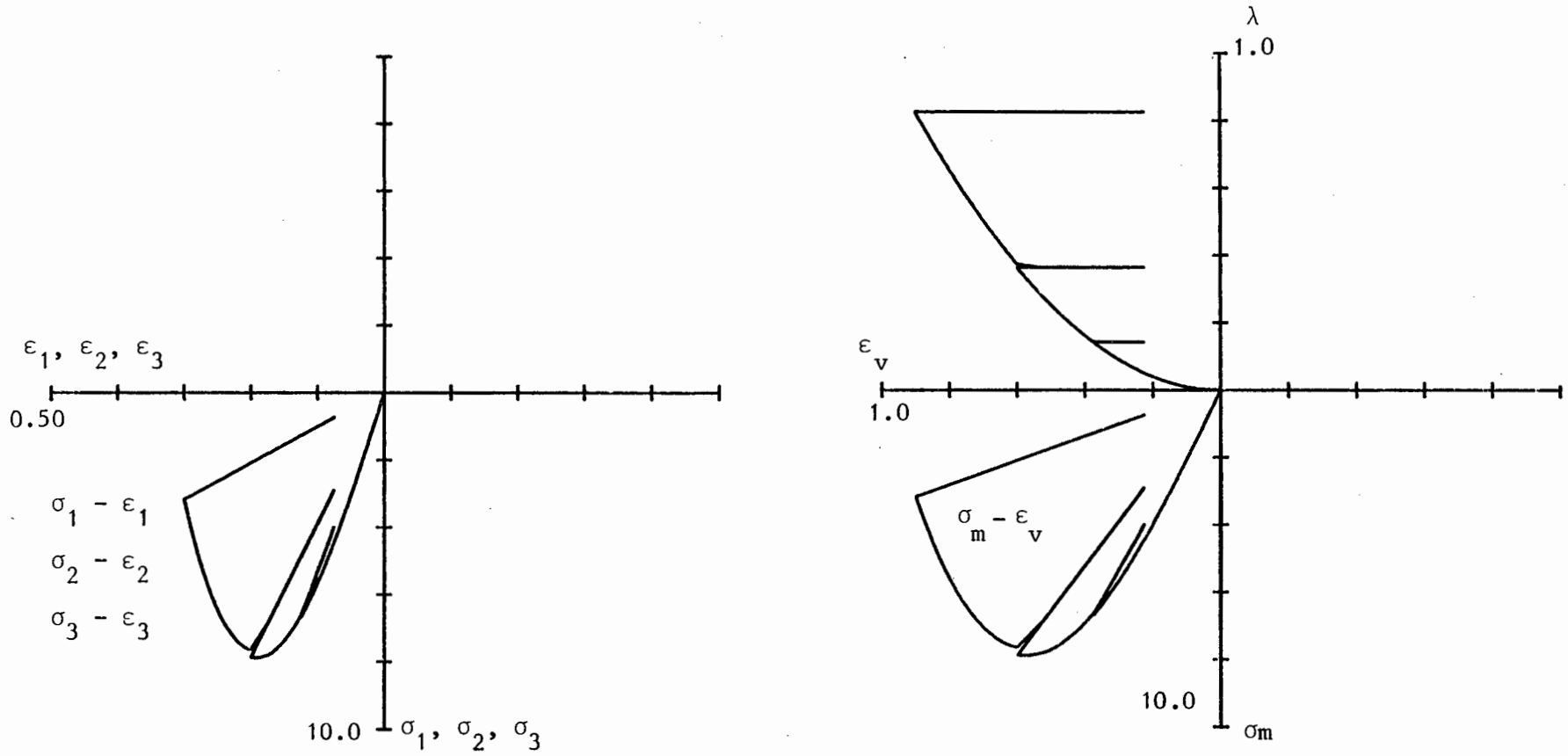

Figure 5.17: Hydrostatic tension test.

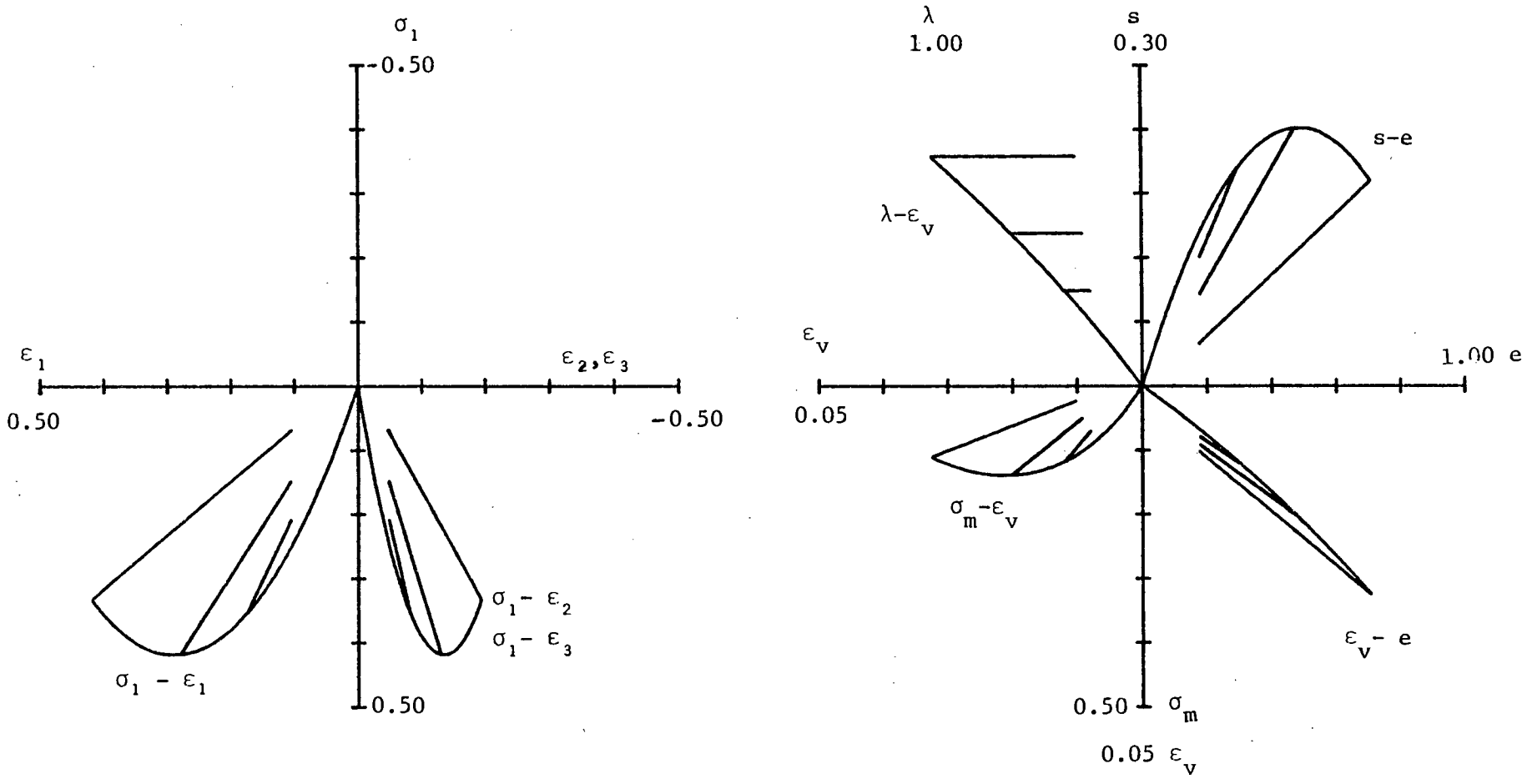

Figure 5.18: Cyclic triaxial tension test.

We conclude this chapter with a comment on the form of the damage evolution laws. This was earlier left as an open question and section 5.6 was used to introduce a few simple forms of damage evolution. It is encouraging to note that even the simplest evolution laws predict behaviour which is in good qualitative agreement with experimental evidence. Realistic forms of damage evolution are explored in the next chapter when calibrating the model for Bushveld Norite.

CHAPTER 6

CALIBRATION OF THE DAMAGE MODEL FOR BUSHVELD NORITE

The material chosen for the first realistic calibration of the damage model developed in the previous chapter is Bushveld Norite. The reason for this lies in the availability of a fairly complete set of experimental data [105] and in the importance of Norite for the mining industry.

This chapter is also used to exploit the question of what form the damage evolution law should take and how sensitive the model is to it.

6.1 Experimental Results for Norite

A vast amount of laboratory experimentation with Norite has been carried out by Stavropoulou [105]. Here we summarise the results that are useful for the damage model calibration.

The isotropy of the rock was first checked by performing uniaxial compression tests on a number of specimens cored out of Norite blocks in two perpendicular directions. The differences observed in uniaxial compressive strength (i.e. peak of shear stress/strain curve) and elastic properties were negligible.

A set of standard triaxial compression tests at constant confining pressures, $\sigma_2 = \sigma_3$, ranging from zero to -250 MPa was carried out. The invariant shear stress/strain curves obtained are shown in Fig. 6.1 where the dashed parts indicate regions of possible doubt due to inadequate stiffness of the testing apparatus. Figure 6.2 shows the volumetric behaviour plotted as hydrostatic stress vs. volumetric strain. Peak and residual invariant shear stresses are plotted against hydrostatic stress in Fig. 6.3 representing envelopes of maximum attainable shear stress and

of residual stress. Note that in some cases the residual stress was calculated by extrapolation from the last recorded part of the stress/strain curve.

Hydrostatic compression tests were also performed and a representative hydrostatic stress/volumetric strain curve is shown in Fig. 6.2. An unloading path is included and it is clear that the damage model assumption of elastic hydrostatic compression behaviour is justified.

Cyclic triaxial compression tests on Norite were carried out by Stavropoulou [105] but the unloading/reloading cycles were performed too early in the loading program so that no reliable conclusions can be drawn. However, the results available suggest shear behaviour similar to that of Fig. 5.2 (i.e. no permanent shear strains) at least up to peak shear stress. We will not try to calibrate the shear cyclic behaviour of the damage model accurately.

Finally, Stavropoulou performed numerous tests in which the peak shear stress was approached following a variety of stress paths. The resulting peak shear stress envelope coincides with that based on the triaxial test results.

6.2 Calibration of Material Parameters

The procedure followed to calibrate the damage model material parameters can be outlined as follows:

(i) The hydrostatic compression test is used to quantify the parameters W and D of equn. (5.16) while $\varepsilon_{vmax(o)}$ is assumed to be zero (no initial volumetric strains);

(ii) the triaxial compression tests provide the information necessary to evaluate the initial shear modulus G_o, the shear damage evolution term $A(e,\sigma_m)$ and the inelastic volumetric behaviour parameters c_1 and c_2. The parameters

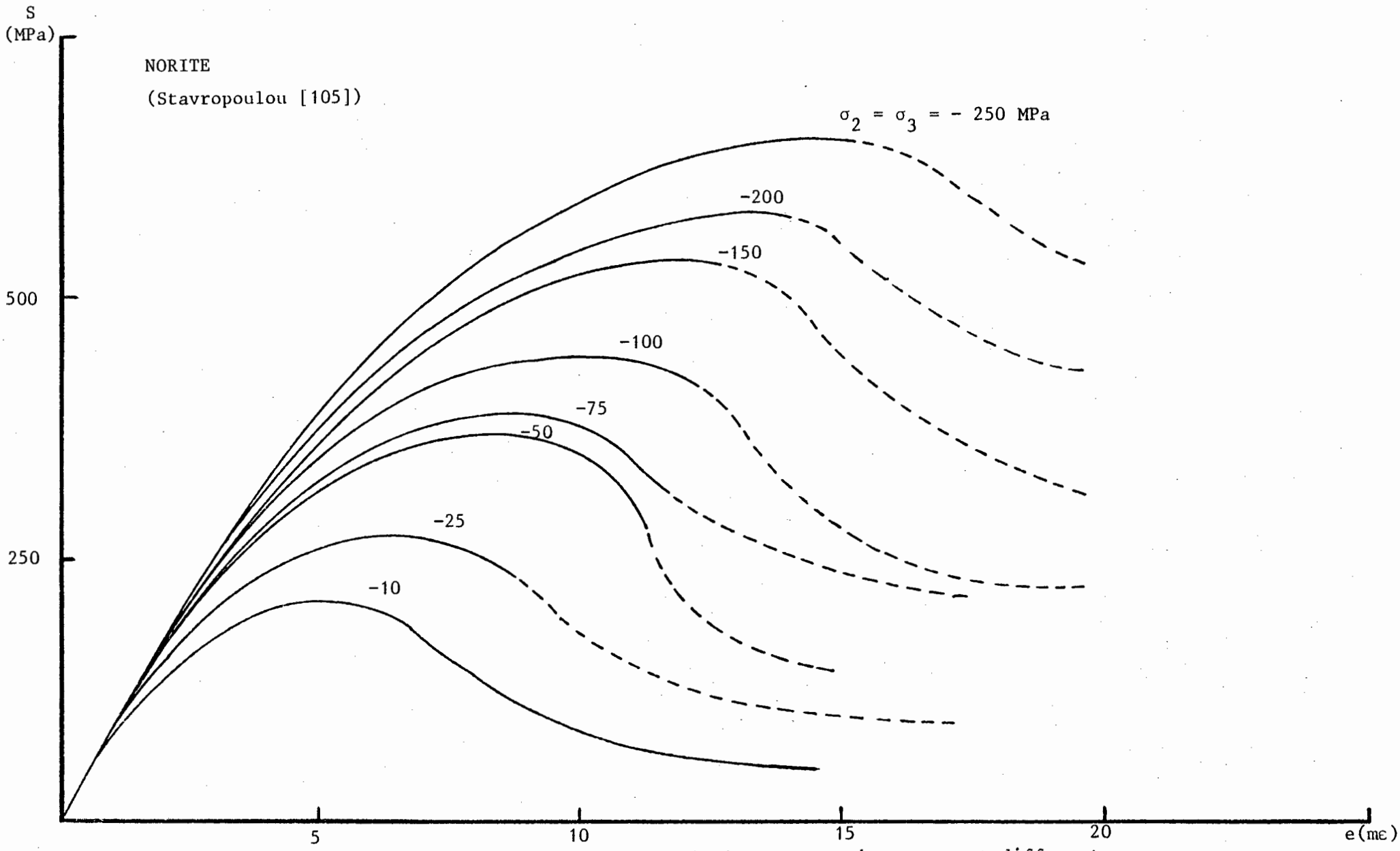

Figure 6.1: Invariant shear stress/strain curves for triaxial compression tests at different confining pressures ($-10 \geqq \sigma_2 = \sigma_3 \geqq -250$ MPa).

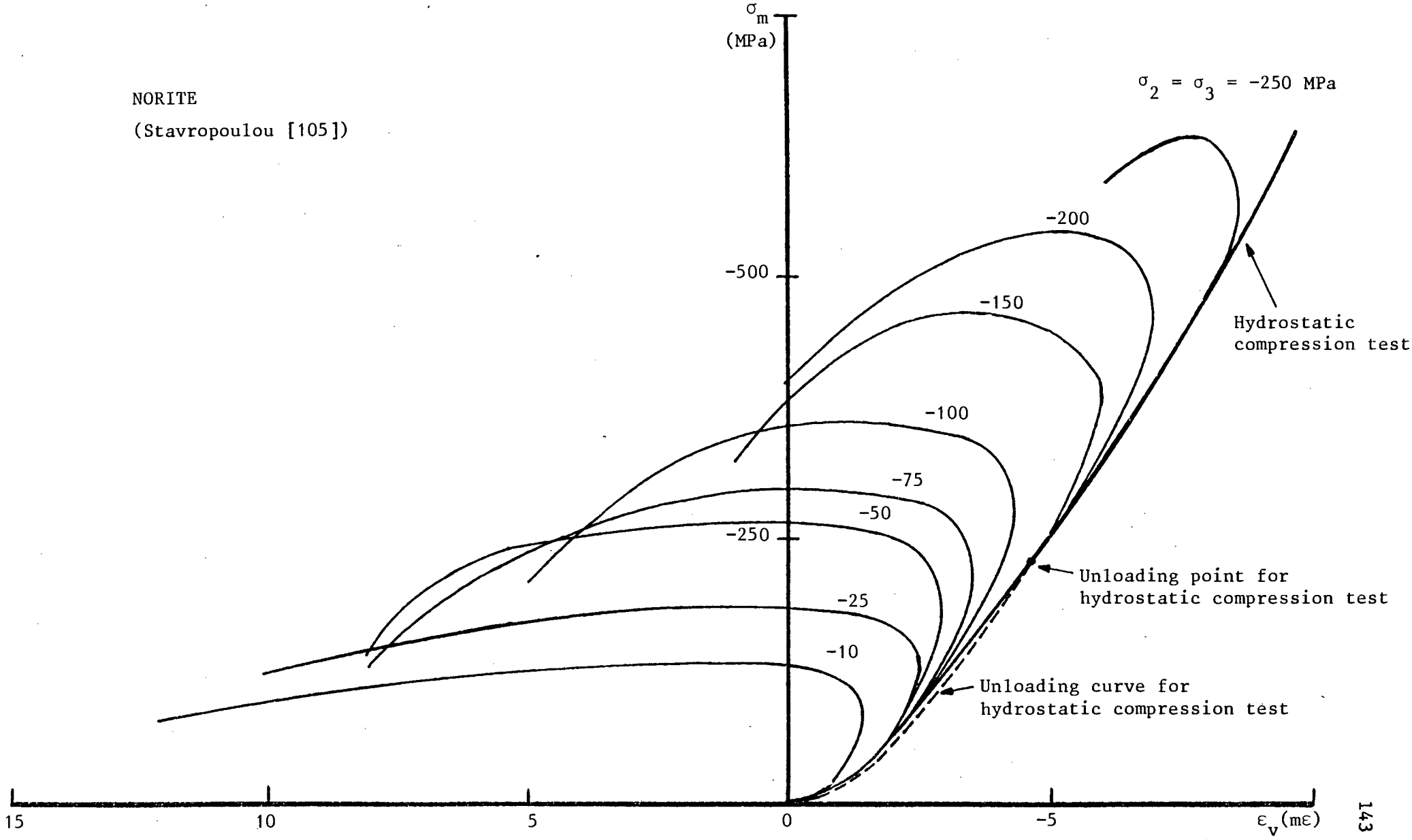

Figure 6.2: Hydrostatic stress/volumetric strain curves for triaxial compression tests at different confining pressures ($-10 \geq \sigma_2 = \sigma_3 \geq -250$ MPa).

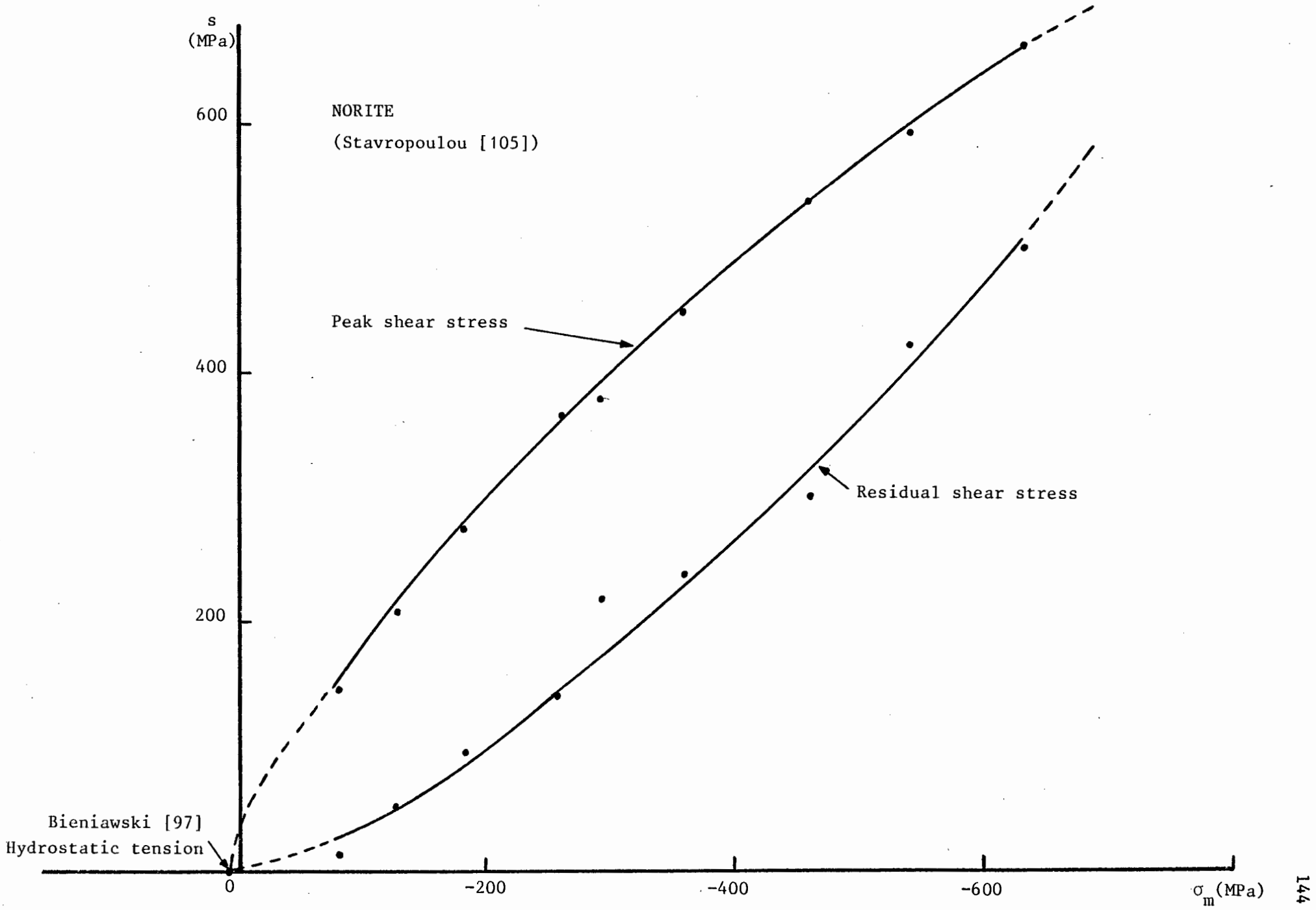

Figure 6.3: Envelopes of maximum attainable shear stress and of residual stress.

c_3 and d_1 cannot be calibrated accurately at present due to limited information obtained from the cyclic triaxial compression tests;

(iii) the limited experimental results on tensile behaviour given by Bieniawski [97] allow us to choose some reasonable values for the hydrostatic tension damage term $B(\varepsilon_v)$.

The hydrostatic compression fit yields $D = .0023\ MPa^{-1}$ for a choice of $W = -.012$. The experimental and mathematical curves are shown in Fig. 6.4.

From the invariant shear stress/strain curves for the triaxial compression tests of Fig. 6.1, we estimate the initial shear modulus as $G_o = 85$ GPa. From the same curves it is possible to draw a curve of accumulated damage (λ) versus shear strain (e) for each test at a constant confining pressure, the result is shown in Fig. 6.5. These curves are not useful for calibration unless they can be drawn for constant hydrostatic stress. To achieve this some degree of interpolation is necessary and the resulting curves are given in Fig. 6.6 (note that the extrapolated experimental values in Fig. 6.5 are not used).

It is now possible to calibrate the shear damage term $\dot{\lambda} = A(e, \sigma_m)\,\dot{e}$. Stavropoulou [105] first suggested

$$\dot{\lambda} = \left(a_1 + a_2\sigma_m + a_3\sigma_m^2 + 2a_4 e\,\sigma_m + 3a_5 e^2\right)\dot{e} \qquad (6.1)$$

where a_1 , a_2 , a_3 , a_4 and a_5 are material parameters. Equn. (6.1) gives plots of accumulated shear damage as illustrated in Fig. 6.7. Although the model resulting from adopting equn. (6.1) predicts reasonably accurate invariant shear stress/strain curves, it is clear that the physical behaviour implied in Figs. 6.5 and 6.6 is not being taken into account. Specifically, the evolution of damage at low shear strains is quite incorrect. More important is the fact that equn. (6.1) yields λ -e curves which have a negative slope after a certain value of shear strain.

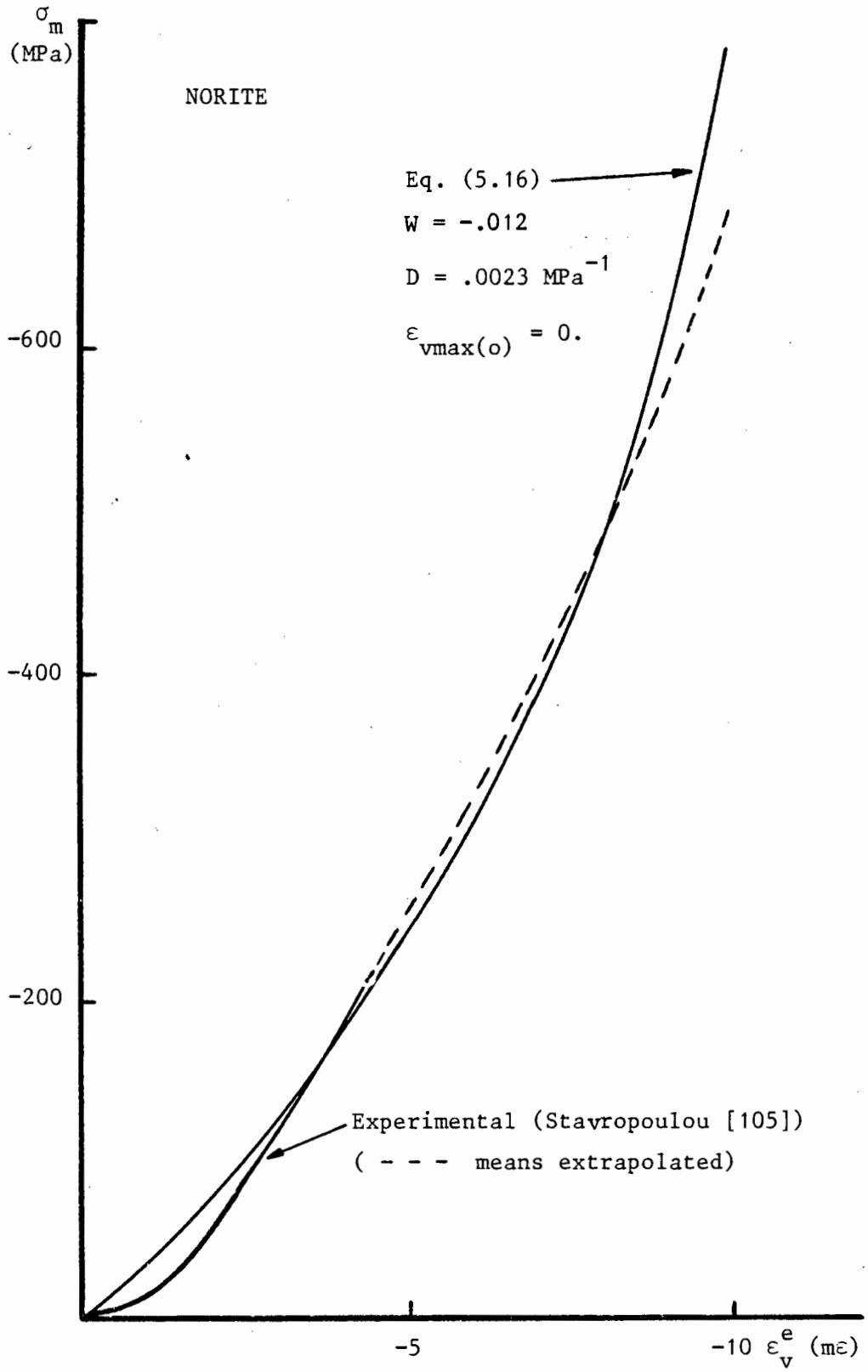

Figure 6.4: Fit of hydrostatic compression test.

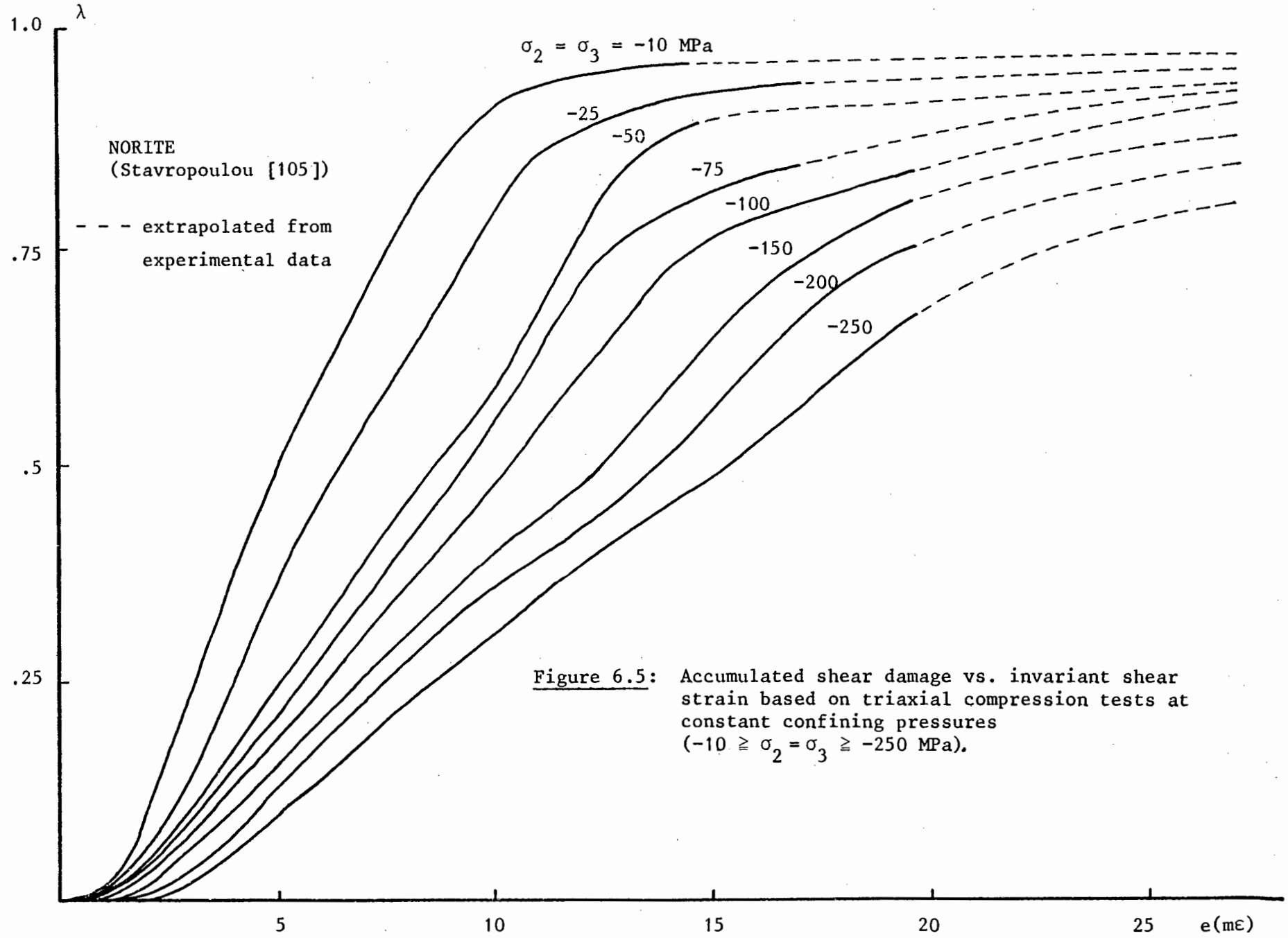

Figure 6.5: Accumulated shear damage vs. invariant shear strain based on triaxial compression tests at constant confining pressures ($-10 \geq \sigma_2 = \sigma_3 \geq -250$ MPa).

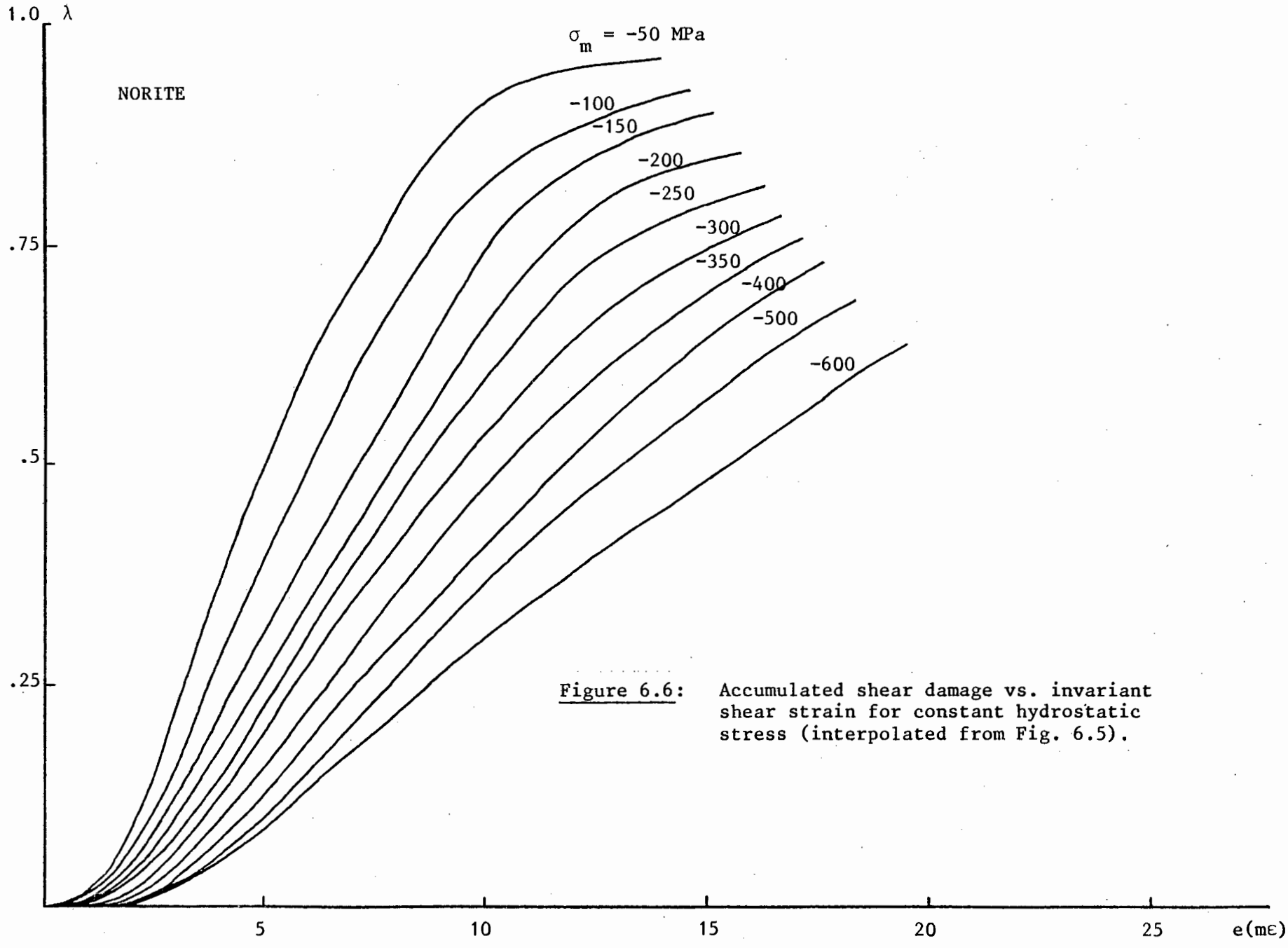

Figure 6.6: Accumulated shear damage vs. invariant shear strain for constant hydrostatic stress (interpolated from Fig. 6.5).

This would mean that damage is reversible and contradicts the basic assumptions of the theory developed.

To improve the representation of shear damage we proposed

$$\dot{\lambda} = \{2(a_1 + a_2 e^{a_3 \sigma_m}) e + 3 (a_4 + a_5 e^{a_6 \sigma_m}) e^2 \} \dot{e} \qquad (6.2)$$

where $a_1 - a_6$ are material parameters to be calibrated. Statistical fits using the data of Fig. 6.6 yield $a_1 = .0002 \times 10^6$, $a_2 = .028613 \times 10^6$, $a_3 = .004448$, $a_4 = -.000045 \times 10^9$, $a_5 = -.002076 \times 10^9$ and $a_6 = .007332$ for MPa stress units.

The resulting accumulated damage curves are shown in Fig. 6.8 where it becomes clear that the damage evolution at low shear strains is now correct but the reversible damage feature is still present. Equn. (6.2) has a further drawback in that it is very inaccurate at high hydrostatic compression values (it predicts too little damage). However, equn. (6.2) can be accepted as a good representation of shear damage behaviour within limited ranges of hydrostatic stress and shear strain. Before resolving the problems associated with extending the range of applicability of equn. (6.2) we proceed to calibrate the remaining material parameters.

The inelastic volumetric behaviour parameters c_1 and c_2 (equn. (5.19)) can be evaluated from the shear stress/strain curves of Fig. 6.1 and the hydrostatic stress/volumetric strain curves of Fig. 6.2. The fit yields $c_1 = 13.6875 \times 10^{-3}$ and $c_2 = -.264$. The parameter c_3 is assumed to be equal to $-c_{2/2}$, i.e. $c_3 = .132$.

Finally, based on Bieniawski's data [97] we define the hydrostatic tension damage as

$$\dot{\lambda} = (b_2 \varepsilon_v + b_3 \varepsilon_v^2) \dot{\varepsilon}_v \qquad (6.3)$$

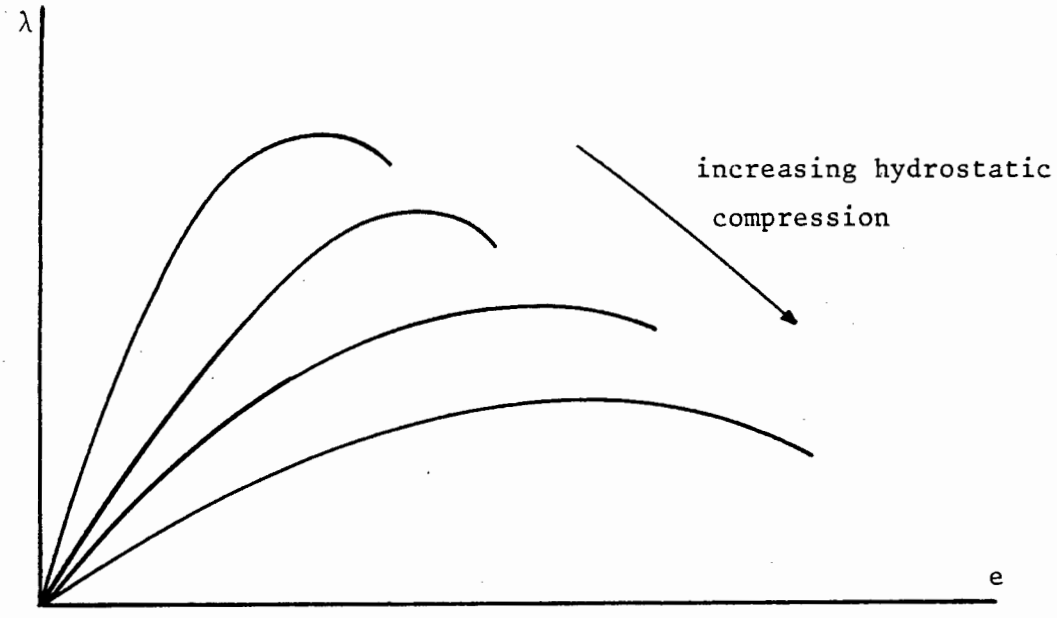

Figure 6.7: Form of accumulated shear damage curves according to equn. (6.1) - Stavropoulou [105].

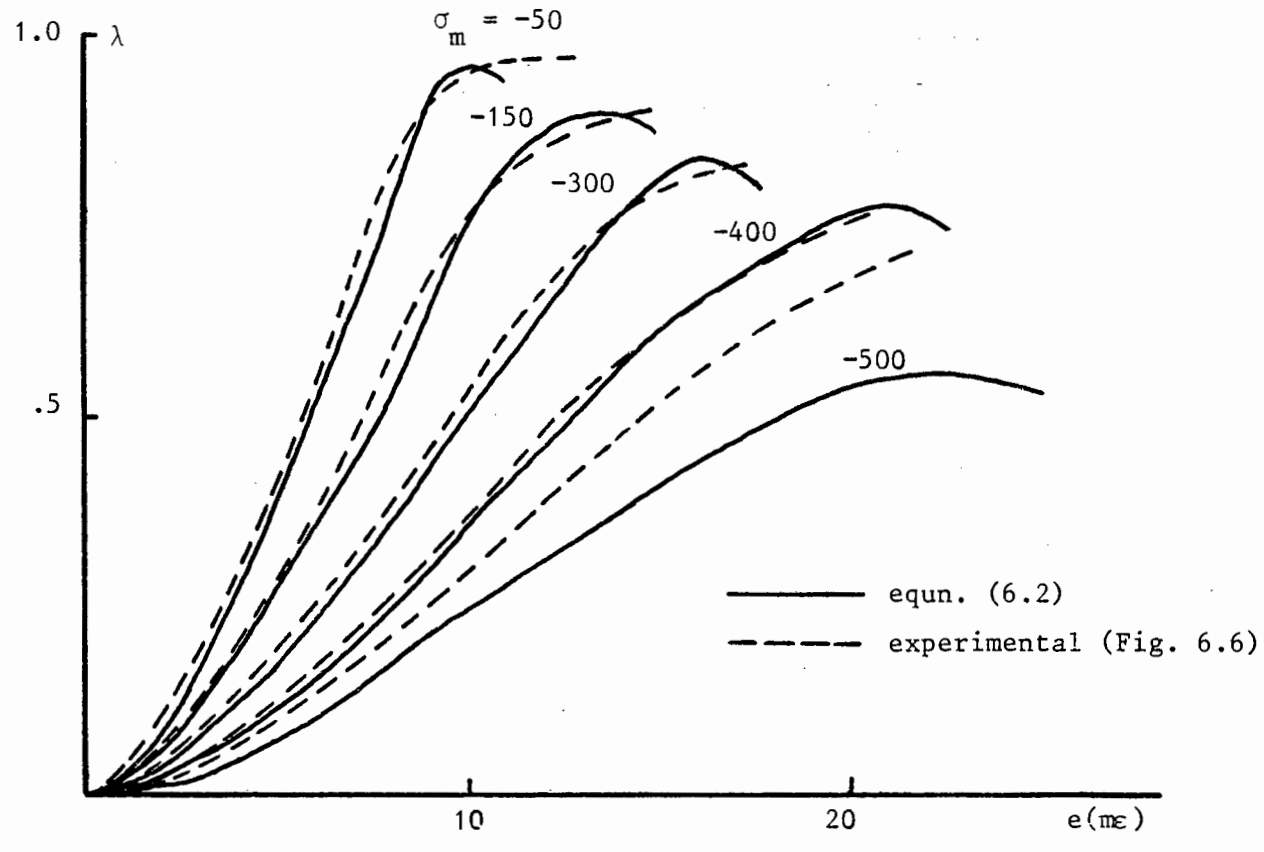

Figure 6.8: Accumulated shear damage curves according to equn. (6.2) - present work.

where $b_2 = 30. \times 10^6$ and $b_3 = -67. \times 10^9$ are material parameters. The resulting hydrostatic tension/volume strain curve is shown in Fig. 6.9. The damage model based on equns. (6.2) and (6.3) thus defines damage evolution as

$$\dot{\lambda} = \{2(a_1 + a_2 e^{a_3 \sigma_m}) e + 3 (a_4 + a_5 e^{a_6 \sigma_m}) e^2 \} \dot{e} + (b_2 \varepsilon_v + b_3 \varepsilon_v^2) \dot{\varepsilon}_v \qquad (6.4)$$

and requires the following 16 material parameters (assuming MPa stress units):

G_o	= 85000.	a_5	= $-.002076 \times 10^9$
W	= -.012	a_6	= .007332
D	= .0023	b_2	= $30. \times 10^6$
$\varepsilon_{vmax(o)}$	= 0.	b_3	= $-67. \times 10^9$
a_1	= $.0002 \times 10^6$	c_1	= 13.6875×10^{-3}
a_2	= $.028613 \times 10^6$	c_2	= -.264
a_3	= .004448	c_3	= .132
a_4	= $-.000045 \times 10^9$	d_1	= 0.

The invariant shear stress/strain and hydrostatic stress/volumetric strain predictions of this model are compared to the experimental results in Figs. 6.10 and 6.11 . Note that results are not shown for triaxial tests at confining pressures exceeding -100 MPa where the model is quite inaccurate.

To resolve the drawbacks experienced with the model using the damage evolution law of equn. (6.4), it was decided to replace equn. (6.4) with the actual experimental data of accumulated damage. The rate of damage is then calculated directly from digitized experimental information rather than through a mathematical expression. The experimental damage curves were extrapolated further along the invariant shear strain axis to broaden the range of strains over which the model will provide answers.

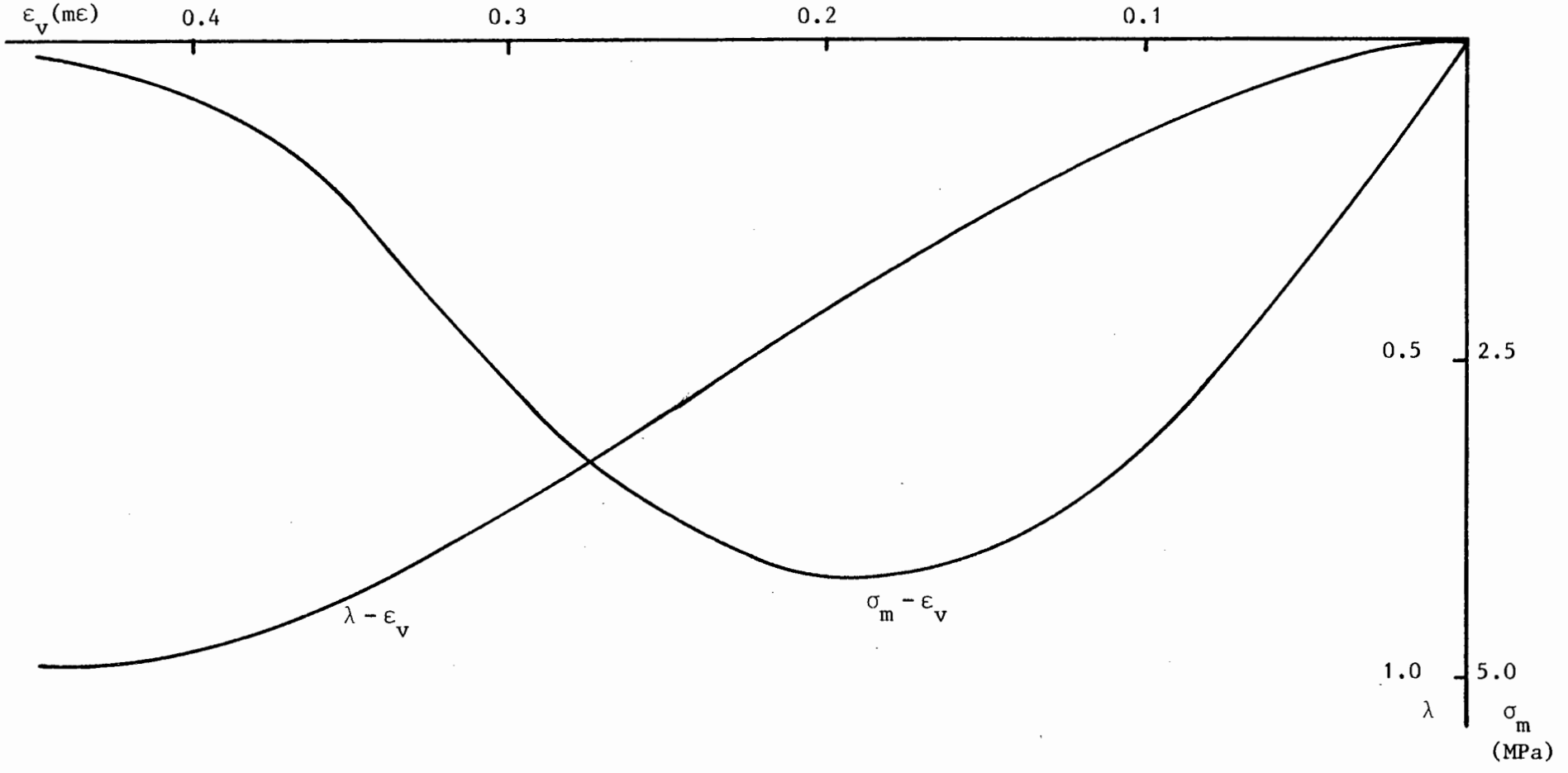

Figure 6.9: Hydrostatic tension/volumetric strain behaviour predicted by equn. (6.3).

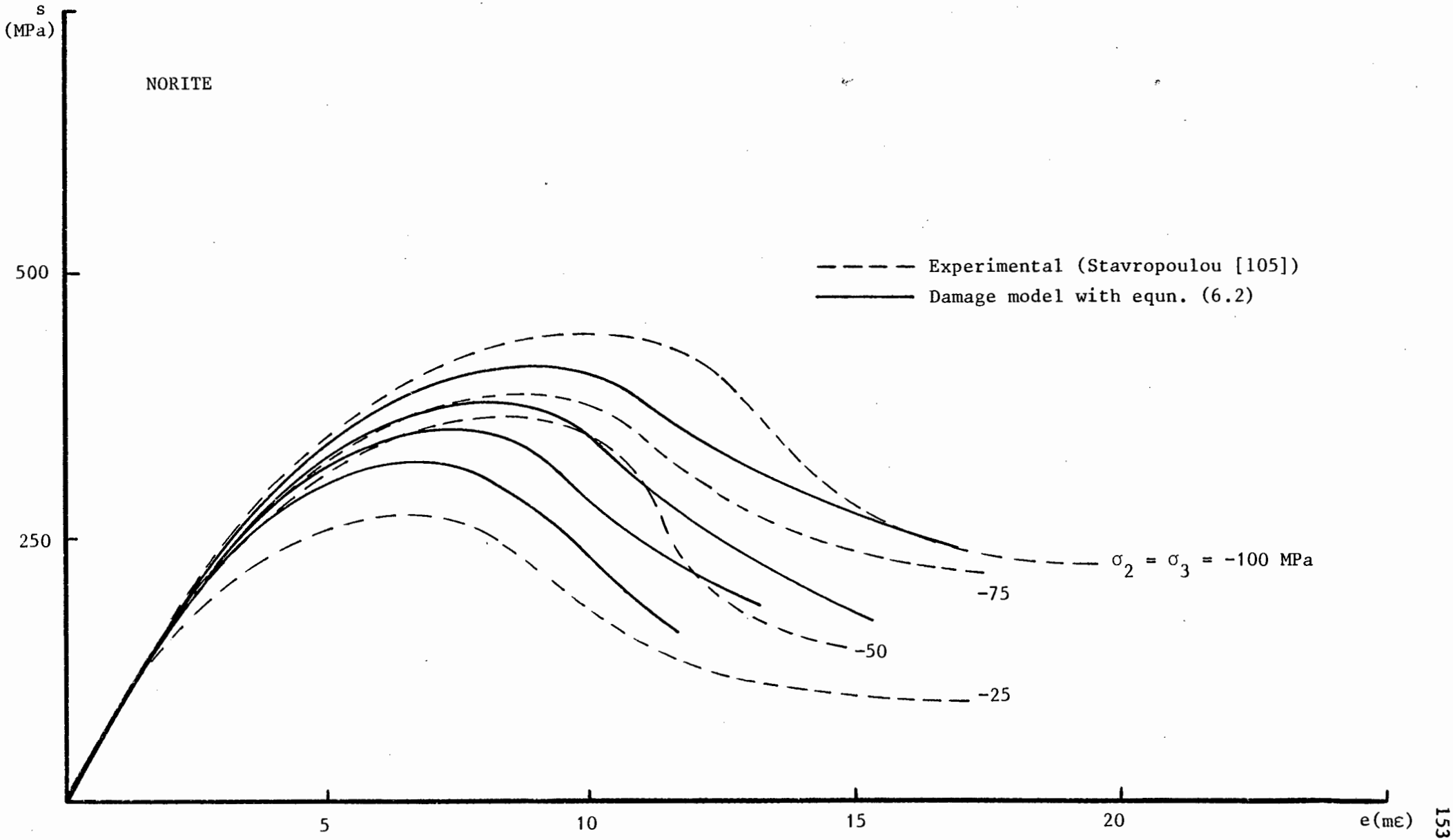

Figure 6.10: Triaxial compression test fits with shear damage evolution equn. (6.2).

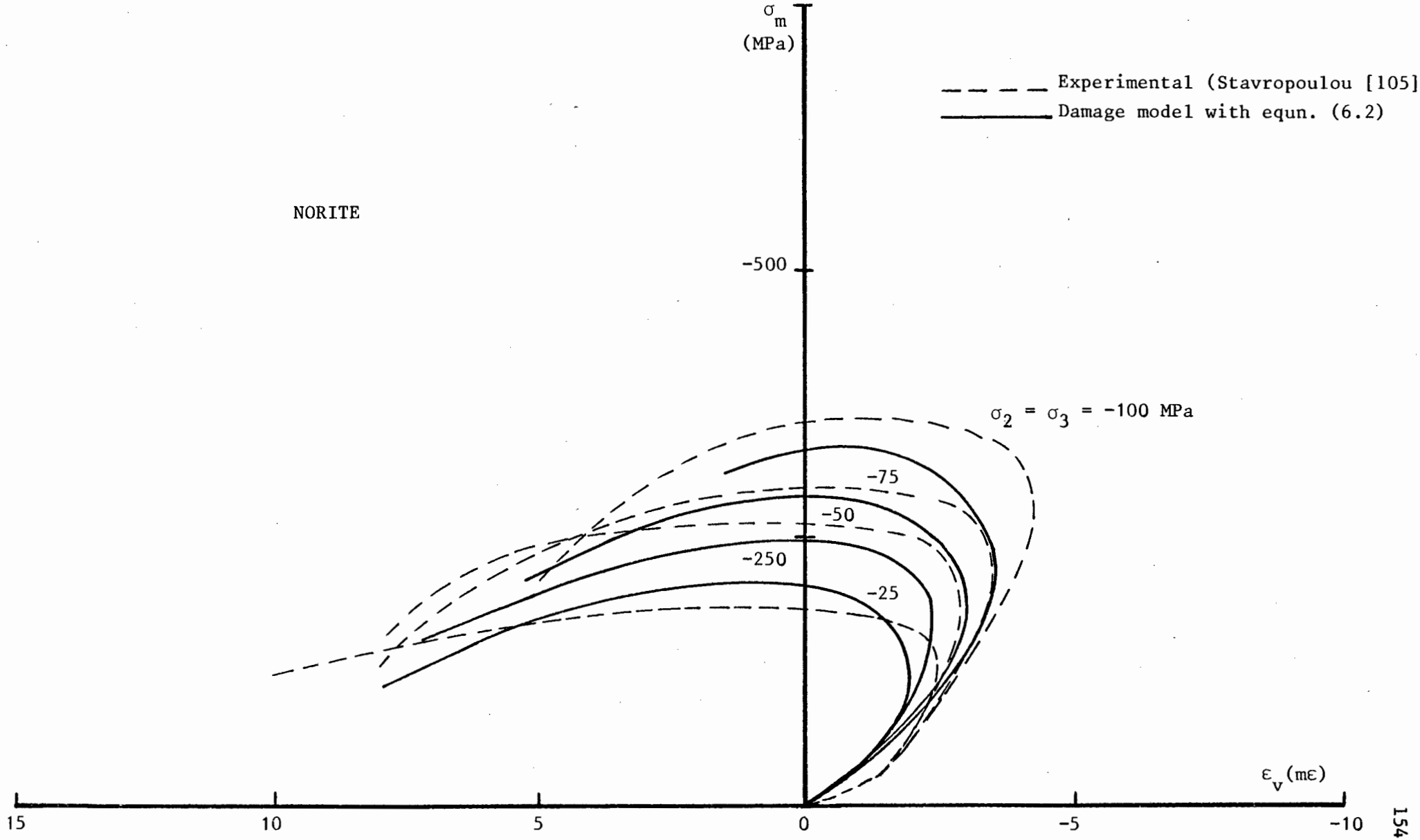

Figure 6.11: Triaxial compression fits with shear damage evolution equn. (6.2).

For the same purpose the range of hydrostatic stresses was also broadened as shown in Fig. 6.12. It must be stressed that these extensions are not based on available experimental data but they are nevertheless realistic in terms of general experimental evidence gathered for these kinds of mateials. The aim is to have a model capable of reasonable predictions over a broad range of conditions. A comparison of the results of the model based on damage as defined in Fig. 6.12 with experiment is shown in Figs. 6.13, 6.14 and 6.15 where good agreement is evident over the complete experimental range.

6.3 Importance and Sensitivity of Damage Parameters

The concept of a damage evolution law introduced in the present model aims to represent physical phenomena which have a fundamental influence in the way geomaterials behave. It would thus not be acceptable if different mathematical forms of damage evolution predicted significantly different behaviour. The fact that this is not the case is confirmed by the essentially similar behaviour predicted by the several forms of shear damage we experimented with. The differences are of detail and it is not the aim at this stage to produce a constitutive model which captures every single detail. We are more interested in investigating what possible forms of damage evolution are acceptable. The process of identification of material parameters has to continue over a few cycles in which the experience gained in using the model for real predictions is fed back to the development of the model.

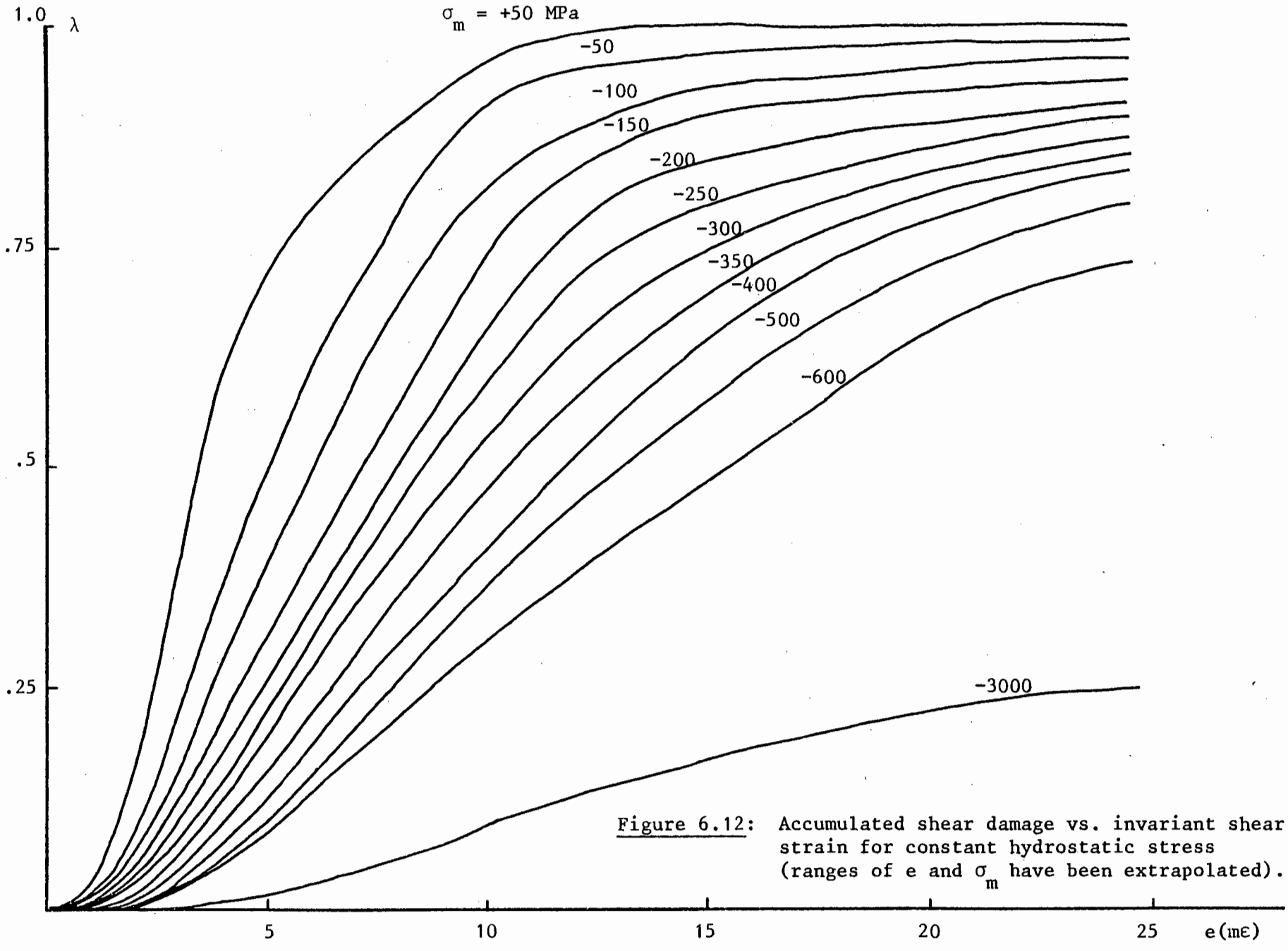

Figure 6.12: Accumulated shear damage vs. invariant shear strain for constant hydrostatic stress (ranges of e and σ_m have been extrapolated).

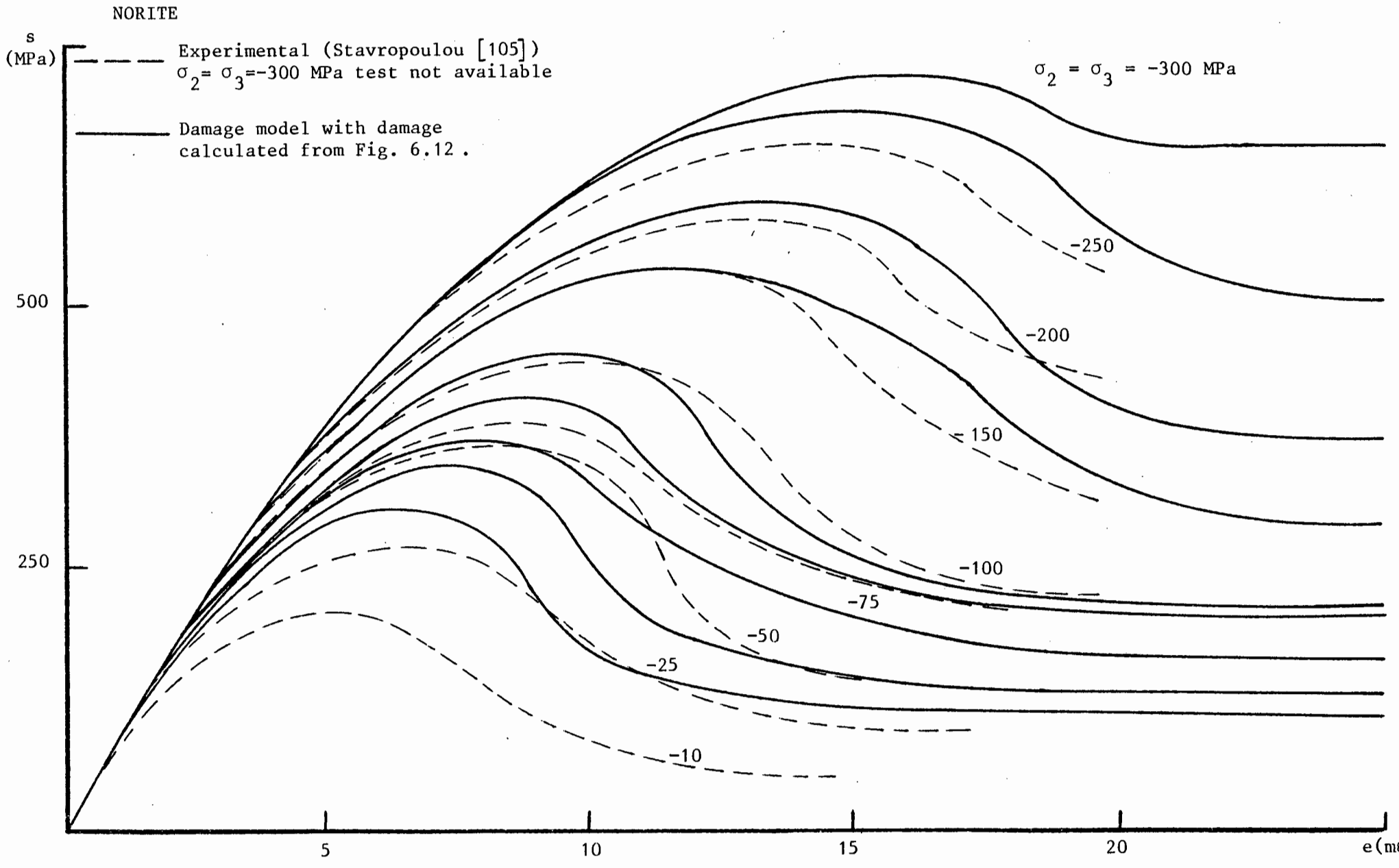

Figure 6.13: Triaxial compression test fits with shear damage calculated from Fig. 6.12 .

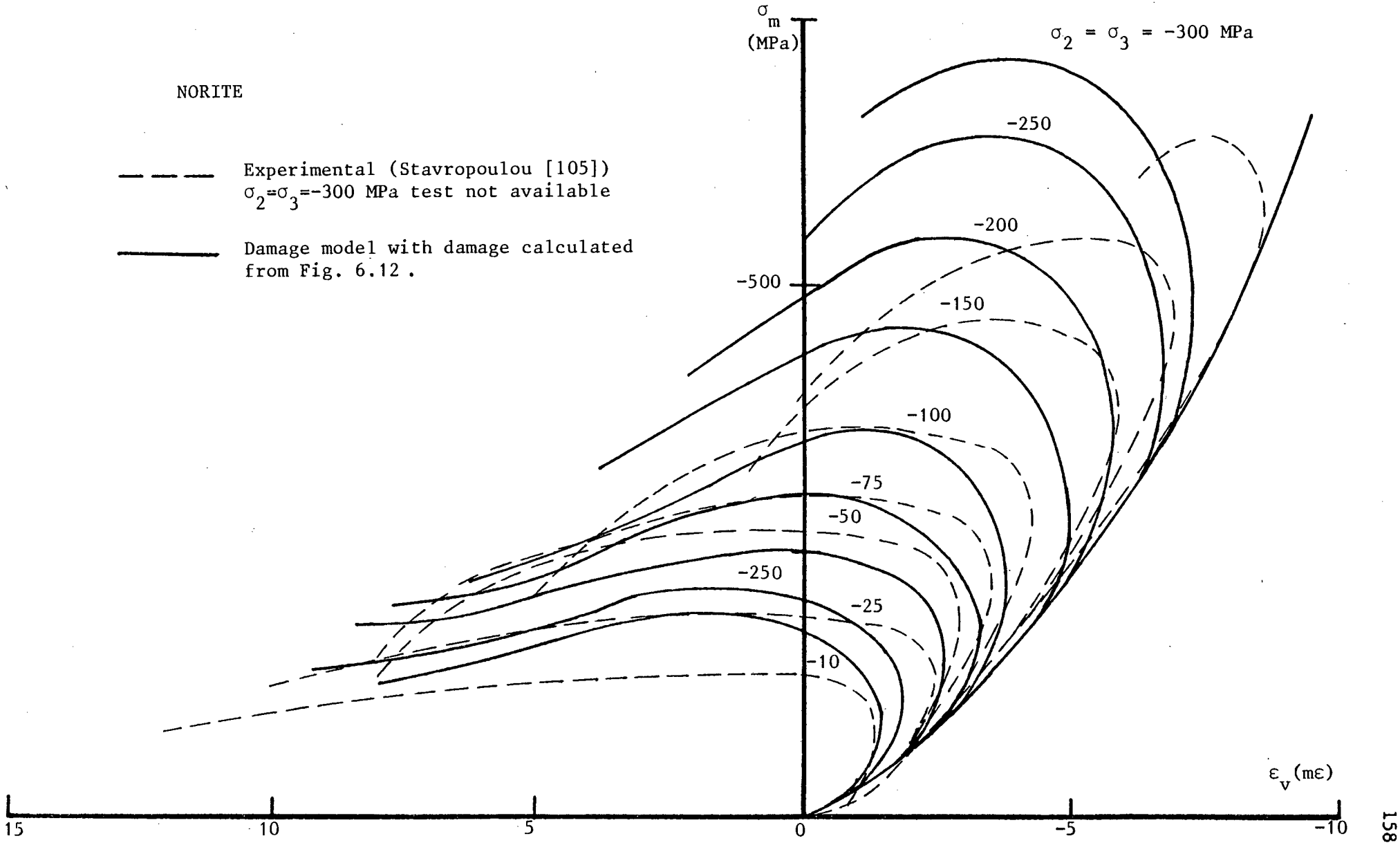

Figure 6.14: Triaxial compression test fits with shear damage calculated from Fig. 6.12 .

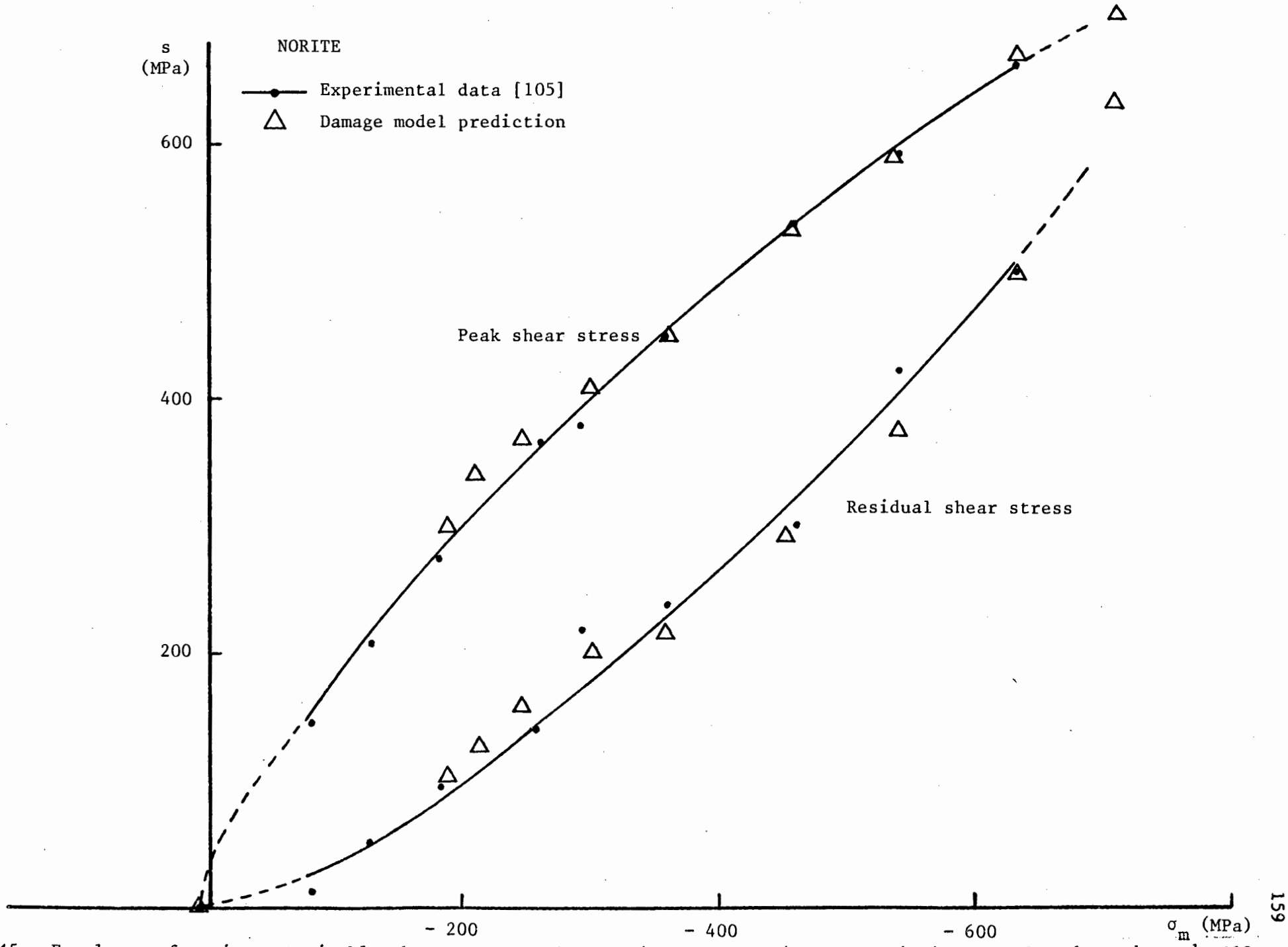

Figure 6.15: Envelopes of maximum attainable shear stress and of residual stress (model predictions are based on shear damage calculated according to Fig. 6.12).

CHAPTER 7

IMPLEMENTATION OF THE DAMAGE MODEL AND APPLICATIONS

In this chapter we deal with the implementation of the damage model in the finite element code NOSTRUM [78-82] and applications to the analysis of standard configurations of relevance as well as the analysis of underground excavation problems.

7.1 Finite Element Implementation Using an Incremental Tangent Approach

A short description of the features of NOSTRUM relevant to the present work was given in Chapter 4 and applies equally to the implementation of the damage model.

An incremental tangent approach with iterative improvement similar to the one described in the case of the plasticity cap model is used for the damage model with the limitation that only a full Newton-Raphson scheme can be employed during each increment. This limitation is not a result of possible difficulties with other schemes but rather a choice that was made. It has also been chosen to estimate the stiffness matrices accurately (i.e. non-symmetric matrices) and thus the equilibrium equations are always solved using the non-symmetric frontal solver.

7.2 Integration of the Constitutive Equations

Again, the scheme used for the integration of the damage constitutive equations is similar to that employed in the case of the plasticity cap model and given by equn. (4.9). Subincrementation of the inelastic strain increment is adopted and a fixed number of 5 subincrements has been chosen. Note that the damage model includes three modes of inelastic

behaviour (cases 2, 4 and 5) and two modes of nonlinear elastic behaviour (cases 1 and 3). However, for consistency of approach, and since the damage model is implemented in incremental form all modes of behaviour are treated as if they were inelastic and the same integration procedure employing subincrementation is used throughout.

The decisions regarding the activation of the different modes of behaviour are important and are now described. Which mode of behaviour is active depends on the total hydrostatic stress (σ_m), the volumetric strain rate ($\dot{\varepsilon}_v$) and the rate of damage ($\dot{\lambda}$) which in turn is dependent on the invariant strain rates and the total stress and strain invariants. The sequence of constraint checks that have to be performed in order to decide which mode of behaviour is active is shown diagrammatically in Fig. 6.1. The first check on σ_m decides whether the material point is in tension or compression. If in compression, the damage rate is given by the expression $\dot{\lambda} = A\dot{e}$ and one has to check if $\dot{\lambda}$ is zero or positive according to equns. (5.14). For $\dot{\lambda} = 0$ we have no further damage (unloading) and for $\dot{\lambda} = A\dot{e}$ we have loading with the shear damage mechanism active.

If in tension, we check the sign of the volumetric strain rate ($\dot{\varepsilon}_v$). If this is negative (i.e. compacting), the damage rate expression is $\dot{\lambda} = A\dot{e}$ and the $\dot{\lambda}$ checks of the compression case apply. If, on the other hand, $\dot{\varepsilon}_v$ is positive (i.e. dilating) the relevant damage rate expression is $\dot{\lambda} = A\dot{e} + B\dot{\varepsilon}_v$. Further damage (loading) will occur if $A\dot{e} + B\dot{\varepsilon}_v > 0$ and we have unloading otherwise. In the loading case, it is possible to have "additive" damage ($A\dot{e} > 0$, $B\dot{\varepsilon}_v > 0$) where both shear and hydrostatic tension damage mechanisms cause further damage or "weighted" damage ($A\dot{e} < 0$, $B\dot{\varepsilon}_v > 0$, $A\dot{e} + B\dot{\varepsilon}_v > 0$) where the shear damage mechanism cancels out the hydrostatic tension damage mechanism to a certain extent. In fact, the boundary line between loading and unloading is $A\dot{e} = -B\dot{\varepsilon}_v$ as shown in Fig. 5.10. This figure also shows the five possible modes of behaviour and their relation to total stress space and strain rate space.

Finally, it must be emphasized that the checks on $\dot{\varepsilon}_v$ and $\dot{\lambda}$ illustrated in Fig. 7.1 are performed from the last previously equilibrated state, thus

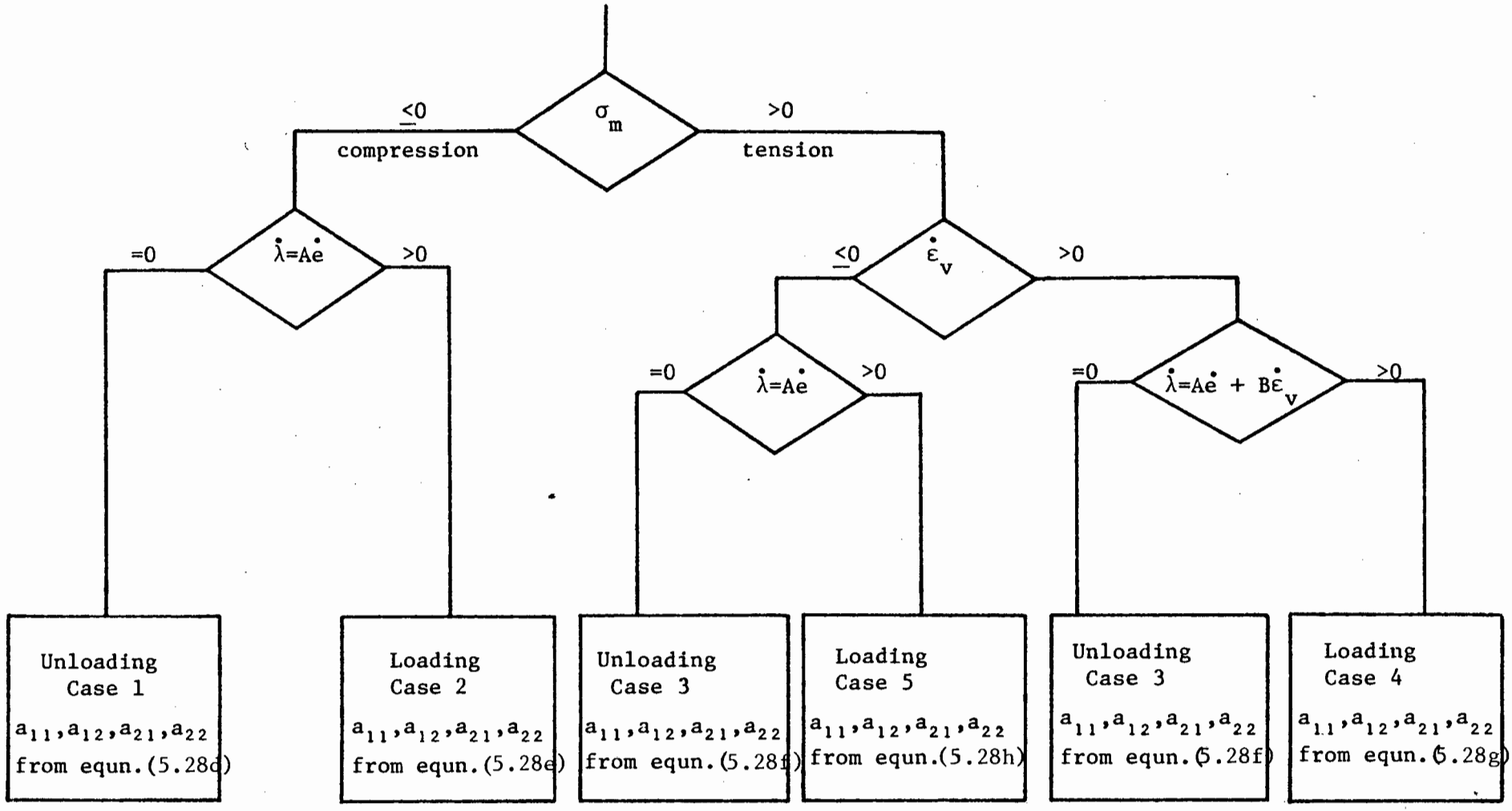

Figure 7.1: Constraint checks to establish mode of behaviour of damage constitutive laws.

contributing to the numerical stability of the model.

7.3 Analysis of Excavation Problems

Techniques for the simulation of the construction and excavation processes have been proposed as early as 1963 by Goodman and Brown [122]. The purpose of the analysis of the excavation process is to determine the change of state (displacements, strains and stresses) resulting from the removal of a stressed region of the domain under consideration. Before excavation certain stresses act on the surfaces which are to form the boundary of the excavated region. These stresses vanish upon the completion of the excavation provided no internal support or pressure is immediately applied.

Within the framework of finite element analysis, many investigators have simulated the process of excavation by calculating the forces acting on the excavation surface due to the natural stress field and applying the opposite of those forces to the finite element model. However, the applicability of such an analysis must be limited to elastic behaviour where path independence is assumed.

A more realistic approach, used in the following sections, is to impose an initial stress field on the model corresponding to the geological state together with a set of equilibrating forces on the excavation surface. These forces are then gradually reduced to zero to simulate the excavation process which when completed produces a stress free excavation surface. This kind of simulation can be refined by modelling the excavation as a series of events where only parts of the excavation region are removed during each event. The previous process of relaxation of the excavation surface forces is then carried out for each event in sequence [123], thus representing a more gradual change in geometry of the excavation. This can be performed with a technique commonly known as 'death' of elements [87] but is not used in the present work. The size and shape of elements used in the excavation process has also been shown to have an influence in the results [124] but again such an investigation

is not the aim of the following sections.

The in situ stresses representing the starting point of the excavation simulation can be calculated as described hereafter. The vertical in situ stress is given as

$$\sigma_{y(o)} = \rho g h \qquad (7.1)$$

where ρ is the mass density of the material
g is the gravity acceleration constant
and h is the depth of the excavation;
the horizontal stresses (for plane strain assumptions) are

$$\sigma_{x(o)} = \sigma_{z(o)} = K_1 \sigma_{y(o)} \qquad (7.2)$$

where K_1 is a known or assumed coefficient of lateral earth pressure; and the shear stress $\tau_{xy(o)}$ is assumed to be zero.

7.3.1 Square Tunnel

The deformational behaviour of the rock mass in the vicinity of a square tunnel during the process of excavation is investigated. A 3m by 3m tunnel, suggested by Peirce [125] as an example of a typical mining excavation, is considered. The problem is modelled in plane strain and two lines of symmetry (one horizontal and one vertical) are used so that only a quarter of the configuration is modelled. The mesh used, Fig. 7.2, is made up of 60 eight noded Serendipity quadrilaterals and 12 five noded compatible infinite elements giving a total of 228 nodes. The mesh arrangement is due to Beer [126] who optimized it for elastic analysis. In the present analyses 3x3 Gauss integration is employed in all elements.

Assuming the tunnel is part of a deep gold mining excavation, Peirce[125] considered it to be ten kilometres below the surface. For a material with a mass density of approximately 2600 kg/m^3, the vertical in situ stress is calculated as

$$\sigma_{y(o)} = 2600 \text{ kg/m}^3 \times 10 \text{ m/s}^2 \times 10000 \text{ m} = 260 \text{ MPa} \qquad (7.3a)$$

where the gravity acceleration is taken as 10 m/s^2. To complete the description of the stress state representing the starting point of the excavation, we calculate the horizontal stresses, for a coefficient of lateral earth pressure $K_1 = .5$, as

$$\sigma_{x(o)} = \sigma_{z(o)} = 130 \text{ MPa} \qquad (7.3b)$$

while the shear stress is assumed to be zero. The loading to simulate the excavation process then simply amounts to the gradual release of the above stresses along the excavation surface. This is achieved by applying pressure loads gradually increasing to 260 MPa on the horizontal faces of the tunnel and 130 MPa on the vertical faces as shown in Fig. 7.2.

In the coupled finite/infinite element mesh the infinite elements are used to model the far field and are assumed to behave elastically. The finite elements represent the area in the vicinity of the excavation and the damage constitutive model is employed. The damage model material parameters established in Chapter 6 for Bushveld Norite are used (MPa units):

$$\begin{aligned} G_o &= 85000. & c_1 &= 13.6875 \times 10^{-3} \\ W &= -.012 & c_2 &= -.264 \\ D &= .0023 & c_3 &= .132 \\ \varepsilon_{vmax(o)} &= 0 & d_1 &= 0. \end{aligned} \qquad (7.4)$$

and damage evolution is defined according to Fig. 6.12.

However, one question remains and it concerns the extent of damage that would have been caused by the in situ stress state (this is important since the model is history dependent). To resolve this question, a single material point was subjected to a stress state corresponding to the in situ stresses and it was found that the resulting amount of internal damage is negligible (in the order of one percent). For this reason it

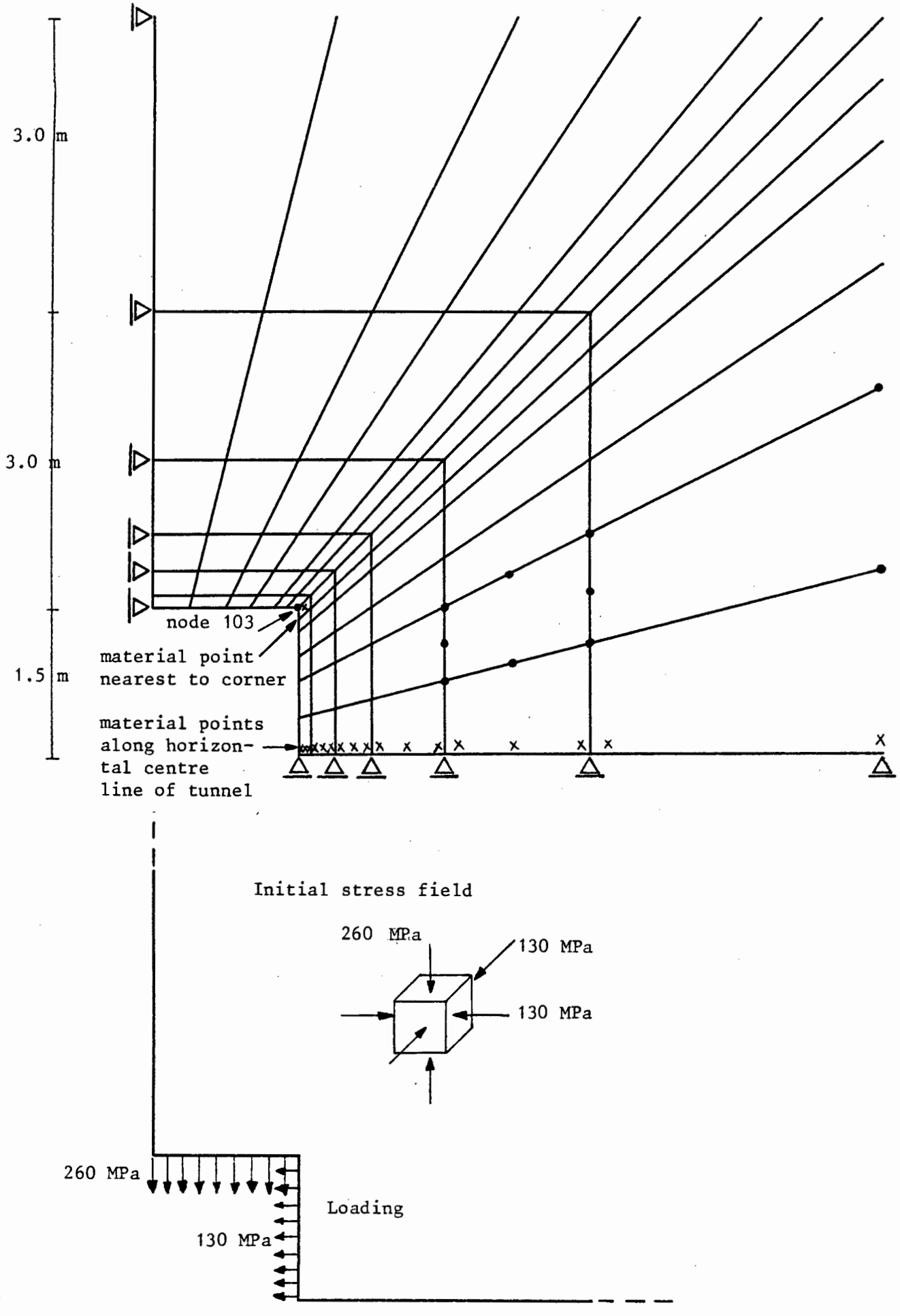

Figure 7.2: Square tunnel finite element model.

was chosen to consider the rock material as totally undamaged at the start of the excavation process. Nevertheless the material is initially under a non-zero stress state and this must be taken into account in calculating the elastic properties (Young's modulus and Poisson's ratio) for the infinite elements. The elastic shear modulus of Norite and its stress dependent bulk modulus calculated from Fig. 6.4 yield the following infinite element elastic properties:

$$E = 171600 \text{ MPa} \quad \text{and} \quad \nu = .09 \quad . \tag{7.5}$$

For comparison purposes, the tunnel excavation problem is also modelled with the plasticity cap model discussed earlier. For this, the cap model material parameters of Bushveld Norite have to be established. The elastic parameters used are those given in equn. (7.5). The cap yield surface hardening parameters are taken from Fig. 6.4 as $W = -.012$ and $D = .0023 \text{ MPa}^{-1}$. Here it should be noted that Fig. 6.4 represents the elastic volumetric behaviour in the damage model (i.e. σ_m vs. ε_v^e) and due to lack of any better information, the same W and D constants are used in the cap model where they refer to the inelastic volumetric behaviour (i.e. σ_m vs. ε_v^p). This will no doubt mean that the volumetric behaviour exhibited by the damage and cap models is expected to be different and we shall discuss it later. The cap is assumed to be of a plane shape ($R = 0.$) and its initial position is taken to coincide with the hydrostatic component of the in situ stress field ($\sigma_m^\circ = -173.33$ MPa). To establish the Drucker-Prager failure surface in the cap model, we fit straight lines through the Norite shear stress envelopes given in Fig. 6.3. Fig. 7.3 shows a straight line fit through the maximum attainable shear stress envelope (the cap model with this failure surface will be referred to as 'peak failure cap'), a fit of the residual shear stress envelope ('residual failure cap'), and an average of the previous two which will be called 'average failure cap'. In the cap model analyses that follow only the peak failure cap and the average failure cap models are investigated. The material properties for these two approximations can then be summarised as:

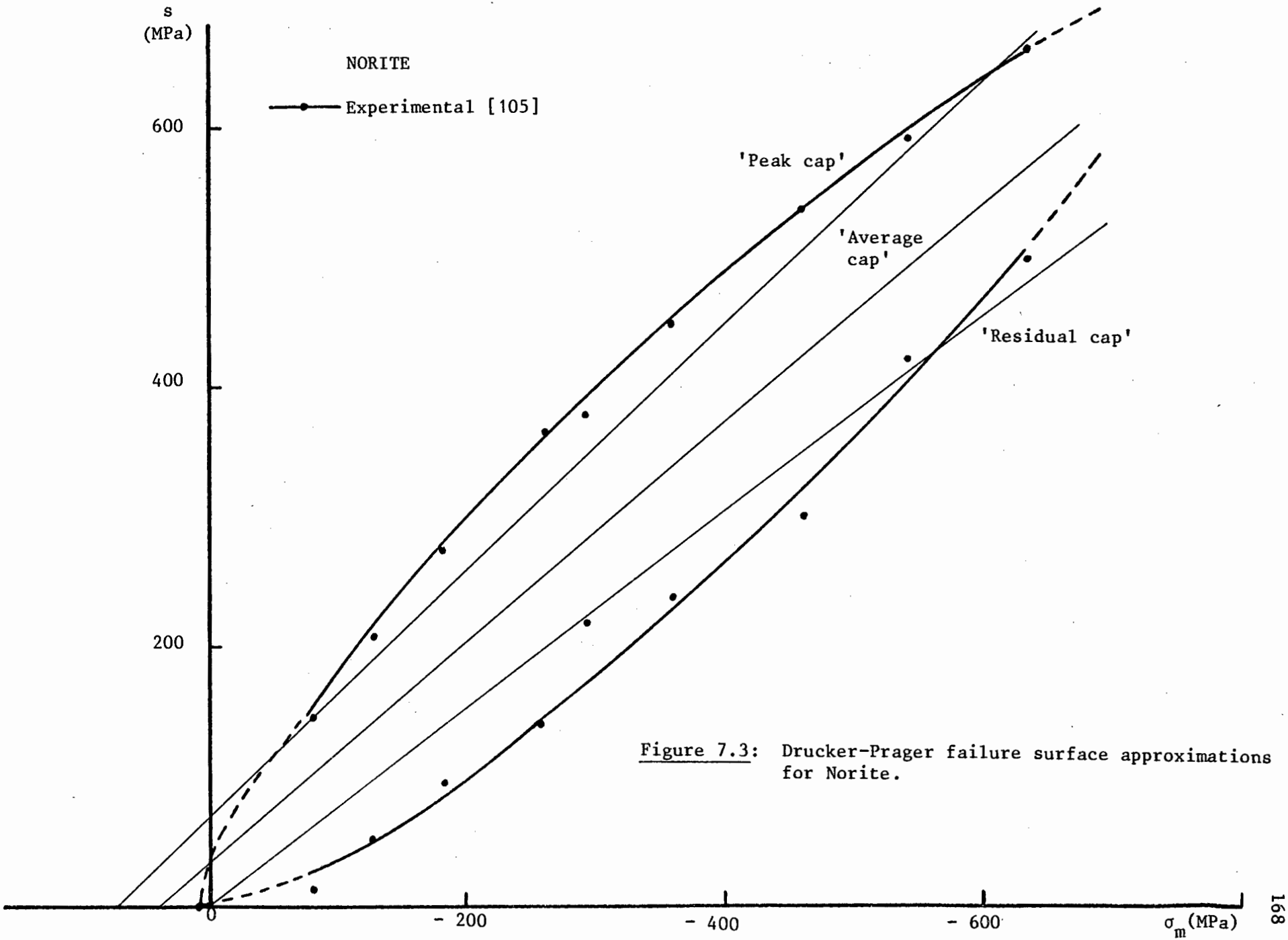

Figure 7.3: Drucker-Prager failure surface approximations for Norite.

Peak failure cap:	Average failure cap:
$E = 171600$ MPa	$E = 171600$ MPa
$\nu = .09$	$\nu = .09$
$W = -.012$	$W = -.012$
$D = .0023$ MPa^{-1}	$D = .0023$ MPa^{-1}
$\sigma_m^\circ = -173.333$ MPa	$\sigma_m^\circ = -173.333$ MPa
$R = 0.$	$R = 0.$
$\alpha = .31372549$	$\alpha = .28413145$
$k = 75.2941$ MPa	$k = 38.5634$ MPa
$T = 240.$ MPa	$T = 135.72$ MPa .

(7.6)

Some of the results obtained for the square tunnel excavation are discussed hereafter. The overall deformation response due to the excavation loading is very close to linear as shown in Fig. 7.4 where applied vertical pressure versus vertical defelection (at node 103) plots are shown. This is expected since most of the deformation is concentrated in a small region around the corner of the excavation. The displacements obtained with the damage model are larger than those obtained with the peak cap model, but not as large as the average cap model displacements. Fig. 7.5 shows displacements of the tunnel at the end of the excavation process calculated using the damage model, while Fig. 7.6 shows the corresponding principal stress vector distribution. Note that in Fig.7.5(b) velocity simply means the change in displacement during the last step of the analysis. A plot of contours of the degree of damage sustained by the material during excavation is given in Fig. 7.7 where the localized natue of the deformation is apparent. The zones of stress state at the end of the excavation for the two cap model analyses are depicted in Figs. 7.8 and 7.9 where it is clear that the predominant inelastic behaviour consists of cap yielding. In Fig. 7.10 we present plots of vertical stress distribution along the horizontal centre line of the tunnel. It can be seen that the damage model predicts higher stresses than elastic assumptions do, while the cap models give vertical streses which are lower than the elastic ones. This can be explained by the stiffening volumetric elastic behaviour in the damage model whereas in the cap model the elastic volumetric behaviour is linear and only the inelastic volumetric behaviour is of a stiffening nature.

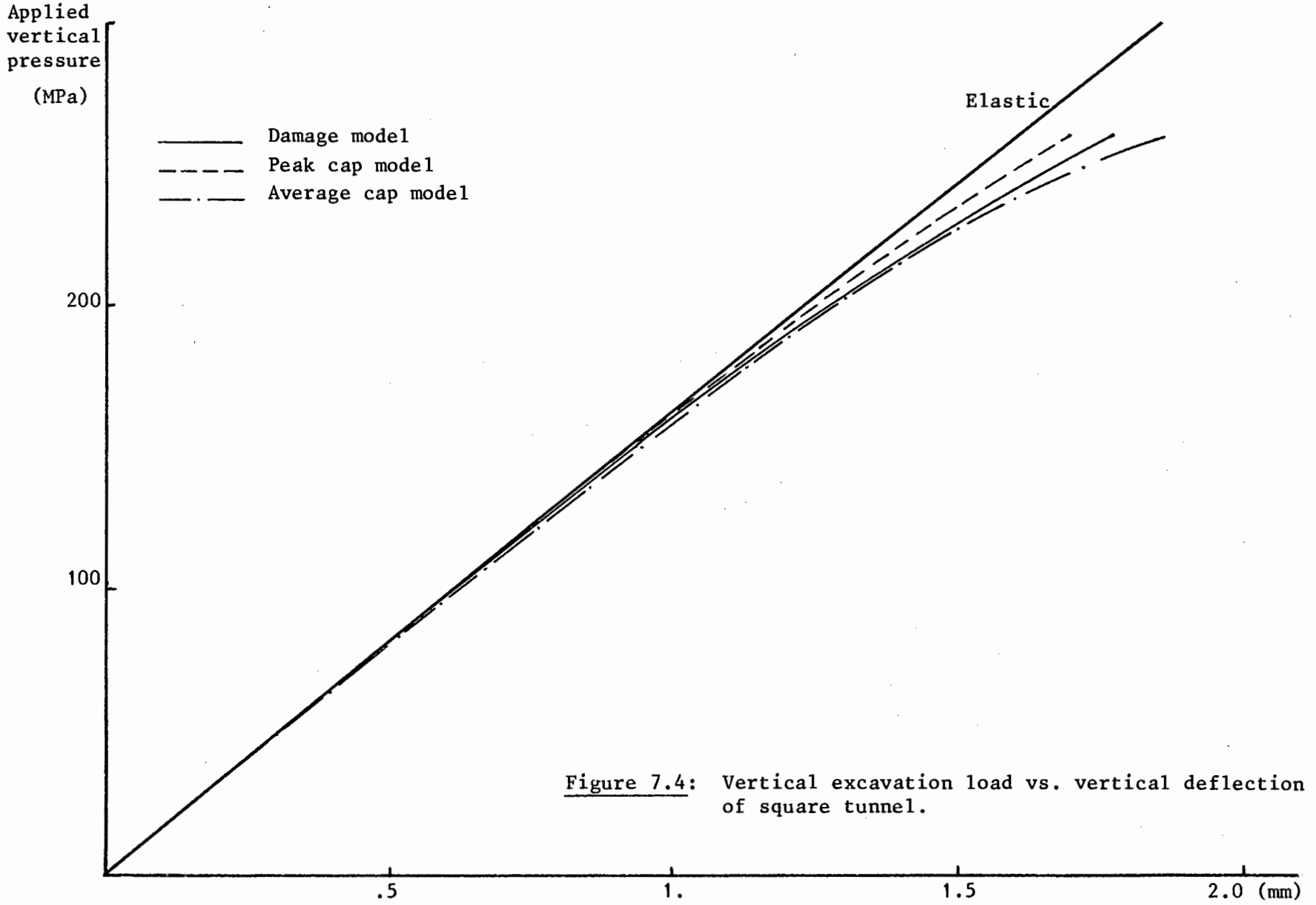

Figure 7.4: Vertical excavation load vs. vertical deflection at corner of square tunnel.

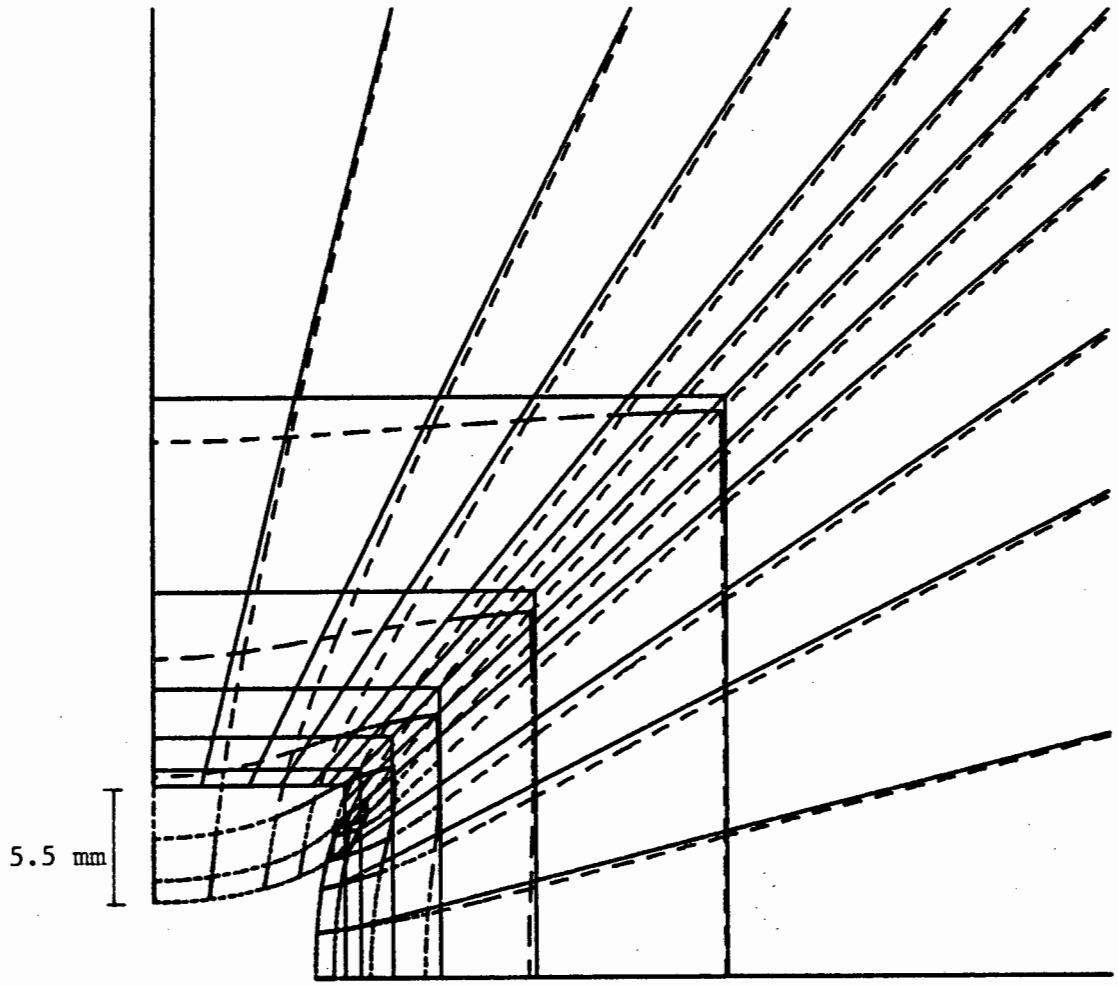

(a) Displaced shape

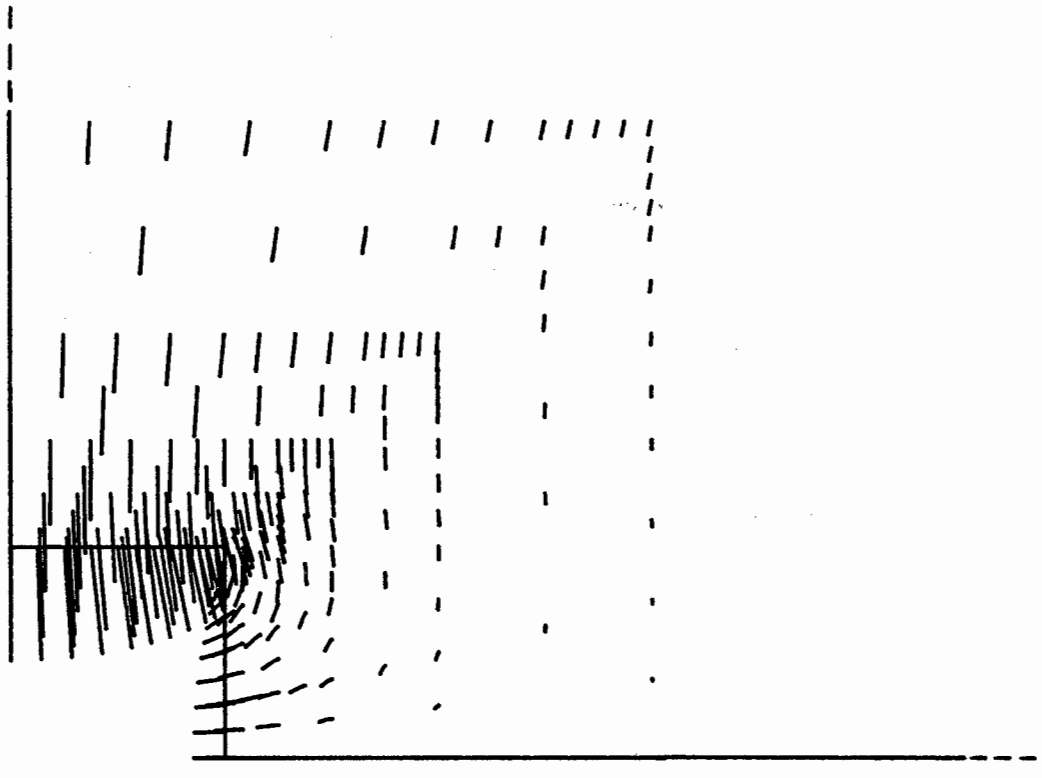

(b) Velocity field

Figure 7.5: Square tunnel: displacements at end of excavation (damage model).

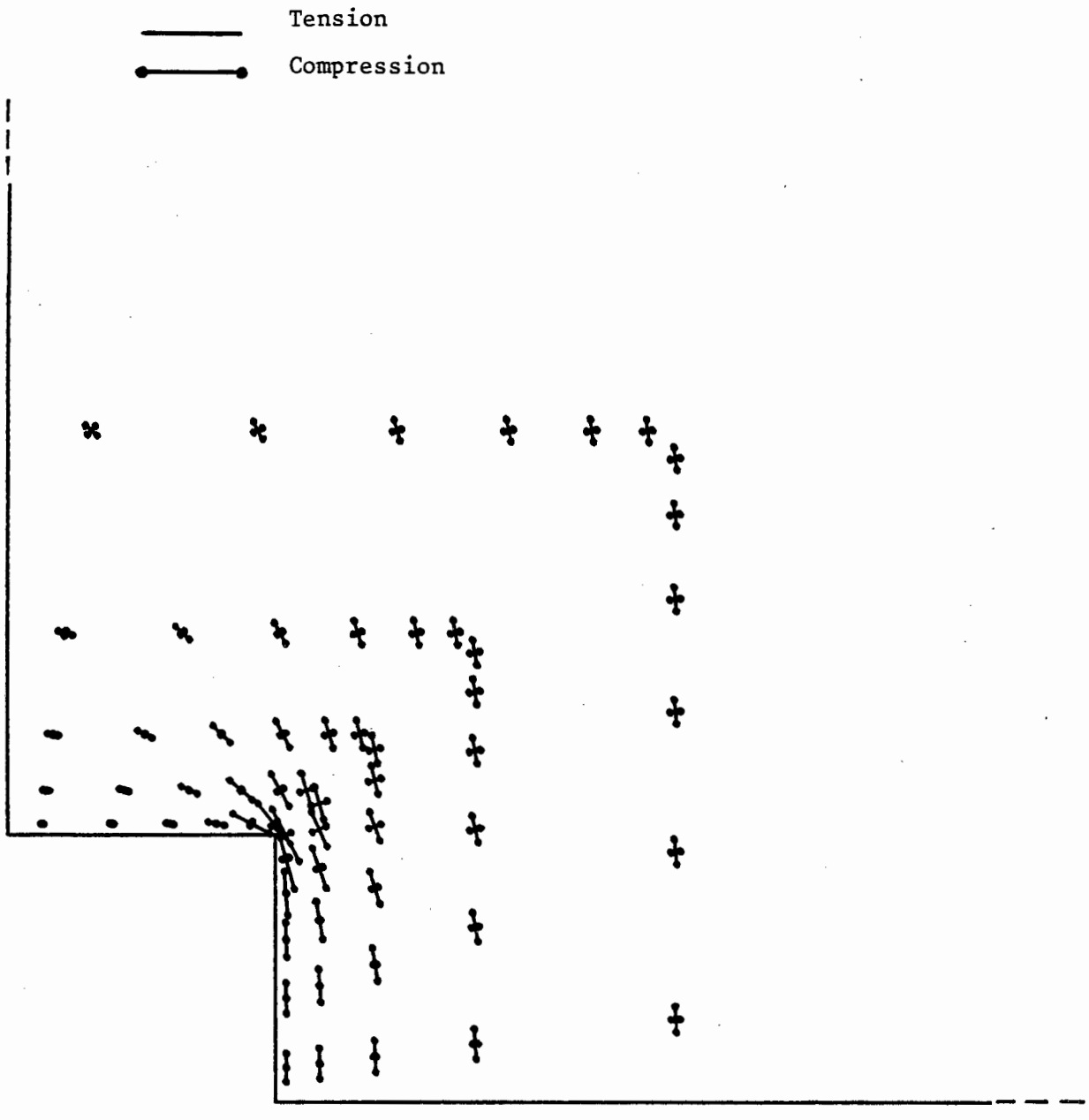

Figure 7.6: Square tunnel: principal stress vectors at end of excavation (damage model). Stress vectors only shown at centre of finite elements.

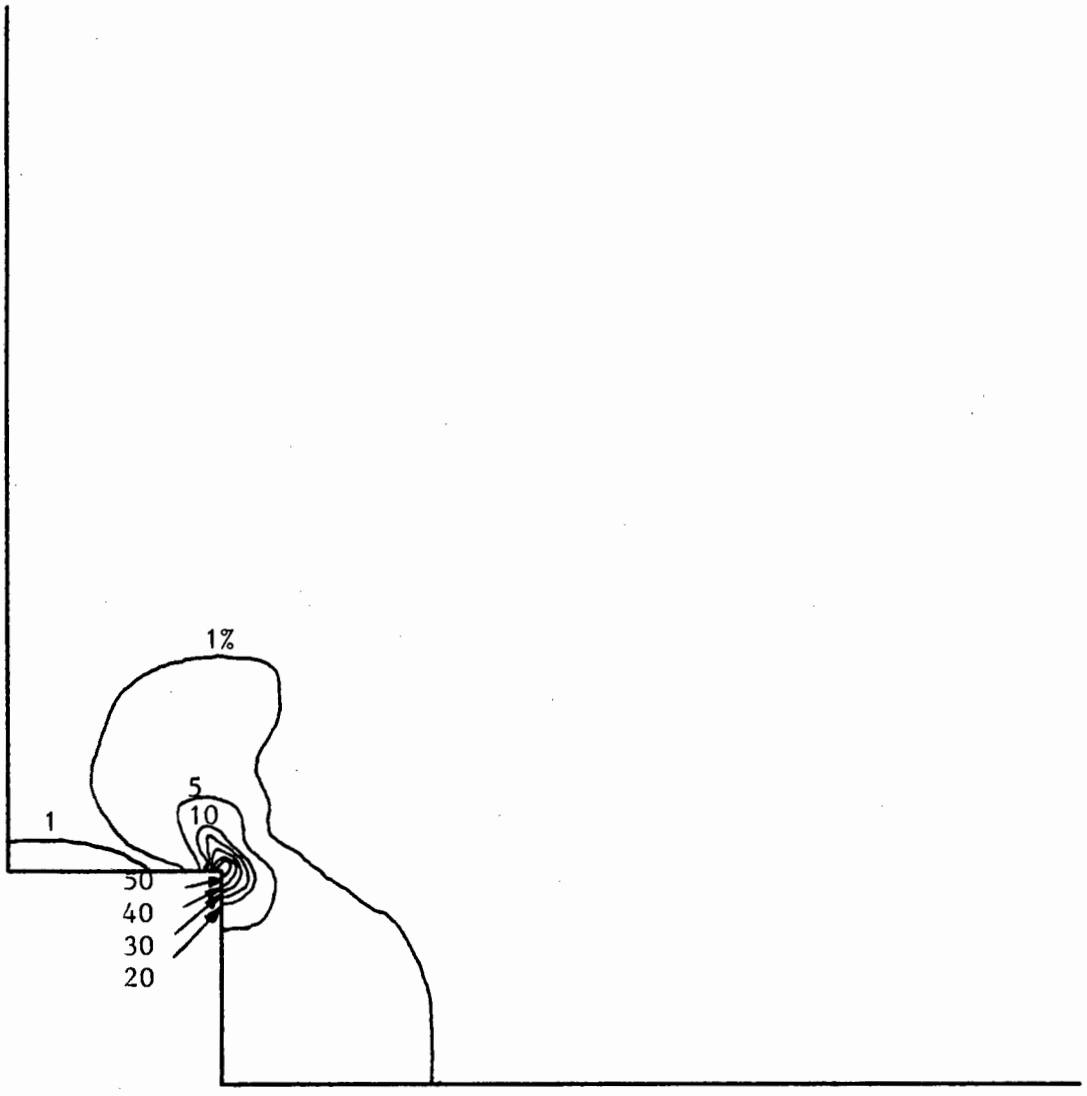

Figure 7.7: Square tunnel: percentage damage contours at end of excavation.

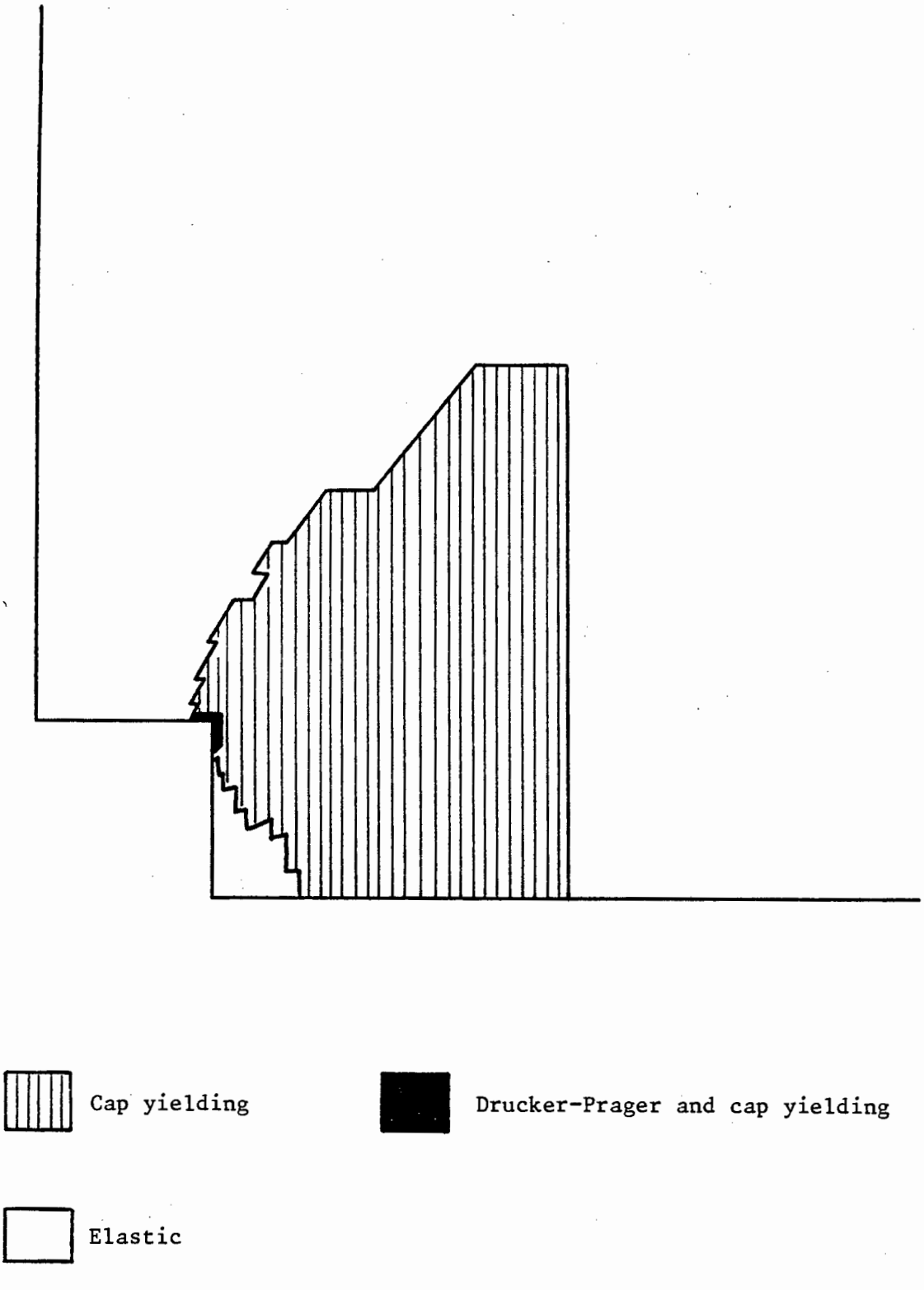

Figure 7.8: Square tunnel: zones of stress state at end of excavation (peak cap model).

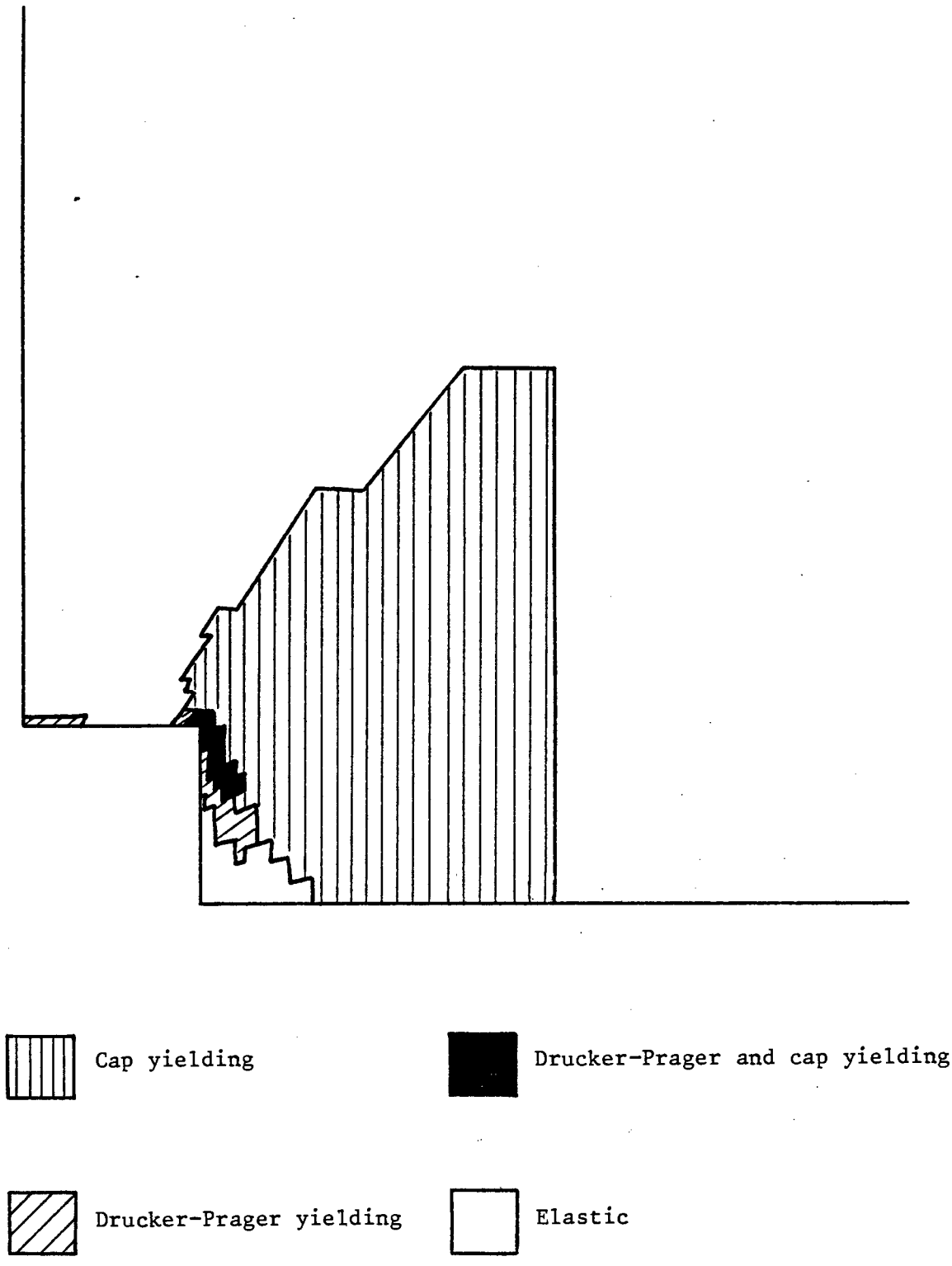

Figure 7.9: Square tunnel: zones of stress state at end of excavation (average cap model).

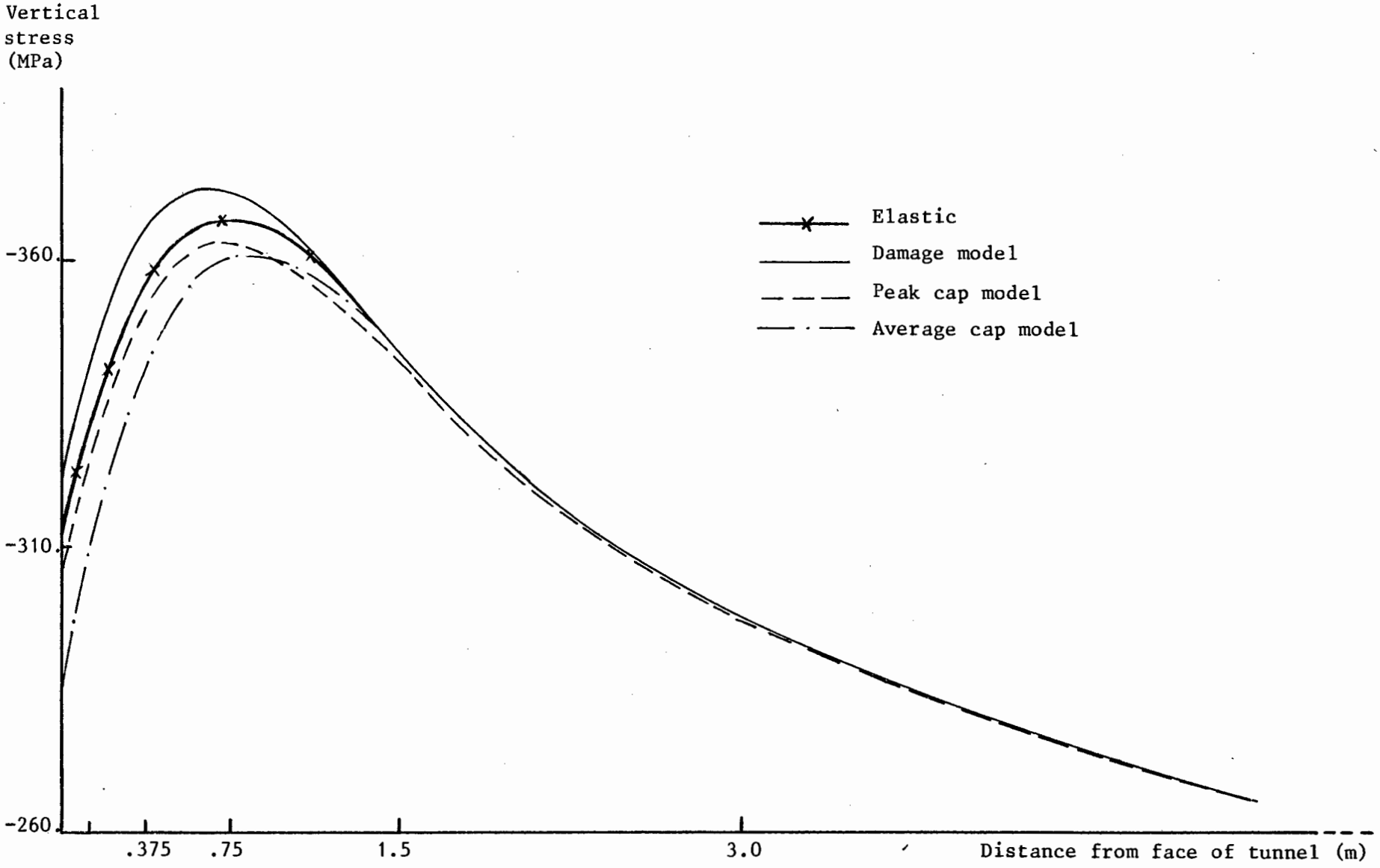

Figure 7.10: Square tunnel: vertical stress distribution along horizontal centre line of tunnel.

The stiffening behaviour expected from the damage model is best illustrated if we consider the most highly stressed material point (nearest to the corner of the tunnel as shown in Fig. 7.2). Table 7.1 shows the vertical stress history of this point through the process of excavation. At the end of step 1, where elastic behaviour prevails, the ratio of the change in vertical stress to applied load is around 3 and this increases progressively as the excavation simulation continues. On the other hand, the cap model analyses show a reverse trend with this ratio decreasing to 2.15 in the case of the average cap model. This is due to the loss of stiffness experienced by the material point as it reaches the cap yield surface first and then the Drucker-Prager/cap corner. The average cap model response is softer because the material point experiences more corner behaviour than in the case of the peak cap model.

Load (MPa)	Damage model σ_{yy} (MPa)	$\frac{\sigma_{yy}-260}{\text{Load}}$	Peak cap model σ_{yy} (MPa)	$\frac{\sigma_{yy}-260}{\text{Load}}$	Average cap model σ_{yy} (MPa)	$\frac{\sigma_{yy}-260}{\text{Load}}$
- 30	- 351.	3.03	- 349.	2.97	- 349.	2.97
- 60	- 455.	3.25	- 429.	2.82	- 429.	2.82
- 90	- 564.	3.38	- 514.	2.82	- 512.	2.80
-120	- 685.	3.54	- 600.	2.82	- 567.	2.56
-150	- 821.	3.74	- 674.	2.76	- 651.	2.61
-180	- 974.	3.97	- 742	2.68	- 723.	2.57
-210	-1158.	4.28	- 831.	2.72	- 774.	2.45
-240	-1353.	4.55	- 907.	2.70	- 814.	2.31
-260	-1502.	4.78	- 957.	2.68	- 819.	2.15

Table 7.1: Vertical stress history at material point closest to tunnel corner.

Lastly, the invariant shear stress/strain and hydrostatic stress/volumetric strain histories are ploted in Fig. 7.11 for the sme material point closest to the corner of the tunnel. The shear behaviour

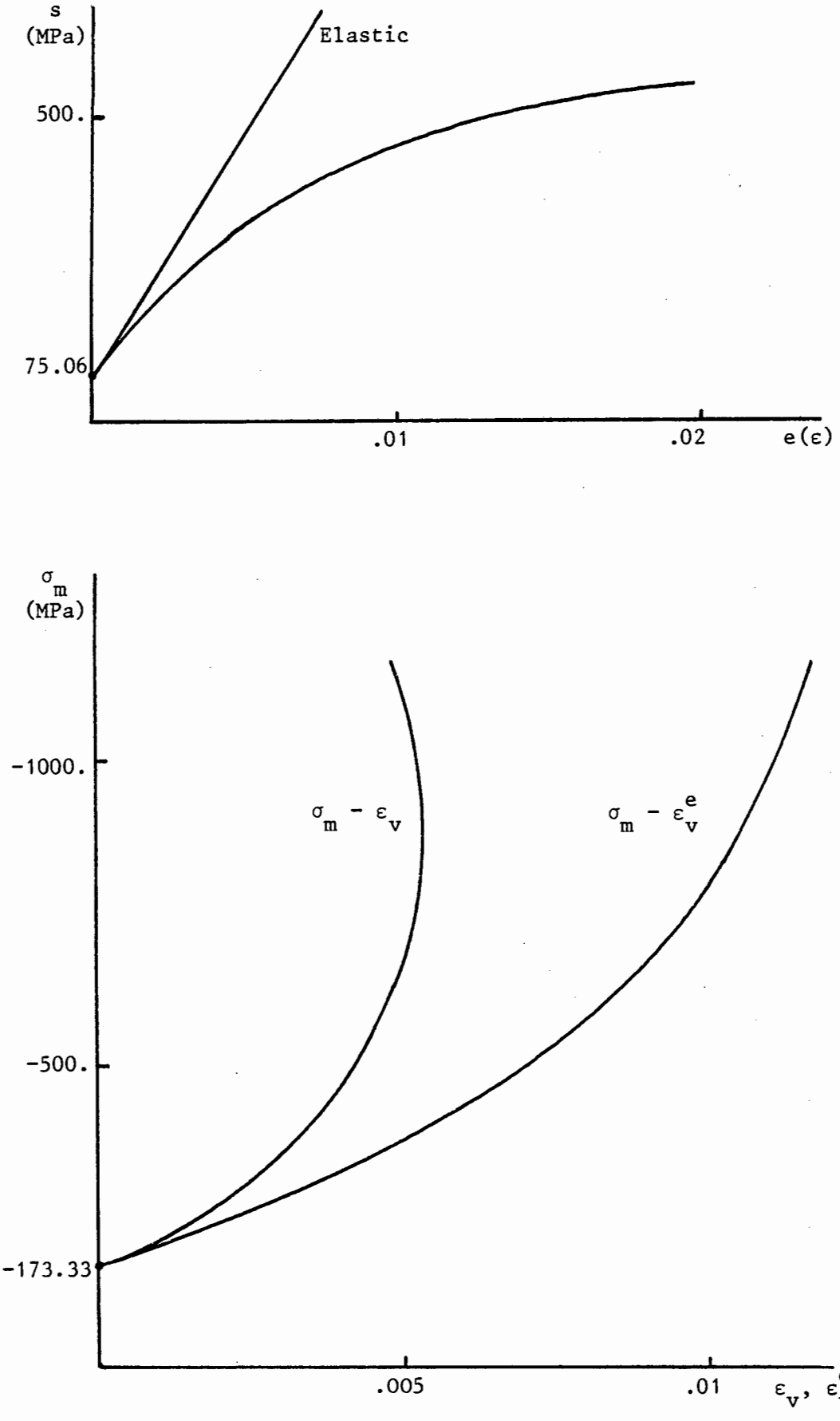

Figure 7.11: Square tunnel: history of invariant stress/strain for material point closest to corner of tunnel (damage model).

exhibits loss of stiffness while the volumetric behaviour is strongly stiffening with the onset of dilatancy apparent towards the end of the excavation simulation.

It must be stressed that the above discussion of the results obtained for the square tunnel problem was primarily aimed at showing that the deformation and stress patterns obtained are reasonable in view of the characteristics of the models employed. In the next problem, greater attention is given to relating the numerical results to the behaviour observed underground in real mining excavations.

7.3.2 Seam Excavation

In South African gold mines, gold is found in narrow seams, called reefs, which are generally less than one meter thick and extend horizontally for many kilometres. Once access is gained to the depth of the reef, mining takes place along the reef giving rise to an excavation which in cross-section rather resembles a slot. The advancing end of the excavation is called the stope face. The length of the slot could be of the order of hundreds of meters while its thickness is around one or two meters. It was chosen to model a 24m by 2.4m slot like configuration as an example of a typical gold mining excavation. The finite element plane strain model used is illustrated in Fig. 7.12 and it consists of 45 eight noded Serendipity quadrilaterals and 9 five noded compatible infinite elements making up a total of 174 nodes. Again 3x3 Gauss integration is employed in all elements. The boundary conditions, initial stress field and excavation loading are all similar to those used in the square tunnel problem. The constitutive models and material parameters used are identical to those of section 7.3.1 with the exception that the constant W in the damage model is now taken as -.024. This choice is made in an attempt to reduce the severity of the disparity between the volumetric behaviour of the damage and cap models discussed earlier.

The overall deformation due to the excavation loading is, as in the case of the square tunnel, close to linear. Again, this is due to the localized nature of the deformation around the stope face. Plots of

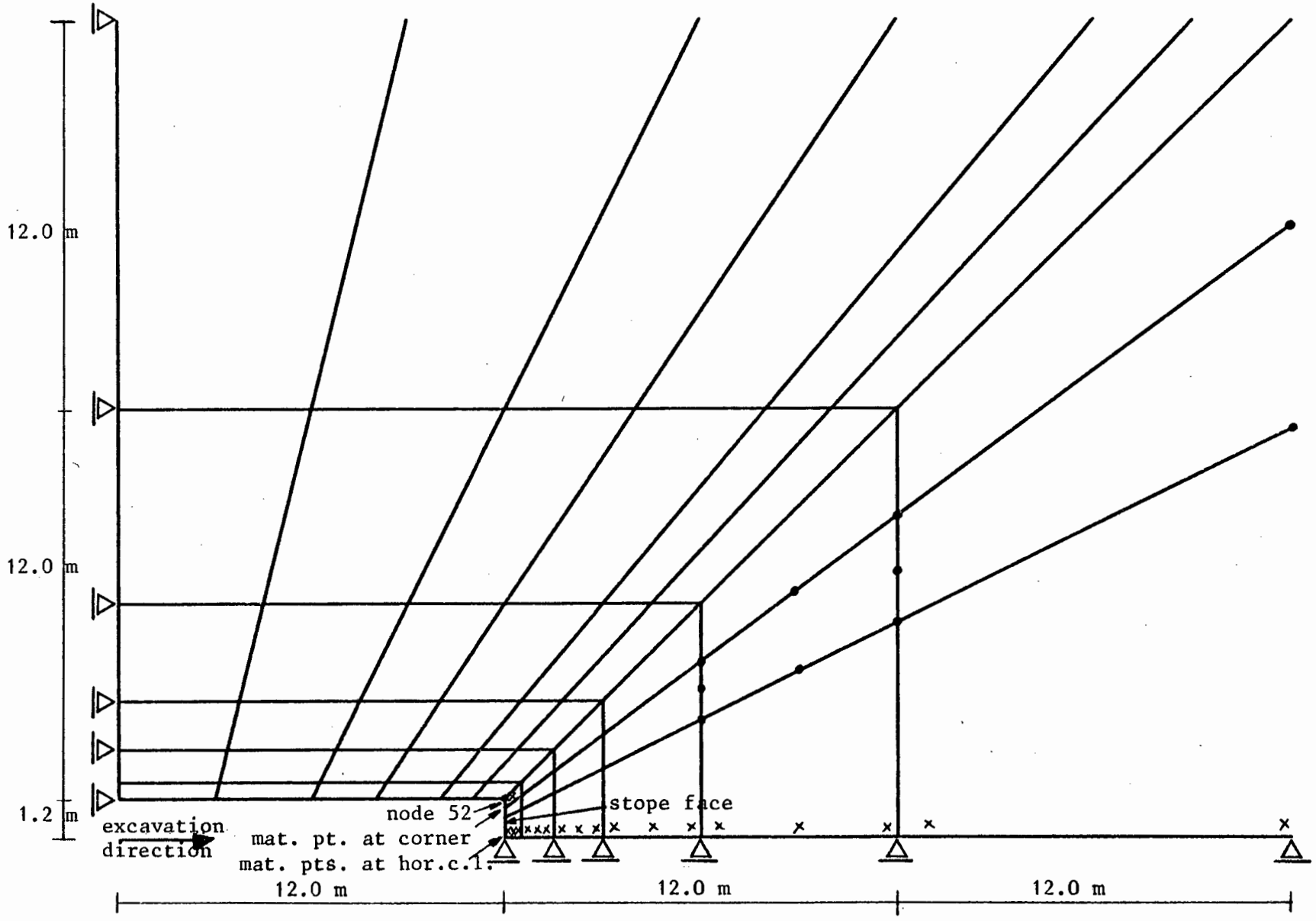

Figure 7.12: Finite element model of seam excavation.

vertical excavation load versus vertical displacement at node 52 (situated at the upper edge of the stope face) are shown in Fig. 7.13 where it is clear that the displacements predicted by the damage model exceed those predicted by the two cap models. Fig. 7.14 shows the displacements of the structure at the end of the excavation as calculated with the damage model and Fig. 7.15 is a representation of the distribution of the corresponding principal stresses. A plot of contours of the degree of damage sustained by the material during excavation is shown in Fig. 7.16 where the localized nature of the deformation is evident. The zones of stress state at the end of the excavation for the two cap model analyses are given in Figs. 7.17 and 7.18. It is clear that the predominant mode of inelastic behaviour is cap yielding and this occurs ahead of the stope face. Drucker-Prager yielding is present in narrow regions adjacent to the floor and roof of the slot like excavation. The material immediatly ahead of the stope face undergoes yielding with the Drucker-Prager and cap surfaces simultaneously active. As in the case ot the square tunnel, the simultaneous yielding region is larger for the average cap model as would be expected. It is important to note that the regions of damage predicted by the damage model are similar to the yielded regions predicted by the cap models. Furthermore, the most highly damaged regions in the damage model prediction coincide with the zones of simultaneous Drucker-Prager and cap yielding predicted by the cap models. This is reasonable since the simultaneous yielding represents, in these problems, a stage of inelastic behaviour following the initial cap yielding.

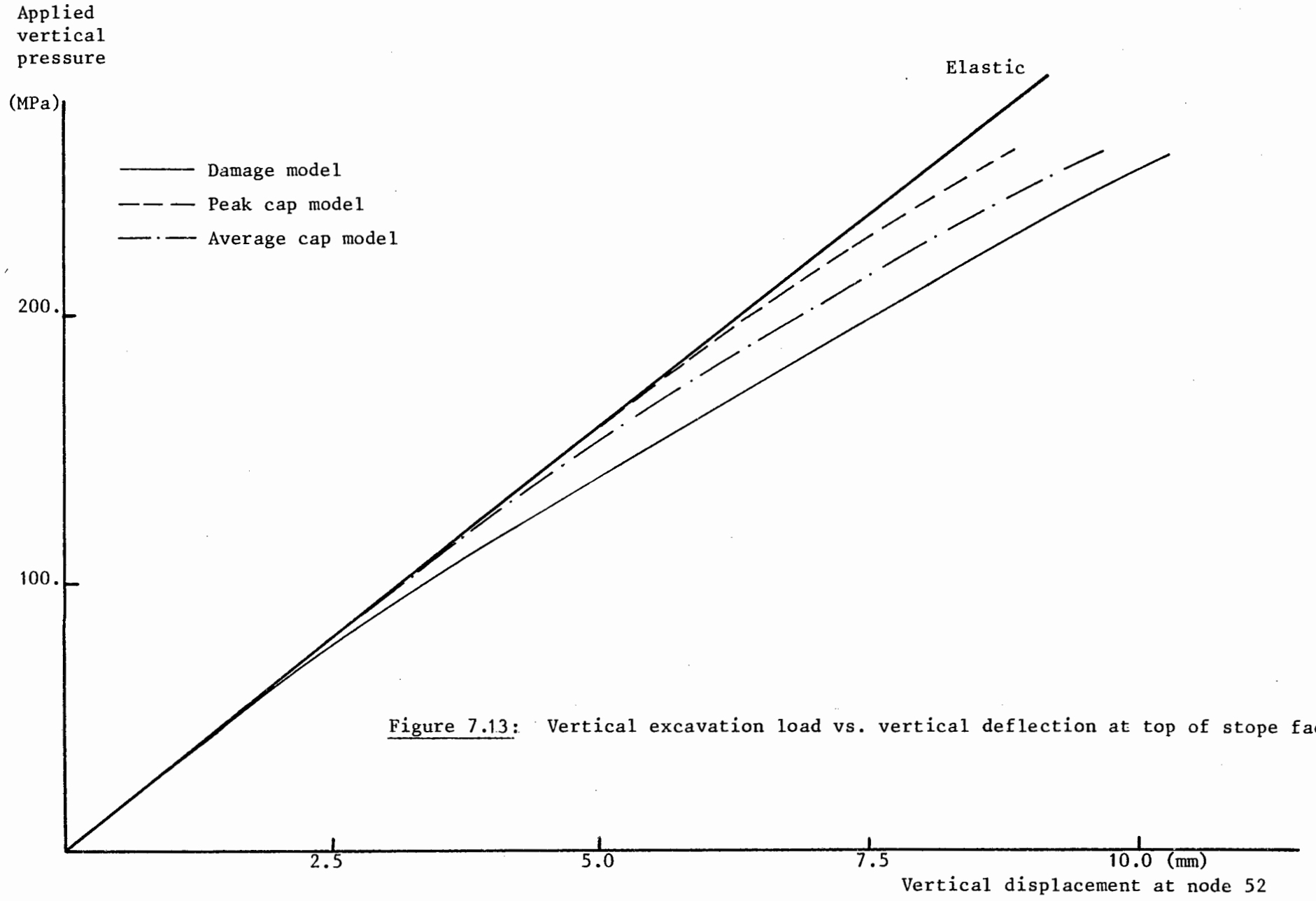

Figure 7.13: Vertical excavation load vs. vertical deflection at top of stope face.

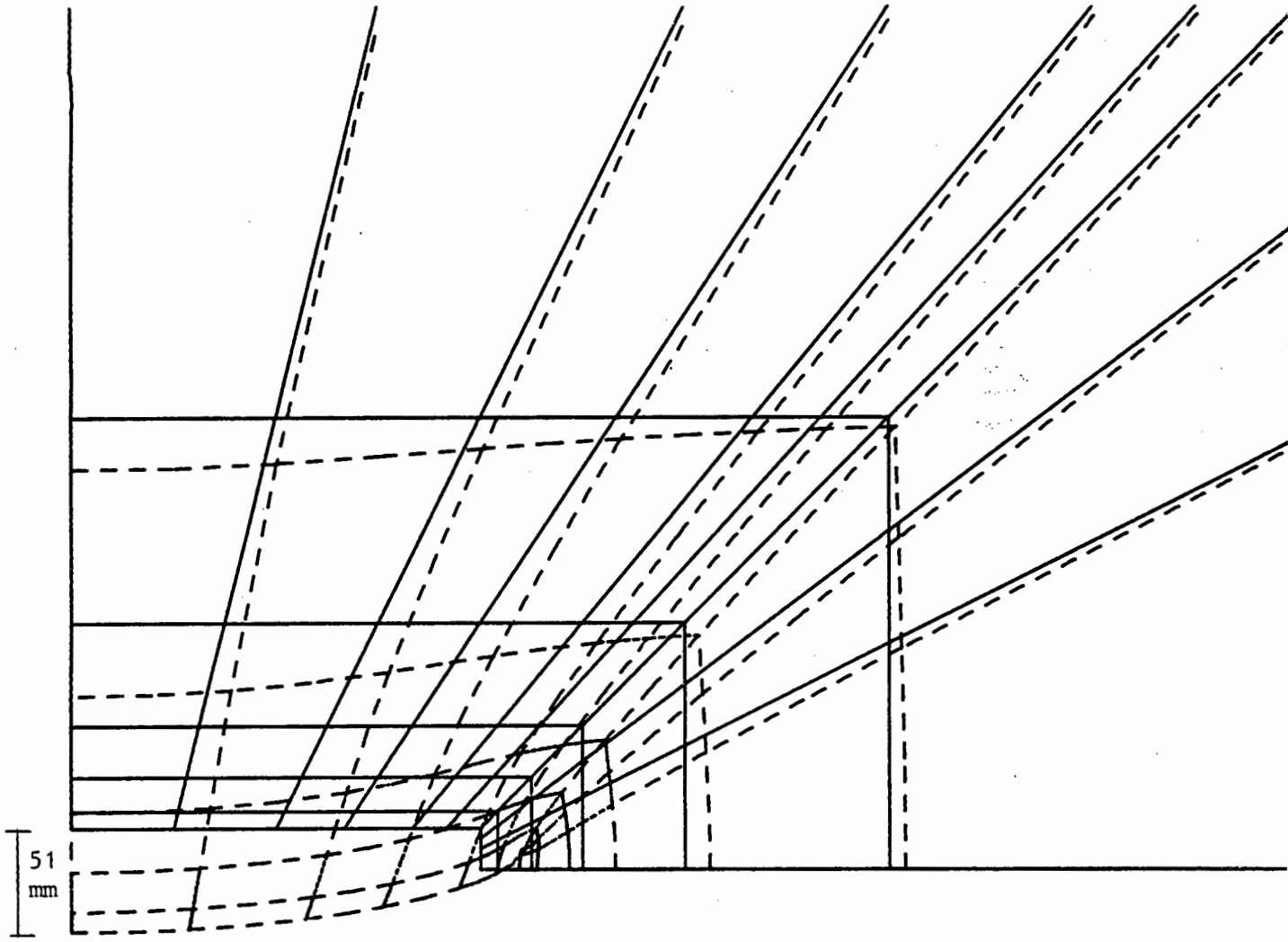

(a) Displaced shape

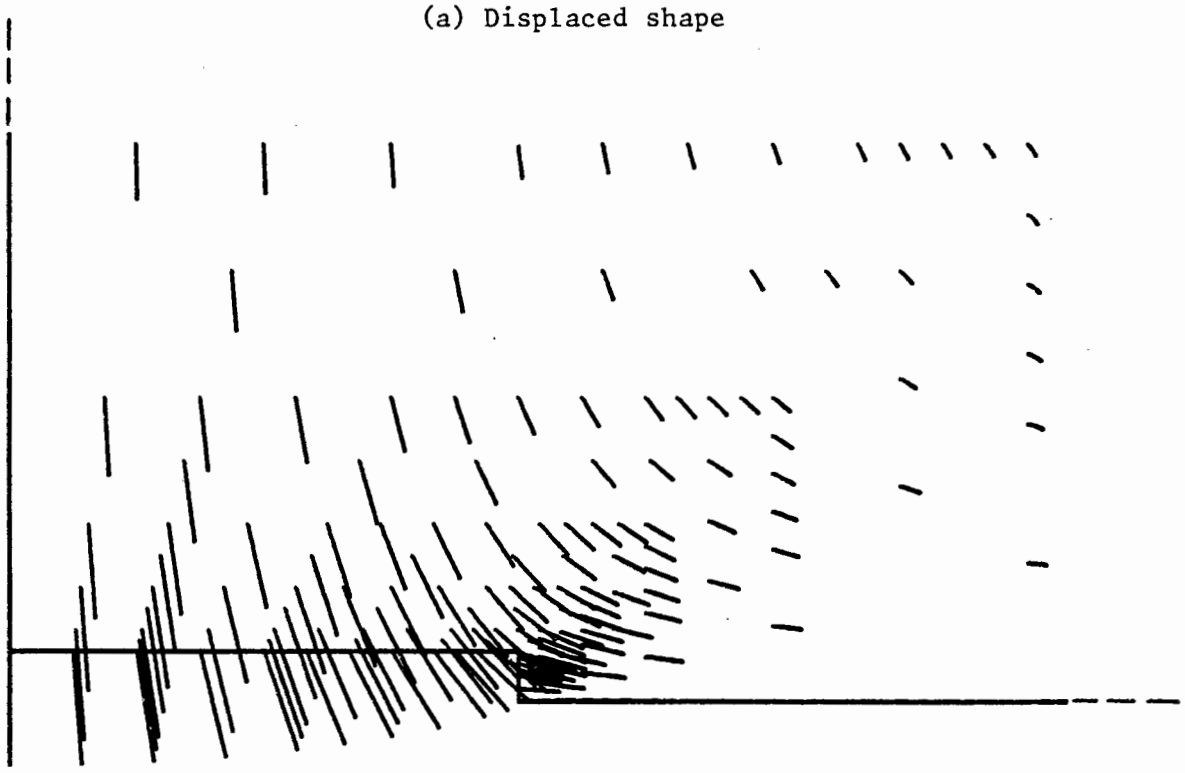

(b) Velocity field

Figure 7.14: Seam excavation: displacements at end of excavation (damage model).

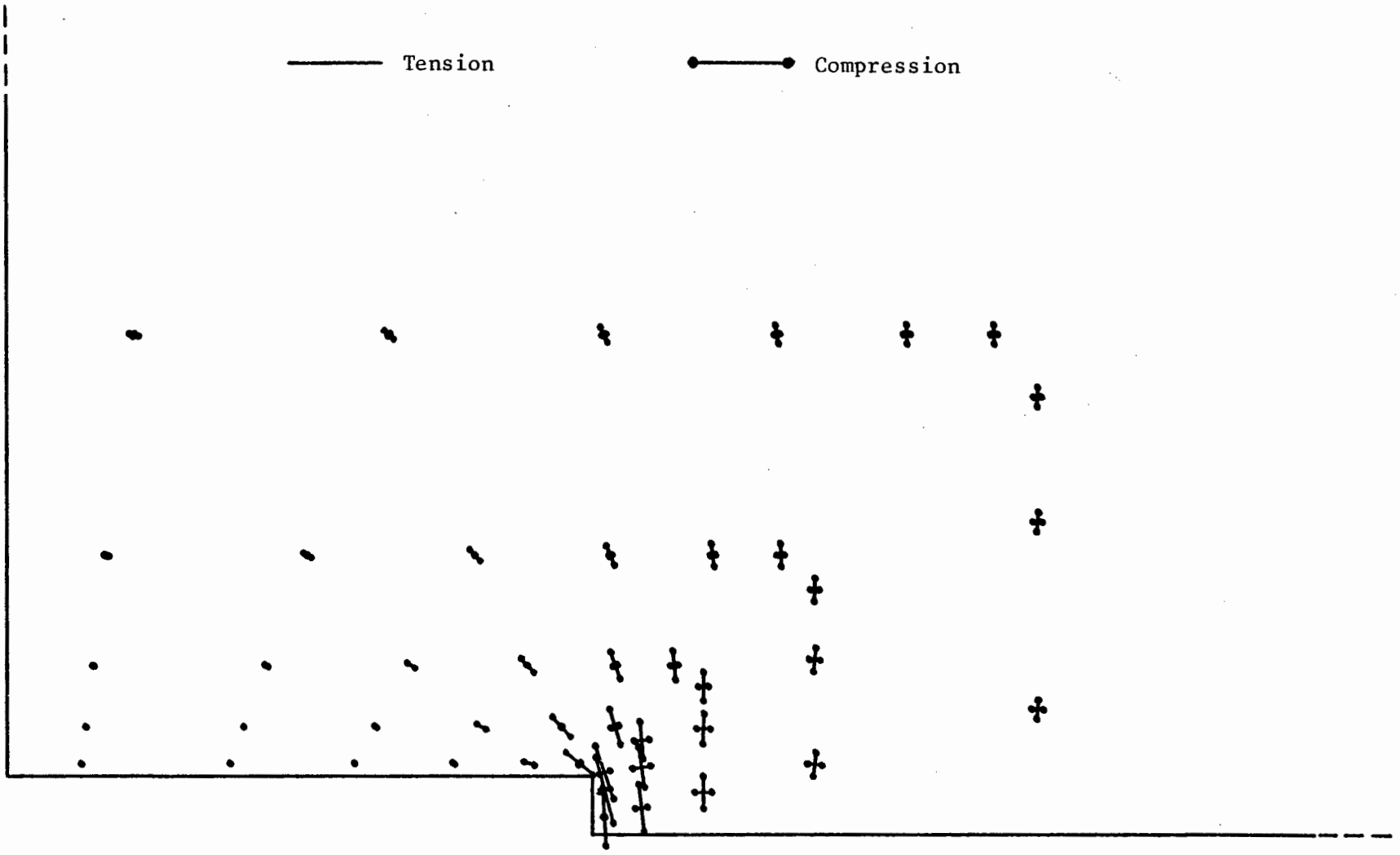

Figure 7.15: Seam excavation: principal stress vectors at end of excavation (damage model). Stress vectors only shown at centre of finite elements.

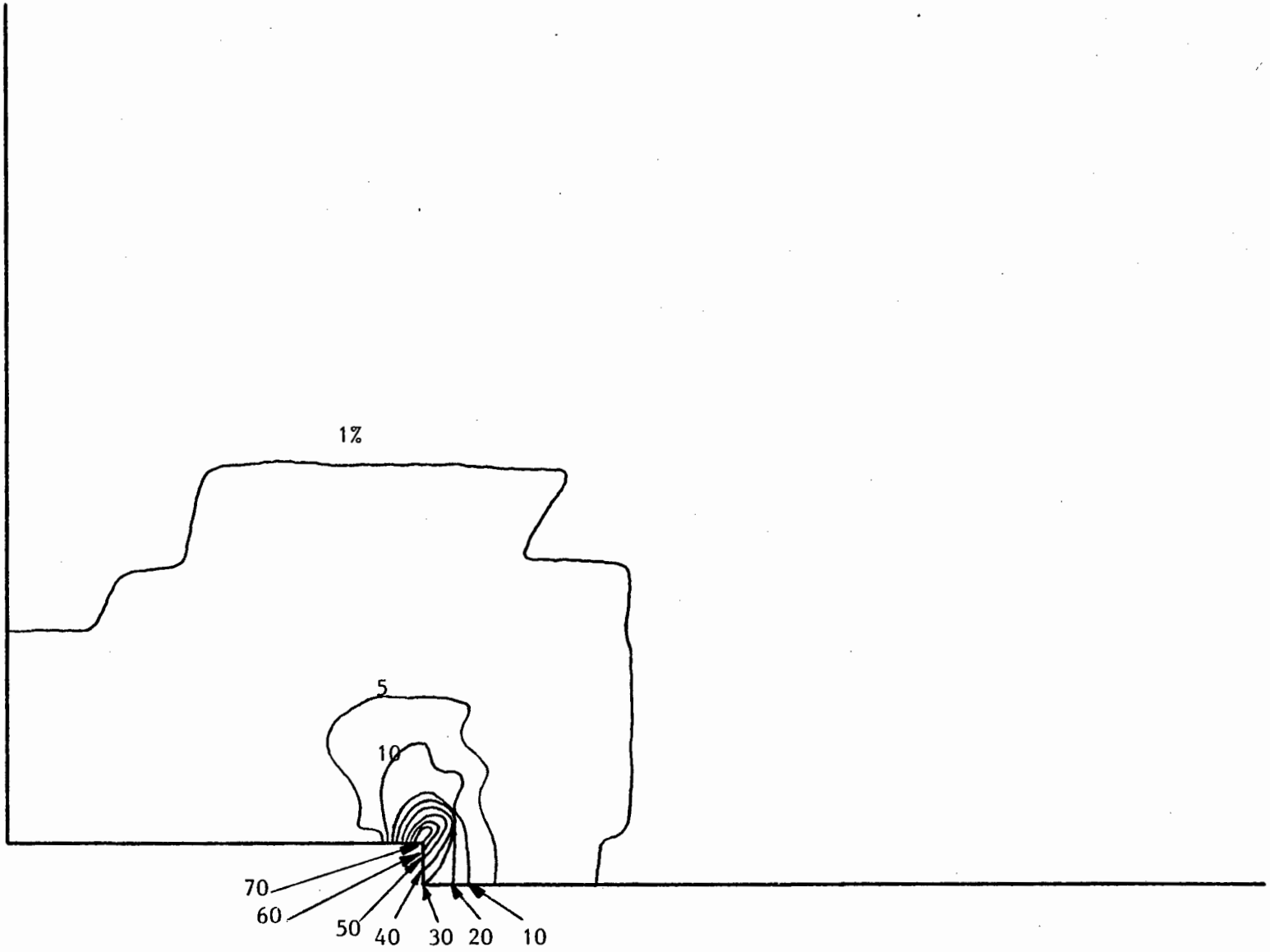

Figure 7.16: Seam excavation: percentage damage contours at end of excavation.

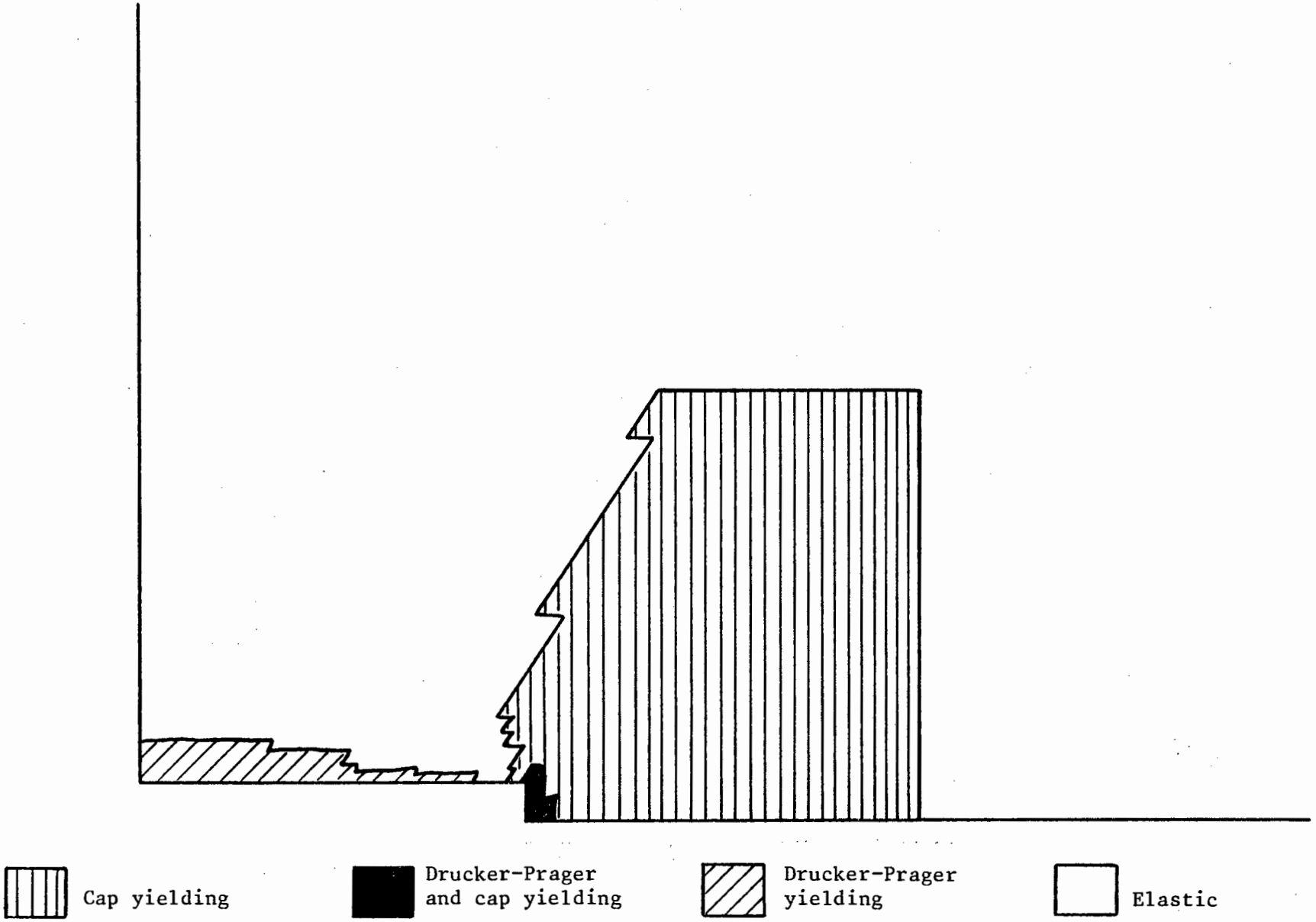

Figure 7.17: Seam excavation: zones of stress state at end of excavation (peak cap model).

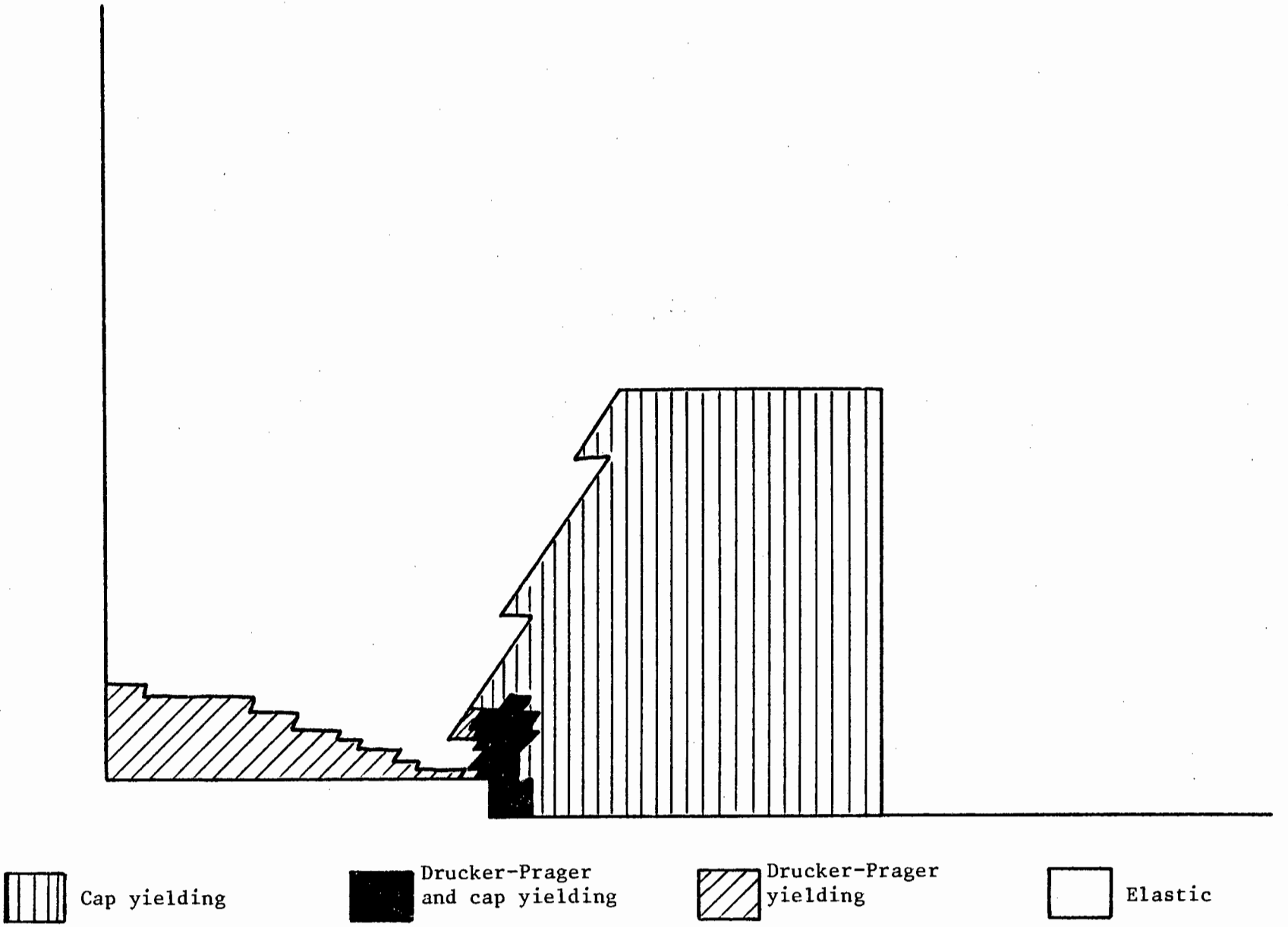

Figure 7.18: Seam excavation: zones of stress state at end of excavation (average cap model).

Fig. 7.19 shows plots of vertical stress distribution along the horizontal centre line of the excavation. The damage model predicts stresses which are lower than the elastic ones and the cap models predict even lower stresses. The lower than elastic stresses can generally be explained by the loss of shear stiffness characteristic of the models used. The fact that the damage model still predicts higher vertical stresses than the cap models is due to the stiffer volumetric behaviour of the damage model. However, it must be realized that until inelastic volumetric behaviour material constants can be found for the cap models which are equivalent to the volumetric behaviour characteristics of the damage model, comparisons ot the kind described earlier are difficult.

The invariant shear stress/strain and hydrostatic stress/volumetric strain histories for a material point close to the upper edge of the stope face are given in Fig. 7.20. Behaviour similar to that observed for the equivalent point in the square tunnel problem is evident.

It is important to conclude section 7.3 with a comment on the significance of the analyses of the two mining excavations considered: the nature of the problems is such that while the overall behaviour predicted by the damage and cap models is not very different from the elastic behaviour, it is in the prediction of the localized behaviour around the excavations that the more sophisticated inelastic models are significantly different from the simple elastic model. This is important in the sense that it is this inelastic localized behaviour that leads to eventual failure of the excavations.

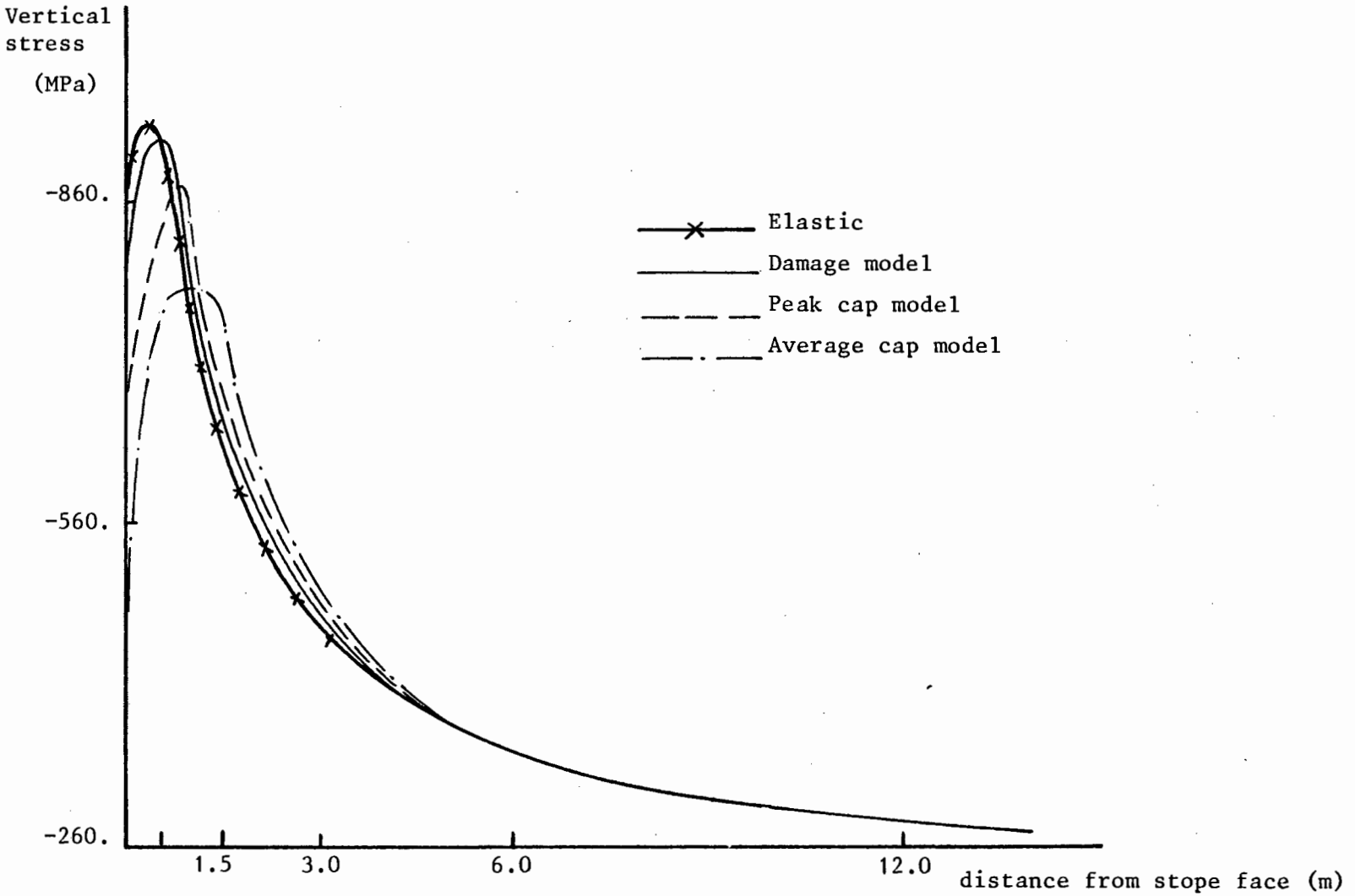

Figure 7.19: Seam excavation: vertical stress distribution along horizontal centre line of excavation.

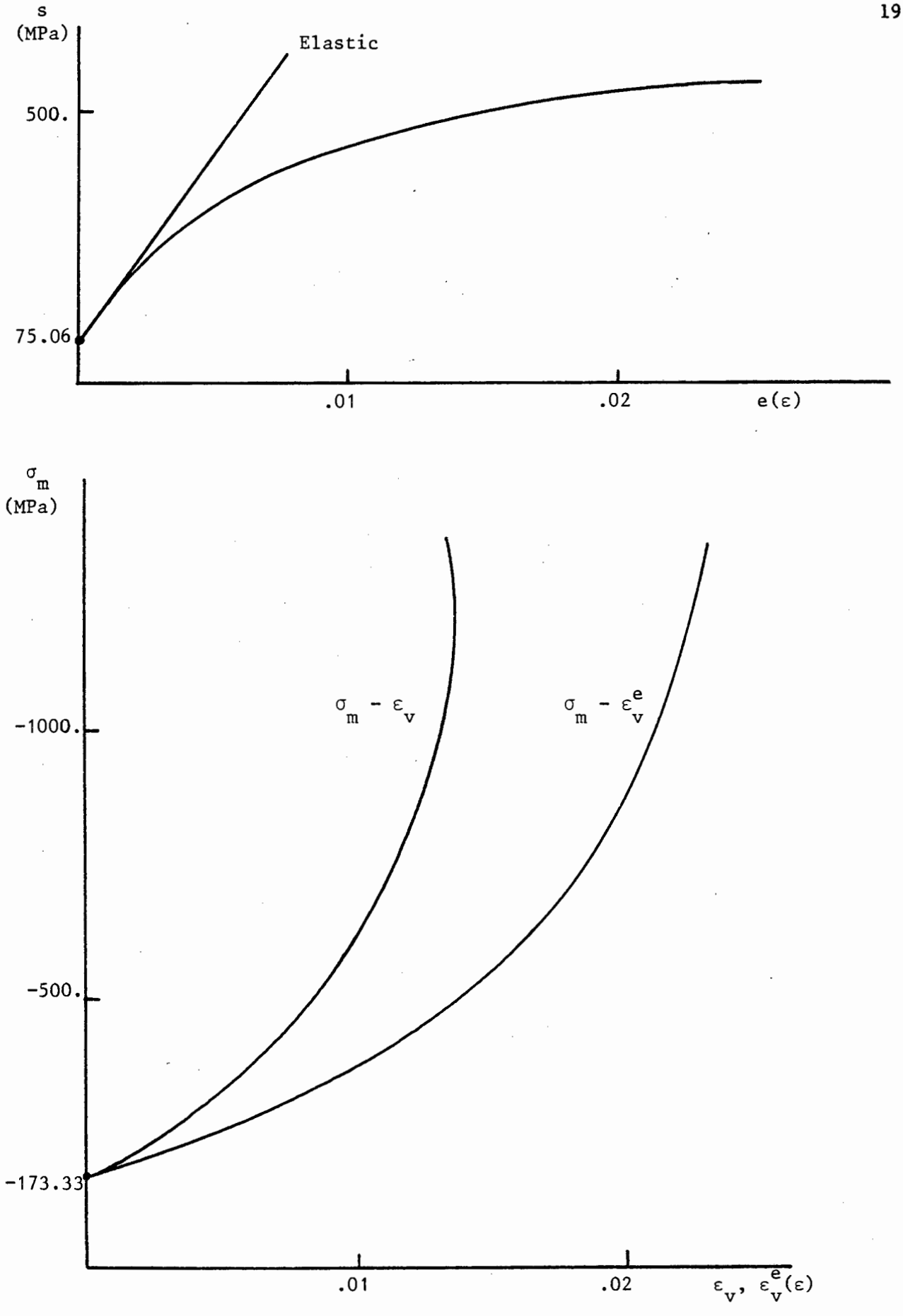

Figure 7.20: Seam excavation: history of invariant stress/strain for material point closest to upper edge of stope face (damage model).

7.4 Analysis of Standard Configurations

The purpose of the following analyses is to test the performance of the damage model in the solution of standard problems of interest. The two main concerns are to investigate how well the model reproduces the known physical behaviour and secondly, how far the numerical solution can be taken.

7.4.1 Brazilian Test

The diametral compression of a disc, or the Brazilian test, is considered to be one of the more reliable methods of assessing the tensile characteristics of brittle materials. Details of the test and its validity can be found in Jaeger and Cook [12] but are not of concern here. The basic configuration of the test is shown in Fig. 7.21 together with typical fractures resulting from the compression of the disc between parallel rigid surfaces. Typical stress distributions along the loaded diameter of the disc are also shown.

The disc is modelled in plane stress and two lines of symmetry are used so that only a quarter of the configuration is modelled. The finite element mesh used is shown in Fig. 7.22 and consists of 64 eight noded Serendipity quadrilaterals (3x3 Gauss integration) making up a total of 221 nodes. The loading consits of prescribed vertical displacements as indicated in Fig. 7.22. The damage material parameters of equn. (7.4) are again used since we assume the disc is made of Bushveld Norite.

A 'load' versus deflection curve obtained with the damage model for the Brazilian test is given in Fig. 7.23. It shows the applied diametral displacement (which is proportional to the resulting average diametral pressure) plotted against the horizontal displacement at node 101 representing a disc splitting displacement. It is clear that the response is markedly nonlinear although the disc still retains an overall positive stiffness. The velocity pattern at the end of the test is shown in Fig. 7.24(b) where the diametral splitting tendency is apparent in contrast with the elastic result shown in Fig. 7.24(a). A contour plot of the

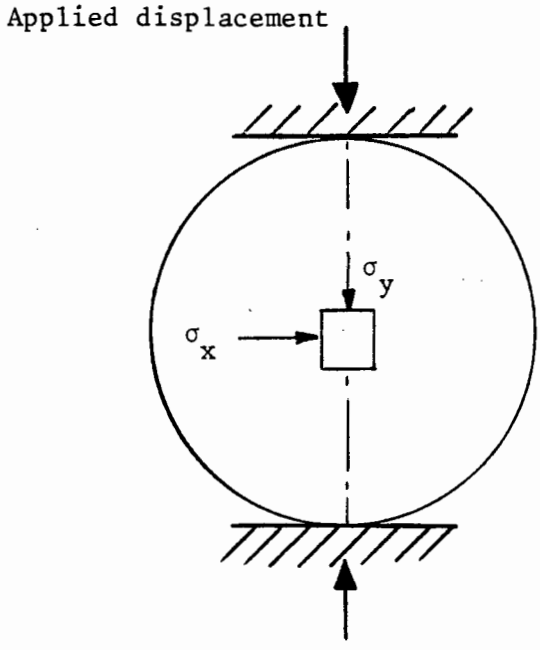

(a) Basic configuration

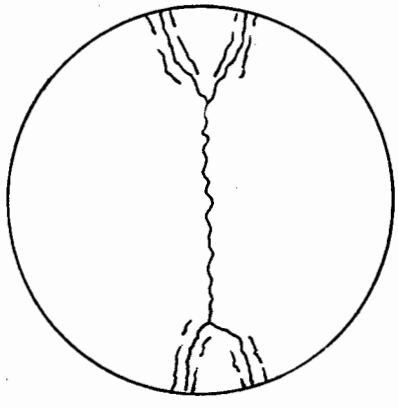

(b) Typical fracture pattern

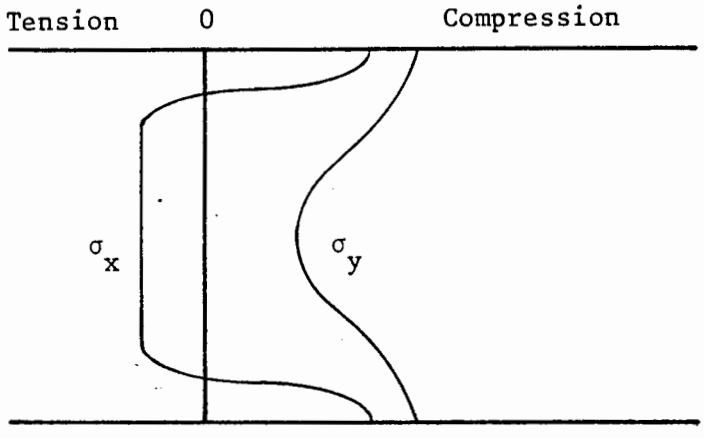

(c) Typical stress distributions along loaded diameter

Figure 7.21: Brazilian test.

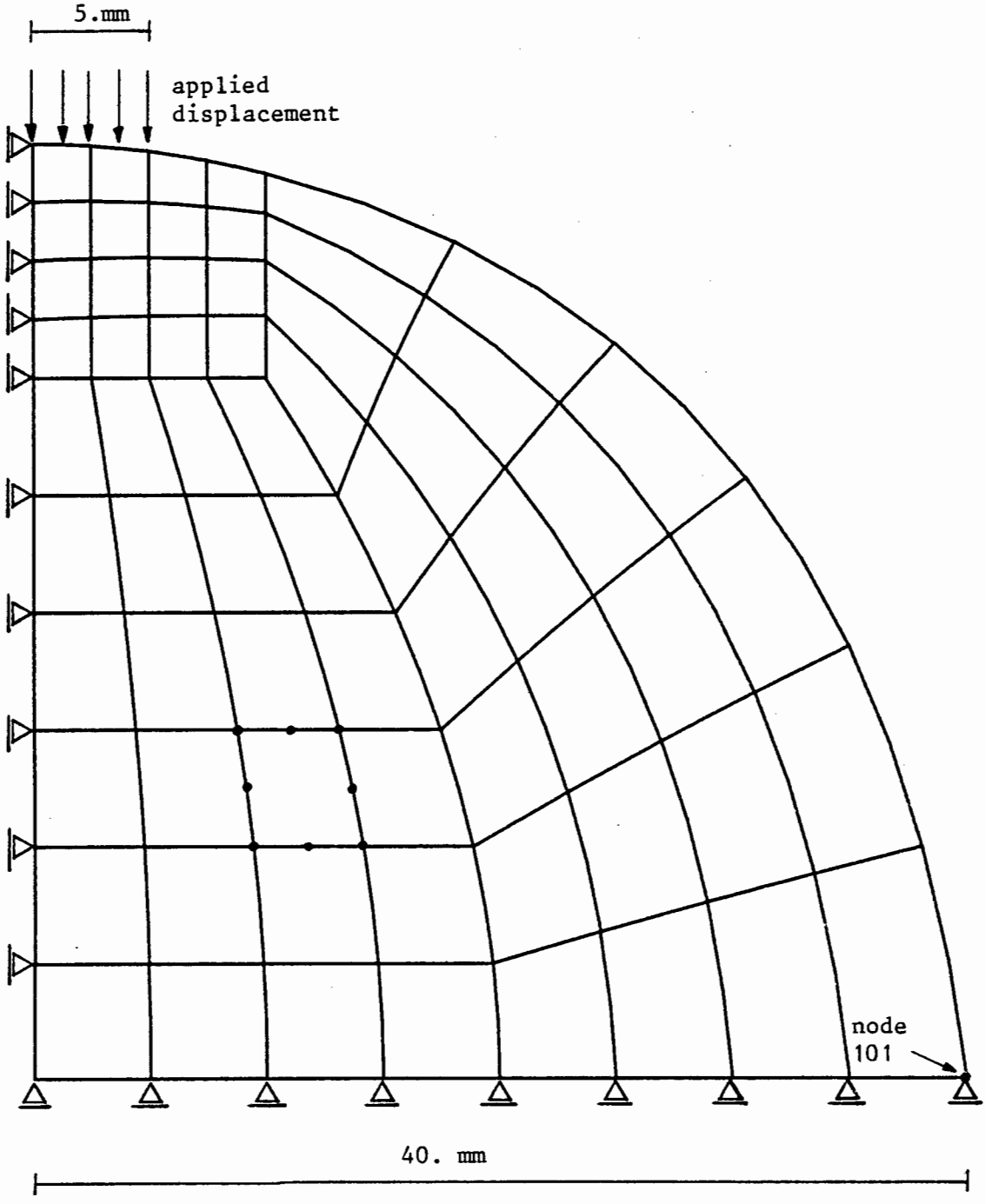

Figure 7.22: Finite element model of Brazilian test.

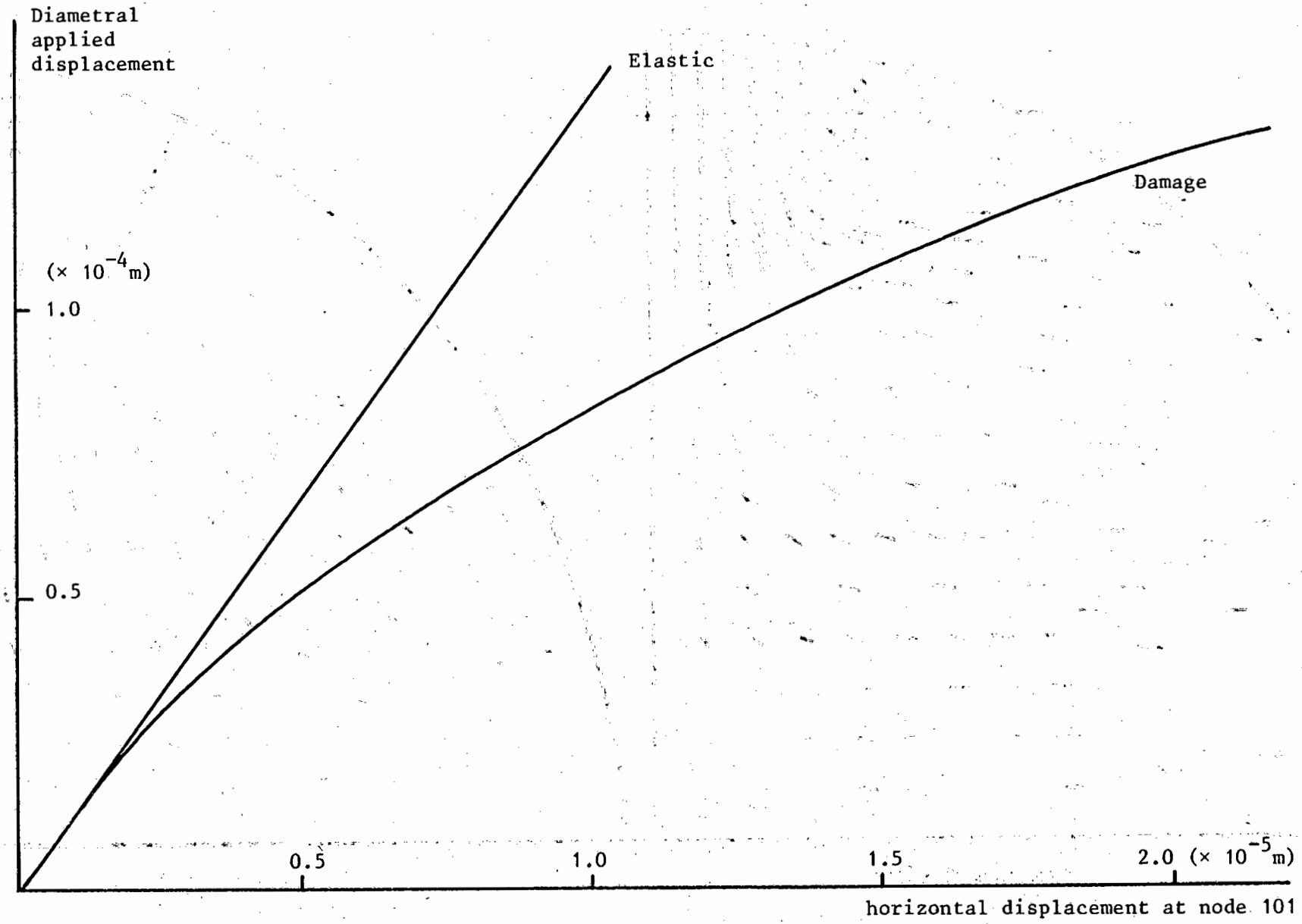

Figure 7.23: Brazilian test: 'load' vs. deflection curve.

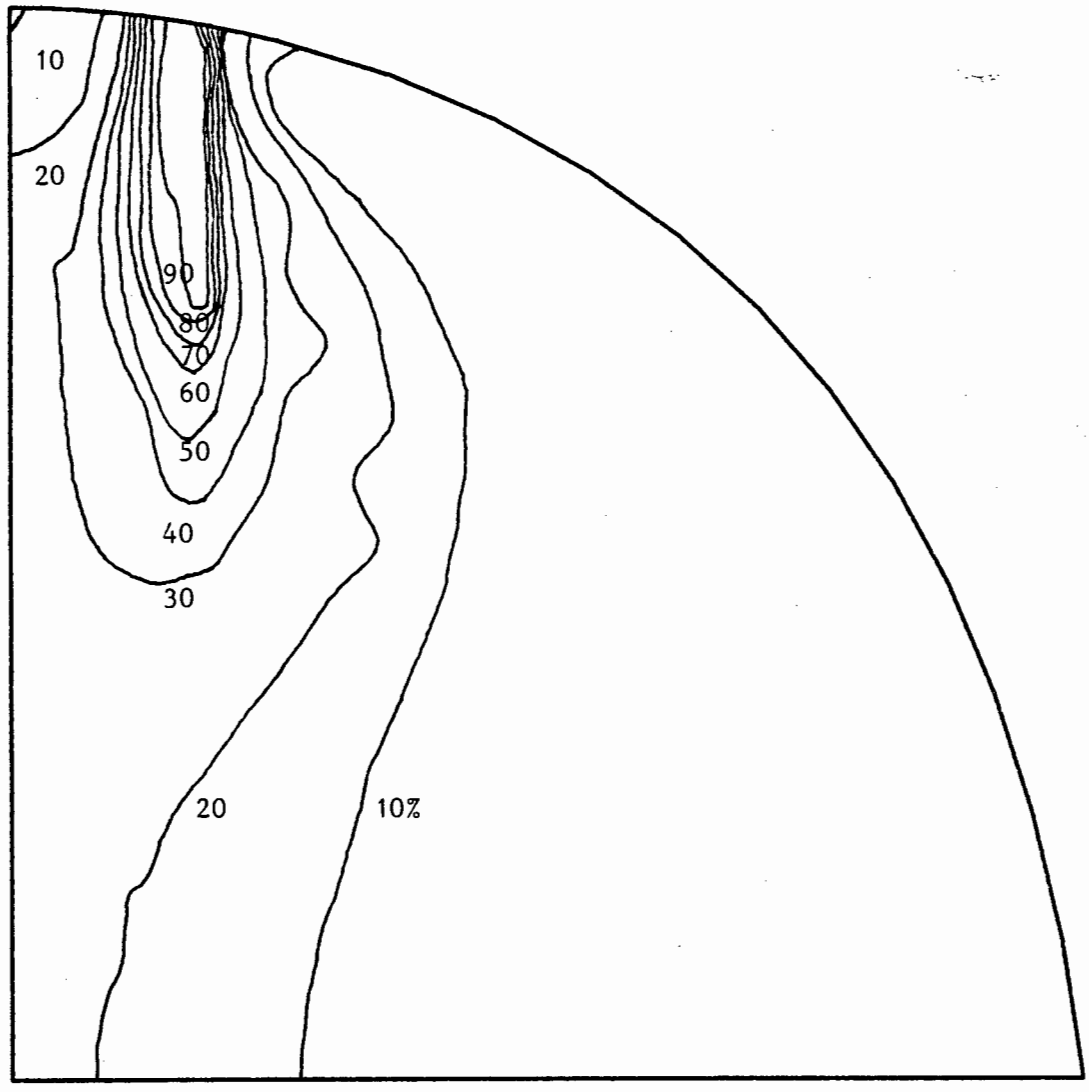

Figure 7.25: Brazilian test: percentage damage contours at end of test.

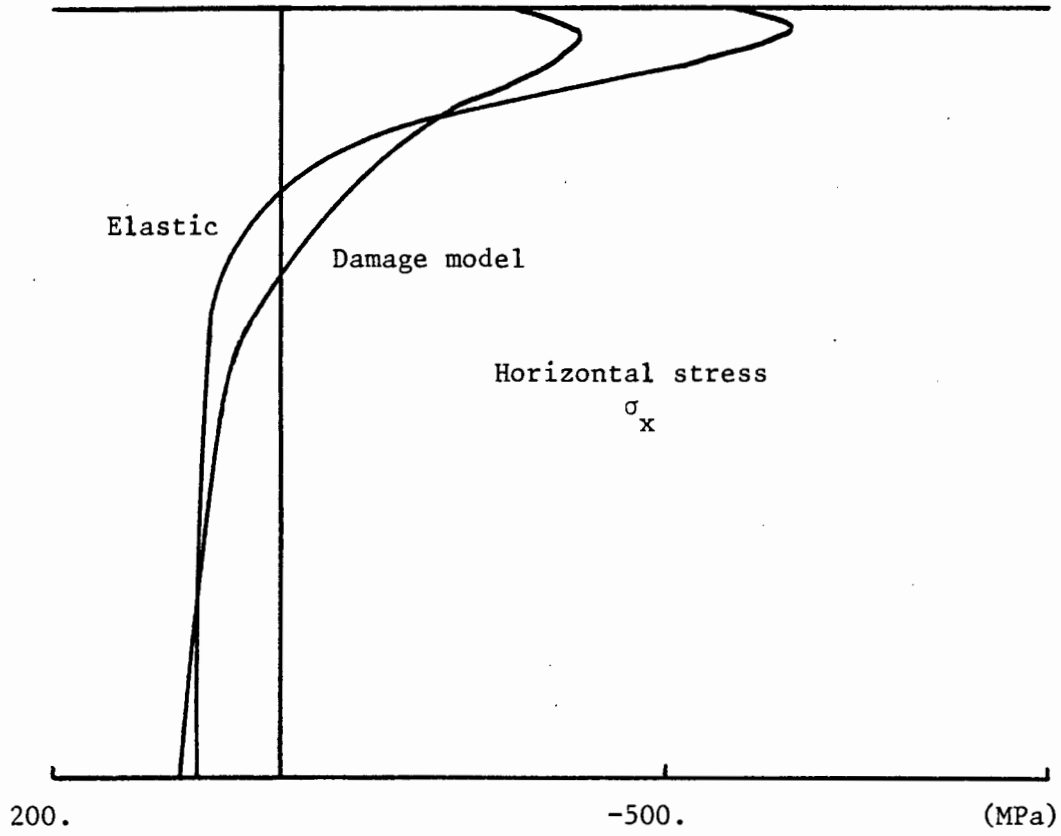

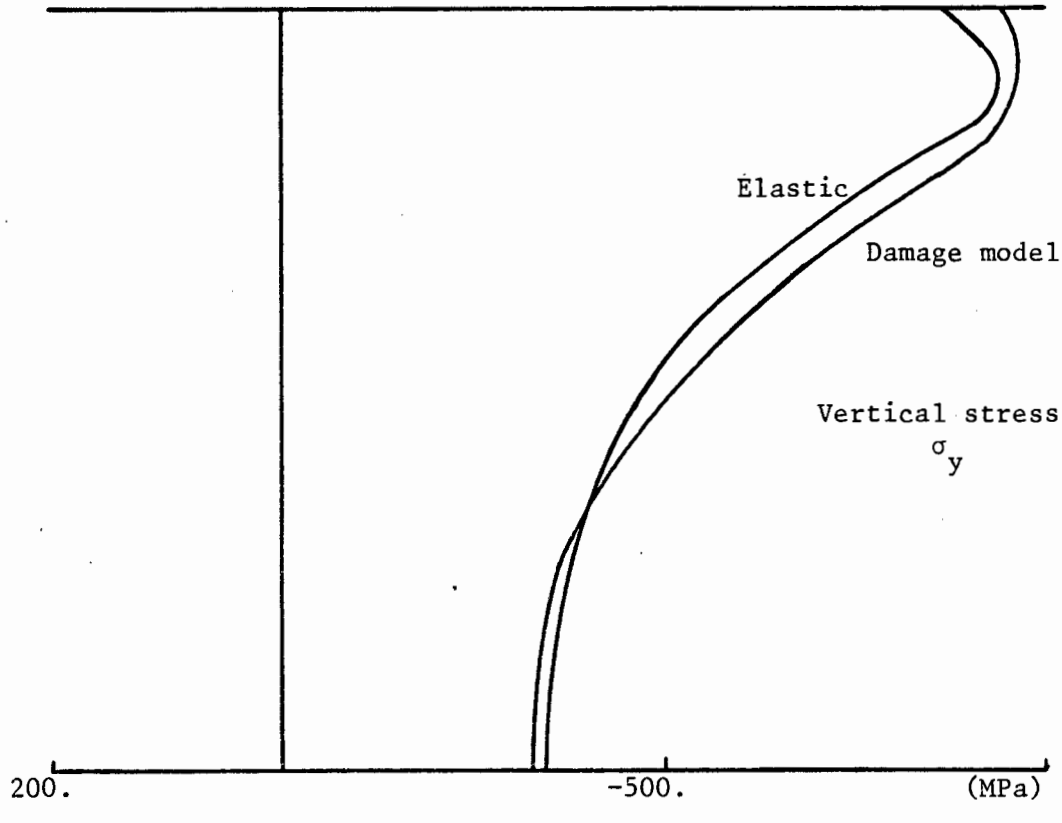

Figure 7.26(a): Brazilian test: stress distributions along loaded diameter.

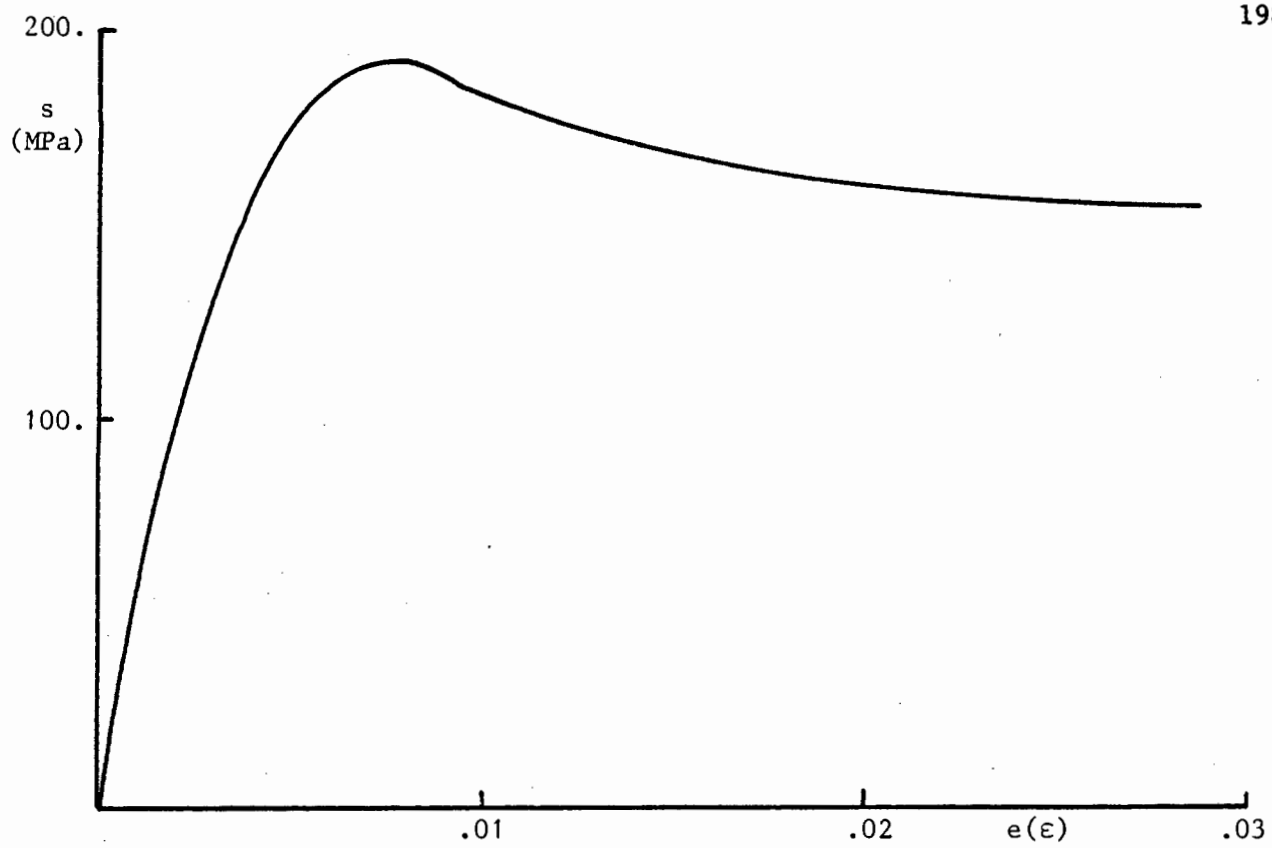

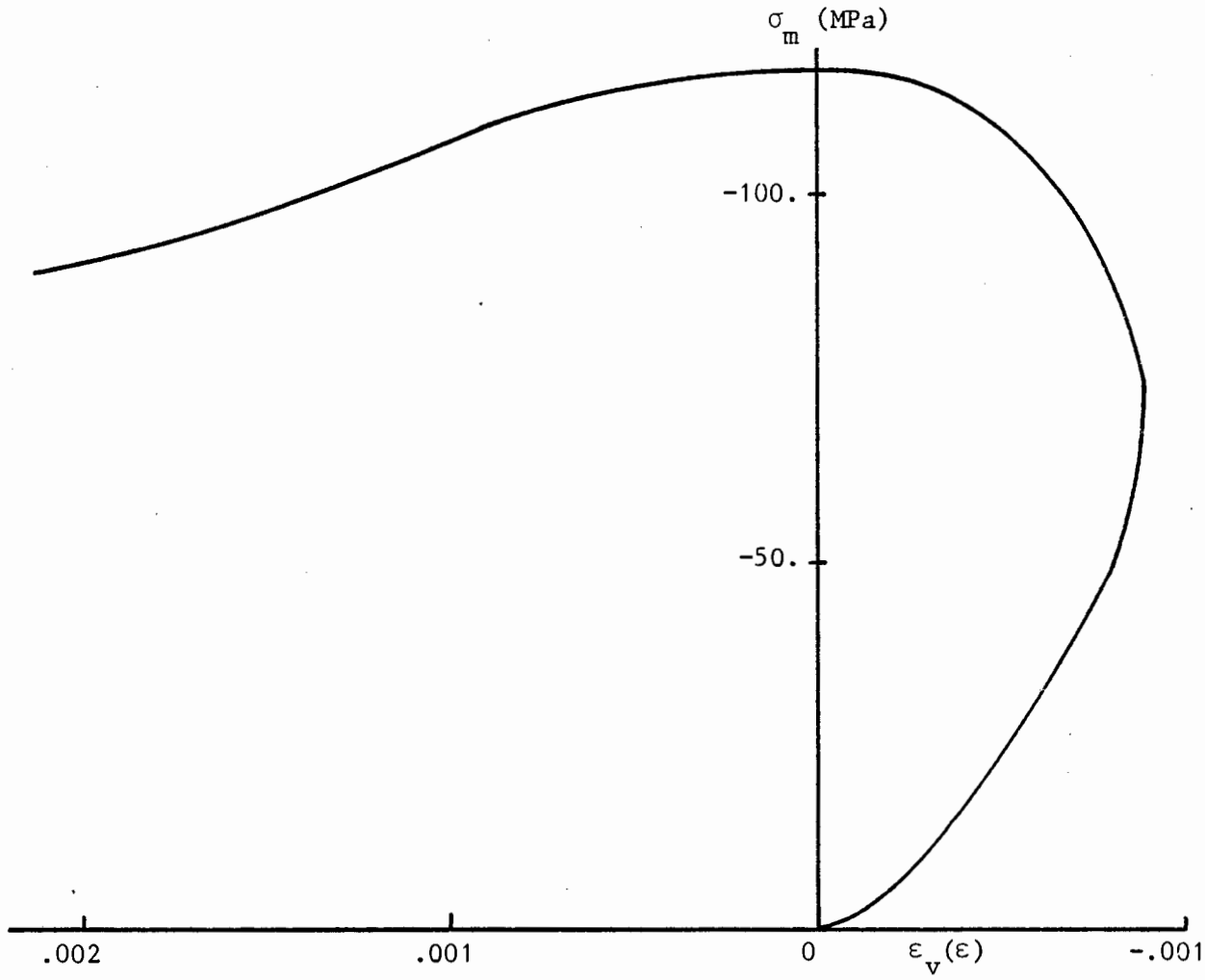

Figure 26(b): Brazilian test : history of invariant stress/strain for typical material point in the highly damaged (> 90%) area.

degree of damage sustained by the material at the end of the test is shown in Fig. 7.25 where a strong resemblance with the fracture pattern of Fig. 7.21(b) is clear. If the history of damage is followed through the test, the process of crack initiation and propagation can be traced. However, it is obvious that the present model will not predict individual cracks. It will rather show zones of highly concentrated damage where crack initiation and propagation are expected to occur. The horizontal and vertical stress distributions along the loaded diameter at the end of the test are given in Fig.7.26(a) where they are compared with the equivalent elastic predictions. As expected the vertical stress distributions are not very different while the horizontal stresses predicted by the damage model in the "cracked" region are greatly reduced. The invariant shear stress/strain history and the hydrostatic stress/ volumetric strain history for a typical material point in the "cracked" region (damage>90%) are shown in Fig 7.26(b) where the shear softening and dilatant characteristics of the damage model are evident.

7.4.2 Bridgman Anvil

The behaviour of a thin axisymmetric disc under uniform compression is investigated. The disc is composed of a frictional material (here it is assumed to have the properties of Norite), and is compressed into the inelastic range. Both experimental results and simple rigid-plastic theory indicate that the vertical stress component should increase exponentially with distance from the outer edge of the disc, giving a peak hydrostatic pressure plateau in the centre of the disc which is substantially higher than the average vertical stress. This pressure amplification is in fact the reason why this configuration is of interest [133].

The disc is modelled using the axisymmetric generator plane shown in Fig. 7.27 where an horizontal line of symmetry is also employed. Twenty eight-noded Serendipity quadrilaterals with 3x3 integration are used and the mesh has a total of 85 nodes. The loading is in the form of applied vertical displacements on the faces of the disc and the Norite material

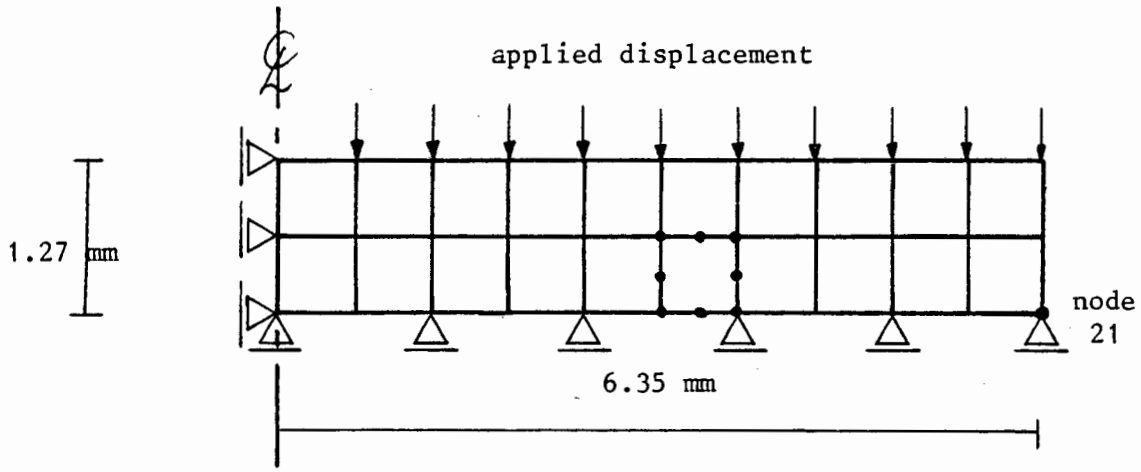

Figure 7.27: Finite element model of one quarter of Bridgman anvil.

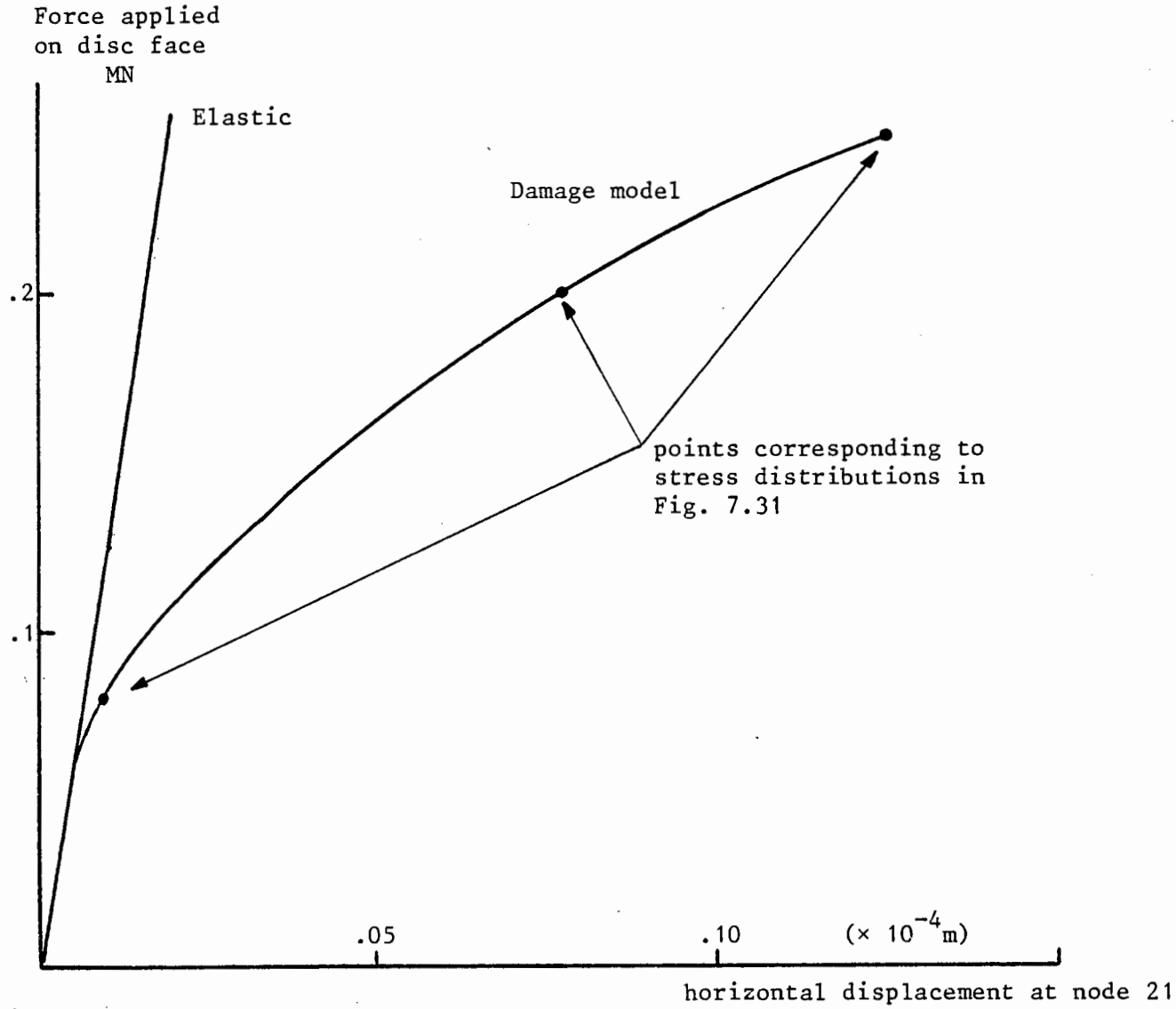

Figure 7.28: Bridgman anvil: load vs. deflection curve.

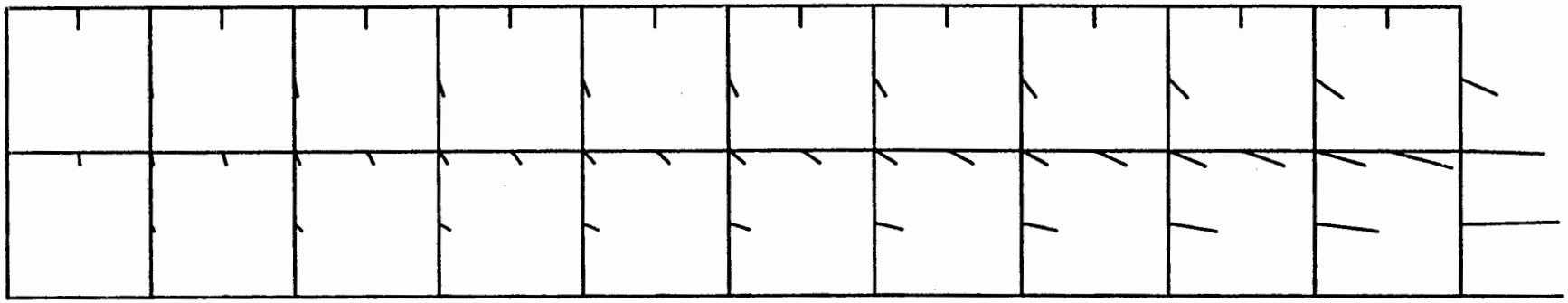

Figure 7.29: Bridgman anvil: velocity field at end of test.

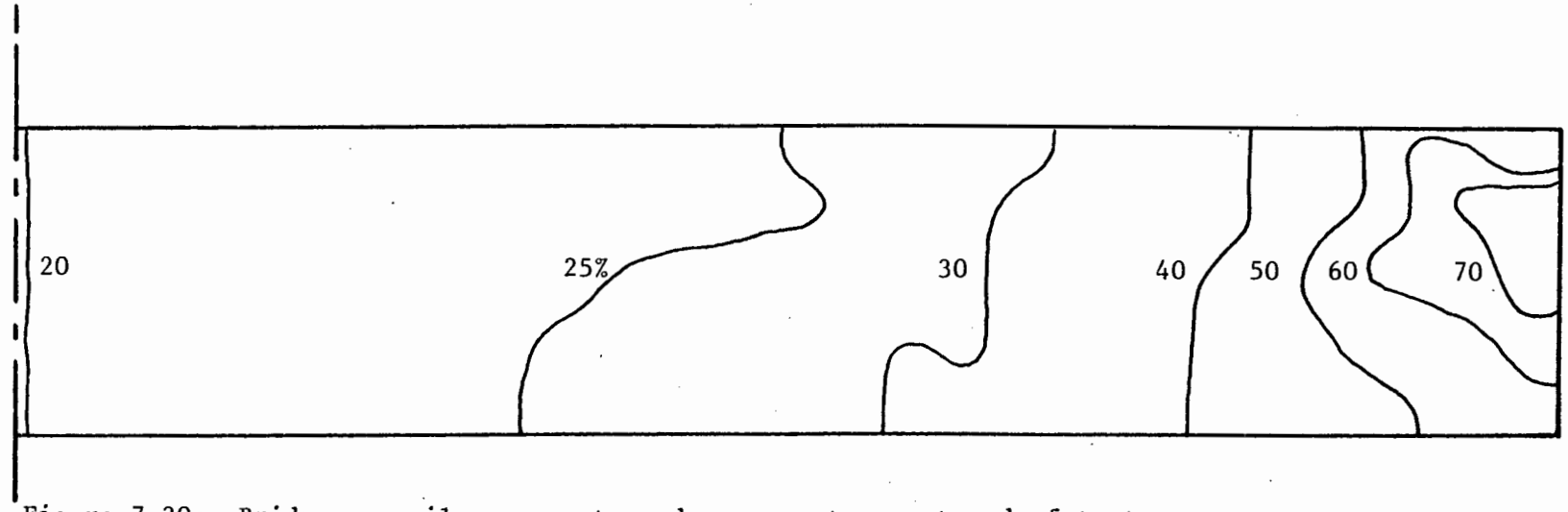

Figure 7.30: Bridgman anvil: percentage damage contours at end of test.

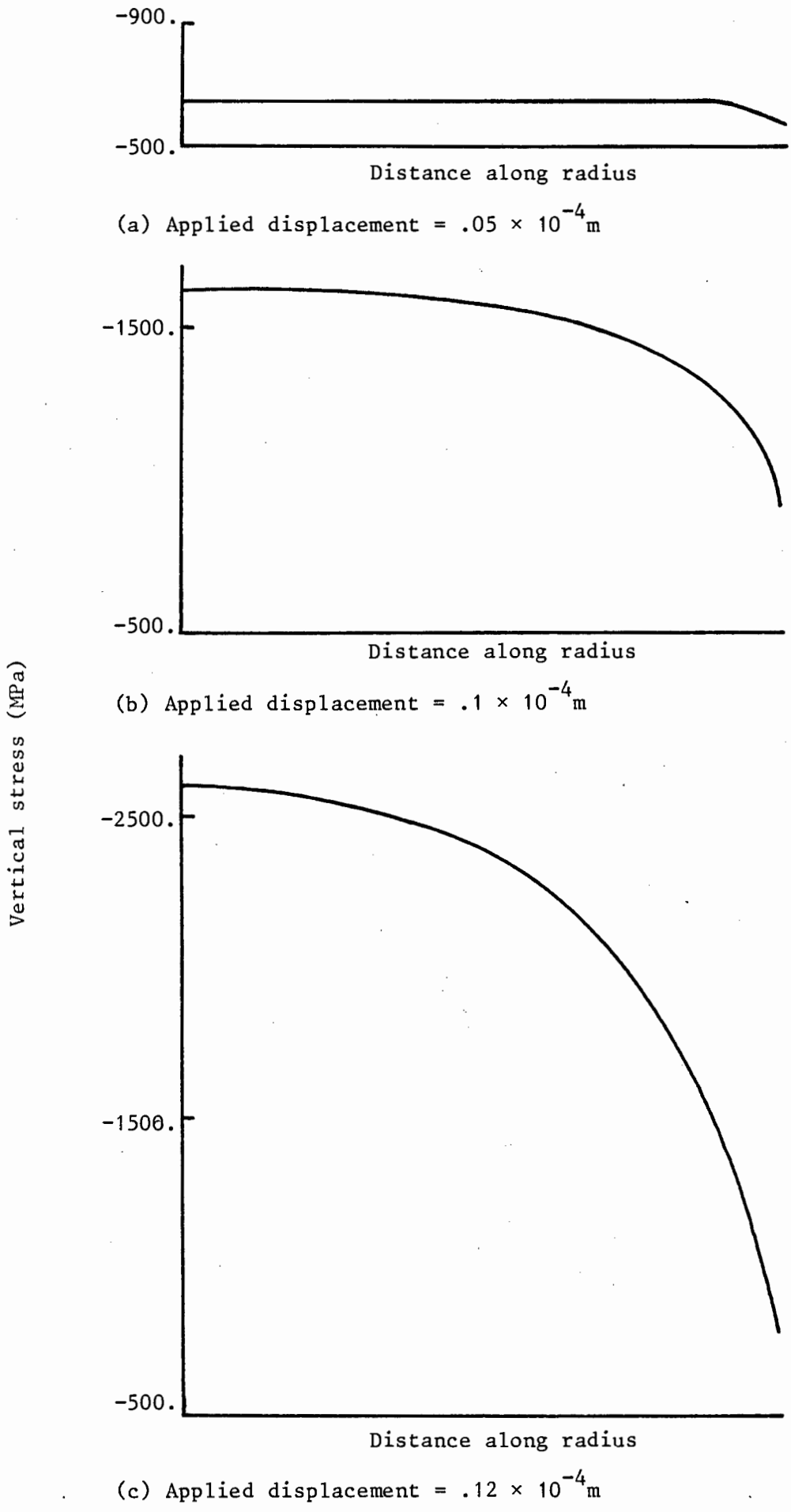

Figure 7.31: Bridgman anvil: vertical stress distribution along the horizontal centre line of disc.

parameters of equn (7.4) are used.

A load versus deflection curve is shown in Fig. 7.28 where the sum of the reactions of the nodes with non-zero prescribed displacements is plotted against the horizontal displacement of node 21. The velocity field at the end of the text is shown in Fig.7.29. Contours of damage sustained by the material are given in Fig. 7.30 where it is apparent that damage is most concentrated on the outer edge of the disc. This is consistent with the deformation pattern observed experimentally. Lastly, the vertical stress distribution along the row of Gauss points closest to the horizontal centre line of the disc is given in Fig. 7.31 for three different stages of the test. It is clear that the peak hydrostatic stress plateau is forming at the centre of the disc but the test has not been taken far enough to make the exponential stress distribution very clear. It is, however, interesting to note that this exponential stress distribution has indeed been obtained with a Drucker-Prager and the Drucker-Prager cap models [133].

CHAPTER 8

CONCLUSIONS AND DIRECTIONS FOR FUTURE WORK

This final chapter includes not only the conclusions drawn directly from the results of the work reported in this thesis, but also directions for future work based on the general experience acquired during the time over which this research spanned.

8.1 Conclusions

A fully coupled Drucker-Prager model with a parabolic hardening/softening cap and a perfectly plastic tension cutoff was developed using well established principles of plasticity theory. Although this model has some shortcomings with regard to the representation of geological material behaviour, it was found to contain a regime of potentially unstable behaviour (in the sense of Drucker's stability postulate) absent in previous cap model formulations. This arises when yielding occurs simultaneously on the Drucker-Prager cone and the cap and special attention was given to this condition. In attempting to eliminate the material instability, previous cap model formulations have led to inconsistent models. The consequences of this inconsistent treatment were illustrated and numerical examples were used to show that significantly different results can be obtained. The present cap model was implemented in a large scale finite element code and some realistic boundary value problems arising in geotechnical engineering were solved succesfully.

To overcome the limitations of plasticity based constitutive models for the representation of the mechanical behaviour of geomaterials, a model based on progressive internal damage was proposed. This model does not require a yield/fracture surface or a flow rule and thus the problems inherent to plasticity models of defining a realistic flow rule are eliminated. The damage model makes use of an internal variable representing the extent of internal damage and an evolution law defines the rate of damage. The volumetric strains are also defined in terms of the

damage parameter. As a first approximation this damage parameter was chosen to be a scalar quantity but nevertheless very satisfactory results were obtained. Various forms of damage evolution were investigated but this process must continue as more experience is gained with the model. However, it is important to note that different forms of the damage evolution law yielded similar results showing that the modelling fundamental physical phenomena was not affected by mathematical representation. This indicates that the model is a sound one.

Motivated by demands of the mining industry, the damage model was first calibrated for a very hard brittle rock, Bushveld Norite, and deep underground excavation problems of interest were solved successfuly using the damage model implemented in the NOSTRUM finite element code. Other configurations of interest were also investigated to evaluate the performance of the model and the results were good.

The two models investigated are based on assumptions of continuum material behaviour and thus certain material instabilities (for example, rock bursting as a result of localized deformation) cannot be modelled accurately. This is subject to some discussion in the next section on directions for further work.

8.2 Directions for Future Work

Directions for further work are discussed in three parts: firstly, the mechanics of constitutive behaviour of geological materials; secondly, the implementation of constitutive models in finite element codes for stress analysis; and finally, the experimental work thought to be necessary.

Regarding the mechanics of material behaviour, it is appropriate to start with the existing plasticity based models. The cap models seem the best for mainly hydrostatic loading while for mainly deviatoric loading, Prevost's model is best. The nested yield surfaces of Prevost's model and the bounding surface plasticity of Dafalias are concepts that go part of the way towards achieving the continuous material behaviour exhibited by

real geological materials. This group of continuous plasticity models warrants further investigation and the main problem areas can be identified as: (a) choice of flow rules in relation to different mechanisms of deformation - non-associated flow rules seem to be inevitable; (b) the transition between the deviatoric and hydrostatic ranges of mechanical response - the necessity, or otherwise, of yield surface corners is not clear. Nikolaevski and Rice [128] have given an excellent discussion of these problem areas in inelastic deformation of geological materials and their comments should be noted for further investigation.

Another obvious direction to pursue seems to be in the area of models based on continuous damage ideas. The damage model proposed in this thesis [129 - 130] is an example where it was shown that the problems associated with continuous inelasticity, inelastic volume behaviour (flow rules in plasticity) and transition between different regimes of behaviour can be overcome in a fairly simple manner. The question of if and when a tensorial measure of damage is necessary must be investigated. The possible advantages of a tensorial measure of damage must be weighted against the simplicity of a scalar damage measure. Lemaitre [132] indicates that much can be achieved with a simple scalar measure of damage.The development of the present damage model to concrete is now a topic of priority in terms of expanding the applicability of the model.

The study of the mechanics of localization of deformation represents a major step towards the modelling of material instabilities such as the ones leading to phenomena like rock bursting. Here, the fundamental work of Rice should be applied to the more sophisticated plasticity models as well as to the models based on damage. The work of Vardoulakis [131] represents a recent attempt in this area.

Finally, an attempt to reconcile continuum mechanics modelling and fracture mechanics modelling should constitute an important area of research. In this area, Lemaitre [132] suggests how continuum damage mechanics should be used and how it fits in with fracture mechanics.

As far as future developments in finite element implementation of

realistic constitutive models, it is clear that even the most complex models can be implemented. The real question is how expensive are they to implement and use for practical applications. Here attempts to reduce the number of material constants necessary for the more sophisticated models must be an important aspect. These material constants should also be chosen so that they can be easily identified from standard tests. Another area for further work is the investigation of better algorithms for the integration of the constitutive equations over the loading history.
Lastly, there are still gaps in the information that can be obtained from currently performed experimental tests. Special rigs are necessary to carry out non-standard tests that would supply the missing information. As stated previously, the development of experimental techniques must be undertaken in conjunction with the development of mechanics models.

In the particular case of Bushveld Norite, cyclic tests, tensile tests and hydrostatic compression tests over a broader range of stresses are still necessary for a complete calibration of the damage model.

REFERENCES

1. CHEN, W.F., 'Plasticity in Reinforced Concrete', McGraw-Hill, 1982.

2. CHEN, W.F. and SALEEB, A.F., 'Constitutive Equations for Engineering Materials', vol.1, 'Elasticity and Modelling', Wiley Interscience, 1982.

3. CHRISTIAN, J.T. and DESAI, C.S. 'Constitutive Laws for Geological Media', in Num. Meth. in Geotech. Eng. (Ed. C.S. Desai and J.T. Christian), 65-115, McGraw-Hill, 1977.

4. DESAI, C.S., 'Some Aspects of Constitutive Models for Geologic Media', Proc. 3rd Int. Conf. Num. Meth. Geomech., Aachen, (Ed. W. Wittke), 299-308, 1979.

5. DOUGILL, J.W., 'Constitutive Relations for Concrete and Rock: applications, and extensions of elasticity and plasticity theory', Prepr. William Prager Symp. Mechanics of Geomaterials: Rocks, Concretes, Soils, (Ed. Z.P. Bazant), 17-54, 1983.

6. MARTI, J. and CUNDALL, P.A., 'Constitutive Laws for Dynamic Modelling of Soils', Report for U.S. Air Force, Air Force Weapons Laboratory, January 1980.

7. NAYLOR, D.J., 'Stress-strain Laws for Soil', in Developments in Soil Mechanics - 1, (Ed. C.R. Scott), 39-68, 1978.

8. NELSON, I., 'Constitutive Models for Use in Numerical Computations', Proc. Conf. Dyn. Meth. Soil Rock Mech., (Ed. G. Gudehus), A.A. Balkema, 1978.

9. KONDNER, R.L., 'Hyperbolic Stress-strain Response: Cohesive Soils', Proc. ASCE, 82, (SM1), 115-143, 1963.

10. DUNCAN, J.M. and CHANG, C.Y., 'Nonlinear Analyses of Stress and Strain in Soils', Proc. ASCE, 96, (SM5), 1629-1653, 1970.

11. KULHAWY, F.H. and DUNCAN, J.M., 'Stresses and Movements in Oroville Dam', Proc. ASCE, 90, (SM7), 653-665, 1972.

12. SEED, H.B., DUNCAN, J.M. and IDRISS, I.M., 'Criteria and Methods for Static and Dynamic Analysis of Earth Dams', Proc. Int. Symp. Criteria and Assumptions for Num. Anal. of Dams, (Eds. D.J. Naylor, K.C. Stagg and O.C. Zienkiewicz), Swansea, 564-588, 1975.

13. NELSON, I. and BARON, M.L., 'Application of Variable Moduli Models to Soil Behaviour', Int. J. Sol. Struct., 7, 399-417, 1971.

14. HILL, R., 'The Mathematical Theory of Plasticity', Clarendon Press, Oxford, 1950.

15. MARTIN, J.B., 'Plasticity: Fundamentals and General Results', M.I.T. Press, 1975.

16. DRUCKER, D.C. and PRAGER, W., 'Soil Mechanics and Plastic Analysis or Limit Design', Quarterly Appl. Math., 10, 157-175, 1952.

17. GUDEHUS, G., 'Elasto-Plastische Stoffgleichungen fur Trockenen Sand', Ingenieur Archiv., 42, 1973.

18. ZIENKIEWICZ, O.C. and PANDE, G.N., 'Some Useful Forms of Isotropic Yield Surfaces for Soil and Rock Mechanics', Num. Meth. Soil Mech. Rock Mech., Vol.II, (Eds. G. Borm and H. Meissner), Karlsruhe, 3-16, 1976.

19. LADE, P.V. and DUNCAN, J.D., 'Elastoplastic Stress-Strain Theory for Cohensionless Soil', J. Geotech. Eng. Div., ASCE, 101, (GT10), 1037-1053, 1975.

20. BRESLER, B. and PISTER, K.S., 'Strength of Concrete Under Combined Stresses', J. Am. Concr. Inst., 55, 321-345, 1958.

21. WILLIAM, K.J. and WARNKE, E.P., 'Constitutive Models for the Triaxial Behaviour of Concrete', Int. Assoc. Bridge Struct. Eng. Proc., 19, 1-30, 1975.

22. OTTOSEN, N.S., 'A Failure Criterion for Concrete', J. Eng. Mech. Div., ASCE, 103, (EM4), 527-535, 1977.

23. REIMANN, H., 'Kritische Spannungszustande der Betons bei mehrachsiger, ruhender Kurzzeitbelastung', Dtsch. Auschuss Stahlbeton, 175, 1965.

24. HSIEH, S.S., TING, E.C. and CHEN, W.F., 'An Elastic-Fracture Model for Concrete', Proc. 3rd Eng. Mech. Div. Spec. Conf., ASCE, Austin, Texas, 437-440, 1979.

25. CHEN, W.F., 'Limit Analysis and Soil Plasticity', Elsevier, Amsterdam, 1975.

26. CHEN, A.C.T. and CHEN, W.F., 'Constitutive Relations for Concrete', J. Eng. Mech. Div., ASCE, 101, (EM4), 465-481, 1975.

27. ZIENKIEWICZ, O.C., HUMPHESON, C. and LEWIS, R.W., 'Associated and Non-associated Visco-plasticity and Plasticity in Soil Mechanics', Geotechnique, 25, (4), 671-689, 1975.

28. MIZUNO, E. and CHEN, W.F., 'Plasticity Analysis of Slope with Different Flow Rules', J. Comp. Struct. 17, (3), 375-388, 1983.

29. DRUCKER, D.C., GIBSON, R.E. and HENKEL, D.J., 'Soil Mechanics and Work-hardening Theories of Plasticity', Trans. Am. Soc. Civ. Eng., 122, 338-346, 1957.

30. DIMAGGIO, F.L. and SANDLER, I.S., 'Material Model for Granular Soils', J. Eng. Mech. Div., ASCE, 97, (EM3), 935-950, 1971.

31. SANDLER, I.S., DIMAGGIO, F.L. and BALADI, G.Y., 'Generalised Cap Model for Geological Materials', J. Geotech. Eng. Div., ASCE, 102, (GT7), 683-699, 1976.

32. SANDLER, I.S. and BARON, M.L., 'Recent Developments in the Constitutive Modelling of Geological Materials', Proc. 3rd Int. Conf. Num. Meth. in Geomech., (Ed. W. Wittke), A.A. Balkema, 363-376, 1979.

33. LADE, P.V., 'Elasto-Plastic Stress-Strain Theory for Cohesionless Soils with Curved Yield Surfaces', Int. J. Solids Struct., 13, 1019-1035, 1977.

34. LADE, P.V. 'Prediction of Undrained Behaviour of Sand', J. Geotech. Eng. Div., ASCE, 104, (GT6), 721-735, 1978.

35. RESENDE, L. and MARTIN, J.B., 'A Consistent Drucker-Prager Cap Model for Geotechnical Materials', Nonl. Struct. Mech. Res. Unit, Tech. Rep. No. 15, University of Cape Town, 1982.

36. RESENDE, L. and MARTIN, J.B., 'The Formulation of the Drucker-Prager Cap Model', J. Eng. Mech. Div., ASCE, to appear.

37. BATHE, K.J., SNYDER, M.D., CIMENTO, A.P. and ROLPH, W.D., 'On Some Current Procedures and Difficulties in Finite Element Analysis of Elasto-Plastic Response', J. Comp. Struct., 12, 607-624, 1980.

38. SANDLER, I.S. and RUBIN, D., 'An Algorithm and Modular Subroutine for the Cap Model', Int. J. Num. Anal. Meth. Geomech., 3, 173-186, 1979.

39. ROSCOE, K.H. and BURLAND, J.B., 'On the Generalised Stress-Strain Behaviour of Wet Clay', In Engineering Plasticity, (Eds. J. Heyman and F. Leckie), Cambridge Univ. Press, 539-609, 1968.

40. PREVOST, J.H., 'Mathematical Modelling of Monotonic and Cyclic Undrained Clay Behaviour', Int. J. Num. Anal. Meth. Geomech., 1, 195-216, 1977.

41. PREVOST, J.H. and HUGHES, T.J.R., 'Mathematical Modelling of Cyclic Soil Behaviour', ASCE Spec. Conf. Earth. Eng. Soil Dyn., Pasadena, California, 746-761, 1978.

42. MROZ, Z., 'On the Description of Anisotropic Workhardening', J. Mech. Phys. Solids, 15, 163-175, 1967.

43. MROZ, Z., 'An Attempt to Describe the Behaviour of Metals Under Cyclic Loads Using a More General Workhardening Model', Acta Mech., 7, 169-212, 1969.

44. PREVOST, J.H., 'Undrained Shear Tests on Clays', J. Geotech. Eng. Div., ASCE, 105, (GT1), 49-64, 1979.

45. PREVOST, J.H., 'Mathematical Modelling of Soil Stress-Strain-Strength Behaviour', Proc. 3rd Int. Conf. Num. Meth. Geomech., Aachen, (Ed. W. Wittke), A.A. Balkema, 347-362, 1979.

46. DAFALIAS, Y.F. and HERRMANN, L.R., 'Bounding Surface Formulation of Soil Plasticity', in Soil Mechanics - Transient and Cyclic Loads, (Eds. G.N. Pande and O.C. Zienkiewicz), John Wiley and Sons, 1982.

47. HERRMANN, L.R., DAFALIAS, Y.F. and DE NATALE, J.S., 'Numerical Implementation of a Bounding Surface Soil Plasticity Model', Proc. Int. Symp. Num. Models Geomech., Zurich, (Eds. R. Dungar, G.N. Pande and J.A. Studer), A.A. Balkema, 334-343, 1982.

48. PANDE, G.N. and PIETRUSZCZAK, ST., 'Reflecting Surface Model for Soils', Proc. Int. Symp. Num. Models Geomech., Zurich, (Eds. R. Dungar, G.N. Pande and J.A. Studer), A.A. Balkema, 50-64, 1982.

49. MROZ, Z., NORRIS, V.A. and ZIENKIEWICZ, O.C., 'An Anisotropic Hardening Model for Soils and its Application to Cyclic Loading', Int. J. Num. Anal. Meth. Geomech., 2, 203-221, 1978.

50. MROZ, Z., NORRIS, V.A. and ZIENKIEWICZ, O.C., 'Application of an Anisotropic Hardening Model in the Analysis of the Elasto-plastic Deformation of Soils', Geotechnique, 29, 1-34, 1979.

51. VALANIS, K.C., 'A Theory of Viscoplasticity Without a Yield Surface - Part I : General Theory', Arch. Mech., 23, (4), 517-533, 1971.

52. VALANIS, K.C., 'A Theory of Viscoplasticity Without a Yield Surface - Part II : Application to Mechanical Behaviour of Metals', Arch. Mech., 23, (4), 535-551, 1971.

53. VALANIS, K.C., 'A New Intrinsic Measure for the Endochronic Description of Plastic Behaviour', Int. J. Solids Struct., 14, 1978.

54. BAZANT, Z.P. and BHAT, P.D., 'Endochronic Theory of Inelasticity and Failure of Concrete', J. Eng. Mech. Div., ASCE, 102,(EM4), 701-722, 1976.

55. BAZANT, Z.P. and KRIZEK, R.J., 'Endochronic Constitutive Law for Liquefaction of Sand', J. Eng. Mech. Div., ASCE, 102, (EM2), 225-238, 1976.

56. DOUGILL, J.W., 'On Stable Progressive Fracturing Solids', J. Appl. Math. & Phys. (ZAMP), 27, 423-437, 1976.

57. LORRAIN, M. and LOLAND, K.E., 'Damage Theory Applied to Concrete', in Facture Mechanics of Concrete, (Ed. F.H. Wittmann), Elsevier, 341-369, 1983.

58. CHEN, W.F. and MIZUNO, E., 'On Material Constants for Soil and Concrete Models', Proc. 3rd ASCE/EMD Spec. Conf., Austin, Texas, 539-542, 1979.

59. MIZUNO, E. and CHEN, W.F., 'Cap Models for Clay Strata to Footing Loads', J. Comp. Struct., 17, (4), 511-528, 1983.

60. RESENDE, L. and MARTIN, J.B., 'A Review of the Consistent Treatment of the Constitutive Equations of Multisurface Plasticity', Nonl. Struct. Mech. Res. Unit Tech. Rep. No.34, University of Cape Town, 1983.

61. DRUCKER, D.C., 'Some Implications of Work-hardening and Ideal Plasticity', Quart. Appl. Math., 7, 411-418, 1950.

62. DRUCKER, D.C., 'On Uniqueness in the Theory of Plasticity', Quart. Appl.Math., 14, 35-42, 1956.

63. LADE, P.V., 'Three-dimensional Behaviour and Parameter Evaluation for an Elasto-Plastic Soil Model', Proc. Int. Symp. Num. Models Geomech., Zurich, (Eds. R. Dungar, G.N. Pande and J.A. Studer), A.A. Balkema, 33-37, 1982.

64. MAIER, G., 'Linear Flow Laws of Elastoplasticity: A Unified General Approach', Acc. Naz. Lincei, Rendic. Sci. Se. 8, 67, (5), 1969.

65. DESAI, C.S., PHAN, H.V. and STURE, S., 'Procedure, Selection and Application of Plasticity Models for a Soil', Int. J. Num. Analyt. Meth. Geomech., 5, 295-311, 1981.

66. MAIER, G., 'A Quadratic Programming Approach for Certain Classes of Nonlinear Problems', Meccanica, Vol.III, (2), 1968.

67. MAIER, G., 'A Matrix Structural Theory of Piecewise-linear Plasticity with Interacting Yield Planes', Meccanica, Vol.V, (1), 1970.

68. MROZ, Z. and SHARMA, K.G., 'Finite Element Applications of Viscoplasticity with Singular Yield Surfaces', Int. J. Num. Meth. Engng., 15, 421-436, 1980.

69. ZIENKIEWICZ, O.C. and CORMEAU, I.C., 'Vicsoplasticity-Plasticity and Creep in Elastic Solids - A Unified Numerical Solution Approach', Int. J. Num. Meth. Engng., 8, 821-845, 1975.

70. ZIENKIEWICZ, O.C. and PANDE,G.N., 'Time-dependent Multi-laminate Model for Rocks : A Numerical Study of Deformation and Failure of Rock Masses', Int. J. Num. Analyt. Meth. Geomech., 1, 219-247, 1977.

71. HUGHES, T.J.R. and TAYLOR, R.L., 'Unconditionally Stable Algorithms for Quasi-static Elasto/viscoplastic Finite Element Analysis', J.Comp. Struct., 8, 169-173, 1978.

72. DAMJANIC, F. and OWEN, D.R.J., 'Implicit Time Integration of Elasto-viscoplastic Solids Subject to the Mohr-Coulomb Yield Criterion', Int. J. Num. Meth. Engng., 18, 1873-1881, 1982.

73. DINIS, L.M.S. and OWEN, D.R.J., 'Elasto-Viscoplastic Analysis of Plates by the Finite Element Method', J. Comp. Struct., 8, 207-215, 1978.

74. KOITER, W.T., 'Stress-strain Relations,Uniqueness and Variational Theorems for Elastic-Plastic Materials with a Single Yield Surface', Quart. Appl. Math., 11, 350-354, 1953.

75. MANDEL, J., 'Generalisation de la Theorie de la Plasticite de W.T. Koiter', Int. J. Solids Struct., 1, 273-295, 1965.

76. MROZ, Z., 'On Forms of Constitutive Laws for Elastic-Plastic Solids', Anchiwum Mechaniki Stosowaney, I, (18), 1966.

77. MAIER, G., 'Sui Legami Associati tra Sforzi e Deformazioni Incrementali in Elastoplasticita', Rendic. Ist. Lomb., 1966.

78. DUFFETT, G.A., GRIFFIN, T.B., MARTIN, J.B., MERCER, C.D., REDDY, B.D. and RESENDE, L., 'NOSTRUM - A Finite Element Program for Nonlinear Structural Mechanics', Nonl. Struct. Mech. Res. Unit Tech. Rep. No.18B, University of Cape Town, 1983.

79. NOSTRUM User's Manual, Version 3.1, Appl. Mech. Res. Unit (formerly Nonl. Struct. Mech. Res. Unit), University of Cape Town, July 1984.

80. NOSTRUM Theoretical Manual, Nonl. Struct. Mech. Res. Unit, University of Cape Town, February 1982.

81. NOSTRUM Applications Manual, Appl. Mech. Res. Unit (formerly Nonl. Struct. Mech. Res. Unit), University of Cape Town, (in preparation).

82. NOSTRUM System Manual, Appl. Mech. Res. Unit, University of Cape Town, (in preparation).

83. BATHE, K-J, 'Finite Element Procedures in Engineering Analysis', Prentice-Hall, 1982.

84. OWEN, D.R.J. and HINTON, E., 'Finite Elements in Plasticity - Theory and Practice', Pineridge Press, 1980.

85. ZIENKIEWICZ, O.C., 'The Finite Element Method', 3rd edition, McGraw-Hill, 1977.

86. RESENDE, L. 'A Review of Infinite Elements', Nonl. Struct. Mech. Res. Unit Tech. Rep. No.20, University of Cape Town, 1982.

87. ADINA - A Finite Element Program for Automatic Dynamic Incremental Nonlinear Analysis, Report AE81-1, ADINA Engineering, September 1981.

88. SIRIWARDANE, H.J. and DESAI, C.S., 'Implementation of Some Constitutive Laws for Three- and Two-dimensional Analysis', Proc. Symp. Implementation Comp. Procedures and Stress-Strain Laws in Geotech. Engng., Chicago, Illinois, (Eds. C.S. Desai and S.K. Saxena), Vol.II, 479-501, 1981.

89. LADE, P.V. and NELSON, R.B., 'Incrementalization Procedure for Elasto-Plastic Constitutive Model with Multiple, Simultaneous Yield Surfaces', Proc.Symp. Implementation Comp. Procedures and Stress-strain Laws in Geotech. Engng., Chicago, Illinois, (Eds. C.S. Desai and S.K. Saxena), Vol.II, 503-518, 1981.

90. MIZUNO, E. and CHEN, W.F., 'Plasticity Models and Finite Element Implementation', Proc. Symp. Implementation Comp. Procedures and Stress-strain Laws in Geotech. Engng., Chicago, Illinois, (Eds. C.S. Desai and S.K. Saxena). Vol.II, 519-533, 1981.

91. MIZUNO, E. and CHEN, W.F., 'Cap Models for Clay Strata to Footing Loads', J. Comp. Struct., 17, (4), 511-528, 1983.

92. MARQUES, J.M.M.C. and OWEN, D.R.J., 'Infinite Elements in Quasi-Static Materially Nonlinear Problems', J. Comp. Struct., to appear.

93. RESENDE, L., BIRD, W.W., MARAIS, N.J. and WISWE, B.K.R., 'Application of Elastic-Plastic and Elastic-Viscoplastic Models to Geotechnical Problems', Proc. Symp. Fin. Elem. Meth. in South Africa, Pretoria, 211-239, January 1984.

94. BIRD, W.W., M.Sc. Thesis, Department of Civil Engineering, University of Cape Town, (in preparation).

95. MARAIS, N.J., B.Sc. Thesis, Department of Civil Engineering, University of Cape Town, 1983.

96. WISWE, B.K.R., B.Sc. Thesis, Department of Civil Engineering, University of Cape Town, 1983.

97. BIENIAWSKI, Z.T., 'Mechanism of Brittle Fracture of Rock', Parts I-III, Int. J. Rock Mech. Min. Sci., 4, 395-430, 1967.

98. BIENIAWSKI, Z.T., DENKHAUS, H.G. and VOGLER, U.W., 'Failure of Fractured Rock', Int. J. Rock Mech. Min. Sci., 6, 323-346, 1970.

99. COOK, N.G.W., 'Failure of Rock', Int. J. Rock Mech. Min. Sci., 2, 289-403, 1965.

100. CROUCH, S.L., 'Experimental Determination of Volumetric Strains in Failed Rock', Int. J. Rock Mech. Min. Sci., 7, 589-603, 1970.

101. BIENIAWSKI, Z.T., 'Deformational Behaviour of Fractured Rock Under Multiaxial Compression', in Structure, Solid Mechanics and Engineering Design, (Ed. M. Te'eni), Proc. Southampton Civil Eng. & Mat. Conf., 589-598, 1969.

102. WAWERSIK, W.R. and FAIRHURST, C., 'A Study of Brittle Rock Fracture in Laboratory Compression Experiments', Int. J. Rock Mech. Min. Sci., 7, 561-575, 1970.

103. BRACE, W.F., PAULDING, B.W., Jr. and SCHOLZ, C., 'Dilatancy in the Fracture of Crystalline Rocks', J. Geophys. Res., 71, 3939-3953, 1966.

104. HUECKEL, T., 'A Model for Dilatant Rock Behaviour under Variable Loading', Proc. Int. Symp. Num. Models, Geomech. Zurich, (Eds. R. Dungar, G.N. Pande and J.A. Studer), 198-207, 1982.

105. STAVROPOULOU, V., 'Constitutive Laws for Brittle Rocks', Ph.D. Thesis, University of the Witwatersrand, Johannesburg, 1982.

106. DOUGILL, J.W., LAU, J.C. and BURT, N.J., 'Towards a Theoretical Model for Progressive Failure and Softening in Rock, Concrete and Similar Materials', in Mechanics in Engineering, (Eds. R.N. Dubey and N.C. Lind), 335-355, Univ. of Waterloo Press, 1977.

107. SPOONER, D.C. and DOUGILL, J.W., 'A Quantitative Assessment of Damage Sustained in Concrete During Compressive Loading', Mag. Conc. Res., 27, 151-160, 1975.

108. HAWLA, D.L., 'Analysis of Reinforced Concrete Using NLFRAM', Proc. Symp. Fin. Elem. Meth. in South Africa, Pretoria, 92-122, January 1984.

109. MAIER, G. and HUECKEL, T., 'Nonassociated and Coupled Flow Rules of Elastoplasticity for Rock-like Materials', Int. J. Rock Mech. Min. Sci. & Geomech. Abstr., 16, 77-92, 1979.

110. DRAGON, A. and MROZ, Z., 'A Continuum Model for Plastic Brittle Behaviour of Rock and Concrete', Int. J. Engng. Sci., 17, 121-137, 1979.

111. GEROGIANNOPOULOS, N.G. and BROWN, E.T., 'The Critical State Concept Applied to Rock', Int. J. Rock Mech. Min. Sci. & Geomech. Abstr., 15, 1-10, 1978.

112. CHANG, K.J. and YANG, T.W., 'A Constitutive Model for the Mechanical Properties of Rock', Int. J. Rock Mech. Min. Sci. & Geomech. Abstr. 19, 123-133, 1982.

113. DOUGILL, J.W., 'Some Remarks on Path Independence in the Small in Plasticity', Q. Appl. Math., 33, 233-243, 1975.

114. DOUGILL, J.W., 'On Stable Progressive Fracturing Solids', J. Appl. Math. & Phys. (ZAMP), 27, 423-437, 1976.

115. DOUGILL, J.W. and RIDA, M.A.M., 'Further Considerations of Progressively Fracturing Solids', J. Eng. Mech. Div., ASCE, 106, (EM5), 1021-1038, 1980.

116. BAZANT, Z.P. and KIM, S.S., 'Plastic-Fracturing Theory for Concrete', J. Eng. Mech. Div., ASCE, 105, (EM3), 407-428, 1979.

117. RUDNICKI, J.W. and RICE, J.R., 'Conditions for the Localization of Deformation in Pressure-Sensitive Dilatant Materials', J. Mech. Phys. Solids, 23, 371-394, 1975.

118. RICE, J.R., 'On the Stability of Dilatant Hardening for Saturated Rock Masses', J. Geophys. Res., 80, 1531-1536, 1975.

119. KUPFER, H.B. and GERSTLE, K.H., 'Behaviour of Concrete Under Biaxial Stresses', J. Eng. Mech. Div., ASCE, 99, (EM4), 853-866, 1973.

120. CEDOLIN, L., CRUTZEN, Y.R.J. and DEI POLI, S., 'Triaxial Stress-Strain Relationship for Concrete', J. Eng. Mech. Div., ASCE, 103, (EM3), 423-439, 1977.

121. 'Finite Element Analysis of Reinforced Concrete', State-of-the-art Report prepared by Task Committee on Fin. El. Anal. R.C. Struct. of the Struct. Div. Com. on Concr. Masonry Struct., ASCE, 1982.

122. GOODMAN, L.E. and BROWN, C.B., 'Dead Load Streses and Instability of Slopes', J. Soil. Mech. Found. Eng. Div., ASCE, 89, (SM3), 1963.

123. GHABOUSSI, J. and RANKEN, R.E., 'Finite Element Simulation of Underground Construction', Proc. Symp. Implementation Comp. Procedures and Stress-Strain Laws in Geotech. Engng., Chicago, Illinois, (Eds. C.S. Desai and S.K. Saxena), Vol.I, 253-265, 1981.

124. KULHAWY, F.H., 'Finite Element Modeling Criteria for Underground Openings in Rock', Int. J. Rock Mech. Min. Sci. & Geomech. Abstr., 11, 465-472, 1974.

125. PEIRCE, A.P., 'The Applicability of the Nonlinear Boundary Element Method in the Modelling of Mining Excavations', M.Sc. Thesis, University of the Witwatersrand, Johannesburg, 1983.

126. BEER, G., 'Infinite Domain Elements in Finite Element Analysis of Underground Excavations', Int. J. Num. Analyt. Meth. Geomech., 7, 1-7, 1983.

127. JAEGER, J.C. and COOK, N.G.W., 'Fundamentals of Rock Mechanics', 3rd Edition, Champman and Hall, London, 1979

128. NIKOLAEVSKII, V.N. and RICE, J.R., 'Current Topics in Nonelastic Deformation of Geological Materials', Proc. 6th AIRAPT Conf. on High-Pressure Science and Technology, Boulder, Colorado, (Eds. K.D. Timmerhaus and M.S. Barber), Vol.2, 455-464, 1977.

129. RESENDE, L. and MARTIN, J.B., 'A Progressive Damage Continuum Model for Granular Materials', Comp. Meth. Appl. Mech. Engng., 42, 1-18, 1984.

130. RESENDE, L. and MARTIN, J.B., 'Damage Constitutive Model for Geotechnical Applications', Int. Conf. Num. Meth. Transient and Coupled Problems, Venice, (Eds. R.W. Lewis, E. Hinton, P. Bettess and B.A. Schrefler), 475-497, 1984.

131. VARDOULAKIS, I., 'Rock Bursting as a Surface Instability Phenomenon', Int.J. Rock Mech. Min. Sci. & Geomech. Abstr., 21, No.3, 137-144, 1984.

132. LEMAITRE, J., 'How to Use Damage Mechanics', Nucl. Eng. Design, 80, 233-245, 1984.

133. MARTIN, J.B. and RESENDE, L., 'Numerical Calculations of the Stress Distribution in the Bridgman Anvil', Rep. to De Beers Diamond Research Laboratory, February 1983.

APPENDIX A

SECOND ORDER WORK

The constitutive model in Chapter 3 is formulated in terms of the invariants s, σ_m and $\dot{e}$, $\dot{\varepsilon}_v$. In terms of these invariants the second order work is

$$\dot{s}\,\dot{e} + \dot{\sigma}_m\,\dot{\varepsilon}_v,$$

and it is necessary to relate this expression to the actual second order work

$$\dot{\sigma}_{ij}\,\dot{\varepsilon}_{ij} = \dot{s}_{ij}\,\dot{e}_{ij} + \frac{1}{3}\,\dot{\sigma}_{kk}\,\dot{\varepsilon}_{kk} = \dot{s}_{ij}\,\dot{e}_{ij} + \dot{\sigma}_m\,\dot{\varepsilon}_v \qquad \text{(A.1)}$$

The contribution from the deviators can be written in terms of elastic and plastic strain rate contributions;

$$\dot{s}_{ij}\,\dot{e}_{ij} = \dot{s}_{ij}\,\dot{e}^{e}_{ij} + \dot{s}_{ij}\,\dot{e}^{p}_{ij}\,, \qquad \text{(A.2a)}$$

$$\dot{s}\,\dot{e} = \dot{s}\,\dot{e}^{e} + \dot{s}\,\dot{e}^{p}\,. \qquad \text{(A.2b)}$$

Using equns. (3.8b), (3.12) and (3.14b), we see that

$$\dot{s}_{ij}\,\dot{e}^{p}_{ij} = \dot{s}_{ij}\,\frac{\lambda_\alpha}{2s}\,\frac{\partial F_\alpha}{\partial s}\,s_{ij} = \frac{1}{2s}\,s_{ij}\,\dot{s}_{ij}\,\lambda_\alpha\,\frac{\partial F_\alpha}{\partial s}$$

$$= \dot{s}\,\dot{e}^{p}$$

Further, from equns. (3.2) and (3.14a),

$$\dot{s}_{ij}\,\dot{e}^{e}_{ij} = \frac{1}{2G}\,\dot{s}_{ij}\,\dot{s}_{ij} \qquad \text{(A.4a)}$$

whereas

$$\dot{s}\,\dot{e}^{e} = \frac{1}{G}\,\dot{s}^2 = \frac{1}{2G}\,\frac{(s_{ij}\,\dot{s}_{ij})(s_{k\ell}\,\dot{s}_{k\ell})}{s_{mn}\,s_{mn}}\,. \qquad \text{(A.4b)}$$

It is evident from simple geometric arguments that

$$\dot{s}\,\dot{e}^{e} \leq \dot{s}_{ij}\,\dot{e}^{e}_{ij} , \tag{A.5}$$

and thus

$$\dot{s}\,\dot{e} + \dot{\sigma}_{m}\,\dot{\varepsilon}_{v} \leq \dot{\sigma}_{ij}\,\dot{\varepsilon}_{ij} . \tag{A.6}$$

APPENDIX B

TREATMENT OF THE CONSTITUTIVE EQUATIONS IN MULTISURFACE PLASTICITY

There are many situations in which one would like to use multisurface plasticity models. The most obvious case is for materials that reasonably obey the classical Tresca or Coulomb yield conditions. Another case refers to the very wide class of geotechnical materials for which different inelastic mechanisms operate at different stress conditions. For instance, the basic Drucker-Prager yield surface is often combined with an intersecting tension cut off yield surface or an intersecting compression cap yield surface [31, 36]. A further case is that of the piecewise-linear yield surfaces of Maier [66-67] which are required in order to formulate plasticity problems using a quadratic programming approach.

One of the important ingredients of the behaviour of plasticity models at singular points is the nature of the yield surface coupling. This coupling depends on the definition of the yield surfaces and different forms of coupling will be illustrated in this review. The character of the flow rules at singular points also influences the corner behaviour in plasticity models. Mroz and Sharma [68] have given useful comparisons of the response of visco-plastic models with different corner flow rules and conclude that the choice of flow rule can greatly affect the deformation mode of the material and to a lesser extent its load-displacement response. This is particularly important in boundary value problems involving flow of granular materials where the load levels can greatly exceed the loads corresponding to first yield and corner behaviour is very predominant.

In many of the present computer applications of plasticity and visco-plasticity [69-73] the corner flow rules have been simplified by averaging the inelastic strain rate vectors from each of the yield surfaces intersecting at the singular point or edge. This leads to a corner behaviour which is overconstrained and eliminates certain corner

regimes which might be important (such a case is studied in Section 3 of this Appendix). This averaging procedure is certainly not legitimate from a theoretical point of view while its physical desirability is doubtful. In formulating cap models for geotechnical materials, Sandler et al [31] and Bathe et al [37] also overconstrain corner behaviour by imposing additional assumptions on the plastic strain rate vector at the intersection of the Drucker-Prager and cap yield surfaces. This results in certain inconsistencies which are reported in Chapter 3 of this thesis.

In Appendix B, we review firstly the formulation of the equations of multisurface plasticity and secondly the classification of constitutive laws of multisurface plasticity. Finally, some important points are highlighted by means of simple illustrations of the treatment of singular yield surfaces.

B.1 Formulation of Equations in Multisurface Plasticity

For the sake of simplicity we will develop the equations in principal stress space. We define the vector of principal stresses as

$$\sigma_i = [\sigma_1 \ \sigma_2 \ \sigma_3]^T , \tag{B.1a}$$

and the corresponding principal strains as

$$\varepsilon_i = [\varepsilon_1 \ \varepsilon_2 \ \varepsilon_3]^T ; \tag{B.1b}$$

$\dot{\sigma}_i$, $\dot{\varepsilon}_i$ denote principal stress and strain rates respectively.

Referring to Fig. B.1, the elastic region is defined in stress space as the domain in which all F_j, $j = 1 \ldots\ldots N$, are negative; $F_j(\sigma_i, \varepsilon_i^p)$ being a vector of N plastic yield functions. The yield locus is represented by the set of points for which at least one of the components of F_j is zero while the others are negative. The vector OY defines the current stress state σ_i^Y as a yield point at the intersection of n active yield surfaces. The active yield surfaces (active meaning

---

Based on these assumptions, Maier [64] derives a wide class of flow

constitutive laws that govern the incremental behaviour for deformation histories starting from point Y. We will now review these.
The strain rate vector is written as the sum of an elastic and a plastic component,

$$\dot{\varepsilon}_i = \dot{\varepsilon}_i^e + \dot{\varepsilon}_i^p \tag{B.4}$$

where the elastic component is given by

$$\dot{\varepsilon}_i^e = (D^{-1})_{ik}\, \dot{\sigma}_k \,. \tag{B.5}$$

D_{ik} is a symmetric positive-definite elasticity matrix and together with N_{ji} and V_{ji} may depend on the state of stress and strain and on the previous history, but does not depend on their rates. The plastic component of the strain rate is given as the sum of the contributions of the n yield modes and it lies in the fan of V_{ji},

$$\dot{\varepsilon}_i^p = V_{ji}\, \lambda_j \quad (j = 1 \ldots n) \tag{B.6}$$

where λ_j are non-negative plastic multipliers.

In the present context, it is assumed that the yield functions $F_j(\sigma_i, \varepsilon_i^p)$ contain terms which depend on the stress state and on the plastic strains arising from all possible yield mechanisms (it should be noted that this does not constitute the most general form of yield surface, but it is adequate to illustrate our point). Thus, we can write the yield function as

$$\dot{F}_j = \frac{\partial F_j}{\partial \sigma_i}\, \dot{\sigma}_i - \frac{\partial F_j}{\partial \varepsilon_i^p}\, \dot{\varepsilon}_i^p \tag{B.7a}$$

or

$$\dot{F}_j = N_{ji}\, \dot{\sigma}_i - H_{jk}\, \lambda_k \quad (j,k = 1 \ldots n) \tag{B.7b}$$

where

$$H_{jk} = \frac{\partial F_j}{\partial \varepsilon_i^p}\, \frac{\partial G_k}{\partial \sigma_i} = \frac{\partial F_j}{\partial \varepsilon_i^p}\, V_{ki} \tag{B.7c}$$

is an $n \times n$ matrix of history dependent, rate independent coupling coefficients. H_{jk} then defines how the activation of yield mode k changes yield surface F_j. Reciprocal coupling of yield surfaces corresponds to $H_{jk} = H_{kj}$, while a diagonal H_{jk} matrix implies uncoupled yield surfaces. H_{jk} also determines whether hardening or softening behaviour is present. Due to the fact that the stress point cannot go outside the yield locus we can write

$$F_j \lambda_j = 0 \text{ (no summation).} \tag{B.8}$$

The constitutive laws can be written from equns. (B.4 - B.6) as

$$\dot{\varepsilon}_i = \left(D^{-1}\right)_{ik} \dot{\sigma}_k + V_{ji} \lambda_j \qquad (j = 1 \ldots n) , \tag{B.9}$$

which upon inverting yields

$$\dot{\sigma}_i = D_{ik} \dot{\varepsilon}_k - D_{i\ell} V_{j\ell} \lambda_j \qquad (j,\ell = 1 \ldots n) \tag{B.10a}$$

with $\lambda_j = \lambda_j(\dot{\varepsilon}_k)$. The constitutive laws are completed by the following constraint conditions.

$$-\dot{F}_k = (H_{kj} + N_{ki} D_{i\ell} V_{j\ell})\lambda_j - N_{ki} D_{i\ell} \dot{\varepsilon}_\ell \quad \begin{matrix}(k,j = 1 \ldots n)\\ (i,\ell = 1 \ldots 3)\end{matrix} \tag{B.10b}$$

$$\lambda_j \geq 0 \tag{B.10c}$$

$$\dot{F}_k \leq 0 \tag{B.10d}$$

and

$$\dot{F}_k \lambda_k = 0 \qquad \text{(no summation).} \tag{B.10e}$$

Eq. (B.10b) is obtained from equns. (B.7b) and (B.10a).

Equations (B.10), as proposed by Maier [64], represent a very general class of constitutive flow laws: they allow singular points in the yield surface, general coupling of yield modes, hardening and softening behaviour and non-associated flow rules.

In this section the constitutive relations were written as stress in

terms of strain rates since this inverse flow law is the one we need to implement plasticity solutions using the finite element displacement method.

B.2 Classification of Constitutive Laws

To identify particular cases of this very general class of constitutive laws, Maier [64] suggests three criteria for classification. Firstly, on the direction of the plastic strain rate vector:

(I) : Associated flow rules (i.e. normality); $V_{ji} = N_{ji}$

(II) : Non-associated flow rules; $V_{ji} \neq N_{ji}$ is allowed.

Secondly, on the nature of the yield surface coupling:

(α) : Regular point on yield surface; $n = 1$; N_{ji}, V_{ji} become vectors and F_j, G_j, H_{jk} become scalars.

(β) : Singular point on yield surface without coupling; $n > 1$; H_{jk} is a diagonal matrix.

(γ) : Singular point on yield surface with reciprocal coupling; $n > 1$; H_{jk} is a symmetric matrix.

(δ) : Singular point on yield surface with general (non-reciprocal) coupling; $n > 1$; H_{jk} is a non-symmetric matrix.

Thirdly, on the movement of the yield surfaces:

(A) : Non-softening behaviour; H_{jk} is a non-negative definite matrix.

(B) : Softening behaviour; H_{jk} can be not positive definite.

The combination of the particular choices in each of the three criteria characterises the type of constitutive law. The classical metal plasticitry Von Mises law is identified as (I,α,A) and represents the least general plasticity law. Koiter [74] has dealt with laws of the

(I,β,A) kind where there is no coupling between yield surfaces. Mandel's [75] generalisation of Koiter's theory produces laws that can be classified as (I,δ,A). Mroz [76] has investigated non-associated non-softening laws without yield surface coupling (II,β,A). Constitutive laws involving softening, unstable behaviour of the (II,α,B) kind have been studied by Maier [77]. Finally, the cap model constitutive equations derived in Chapter 3 can be classified as (I,δ,B).

B.3 Illustrations

In order to illustrate the treatment of the equations of multi-surface plasticity, exercises with simple yield surfaces will be carried out. These exercises highlight the important points of the theory described in the earlier sections. The illustrations are carried out in the space of the mean hydrostatic stress σ and the second invariant of the stress deviator s. The conjugate strain quantities are volumetric strain ε and deviator strain e (c.f. Section 3.2 for the definition of the stress and strain quantities). This choice of quantities is quite arbitrary and does not affect the basic principles.

Throughout the exercises, we assume the plastic strain rate vector to be associated.

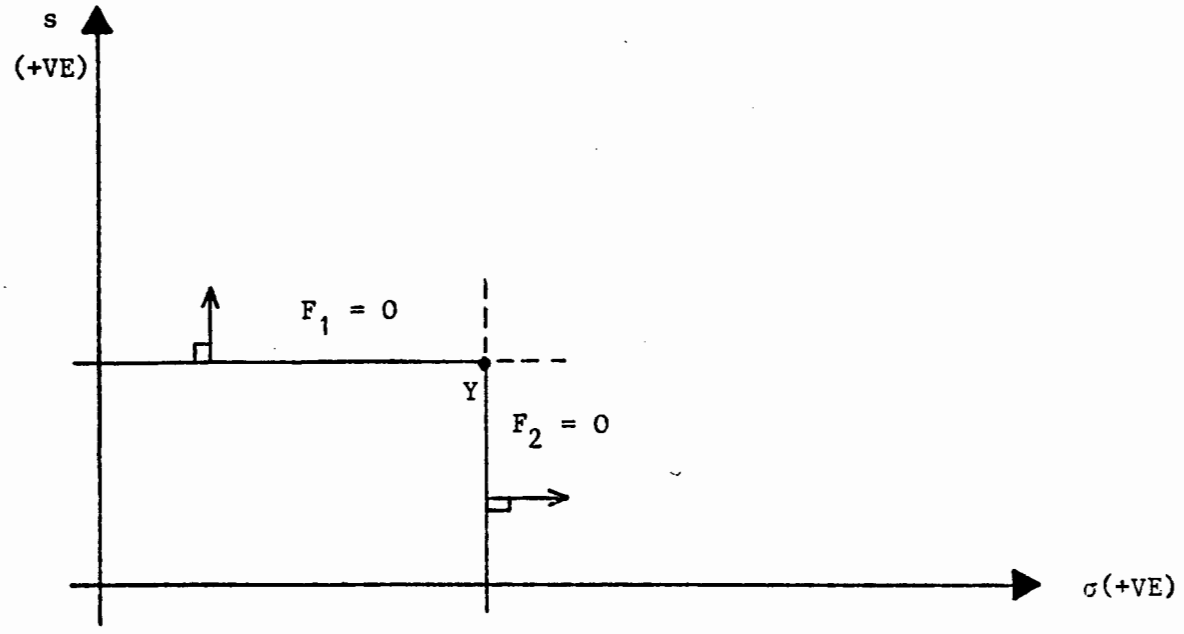

Figure B.2 : Yield surface.

Consider a stress point Y at the intersection of yield surfaces F_1 and F_2 in figure B.2. We seek to write the constitutive equations and associated constraints for all possible yield mechanisms starting from stress point Y. This is done for three different categories of yield surfaces: in the first instance we define the yield surfaces F_1 and F_2 as uncoupled; the second choice involves non-reciprocal coupling of the yield surfaces; finally, we write the yield surfaces as coupled but assume an average plastic strain rate vector for the yield mechanism under which both surfaces are loading.

Before proceeding we write the following basic relations:

$$\dot{e}^p = \dot{e}_1^p + \dot{e}_2^p = \lambda_1 \frac{\partial F_1}{\partial s} + \lambda_2 \frac{\partial F_2}{\partial s} \qquad (B.11)$$

$$\dot{\varepsilon}^p = \dot{\varepsilon}_1^p + \dot{\varepsilon}_2^p = \lambda_1 \frac{\partial F_1}{\partial \sigma} + \lambda_2 \frac{\partial F_2}{\partial \sigma} \; ;$$

the yield mode on surface F_1 occurs when

$$\dot{F}_1 = 0 \qquad (B.12a)$$

and similarly, F_2 is loading when

$$\dot{F}_2 = 0 \; ; \qquad (B.12b)$$

the elastic relations are (c.f. Section 3.2)

$$\dot{s} = G(\dot{e} - \dot{e}^p) \qquad (B.13)$$

$$\dot{\sigma} = K(\dot{\varepsilon} - \dot{\varepsilon}^p) \; ;$$

and finally we define the plastic works

$$W_1^p = \int (s\ \dot{e}_1^p + \sigma\ \dot{\varepsilon}_1^p)\ dt$$

$$W_2^p = \int (s\ \dot{e}_2^p + \sigma\ \dot{\varepsilon}_2^p)\ dt \qquad \text{(B.14)}$$

$$W^p = \int (s\ \dot{e}^p + \sigma\ \dot{\varepsilon}^p)\ dt\ .$$

For the first case (uncoupled yield surfaces), we define the yield surfaces as

$$F_1 = s - W_1^p \qquad \text{(B.15)}$$

$$F_2 = \sigma - W_2^p\ .$$

Then, the plastic strain rates are

$$\dot{e}^p = \lambda_1 \qquad \text{(B.16)}$$

$$\dot{\varepsilon}^p = \lambda_2\ .$$

For the yield mechanism corresponding to both yield surfaces loading we must have

$$\dot{F}_1 = \dot{s} - s\ \dot{e}_1^p = \dot{s} - s\lambda_1 = 0 \qquad \text{(B.17)}$$

$$\dot{F}_2 = \dot{\sigma} - \sigma\ \dot{\varepsilon}_2^p = \dot{\sigma} - \sigma\lambda_2 = 0\ .$$

Writing equns. (B.17) in the matrix form of equn. (B.17b)

$$\begin{bmatrix} \dot{F}_1 \\ \dot{F}_2 \end{bmatrix} = \begin{bmatrix} 1 & 0 \\ 0 & 1 \end{bmatrix} \begin{bmatrix} \dot{s} \\ \dot{\sigma} \end{bmatrix} - \begin{bmatrix} s & 0 \\ 0 & \sigma \end{bmatrix} \begin{bmatrix} \lambda_1 \\ \lambda_2 \end{bmatrix}\ , \qquad \text{(B.18)}$$

we recognise a constitutive law of the (I,β,A) kind. In addition we have the elastic relations.

$$\dot{s} = G(\dot{e} - \lambda_1) \qquad (B.19)$$

$$\dot{\sigma} = K(\dot{\varepsilon} - \lambda_2)$$

which can be substituted into equns. (B.17) to give

$$\lambda_1 = \frac{G\dot{e}}{G + s}$$

$$\lambda_2 = \frac{K\dot{\varepsilon}}{K + \sigma} \cdot \qquad (B.20)$$

Substitute back into (B.19), to get

$$\begin{bmatrix} \dot{s} \\ \dot{\sigma} \end{bmatrix} = \begin{bmatrix} G - \frac{G^2}{G + s} & 0 \\ 0 & K - \frac{K^2}{K + \sigma} \end{bmatrix} \begin{bmatrix} \dot{e} \\ \dot{\varepsilon} \end{bmatrix} \cdot \qquad (B.21)$$

Note that the plastic strain rate vector is always uniquely defined. Similar manipulations give the constitutive equations for the other three possible corner yield mechanisms:

$$\dot{F}_1 = 0, \quad \dot{F}_2 < 0$$

$$\dot{F}_1 < 0, \quad \dot{F}_2 = 0$$

$$\dot{F}_1 < 0, \quad \dot{F}_2 < 0 \quad \text{(elastic unloading).}$$

The four sets of corner constitutive equations for this first choice of yield surfaces are summarised in figure B.3(a). Note that the loading/unloading constraints for each mode of behaviour are given in terms of total strain rates.

In the second case of coupled yield surfaces, we define the yield functions as

$$F_1 = s - W^p$$
$$F_2 = \sigma - W^p \,. \tag{B.22}$$

From (B.11), the plastic strain rates are

$$\dot{e}^p = \lambda_1$$
$$\dot{\varepsilon}^p = \lambda_2 \tag{B.23}$$

and for the mechanism under which both F_1 and F_2 are loading we have

$$\dot{F}_1 = \dot{s} - s\dot{e}_1^p - \sigma\dot{\varepsilon}_2^p = \dot{s} - s\lambda_1 - \sigma\lambda_2 = 0$$
$$\dot{F}_2 = \dot{\sigma} - s\dot{e}_1^p - \sigma\dot{\varepsilon}_2^p = \dot{\sigma} - s\lambda_1 - \sigma\lambda_2 = 0 \,. \tag{B.24}$$

If we write (B.24) in matrix form

$$\begin{bmatrix} \dot{F}_1 \\ \dot{F}_2 \end{bmatrix} = \begin{bmatrix} 1 & 0 \\ 0 & 1 \end{bmatrix} \begin{bmatrix} \dot{s} \\ \dot{\sigma} \end{bmatrix} - \begin{bmatrix} s & \sigma \\ s & \sigma \end{bmatrix} \begin{bmatrix} \lambda_1 \\ \lambda_2 \end{bmatrix} \,, \tag{B.25}$$

we recognise a (I,δ,A) constitutive law where the non-reciprocal nature of the coupling is apparent from the non-symmetry of the $\begin{bmatrix} s & \sigma \\ s & \sigma \end{bmatrix}$ matrix.

From the form of equn. (B.24) we note (i) loading on both surfaces can only occur when $\dot{s} = \dot{\sigma}$; (ii) in this case λ_1, λ_2 cannot be uniquely determined in terms of $\dot{s}$, $\dot{\sigma}$ alone. The elastic relations

$$\dot{s} = G(\dot{e} - \lambda_1)$$
$$\dot{\sigma} = K(\dot{\varepsilon} - \lambda_2) \tag{B.26}$$

are substituted into (B.24), and solving for λ_1, λ_2 we obtain

$$\lambda_1 = \frac{(K + \sigma)G\dot{e} - K\sigma\dot{\varepsilon}}{GK + Ks + G\sigma}$$

$$\lambda_2 = \frac{-sG\dot{e} + (G + s)K\dot{\varepsilon}}{GK + Ks + G\sigma} \quad . \tag{B.27}$$

Now we note that there is no lack of uniqueness of λ_1, λ_2. Substituting equns. (B.27) back into (B.26), we get the stress strain relation

$$\begin{bmatrix} \dot{s}' \\ \dot{\sigma} \end{bmatrix} = \begin{bmatrix} \frac{GKs}{GK + Ks + G\sigma} & \frac{GK\sigma}{GK + Ks + G\sigma} \\ \frac{GKs}{GK + Ks + G\sigma} & \frac{GK\sigma}{GK + Ks + G\sigma} \end{bmatrix} \begin{bmatrix} \dot{e} \\ \dot{\varepsilon} \end{bmatrix} \tag{B.28}$$

which confirms that $\dot{s} = \dot{\sigma}$ for both yield surfaces loading. Again, we can derive the equations for the full spectrum of behaviour at the singular point Y and the result is summarised in figure B.3(b).

Lastly, let us consider the situation when the yield surfaces are coupled (as in the previous case) but the plastic strain rate vector for the case when both yield surfaces are loading is calculated by averaging the plastic strain rate vectors of the two individual yield surfaces for the case when they are independently loading. We define the yield functions as in equn. (B.22).

$$F_1 = s - W^p$$

$$F_2 = \sigma - W^p \tag{B.29}$$

and write the averaged plastic strain rates (for the case when both F_1 and F_2 are loading) as

$$\dot{e}^p = \frac{1}{2}\lambda\frac{\partial F_1}{\partial s} + \frac{1}{2}\lambda\frac{\partial F_2}{\partial s} = \frac{1}{2}\lambda \quad ,$$

$$\dot{\varepsilon}^p = \frac{1}{2}\lambda\frac{\partial F_1}{\partial \sigma} + \frac{1}{2}\lambda\frac{\partial F_2}{\partial \sigma} = \frac{1}{2}\lambda \quad . \tag{B.30}$$

The conditions for yielding on both surfaces are

$$\dot{F}_1 = \dot{s} - (s\dot{e}^p + \sigma\dot{\varepsilon}^p) = \dot{s} - \frac{1}{2}(s+\sigma)\lambda = 0 \qquad \text{(B.31a)}$$

$$\dot{F}_2 = \dot{\sigma} - (s\dot{e}^p + \sigma\dot{\varepsilon}^p) = \dot{\sigma} - \frac{1}{2}(s+\sigma)\lambda = 0 \qquad \text{(B.31b)}$$

and again this requires $\dot{s} = \dot{\sigma}$.
The elastic relations are

$$\dot{s} = G(\dot{e} - \frac{1}{2}\lambda) \qquad \text{(B.32a)}$$

$$\dot{\sigma} = K(\dot{\varepsilon} - \frac{1}{2}\lambda) \quad . \qquad \text{(B.32b)}$$

Substituting equn. (B.32a) into equn. (B.31a) and solving for λ we obtain

$$\lambda = \frac{2G\dot{e}}{G+s+\sigma} \qquad \text{(B.33a)}$$

which when substituted back into equn. (B.32a) gives

$$\dot{s} = \frac{G(s+\sigma)}{G+s+\sigma}\dot{e} \quad . \qquad \text{(B.33b)}$$

Similarly, equns. (B.31b) and (B.32b) yield

$$\lambda = \frac{2K\dot{\varepsilon}}{k+s+\sigma} \qquad \text{(B.33c)}$$

and

$$\dot{\sigma} = \frac{K(s+\sigma)}{K+s+\sigma}\dot{\varepsilon} \quad . \qquad \text{(B.33d)}$$

Equality of λ requires

$$\frac{2G\dot{e}}{G+s+\sigma} = \frac{2K\dot{\varepsilon}}{K+s+\sigma} \qquad \text{(B.34)}$$

and we note that this also gives $\dot{s} = \dot{\sigma}$.

If we now look at $F_1 = F_2 = 0$, $\dot{s} < \dot{\sigma}$ and $F_1 = F_2 = 0$, $\dot{s} > \dot{\sigma}$ we find the same range of behaviour for loading on F_1 only, loading on F_2 only and elastic unloading as before. We are then left with a gap in the $\dot{e}$, $\dot{\varepsilon}$ space which is not accounted for, as can be seen in Figure

B.3(c). This means that by choosing the average plastic strain rate vector, we have overconstrained the behaviour at the singular point and thus the model has been rendered incomplete.

The averaging of the plastic strain rate vector at singular points is only one of the methods used currently which results in an overconstrained formulation of the constitutive equations. Bathe et al [37] for example, when deriving the compression corner constitutive relations for the Drucker-Prager cap model also overconstrain the behaviour of the model. As well as imposing additional assumptions on the plastic strain rate vector, they calculate the values of the plastic multipliers λ_1 and λ_2 for the case when both yield surfaces are loading as the sum of the solutions for the Drucker-Prager loading alone and the cap loading alone. It is shown in Chapter 3 that this results in behaviour which is inconsistent with the definition of the yield functions and more important, it leads to the elimination from the model of a certain regime of behaviour which is potentially unstable.

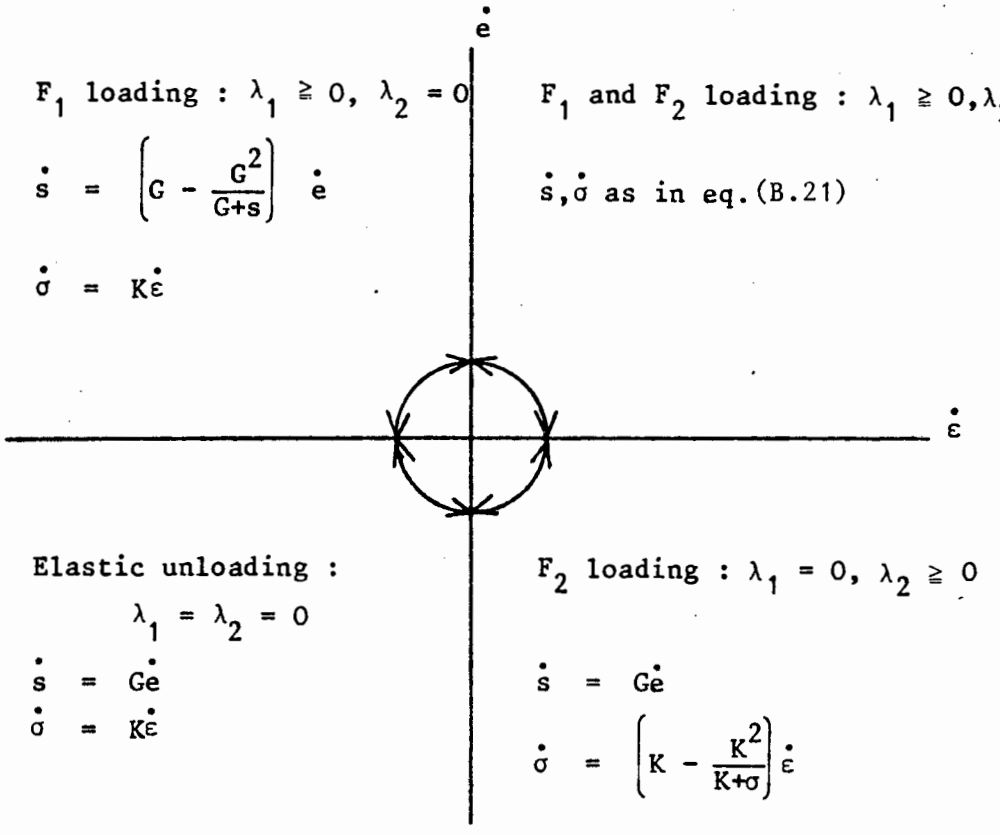

(a) Uncoupled yield surfaces

Figure B.3: Constitutive behaviour and constraints in total strain rate space.

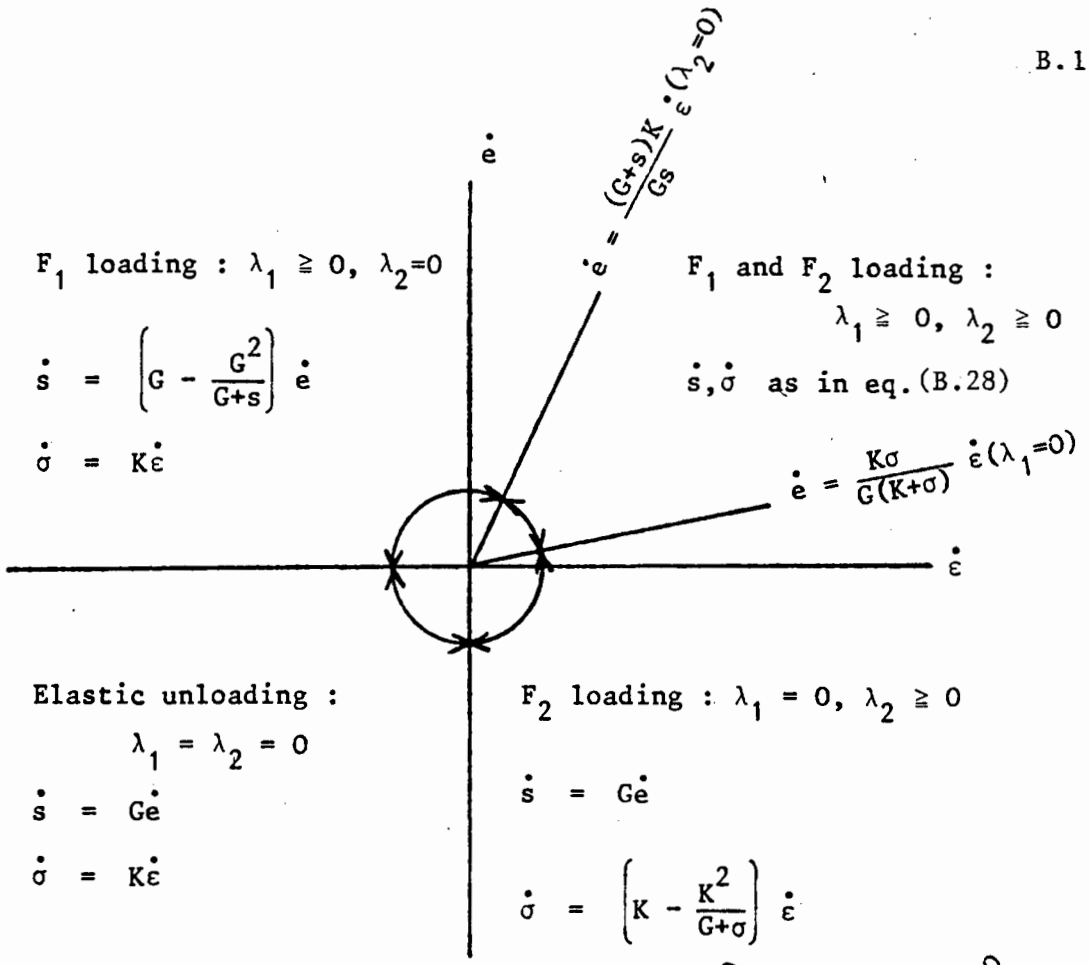

(b) Coupled yield surfaces

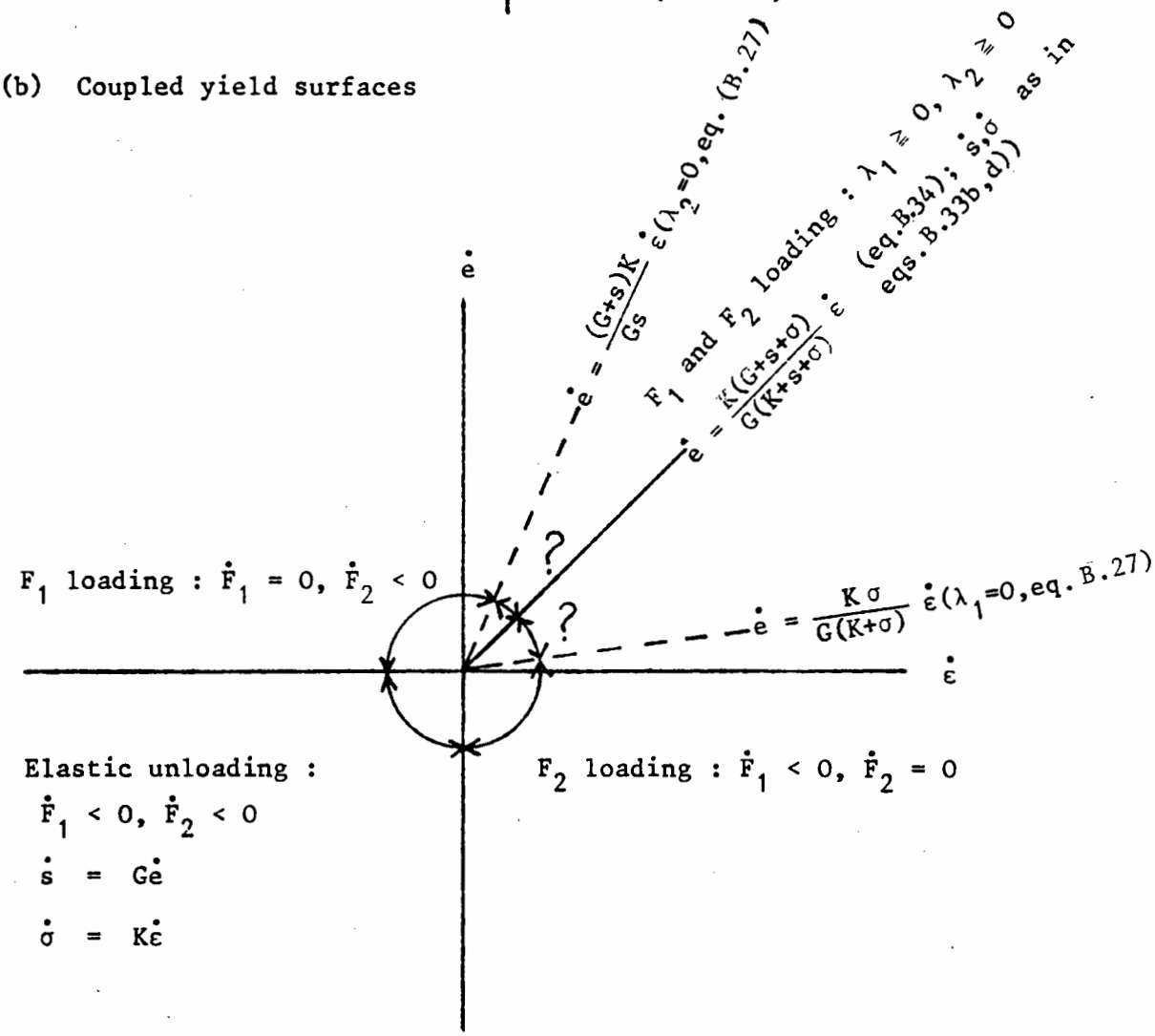

(c) Coupled yield surfaces with average strain rate vector

Figure B.3: Constitutive behaviour and constraints in total strain rate space.

APPENDIX C

EXTRACTS FROM NOSTRUM USER'S MANUAL

In this appendix we include brief extracts from the NOSTRUM User's Manual [79] describing the input parameters necessary to define the constitutive models developed and used in the present work. These include the Mohr-Coulomb, Drucker-Prager, and Cap plasticity models and the internal Damage model.

C.1. Plasticity Models

Elastic-plastic, Mohr-Coulomb yield criterion, isotropic hardening (NCRIT = 4)

The Mohr-Coulomb yield criterion is applicable to frictional materials (e.g. soil, rock, concrete) for which yielding depends on the hydrostatic pressure. It is a generalisation of the Coulomb friction law defined by

$$\tau = c - \sigma_n \tan \phi.$$

Flow rule normality is assumed and thus inelastic deformations are of a dilatant (volume increase) nature.

Elastic-plastic, Drucker-Prager yield criterion, isotropic hardening (NCRIT = 5)

This is the classical Drucker-Prager model with the compression side of the yield surface unbounded. It represents an extension of the von Mises yield criterion to include the influence of the hydrostatic stress on yielding. Inelastic deformations are of a dilatant nature since normality is assumed. It is applicable to frictional materials such as soils, rock and concrete.

Elastic-Plastic, Druker-Prager yield criterion with hardening/softening compression cap and tension cut-off (NCRIT = 6)

This constitutive model uses a perfectly plastic Drucker-Prager yield criterion coupled to a compression cap which can harden or soften depending on the volume plastic strain. The tension side is bounded by a perfectly plastic tension cut-off yield surface.

The equations which define the yield surfaces for this model are as follows (refer to Fig. 4.5):

Drucker-Prager: $\alpha J_1 + \sqrt{J_2'} - k = 0$

Cap: $- J_1 + R^2 J_2' + J_{1Bcurrent} = 0$

Tension Cut-off: $J_1 - T = 0$

(Note that $J_1 = 3\sigma_m$ and $J_2' = s^2$).

Normality of the flow rule is assumed for all yield surfaces.

This model is applicable to frictional materials which exhibit strain softening in shear and stiffening due to volumetric compaction. Pure shear plastic yield is also provided for in this model.

The analyst is advised to study the NOSTRUM theoretical manual before attempting to use this model.

MATERIAL PROPERTIES: **NCRIT** = 4

ELASTIC-PLASTIC, MOHR-COULOMB YIELD CRITERION,

ISOTROPIC HARDENING

The material properties required are as follows:

E	ν	c	H	ø

E Young's modulus

ν Poisson's ratio

c cohesion

H strain hardening parameter

ø angle of internal friction (in degrees)

The parameter **H** is defined as for constitutive models 2 and 3 - see also Fig. 4.3. Refer to Fig. 4.4 for shape of yield surface.

MATERIAL PROPERTIES: **NCRIT** = 5
ELASTIC-PLASTIC, DRUCKER-PRAGER YIELD CRITERION,
ISOTROPIC HARDENING

The material properties required are as follows:

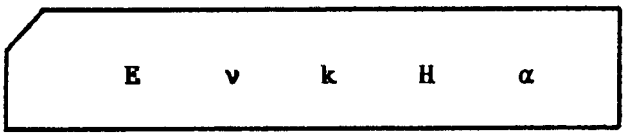

E	Young's modulus
ν	Poisson's ratio
k	Drucker-Prager constant
H	strain hardening parameter
α	Drucker-Prager constant

The parameter **H** is defined as for constitutive models 2 and 3 - see also Fig. 4.3. Refer to Fig. 4.4 for shape of yield surface

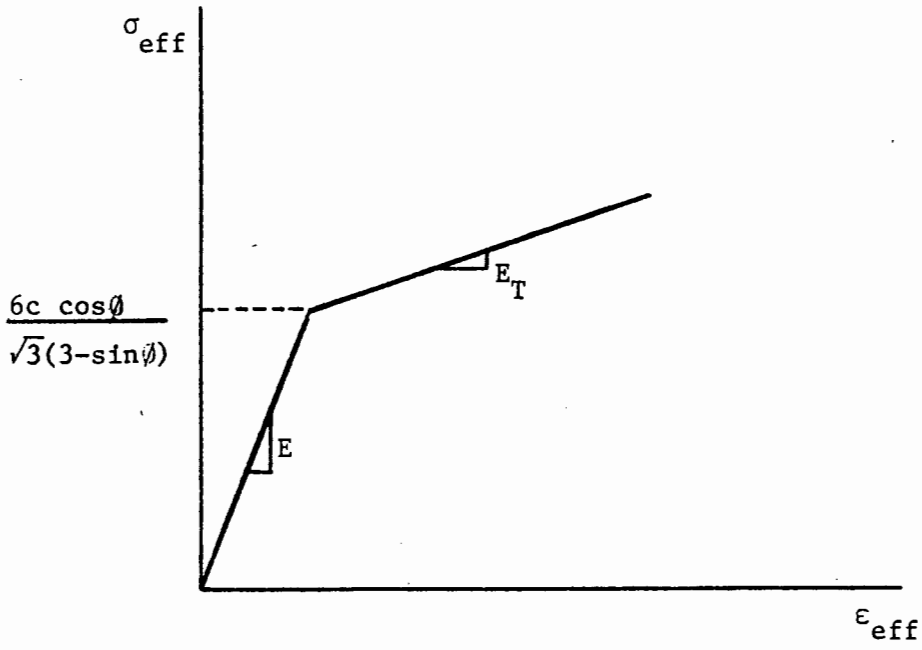

Fig. 4.3 Effective stress/strain relation

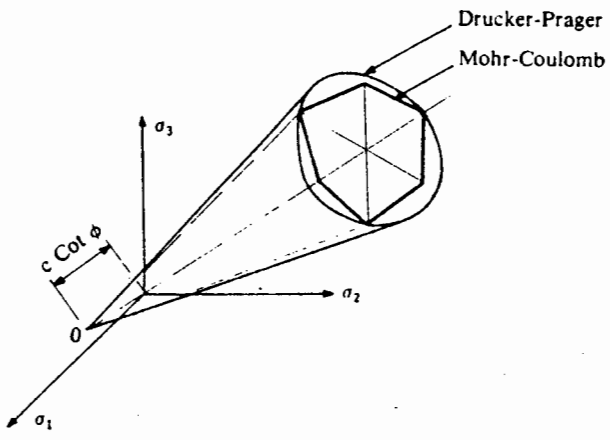

Fig. 4.4 Mohr-Coulomb and Drucker-Prager yield surfaces

MATERIAL PROPERTIES: **NCRIT** = 6

ELASTIC-PLASTIC, DRUCKER-PRAGER YIELD CRITERION WITH COMPRESSION CAP AND TENSION CUT-OFF

The analyst is advised to consult Section 4.1.2.2 of this manual as well as the NOSTRUM Theoretical Manual before attempting to use this material model. The material properties required are as follows:

E	**ν**	**k**	**α**	**R**	$J_{1B\text{initial}}$	**W**	**D**	**T**

Elastic parameters:

E Young's modulus

ν Poisson's ratio

Drucker-Prager parameters:

k Drucker-Prager constant (in stress units and positive)

α Drucker-Prager constant (dimensionless and positive)

For different Drucker-Prager fits of the Mohr-Coulomb yield criterion, refer to the NSMRU report number 40.

Cap parameters (see Fig. 4.5(a))

R cap shape factor (positive); **R** = 0 is a straight vertical cap

$J_{1B\text{initial}}$ initial cap position (in stress units and negative or zero)

$$\varepsilon^{p}_{kk} = W\left(1 - e^{DJ_{1B\text{current}}}\right)$$

W limiting volumetric plastic strain (V.P.S.) (dimensionless and negative)

D "rate" of plastic compaction (in inverse stress units and positive)

Tension cut-off parameter:

T tension cut-off limit (in stress units and positive)

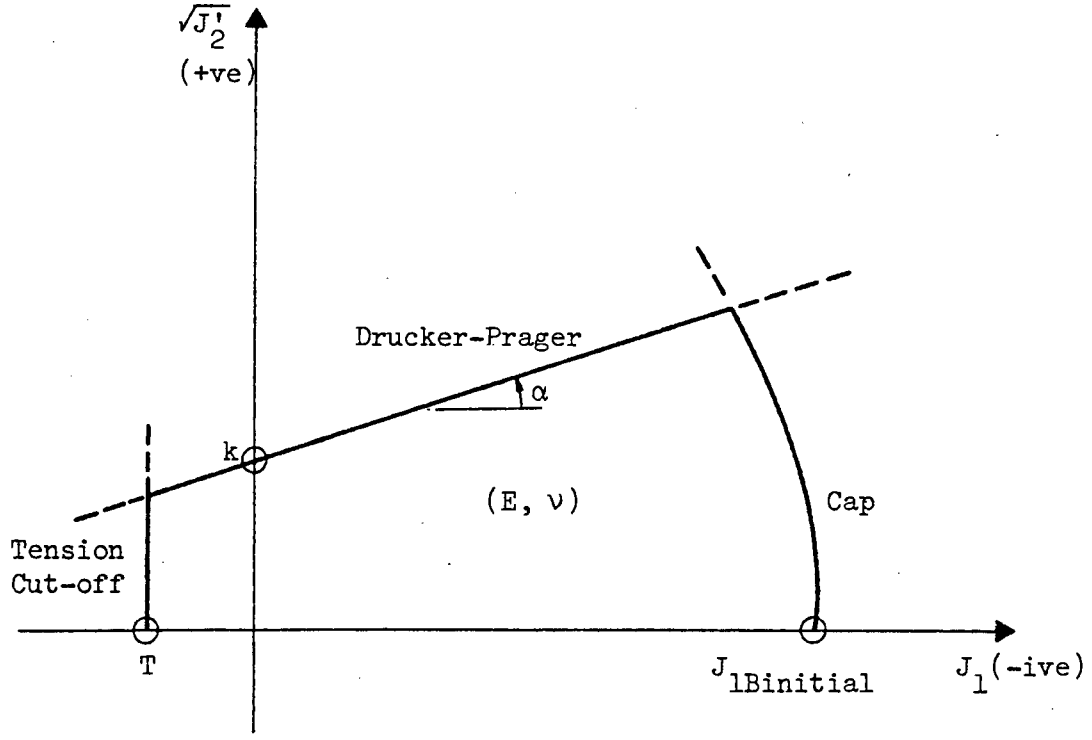

Fig.4.5(a): Granular material plasticity yield surface

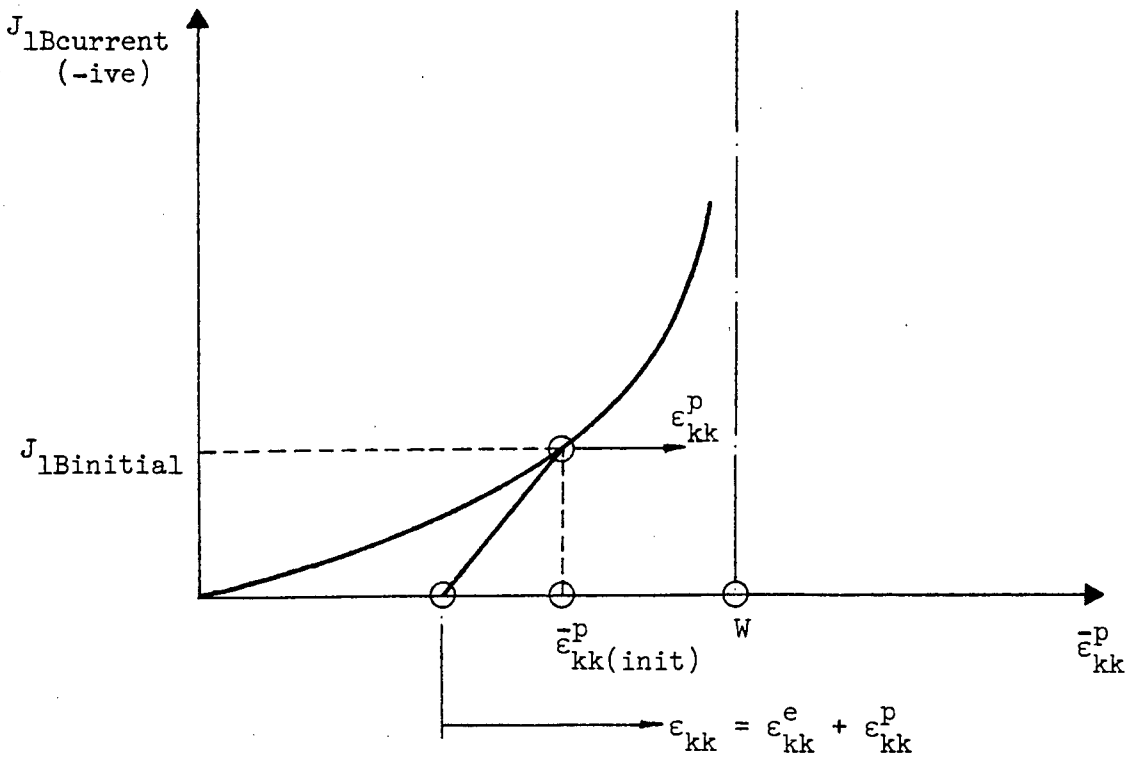

Fig.4.5(b): Cap nonlinear hardening law

C.2 Damage Model

Internal Damage (NCRIT = 9)

This model is based on progressive fracturing theory for the shear behaviour whereas the volumetric behaviour is formulated using ideas arising from the hydrostatic compression cap yield surfaces of plasticity fitted into a broadened progressive fracturing framework. The hydrostatic tension behaviour is also based on some form of progressive fracturing. The progressive fracturing leads to degradation of the elastic properties and is expressed in terms of an internal variable which is defined as a damage parameter. An evolution law relates the rate of damage to the stress and strain history.

This model is applicable to frictional materials such as rock and concrete which exhibit possible strain softening in shear accompanied by predominantly dilatant volumetric behaviour. These materials also exhibit stiffening due to volumetric compaction and dilatant strain softening behaviour in volumetric tension.

The analyst is urged to study the Nonlinear Structural Mechanics Research Unit Technical Reports 27 and 44 before attempting to use this model.

MATERIAL PROPERTIES: **NCRIT** = 9

INTERNAL DAMAGE MODEL

The analyst is advised to consult Section 4.1.2.2 of this manual as well as the Nonlinear Structural Mechanics Research Unit Technical Reports 27 and 44 before attempting to use this model. The material properties required should be input in 3 separate cards as follows:

G_o	W	D	$\varepsilon_{vmax(o)}$

NEVOL	a_1	a_2	a_3	a_4	a_5	b_1 or a_6	b_2	b_3

c_1	c_2	c_3	d_1

G_o initial elastic shear modulus (positive and in stress units)

W elastic volumetric hardening parameter (negative and dimensionless)

D elastic volumetric hardening parameter (positive and in inverse stress units)

$\varepsilon_{vmax(o)}$ initial volume strain (negative, zero or positive and dimensionless)

NEVOL type of evolution law

1. $\dot{\lambda} = \{a_1+a_2\sigma_m+a_3\sigma_m^2+2a_4 e\sigma_m +3a_5 e^2\}\,\dot{e} + \{b_1+b_2\varepsilon_v+b_3\varepsilon_v^2\}\,\dot{\varepsilon}_v$

2. $\dot{\lambda} = \{2\,[a_1+a_2\,\exp(a_3\sigma_m)]e + 3[a_4+a_5\,\exp(a_6\sigma_m)]e^2\}\dot{e} + \{b_2\varepsilon_v+b_3\varepsilon_v^2\}\dot{\varepsilon}_v$

3. Bushveld Norite, enter ϕ.'s for a_1-a_6 , b_1-b_3 (experimental damage curves are used)

a_1 - a_6 shear damage evolution constants

b_1 - b_3 hydrostatic tension damage evolution constants

c_1 - c_3 inelastic volumetric behaviour material constants

d_1 inelastic shear behaviour material constant

APPENDIX D

PUBLISHED WORK

The following works, co-authored with Professor J.B. Martin, have been published or accepted for publication:

1. RESENDE, L. and MARTIN, J.B., 'The Formulation of the Drucker-Prager Cap Model', J. Eng. Mech. Div., ASCE, to appear.

2. RESENDE, L. and MARTIN, J.B., 'A Progressive Damage Continuum Model for Granular Materials', CMAME, 42, 1-18, 1984.

3. RESENDE, L. and MARTIN, J.B., 'Damage Constitutive Model for Geotechnical Applications', Int. Conf. Num. Meth. Transient and Coupled Problems, Venice, 475-497, July 1984.

4. RESENDE, L. and MARTIN, J.B., 'Constitutive Modelling and Finite Element Analysis in Rock Mechanics', to be presented at the 5th Symp. F.E. Meth. in S.A., University of Stellenbosch, February 1985.